3D brain tumors and internal brain structures segmentation in MR images

Hassan Khotanlou

Thèse

présentée pour obtenir le grade de docteur
de l'École Nationale Supérieure des Télécommunications

Spécialité : **Signal et Images**

Hassan KHOTANLOU

Segmentation 3D de tumeurs et de structures internes du cerveau en IRM

3D brain tumors and internal brain structures segmentation in MR images

Soutenue le 7 Février 2008 devant le jury composé de:

Nicole Vincent	Président
Su Ruan	Rapporteur
Christophe Léger	Rapporteur
Hubert Cardot	Examinateur
Isabelle Bloch	Directeur de thèse

Acknowledgements

The completion of this dissertation would not have been possible without the encouragement, help and friendship of many individuals. It is my privilege to thank the people who have supported and guided me throughout my pursuit of this thesis, and my sincere apologies to the people I may miss.

I could not be thankful enough for having had professor Isabelle Bloch as my supervisor, who is a true friend to me. Under her guidance, I have learnt to identify and approach research problems, and to develop and present the solutions in a comprehensible manner. Whenever I had a problem of personal, academic, research, of any nature, her door of help was always opened for me.

I would like thank professor Nicole Vincent, professor Su Ruan, professor Christophe Léger and professor Hubert Cardot for serving on my dissertation committee. Their insightful feedback and approval of my research goals and objectives have helped me to complete this thesis.

I would like to express my sincere thanks to professor Henri Maitre, professor Elsa Angelini and professor Francis Schmitt for their help and friendship.

During these years I have collaborated with many people. My sincere thanks to Olivier Colliot, Jamal Atif, Celine Hudelot and Najib Gadi for his encouragements and his friendship during their post doctoral stay at ENST. I must appreciate for their helping attitude which was the constant motivating factor for me to complete this thesis.

Special thanks to my colleagues at ENST, Antonio Moreno, Sylvie Chambon, Geoffroy Fouquier, Jeremie Anquez, Olivier Nempont, Adel Kermi, Avik Bhattacharya, Bin Luo, Saied Homayouni, Hassan Teimoori, Mehdi Ebad Zadeh, Mohammad Vahdani and Mohammad Gharaie for their moral support and for sharing my workload during my thesis period.

I am especially grateful to the members of the TSI department, Patricia Friedrich, Catherine Vazza, Bahman Nabati, Dominique Asselineau, Sophie-Charlotte Barriere and Gilbert Papalia.

I would like to thank the members of the Graduate School (EDIT), Florence Besnard and Iwona Fagot for their help and friendship.

I wish to express my sincere thanks to professor Mansour Gholami and professor Ardeshir Khazaei, presidents of Bu-Ali Sina (avecina) university during my thesis, for their encouragement and help.

Finally, I would like to express special thanks to my family. The encouragement and support from my beloved wife, Tayebeh, and our always positive and joyful children, Zahra and Mohammad, is a powerful source of inspiration and energy.

Abstract

The main topic of this thesis is to segment brain tumors, their components (edema and necrosis) and internal structures of the brain in 3D MR images. For tumor segmentation we propose a framework that is a combination of region-based and boundary-based paradigms. In this framework, we first segment the brain using a method adapted for pathological cases and extract some global information on the tumor by symmetry-based histogram analysis. The second step segments the tumor and its components. For this, we propose a new and original method that combines region and boundary information in two phases: initialization and refinement. For initialization, which is mostly region-based, we present two new methods. The first one is a new fuzzy classification method which combines the membership, typicality and neighborhood information of the voxels. The second one relies on symmetry-based histogram analysis. The initial segmentation of the tumor is refined relying on boundary information of the image. This method is a deformable model constrained by spatial relations. The spatial relations are obtained based on the initial segmentation and surrounded tissues of the tumor. The proposed method can be used for a large class of tumors in any modality of MR images. To segment a tumor and its components full automatically the proposed framework needs only a contrast enhanced T1-weighted image and a FLAIR image. In the case of a contrast enhanced T1-weighted image only, some user interaction will be needed.

We evaluated this method on a data set of 20 contrast enhanced T1-weighted and 10 FLAIR images with different types of tumors.

Another aim of this thesis is the segmentation of internal brain structures in the presence of a tumor. For this, a priori knowledge about the anatomy and the spatial organization of the structures is provided by an ontology. To segment each structure, we first exploit its relative spatial position from a priori knowledge. We then select the spatial relations which remain consistent using the information on the segmented tumor. These spatial relations are then fuzzified and fused in a framework proposed by our group. As for the tumor, the segmentation process of each structure has two steps. In the first step we search the initial segmentation of the structure in a globally segmented brain. The search process is done in the region of interest (ROI) provided by the fused spatial relations. To globally segment the brain structures we use two methods, the first one is the proposed fuzzy classification and the second one

is a multiphase level sets. To refine the initial segmentation, we use a deformable model which is again constrained by the fused spatial relations of the structure. This method was also evaluated on 10 contrast enhanced T1-weighted images to segment the ventricles, caudate nucleus and thalamus.

Résumé

Le sujet principal de cette thèse est la segmentation 3D de tumeurs du cerveau et de leurs différentes composantes (oedème et nécrose), ainsi que de structures internes du cerveau en IRM. Pour la segmentation de tumeurs nous proposons un cadre général qui est une combinaison des paradigmes fondés sur les régions et les contours. Dans ce cadre, nous segmentons d'abord le cerveau en utilisant une méthode adaptée aux cas pathologiques et extrayons des informations globales sur la tumeur par analyse de symétrie. La deuxième étape segmente la tumeur et ses composantes. Pour cela, nous proposons une méthode nouvelle et originale qui combine l'information de régions et de contours en deux phases. Pour la première, l'initialisation, nous présentons deux nouvelles méthodes. La première est une nouvelle méthode de classification floue qui exploite à la fois l'information des voxels et leurs voisinages (inspirés des champs Markov (MRF)), l'appartenance et la typicalité. La seconde se fonde sur l'analyse de la symétrie. La segmentation initiale de la tumeur est raffinée dans la deuxième phase par un modèle déformable contraint par des relations spatiales. Les relations spatiales sont obtenues en utilisant la segmentation initiale et les tissus environnant la tumeur. La méthode proposée peut être employée pour une grande classe de tumeurs dans n'importe quelle modalité en IRM. Pour segmenter une tumeur et ses composantes automatiquement, le cadre proposé a besoin seulement d'une image CE-T1w (*contrast enhanced T1-weighted*) et d'une image FLAIR. Dans le cas d'une image CE-T1w seulement, l'interaction de l'utilisateur peut être nécessaire. Nous avons évalué cette méthode sur une base de données de 20 images CE-T1w et 10 images FLAIR avec différents types de tumeurs.

Un autre but de cette thèse est la segmentation de structures internes du cerveau en présence d'une tumeur. Pour cela, une connaissance a priori sur l'anatomie et l'organisation spatiale des structures est fournie par une ontologie. Pour segmenter chaque structure, nous exploitons ses relations spatiales par rapport à d'autres structures, selon la connaissance a priori. Nous choisissons alors les relations spatiales qui sont valables en fonction de la tumeur segmentée. Ces relations spatiales sont alors modélisées dans un cadre flou proposé par notre groupe. Comme pour la tumeur, la procédure de segmentation de chaque structure comporte deux étapes. Dans la première étape nous recherchons la segmentation initiale de la structure dans le cerveau globalement segmenté. Le processus de recherche est fait dans la région d'intérêt fournie par la fusion des relations spatiales. Pour segmenter globalement les structures

du cerveau nous employons deux méthodes. La première est la classification floue proposée et la seconde repose sur les ensembles de niveaux multi-phases. Pour raffiner la segmentation initiale, nous employons un modèle déformable qui est contraint par les relations spatiales de la structure. Cette méthode a été également évaluée sur 10 images CE-T1w pour segmenter les ventricules, les noyaux caudés et les thalami.

Table of contents

List of figures xv

List of tables xxi

Résumé en français xxiii

Introduction 1

1 Brain tumor classification 5

1.1 Introduction . . . 5

1.2 Anatomy of the brain . . . 5

1.3 Magnetic resonance imaging (MRI) of brain tumors . . . 6

1.3.1 Pros and cons of MRI . . . 8

1.3.2 MRI physics . . . 9

1.3.3 MRI modalities . . . 9

1.4 Brain tumors . . . 12

1.5 Classification of brain tumors . . . 14

1.6 The tumors of WHO classification . . . 15

1.6.1 Gliomas . . . 15

1.6.2 Medulloblastoma (Primitive Neuroectodermal Tumor (PNET)) 23

1.6.3 Lymphoma . . . 23

1.6.4 Meningioma 25
1.6.5 Craniopharyngioma 25
1.6.6 Pituitary adenoma 26
1.6.7 Summary 27
1.7 Classification of tumors based on their location 28
1.8 Classification of tumors based on their radiologic appearance 29
1.8.1 Non-enhanced tumors 29
1.8.2 Full-enhanced tumors without edema 29
1.8.3 Full-enhanced tumors with edema 30
1.8.4 Ring-enhanced tumors 30
1.9 Classification of tumors based on their alterations 31
1.9.1 Small deforming tumors (SD) 31
1.9.2 Large deforming tumors (LD) 32
1.10 Evaluation data set 32
1.11 Conclusion 32

2 Tumor segmentation methods: a survey **35**
2.1 Introduction 35
2.2 Region-based methods 36
2.2.1 Classification-based 40
2.2.2 Clustering-based 45
2.2.3 Morphology-based 46
2.2.4 Atlas-based 47
2.2.5 Knowledge based 49
2.2.6 Texture-based 49
2.2.7 Feature extraction 51

2.2.8 Neural network-based . . . 52
2.2.9 Fusion-based . . . 53
2.2.10 Fuzzy methods . . . 54
2.2.11 Fractal-based . . . 55
2.2.12 Summary of region-based methods . . . 56
2.3 Boundary-based methods . . . 56
2.3.1 Parametric deformable models (snakes) . . . 57
2.3.2 Geometric deformable model . . . 58
2.3.3 Summary of boundary-based methods . . . 59
2.4 Fusion of region and boundary-based methods . . . 60
2.4.1 Combination of region-based methods with snakes . . . 60
2.4.2 Combination of region-based methods with level sets . . . 62
2.4.3 Summary of fusion of region and boundary . . . 62
2.5 Conclusion . . . 63

3 Brain tumor segmentation: part I, preprocessing 65

3.1 Introduction . . . 65
3.2 Method overview . . . 66
3.3 Preprocessing . . . 68
3.3.1 Image preprocessing . . . 68
3.3.2 Registration and spatial interpolation . . . 68
3.3.3 Symmetry plane computation . . . 70
3.3.4 Brain segmentation . . . 73
3.3.5 Symmetry-based histogram analysis . . . 75
3.4 Conclusion . . . 82

4 Brain tumor segmentation: part II, segmentation **87**

4.1 Introduction . . . 87

4.2 Method overview . . . 88

4.3 Detection and initial segmentation . . . 89

4.3.1 Detection by modified PFCM . . . 89

4.3.2 Tumor detection by symmetry analysis . . . 105

4.4 Segmentation refinement . . . 113

4.4.1 Deformable model . . . 113

4.4.2 Deformable model constrained by spatial relations . . . 116

4.5 Segmentation of edema and necrosis . . . 123

4.6 Results and discussion . . . 126

4.7 Conclusion . . . 129

5 Segmentation of Internal Brain Structures **143**

5.1 Introduction . . . 143

5.2 Brain structures segmentation: a survey . . . 144

5.3 Method overview . . . 151

5.4 A priori knowledge . . . 152

5.4.1 Ontological engineering . . . 152

5.4.2 The reference ontology for biomedical informatics (FMA) . . . 153

5.4.3 Spatial relation ontology . . . 155

5.5 Spatial relations representation . . . 156

5.6 Tumor-specific spatial relations . . . 159

5.6.1 Tumor classification . . . 160

5.6.2 Stable spatial relations . . . 161

5.7 Structure segmentation . . . 163

5.8 Evaluation and results 171
5.9 Conclusion 171

6 Conclusion **181**
6.1 Review of the contributions 181
6.2 Future work 183

A MPFCM objective function solving **185**
A.1 Membership 185
A.2 Typicality 186
A.3 Class centers 186

B Evaluation of segmentation **189**
B.1 Volume metrics 189
B.2 Surface or distance-based metrics 192

C Multiphase level sets segmentation **195**
C.1 Multiphase level sets model 195
C.2 3D 4-phase level sets numerical algorithm 197

Publications **201**

Bibliography **203**

Index of citations by papers **223**

Glossary **227**

Liste of figures

1 Schéma général de la méthode proposée xxiv

2 Méthodes existantes pour la segmentation de tumeurs cérébrales. . xxvi

3 Cadre général proposé pour la segmentation de tumeurs du cerveau. xxvii

4 Schéma de la méthode proposée pour la segmentation de tumeurs . xxviii

5 Détection d'une tumeur par MPFCM xxx

6 Graphes de $\mathbf{H}_s$, $\mathbf{H}_n$ et $\mathbf{H}_p$ pour une tumeur NEN xxxii

7 Graphes de $\mathbf{H}_s$, $\mathbf{H}_n$ et $\mathbf{H}_p$ pour une tumeur FEN xxxiii

8 Graphes de $\mathbf{H}_s$, $\mathbf{H}_n$ et $\mathbf{H}_p$ pour une tumeur FEN avec œdème . . . xxxiv

9 Graphes de $\mathbf{H}_s$, $\mathbf{H}_n$ et $\mathbf{H}_p$ pour une tumeur NEN xxxv

10 Graphes de $\mathbf{H}_s$, $\mathbf{H}_n$ et $\mathbf{H}_p$ pour une tumeur dans une image FLAIR xxxvi

11 Relations spatiales utilisées pour raffiner la segmentation xxxvi

12 Force externe $\mathbf{F}_R$ calculée pour un sous-ensemble flou μ_R xxxvii

13 Graphe des résultats quantitatifs pour les tumeurs FEN xxxviii

14 Graphe des résultats quantitatifs pour les tumeurs NEN xxxix

15 Graphe des résultats quantitatifs pour les tumeurs dans les images FLAIR xxxix

16 Comparaison des segmentations manuelle et automatique xl

17 Comparaison des segmentations manuelle et automatique xli

18 Schéma général de la méthode proposée xlii

19 Une partie de l'ontologie du FMA et l'ontologie de relations spatiales xliii
20 Représentation d'une relation directionnelle par ensemble flou . . . xliv
21 Une partie de l'ontologie de tumeurs xlv
22 Résultats de segmentation xlvii
23 Vue 3D des structures, de la tumeur et de l'œdème segmentés . . . xlviii

24 Proposed methods for tumor and brain structures segmentation . . 3

1.1 Some brain structures illustrated on a schematic drawing 7
1.2 Anatomy of the brain 7
1.3 MRI of brain 13
1.4 One axial slice of a MR image of the brain showing tumor areas . . 14
1.5 Low grade astrocytoma 18
1.6 Diffuse low grade astrocytoma 19
1.7 Glioblastoma multiform 19
1.8 Glioblastoma multiform 20
1.9 Ganglioglioma 20
1.10 Low grade oligodendroglioma 21
1.11 A cystic oligodendroglioma 22
1.12 High grade oligodendroglioma 22
1.13 Ependymoma 23
1.14 Medulloblastoma 24
1.15 Lymphoma tumor 24
1.16 Meningioma tumor 26
1.17 Craniopharyngioma 26
1.18 Pituitary adenoma 27

1.19 Various types of brain tumors in various places in the CNS 28
1.20 A non-enhanced tumor 29
1.21 A full-enhanced tumor without edema 30
1.22 A full-enhanced tumor with edema 30
1.23 A ring-enhanced tumor 31
1.24 Classification based on the tumor alterations 32

2.1 Classification of existing tumor segmentation methods. 37
2.2 Block diagram of the method proposed by [Chen and Metaxas, 2003] 61

3.1 Proposed framework for brain tumor segmentation 67
3.2 Bias field correction 69
3.3 Result of rigid registration methods 71
3.4 Symmetry plane computation 73
3.5 Pathological brain segmentation using existing methods 74
3.6 The proposed algorithm for pathological brain segmentation 75
3.7 Histograms of the brain, right hemisphere and left hemisphere . . . 76
3.8 Histogram filtering (with low noise) 77
3.9 Histogram filtering (with high noise) 78
3.10 Histograms difference 79
3.11 The extrema of a pathological brain 80
3.12 The signatures and scale selections of GM and WM modes 81
3.13 Detection of tumor type and pathological hemisphere 82
3.14 Detection of tumor type and pathological hemisphere 84
3.15 Detection of pathological hemisphere in a FLAIR image 85

4.1 The segmentation method diagram. 88

4.2 Comparison of classification results 94
4.3 Comparison of classification accuracy (C_A) of algorithms. 95
4.4 Comparison of the convergence of classification algorithms 95
4.5 Comparison of classification results for a large full-enhanced tumor 97
4.6 Comparison of classification results for a small tumor 98
4.7 Comparison of classification results for a ring-enhanced tumor . . . 99
4.8 Comparison of classification results for a non-enhanced tumor . . . 100
4.9 Comparison of classification results for a tumor in a FLAIR image . 101
4.10 Tumor detection result for a relatively large full-enhanced tumor . . 101
4.11 Tumor detection result for a small full-enhanced tumor 102
4.12 Tumor detection result for a ring-enhanced tumor 102
4.13 Tumor detection result for a non-enhanced tumor in a FLAIR image 103
4.14 Comparison of histograms for a normal and a pathological image . . 107
4.15 Tumor (non-enhanced) detection by symmetry analysis 107
4.16 Tumor (full-enhanced without edema) detection by symmetry analysis 108
4.17 Tumor (full-enhanced with edema) detection by symmetry analysis 109
4.18 Tumor (full-enhanced without edema) detection by symmetry analysis 110
4.19 Tumor (ring-enhanced) detection by symmetry analysis 111
4.20 Tumor detection by symmetry analysis in a FLAIR image 112
4.21 Fuzzy interval on the set of the relation “near” 119
4.22 Spatial relations used for segmenting the tumor 120
4.23 External force $\mathbf{F}_R$ computed from a fuzzy subset μ_R 121
4.24 Segmentation of edema 125
4.25 Segmentation of edema 126
4.26 Graph of the quantitative results for enhanced tumors 128

4.27 Graph of the quantitative results for non-enhanced tumors 128
4.28 Graph of the quantitative results for tumors in FLAIR images . . . 129
4.29 Comparison of manual and automatic segmentation results 130
4.30 Comparison of manual and automatic segmentation results 131
4.31 Comparison of manual and automatic segmentation results 132
4.32 Comparison of manual and automatic segmentation results 133
4.33 Comparison of manual and automatic segmentation results 134
4.34 Comparison of manual and automatic segmentation results 135
4.35 Comparison of manual and automatic segmentation results 136
4.36 Comparison of manual and automatic segmentation results 137
4.37 Comparison of manual and automatic segmentation results 138
4.38 Axial and coronal slices of a segmented tumor 139
4.39 Axial and coronal slices of a segmented tumor 140
4.40 Axial and coronal slices of a segmented tumor 141

5.1 The segmentation method diagram. 152
5.2 A part of the FMA ontology 154
5.3 Excerpt of the hierarchical organization of spatial relations 155
5.4 Main concepts of the spatial relation ontology 156
5.5 A part of the FMA ontology and the spatial relation ontology . . . 157
5.6 Fuzzy set representing a directional relation 158
5.7 Fuzzy set representing a distance relation 159
5.8 Main concepts of the tumor ontology 161
5.9 A part of the tumor ontology visualized by Protégé. 162
5.10 Segmentation by multiphase level sets 164
5.11 Segmentation of the right and the left caudate nucleus 166

5.12 Segmentation of the right and the left caudate nucleus 167

5.13 Segmentation of the right and the left thalamus 168

5.14 Segmentation of the right and the left thalamus 169

5.15 Ventricular segmentation 171

5.16 Segmentation results 176

5.17 Segmentation results 177

5.18 Segmentation results 178

5.19 3D view of the segmented structures, tumor, edema and necrosis . . 179

B.1 Representation of M, A, T_p, F_p and F_n as a Venn diagram. 190

B.2 Illustrative examples for similarity index 190

B.3 Illustrative example for correct detection ratio 191

Liste of tables

1 Relations spatiales spécifiques à chaque type de tumeurs. xlv

1.1 Some terms used to describe magnetic resonance imaging techniques 11

1.2 Primary brain and central nervous system tumors 16

1.3 Brain tumors properties 27

1.4 Specifications of the CE-T1w images in our data set 33

1.5 Specifications of the FLAIR images in our data set. 34

2.1 Region-based methods in the literature. 38

2.2 Boundary-based and fusion of region- and boundary-based methods 39

3.1 Result of tumor type and pathological hemisphere detection 83

3.2 Result of pathological hemisphere detection in FLAIR images . . . 86

4.1 Quantitative comparison of classification results 96

4.2 Tumor detection result for a non-enhanced tumor in a FLAIR image 104

4.3 Evaluation of the segmentation results of tumors in FLAIR images . 105

4.4 Evaluation of the initial segmentation results of tumors 114

4.5 Evaluation of the initial segmentation results of tumors 115

4.6 Evaluation of the refined segmentation results by deformable model 117

4.7 Evaluation of the refined segmentation results by deformable model 118

4.8 Evaluation of the refined segmentation results by deformable model 119

4.9 Evaluation of the refined segmentation results in FLAIR images . . 120

4.10 Evaluation of the refined segmentation results 122

4.11 Evaluation of the refined segmentation results 123

4.12 Evaluation of the segmentation results of edema 124

5.1 Spatial relations for internal brain structures depending on the tumor's type. 162

5.2 Evaluation of segmentation result of the caudate nuclei 172

5.3 Evaluation of segmentation result of the thalamus 173

5.4 Evaluation of segmentation result of the caudate nuclei 174

5.5 Evaluation of segmentation result of the thalamus 175

Résumé en français

Introduction

A des fins aussi diverses que l'aide au diagnostic, le suivi et la planification thérapeutiques, le support à l'enseignement, le raisonnement à partir de cas, l'indexation et la fouille de données, il est primordial de disposer d'une description intégrant, dans la modélisation du cerveau humain, la localisation de la tumeur, son type, sa segmentation, son positionnement anatomo-fonctionnel, la description des structures environnantes et de leurs relations spatiales. Si la littérature est riche en travaux sur la segmentation des structures cérébrales et celle de pathologies, ces deux composantes sont rarement intégrées, et la description de la pathologie via ses relations spatiales aux structures normales a connu peu de développements en traitement d'images. De plus les méthodes dédiées à la segmentation des pathologies tumorales souffrent d'un manque de robustesse, de précision et sont dans la plupart des cas supervisées. Elles sont ainsi difficilement généralisables à divers types de tumeurs.

Dans cette thèse, nous avons d'abord étudié les caractéristiques et les apparences de différents types de tumeurs dans les images médicales et nous avons proposé trois classifications différentes des types de tumeurs. En utilisant ces classifications nous présentons une méthode originale de segmentation 3D de tumeurs cérébrales en imagerie par résonance magnétique (IRM), ainsi que leur intégration dans un modèle anatomique du cerveau construit à partir de la segmentation et la reconnaissance de structures normales dans l'image IRM. Le modèle proposé est donc spécifique et adapté au cas individuel traité.

L'approche globale suit le schéma suivant (figure 1) :

- **Détection et segmentation de la pathologie tumorale** : cette étape repose sur une méthode de segmentation originale en deux étapes : une segmentation initiale est réalisée par deux méthodes : une méthode de classification floue et une méthode d'analyse de symétrie ; puis la segmentation est raffinée par un modèle déformable paramétrique utilisant le flux de vecteur gradient généralisé.
- **Segmentation des structures cérébrales internes** : cette partie s'appuie

sur une méthode développée pour les images normales. Il s'agit d'une approche contextuelle de la segmentation s'appuyant sur des descriptions structurelles (essentiellement des relations spatiales) décrites dans des manuels d'anatomie. La méthode s'appuie sur la fusion de contraintes ou connaissances a priori modélisées par des ensembles flous et leur intégration dans un modèle déformable comme une force externe supplémentaire. Dans le cadre des images pathologiques, nous montrons que la méthode reste robuste pour certaines structures internes.

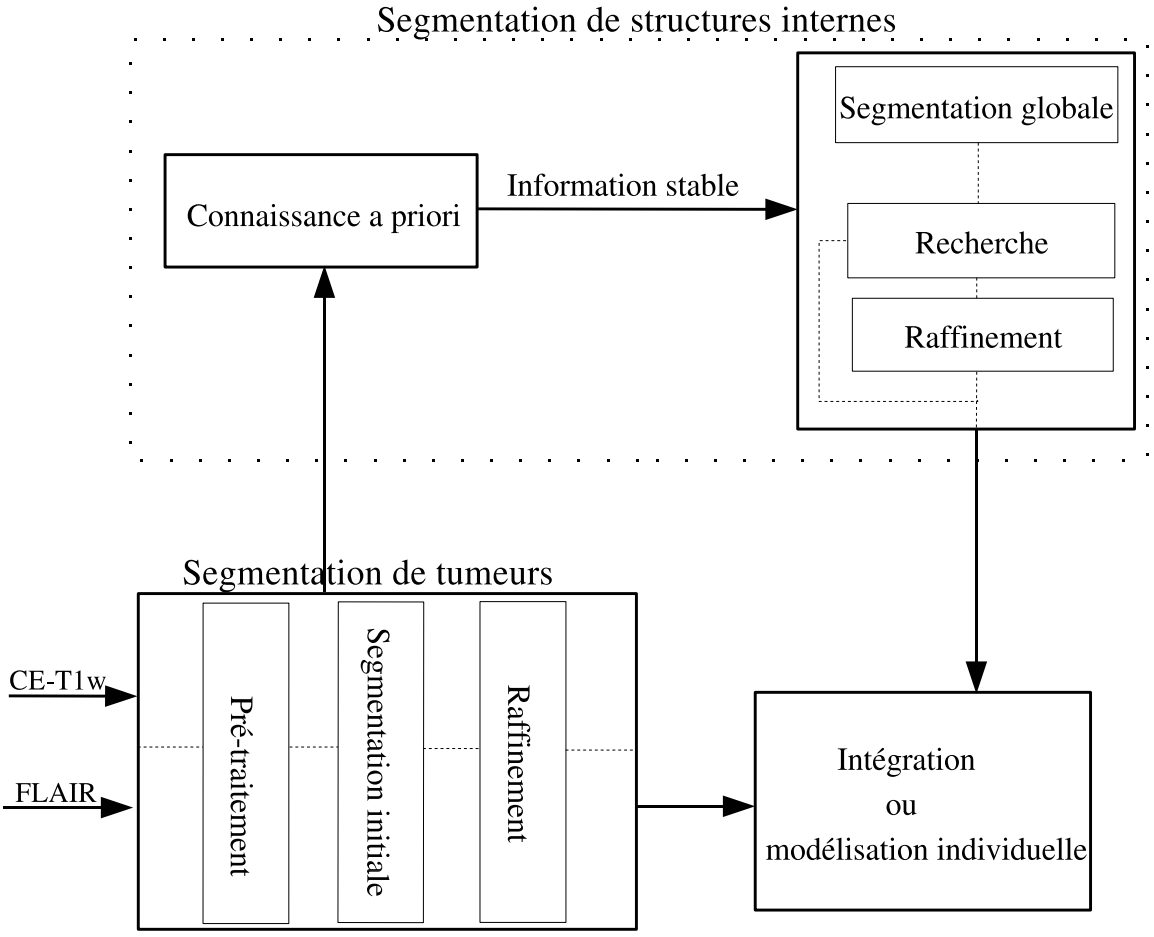

Figure 1: Schéma général de la méthode proposée pour la segmentation de tumeurs et de structures internes du cerveau.

Segmentation automatique de tumeurs cérébrales

En général, le but le plus important de l'analyse d'images médicales, et en particulier l'analyse de l'IRM du cerveau, est l'extraction de l'information clinique qui permet le diagnostic et le traitement de la maladie. Les tumeurs du cerveau sont une maladie

grave, ce qui nécessite la détection et la segmentation de tumeurs du cerveau dans les IRM pour le diagnostic médical.

La littérature en traitement d'images est riche en méthodes de segmentation de structures cérébrales normales, mais peu de méthodes concernent les pathologies. Force est de constater que ces méthodes, initialement conçues pour les structures saines, trouvent leurs limites dès qu'une pathologie vient désorganiser l'agencement structurel et altérer les valeurs radiométriques des tissus cérébraux. Les méthodes dédiées à la détection de tumeurs cérébrales en sont encore à un stade exploratoire, et les quelques techniques publiées à ce jour souffrent d'un manque de robustesse, de précision, et nécessitent dans leur majorité une interaction manuelle.

Les méthodes traitant de la segmentation de tumeurs cérébrales se divisent en trois classes : les approches par régions, les approches par contours et les approches combinant une approche par régions et une approche par contours. La figure 2 présente une classification des méthodes existantes pour la segmentation de tumeurs cérébrales.

Le cadre général de la segmentation de tumeurs du cerveau que nous avons développé comprend deux composantes principales : prétraitement et segmentation, comme illustré dans la figure 3. Les entrées de ce système sont deux modalités différentes d'IRM : CE-T1w (*contrast enhanced T1-weighted*) et FLAIR. Nous pensons qu'elles sont suffisantes pour la segmentation de tumeurs du cerveau. L'étape de prétraitement comprend les opérations de réduction d'hétérogénéité d'intensité et de variation d'intensité inter-coupes des images, de recalage des images d'entrée, de segmentation du cerveau et le calcul du plan de symétrie inter-hémisphérique.

L'étape de segmentation, fondée sur les informations fournies à l'issue du prétraitement, est divisée en deux branches. Dans le cas d'une tumeur qui ne prend pas de contraste en CE-T1w (*non-enhanced*), sans œdème et sans nécrose, nous segmentons la tumeur dans l'image FLAIR avec une nouvelle méthode de segmentation. Dans le cas d'une tumeur qui prend le contraste (*enhanced*), on constate souvent la présence d'un œdème et d'une partie nécrotique. Nous les segmentons en CE-T1w et FLAIR avec la méthode de segmentation. Ce système peut également effectuer la segmentation en utilisant seulement une image CE-T1w, mais parfois (particulièrement pour des petites tumeurs) l'interaction de l'utilisateur (un clic dans la tumeur) est nécessaire.

La méthode automatique de segmentation que nous avons développée se compose de deux phases : initialisation et raffinement, comme nous le montrons dans le schéma 4. Dans la première phase, nous détectons et segmentons initialement la tumeur ou l'œdème. Pour cette opération, la tumeur ou l'oedème est détecté et segmenté en utilisant une méthode de classification floue ou une méthode fondée sur l'analyse de symétrie et quelques opérations morphologiques. La première méthode s'appuie sur l'hypothèse que la tumeur ou l'œdème apparaît dans l'image avec des niveaux gris spécifiques, correspondant à une classe supplémentaire. La deuxième méthode est fondée sur l'hypothèse que la forme du cerveau est approximativement

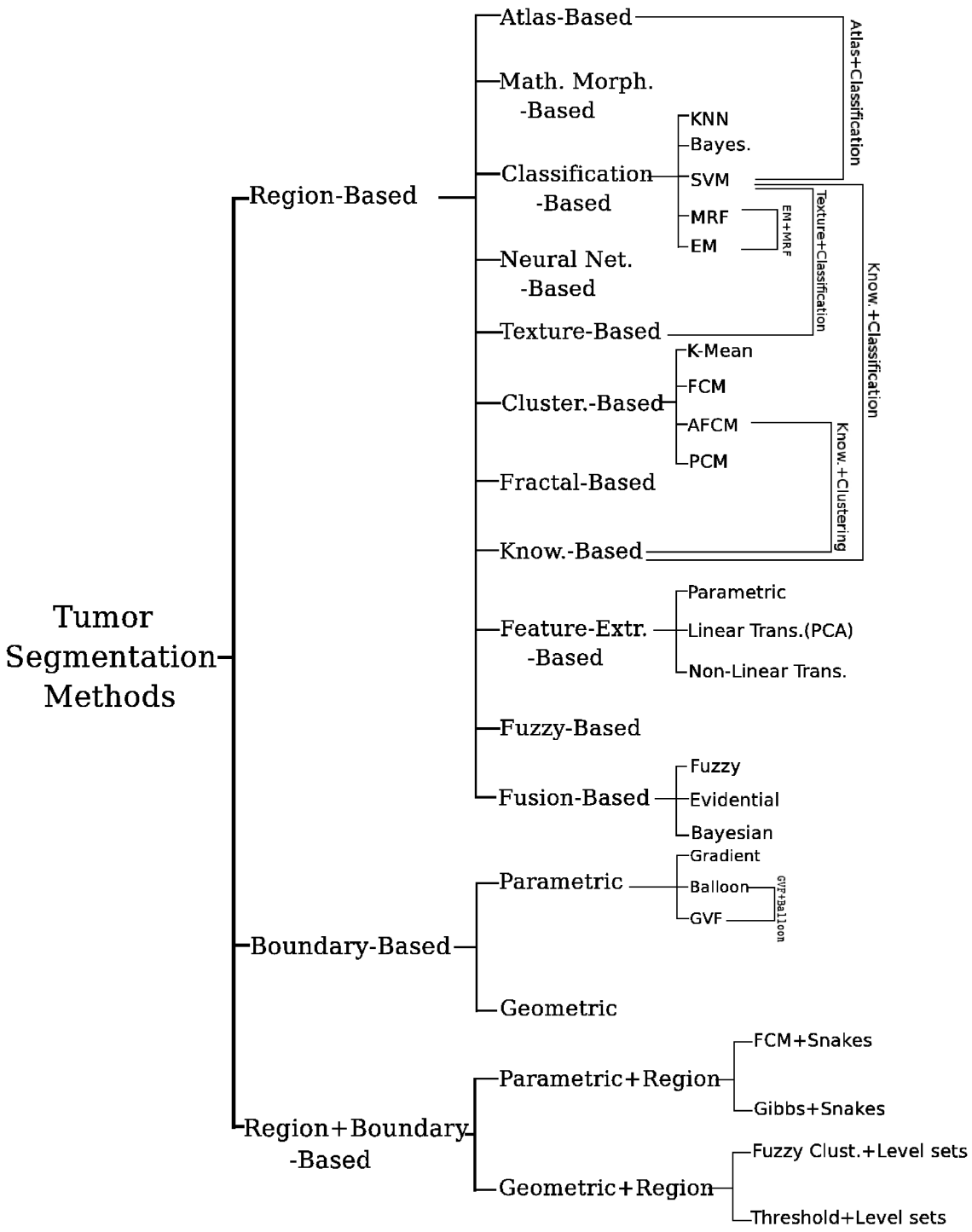

Figure 2: Méthodes existantes pour la segmentation de tumeurs cérébrales.

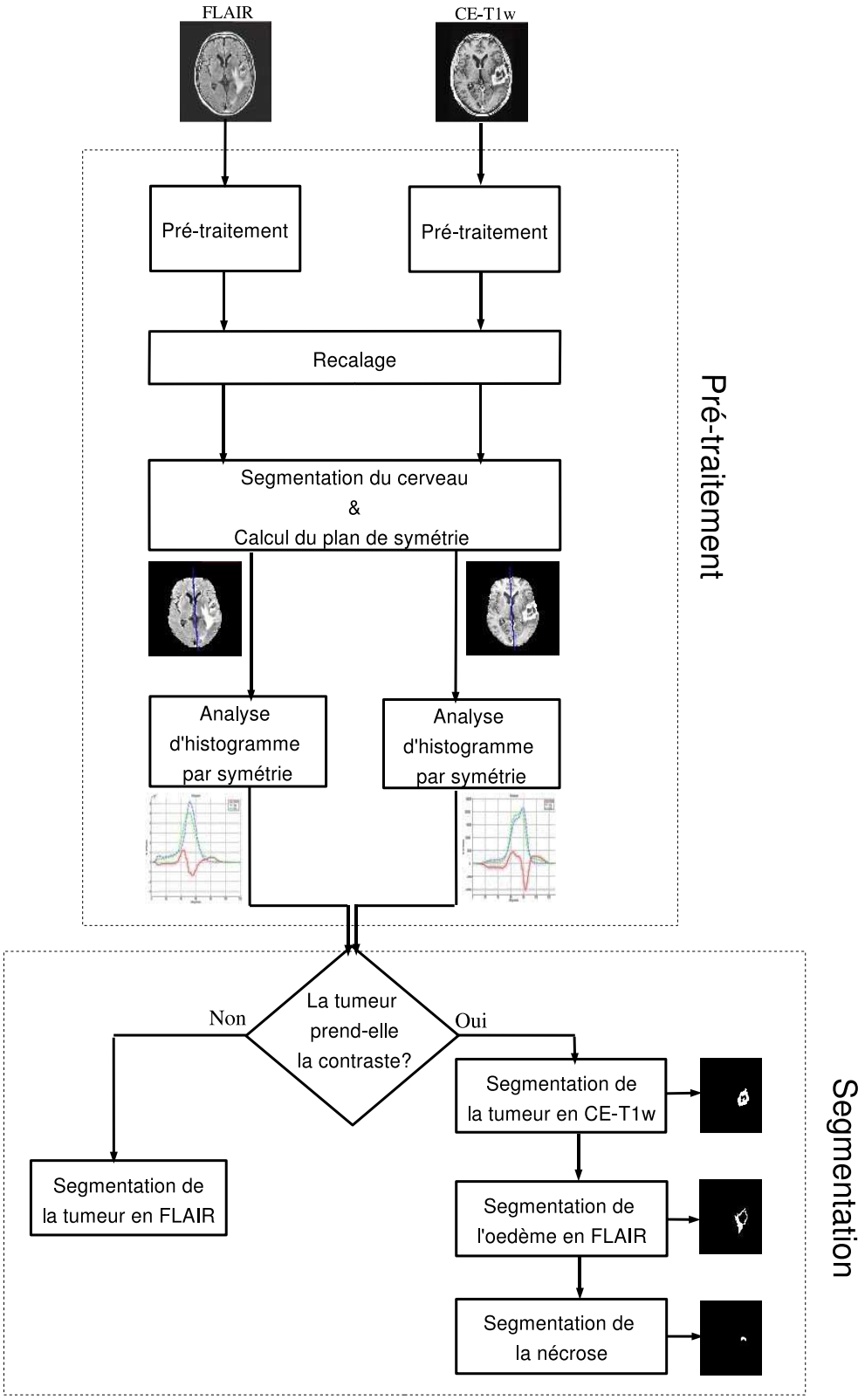

Figure 3: Cadre général proposé pour la segmentation de tumeurs du cerveau.

symétrique, et que la tumeur peut changer la symétrie. Elle peut donc être détectée par l'analyse d'asymétries. Cette détection fournit l'initialisation pour une segmentation plus précise en utilisant un modèle déformable paramétrique contr aint par des relations spatiales.

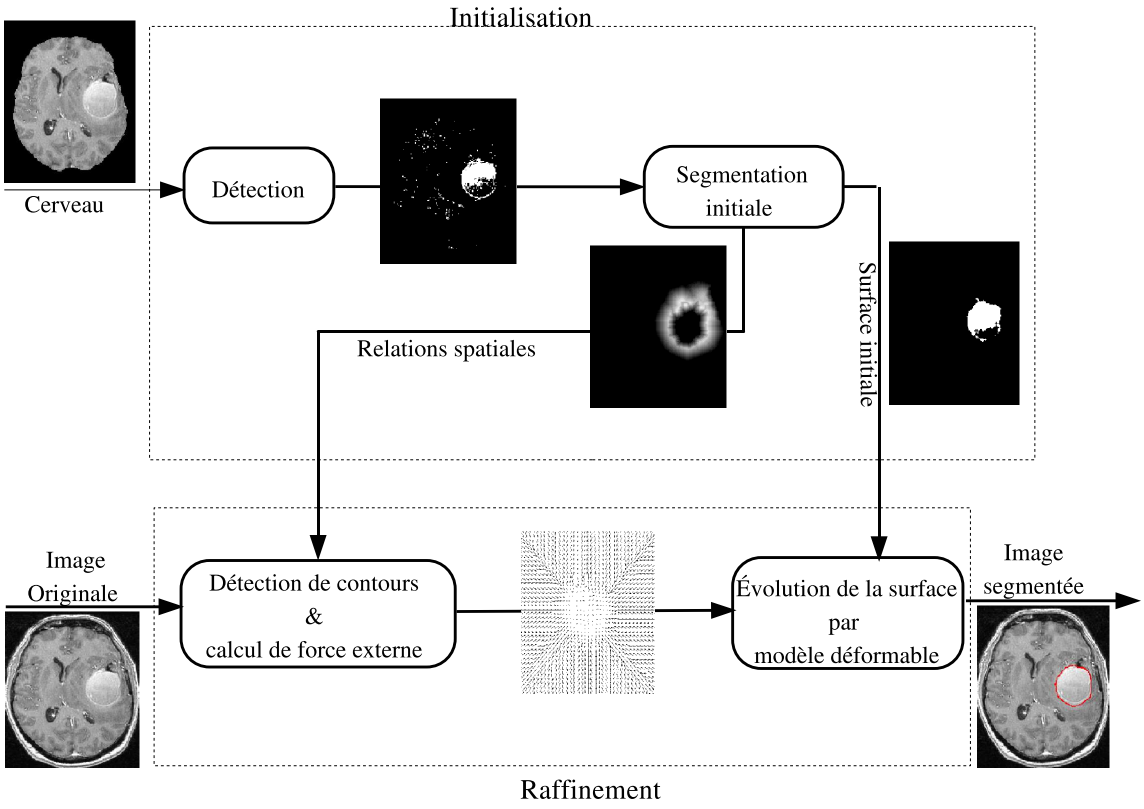

Figure 4: Schéma général de la méthode proposée pour la segmentation automatique de tumeurs.

Segmentation initiale

Détection par MPFCM

L'algorithme PFCM (*Possibilistic fuzzy C-means*) a été introduit par [Pal et al., 2005]. C'est une combinaison entre des algorithmes de classification possibiliste (PCM, *possibilistic C-means*) et de classification floue (FCM, *fuzzy C-means*). Cette combinaison permet de prendre en considération à la fois le degré d'appartenance et le degré de typicalité des données, ces deux aspects étant importants en classification. L'algorithme PFCM a été conçu dans ce sens.

La fonction objectif de PFCM s'écrit :

$$J_{m,\eta}(U,T,V;X) = \sum_{i=1}^{c}\sum_{k=1}^{n}(au_{ik}^{m} + bt_{ik}^{\eta})D_{ik} + \sum_{i=1}^{c}\gamma_i\sum_{k=1}^{n}(1-t_{ik})^{\eta} \tag{1}$$

où $\sum_{i=1}^{c} u_{ik} = 1,\ \forall k,\ 0 \leq u_{ik}, t_{ik} \leq 1$ et $a > 0,\ b > 0,\ \gamma_i > 0,\ m > 1,\ \eta > 1$ sont des constantes. Le degré d'appartenance u_{ik} (comme dans FCM) et la typicalité t_{ik} (comme dans PCM) sont pondérés dans la fonction objectif par les constantes a et b. Si $a = 1$, $b = 0$ et $\gamma_i = 0, \forall i$, PFCM se réduit à FCM et si $a = 0$ et $b = 1$, il se réduit à PCM.

L'équation (1) montre que la fonction objectif de PFCM ne prend en compte aucune information spatiale. Par conséquent, elle est sensible à l'hétérogénéité d'intensité et au bruit, et son application pour la classification d'images IRM est très limitée.

Ici nous proposons un nouvel algorithme (MPFCM, PFCM modifié) qui exploite à la fois l'information des voxels et leurs voisinages (inspirés des champs Markov (MRF)), l'appartenance et la typicalité. Nous modifions l'équation (1) en ajoutant un terme qui permet à l'étiquetage d'un voxel d'être influencé par son voisinage immédiat [Ahmed et al., 2002] :

$$J_{m,\eta}(U,T,V;X) = \sum_{i=1}^{c}\sum_{k=1}^{n}(au_{ik}^{m}+bt_{ik}^{\eta})D_{ik}+\sum_{i=1}^{c}\gamma_i\sum_{k=1}^{n}(1-t_{ik})^{\eta}+\beta\sum_{i=1}^{c}\sum_{k=1}^{n}(au_{ik}^{m}+bt_{ik}^{\eta})S_{ik} \tag{2}$$

Ici $S_{ik} = \sum_{w=1}^{n_w} \|x_w - v_i\|^2$ et x_w est un pixel/voxel voisin de x_k dans une fenêtre autour de x_k et n_w est le nombre des pixels/voxels voisins. L'importance relative du terme ajouté (effet de voisinage) est contrôlé par β.

Afin de détecter et d'étiqueter la tumeur, nous effectuons une classification en cinq (ou six) classes [Khotanlou et al., 2005] : le liquide céphalo-rachidien (LCR), la matière grise (MG), la matière blanche (MB), la tumeur (et l'œdème) et le fond. Puisque les pathologies tumorales que nous traitons présentent une hyper-intensité, elles portent, après classification, l'étiquette la plus élevée. Par la suite, des opérations morphologiques sont appliquées à l'image résultat pour corriger les erreurs éventuelles de classification (ouverture et sélection de composantes connexes). La figure 5 montre un exemple de la détection d'une tumeur par MPFCM.

Détection par analyse de symétrie

Pour résoudre le manque de généralité de la méthode précédente, nous suggérons une autre approche, à l'aide du plan de symétrie approximatif [Khotanlou et al., 2007c;b]. Le plan de symétrie du cerveau est une bonne approximation du plan moyen-sagittal,

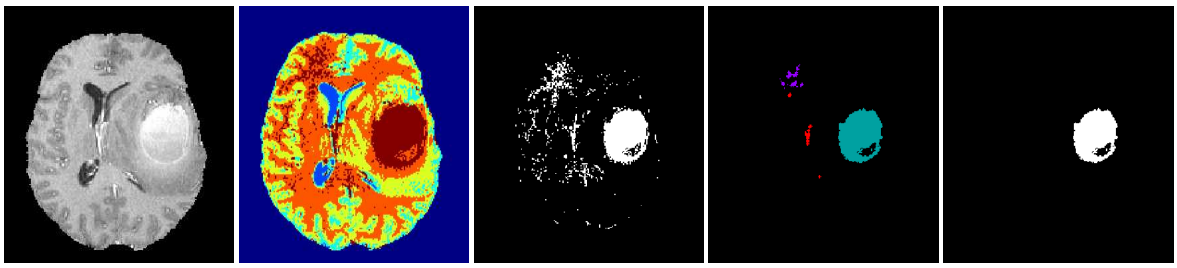

(a) (b) (c) (d) (e)

Figure 5: Détection d'une tumeur par MPFCM : (a) image originale, (b) classification par MPFCM, (c) classe de la tumeur, (d) composantes connexes de la classe de la tumeur et (e) tumeur détectée.

qui réalise la meilleure séparation des hémisphères. La détection automatique de ce plan dans l'image du cerveau est très utile. Ici nous l'utilisons pour détecter des tumeurs du cerveau. Le calcul du plan de symétrie approximatif du cerveau est exécuté selon une méthode proposé par [Tuzikov et al., 2003], qui est fondée sur la maximisation d'une mesure de similarité.

Le plan de symétrie de l'image en niveaux de gris et celui du masque binaire du cerveau segmenté dans le cas normal sont approximativement égaux. Pour augmenter l'exactitude et pour accélérer l'algorithme dans les cas pathologiques nous calculons donc le plan de symétrie sur le masque binaire du cerveau segmenté. Maintenant des tumeurs peuvent être détectées en évaluant les asymétries éventuelles. Nous supposons que les tumeurs sont localisées dans seulement un hémisphère ou ne sont pas symétriques. Notons $H_n(x)$ l'histogramme de l'hémisphère normal et $H_p(x)$ l'histogramme de l'hémisphère pathologique. La différence $H_s(x) = H_p(x) - H_n(x)$ entre les histogrammes fournit des informations sur de nouvelles classes d'intensités induites par la tumeur comme le montrent les figures 6, 7, 8 et 9.

Ici nous classifions les tumeurs à partir de leur apparence dans l'image CE-T1w en 4 classes [Khotanlou et al., 2007b] :

- tumeur qui ne prend pas de contraste (NEN) : la tumeur est plus foncée que la matière grise (MG) dans l'image CE-T1w (figure 6) ;
- tumeur qui prend le contraste et sans œdème (FEN) : les voxels de la tumeur sont hyperintenses (plus clairs que la matière blanche (MB)) dans l'image CE-T1w (figure 7) ;
- tumeur qui prend le contraste et avec œdème (FEN), où la partie qui prend le contraste est hyperintense en CE-T1w et l'œdème environnant est plus foncé que la MG (figure 8) ;

- tumeur qui prend le contraste partiellement (REN), qui a trois parties : une partie centrale, la nécrose, plus foncée que MG, une partie qui entoure la nécrose et apparaît hyperintense, et l'œdème environnant qui est plus foncé que MG dans l'image CE-T1w (figure 9).

Dans le cas d'une tumeur NEN, il y a un pic positif entre LCR et MG dans H_s qui montre la gamme d'intensités de la tumeur (figure 6), tandis que dans le cas d'une tumeur FEN sans œdème il y a un pic positif après MB dans H_s qui montre la gamme de la tumeur (figure 7). Quand une tumeur FEN avec œdème (figure 8) ou une tumeur REN (figure 9) existe dans l'image, nous avons deux pics positifs dans H_s, où le premier pic montre la gamme d'intensités de l'œdème et le deuxième pic montre la gamme d'intensités de la tumeur (figures 8 et 9), parce que l'intensité de l'œdème est toujours inférieure à celle de la tumeur.

Pour extraire la tumeur nous employons d'abord un seuillage avec des valeurs dans la gamme du pic de la tumeur. Quelques voxels mal classifiés sont enlevés en utilisant des opérations morphologiques. D'abord une ouverture est employée pour déconnecter les composantes. La plus grande composante connexe est alors choisie puisqu'elle correspond à la tumeur. Pour obtenir les tissus environnants de la tumeur, nous devons distinguer deux cas : les tumeurs avec œdème et les tumeurs sans œdème. Dans le cas d'une tumeur avec œdème le pic positif précédant le pic de la tumeur correspond à l'œdème et il peut être extrait par seuillage en utilisant la gamme d'intensités de l'œdème (figures 8 et 9). Dans le cas d'une tumeur sans œdème le pic négatif observé dans H_s correspond aux tissus normaux autour de la tumeur. Ces tissus peuvent également être obtenus par seuillage (figures 6 e t 7). Ils seront employés pour représenter des relations spatiales dans la prochaine section.

Nous pouvons appliquer cette méthode pour détecter et extraire des anomalies dans tous les types d'images du cerveau telles que T2-weighted, FLAIR, PD-weighted, CT et PET. Ici nous employons cette méthode pour détecter et extraire des tumeurs dans les images FLAIR. Puisque les tumeurs dans les images FLAIR apparaissent comme des tissus hyperintenses, un pic positif qui correspond à la tumeur se produira dans $H_s(x)$ après le pic de MB comme illustré dans la figure 10.

Raffinement

Le résultat de la segmentation des tumeurs par analyse de symétrie et classification par MPFCM n'est pas assez précis, en particulier sur les bords des tumeurs. Nous avons donc besoin d'une méthode pour raffiner la segmentation. Pour cela, un modèle déformable contraint spatialement est employé.

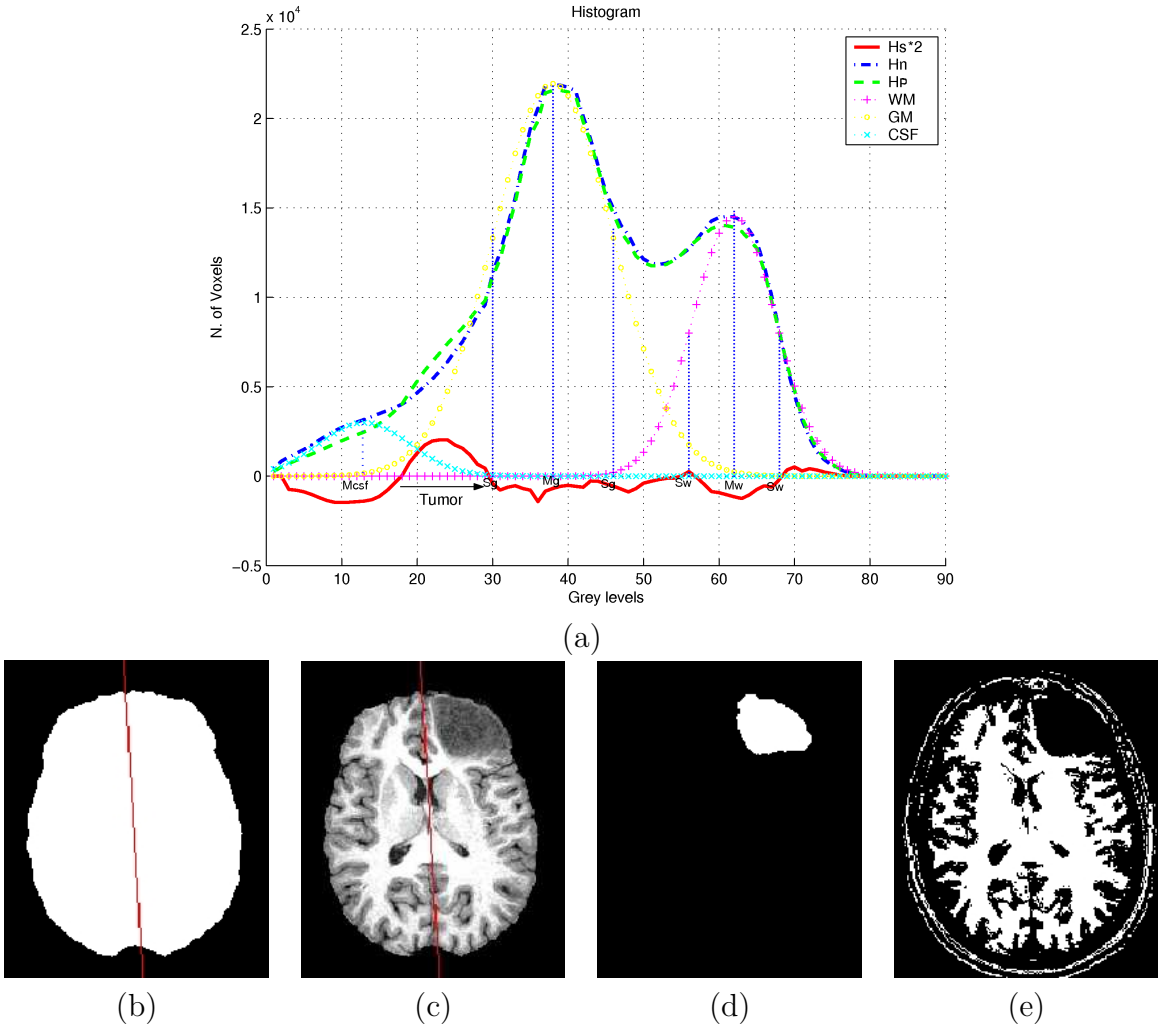

Figure 6: (a) Graphes de $\mathbf{H}_s$, $\mathbf{H}_n$ et $\mathbf{H}_p$ pour une tumeur NEN. (b) Plan de symétrie superposé sur le masque du cerveau. (c) Plan de symétrie superposé sur le cerveau segmenté. (d) Tumeur détectée. (e) Tissus environnants.

Modèle déformable contraint spatialement

Notre méthode de raffinement de la segmentation repose sur la combinaison d'un modèle déformable et de relations spatiales entre des objets [Colliot et al., 2006]. Dans le cas de la détection de tumeurs par analyse de symétrie, deux types d'informations sont disponibles : la détection initiale et les tissus environnants. Par conséquent nous employons la distance à la tumeur segmentée initialement, et aux tissus environnants. L'idée est que les contours de la tumeur devraient être situés entre la frontière de la détection initiale et la frontière des tissus environnants. Ces relations spatiales sont représentées par des sous-ensembles flous de l'espace de l'image [Bloch, 2005].

Leur intégration dans le schéma d'évolution du modèle déformable repose sur

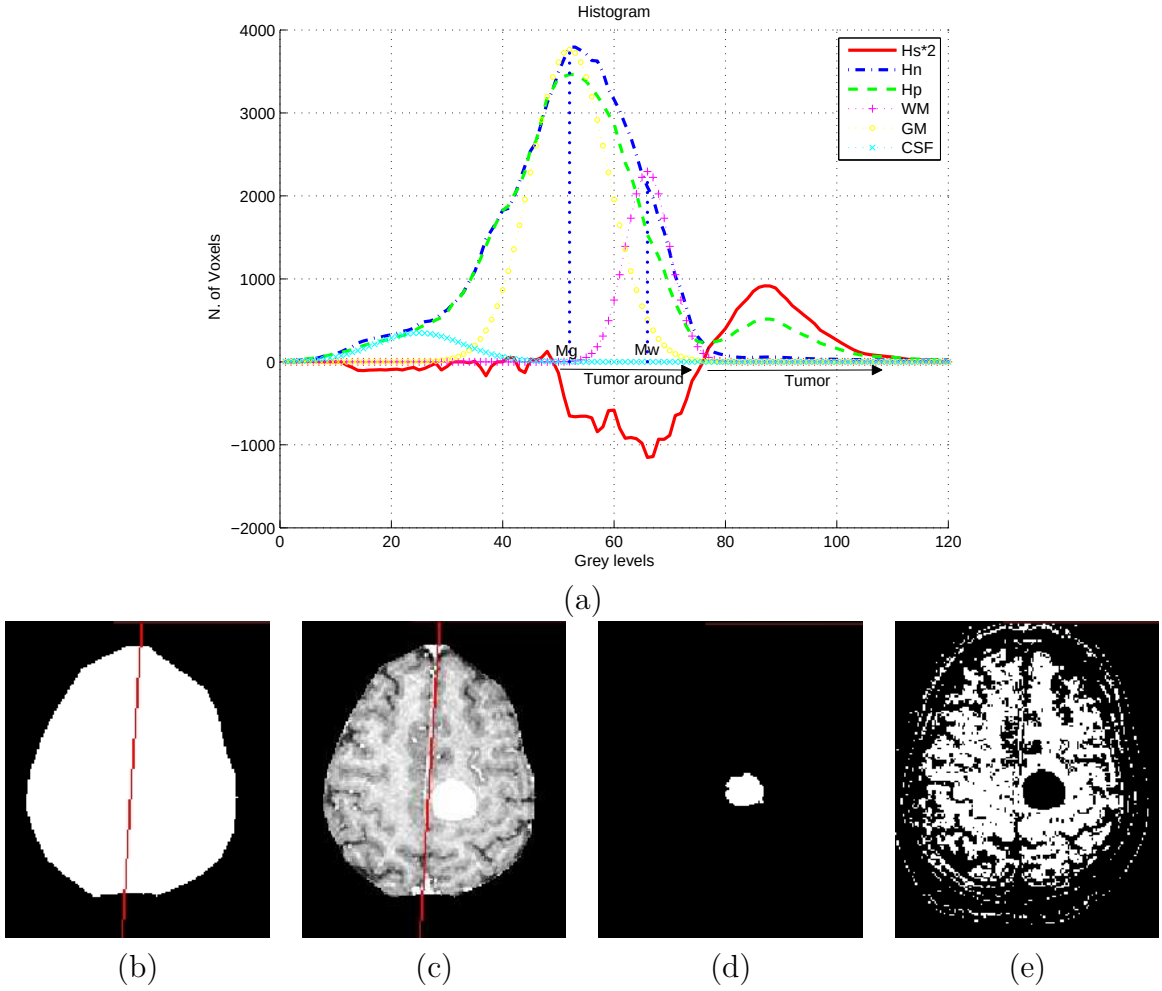

Figure 7: (a) Graphes de $\mathbf{H}_s$, $\mathbf{H}_n$ et $\mathbf{H}_p$ pour une tumeur FEN sans œdème. (b) Plan de symétrie superposé sur le masque du cerveau. (c) Plan de symétrie superposé sur le cerveau segmenté. (d) Tumeur détectée. (e) Tissus environnants.

l'introduction d'une nouvelle force calculée à partir d'un ensemble flou. Cette force permet de contraindre le modèle déformable à vérifier les relations spatiales décrivant l'objet cible et améliore significativement la segmentation des objets aux frontières mal définies [Colliot et al., 2006].

L'évolution du modèle déformable est décrite par l'équation dynamique de forces suivante [Kass et al., 1988 ; Xu et al., 2000] :

$$\gamma \frac{\partial \mathbf{X}}{\partial t} = \mathbf{F}_{int}(\mathbf{X}) + \mathbf{F}_{ext}(\mathbf{X}) \tag{3}$$

où $\mathbf{F}_{int}$ est la force interne et $\mathbf{F}_{ext}$ la force externe.

Cependant, au lieu de correspondre uniquement à l'attache aux données, comme c'est classiquement le cas, la force externe $\mathbf{F}_{ext}$ contient également un terme décrivant

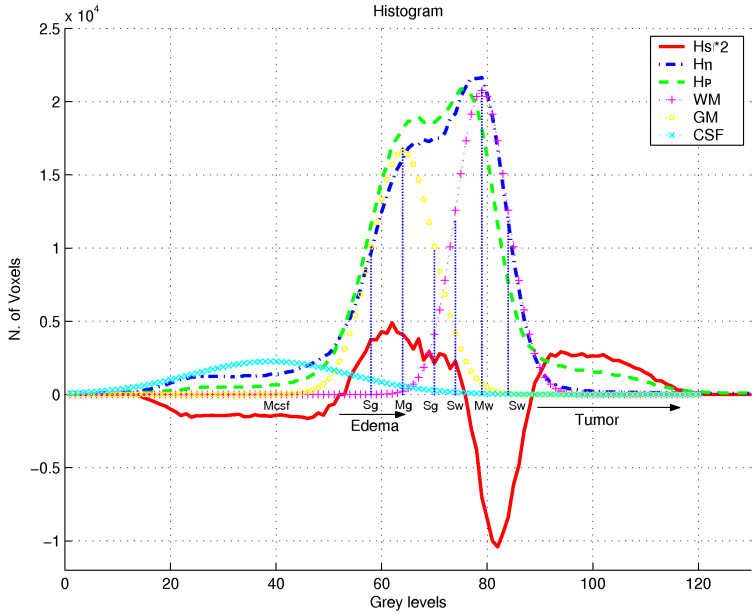

(a)

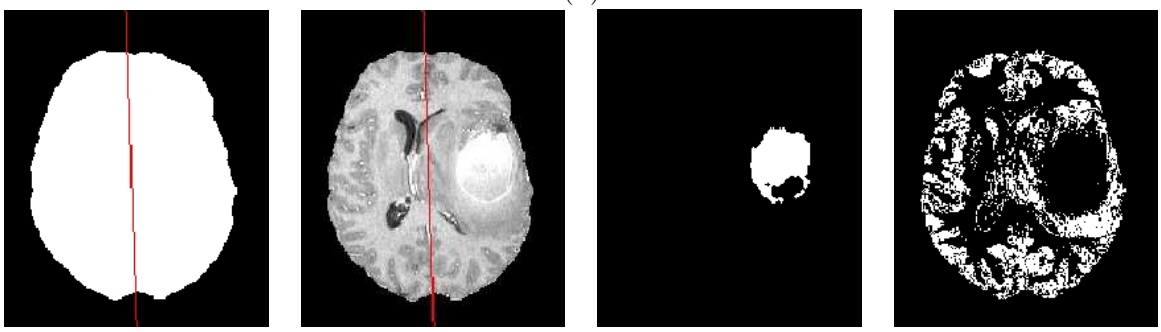

(a) (b) (c) (d)

Figure 8: (a) Graphes de $\mathbf{H}_s$, $\mathbf{H}_n$ et $\mathbf{H}_p$ pour une tumeur FEN avec œdème. (b) Plan de symétrie superposé sur le cerveau segmenté. (c) Tumeur détectée. (d) Tissus environnants.

les relations spatiales :

$$\mathbf{F}_{ext} = \lambda \mathbf{F}_C + \nu \mathbf{F}_R \tag{4}$$

où λ et ν sont des coefficients de pondération, $\mathbf{F}_C$ est un terme classique d'attache aux données et $\mathbf{F}_R$ est une force associée aux relations spatiales.

Plusieurs méthodes de construction de $\mathbf{F}_R$ ont été proposées dans [Colliot et al., 2006]. Une de ces approches consiste en la création d'un potentiel d'énergie par prolongation de l'ensemble flou en dehors de son support :

$$P_R(P) = 1 - \mu_R(P) + d_{supp(R)}(P) \tag{5}$$

où μ_R est la fonction d'appartenance à l'ensemble flou R représentant une relation spatiale et $d_{supp(R)}$ est la distance au support de R. La force $\mathbf{F}_R$ est dérivée du potentiel

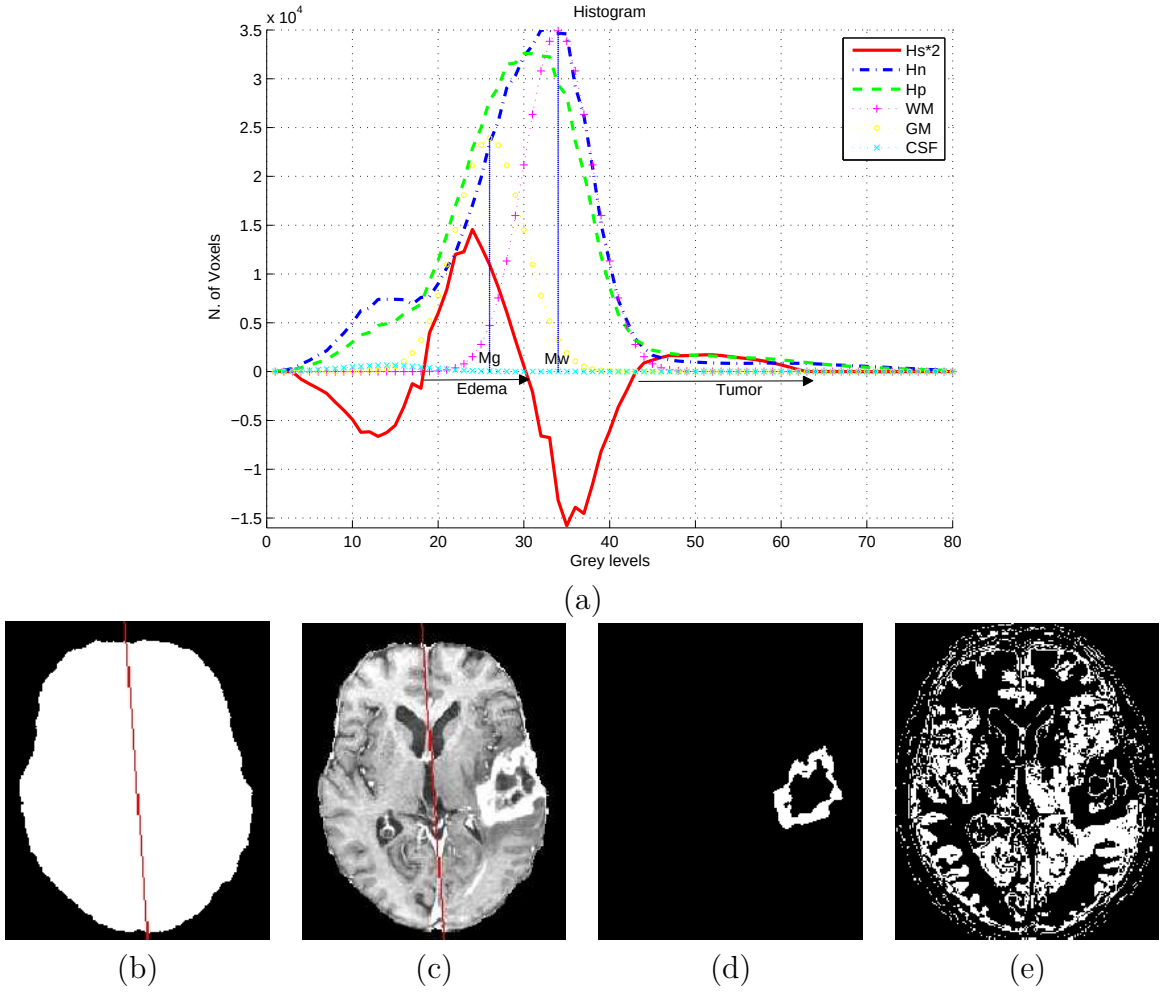

Figure 9: (a) Graphes de $\mathbf{H}_s$, $\mathbf{H}_n$ et $\mathbf{H}_p$ pour une tumeur NEN. (b) Plan de symétrie superposé sur le masque du cerveau. (c) Plan de symétrie superposé sur le cerveau segmenté. (d) Tumeur détectée. (e) Tissus environnants.

P_R et normalisée par :

$$\mathbf{F}_R(P) = -(1 - \mu_R(P))\frac{\nabla P_R(P)}{\|\nabla P_R(P)\|} \tag{6}$$

Résultats

Nous avons appliqué les méthodes proposées à 30 jeux de données d'IRM avec des tumeurs cérébrales. Les résultats pour deux images sont illustrés dans les figures 16 et 17. Pour évaluer les méthodes nous avons fourni des résultats quantitatifs pour chaque méthode en comparant les résultats et segmentations manuelles en utilisant les mesures de volume et de surface. Les segmentations manuelles sont fournies par les experts

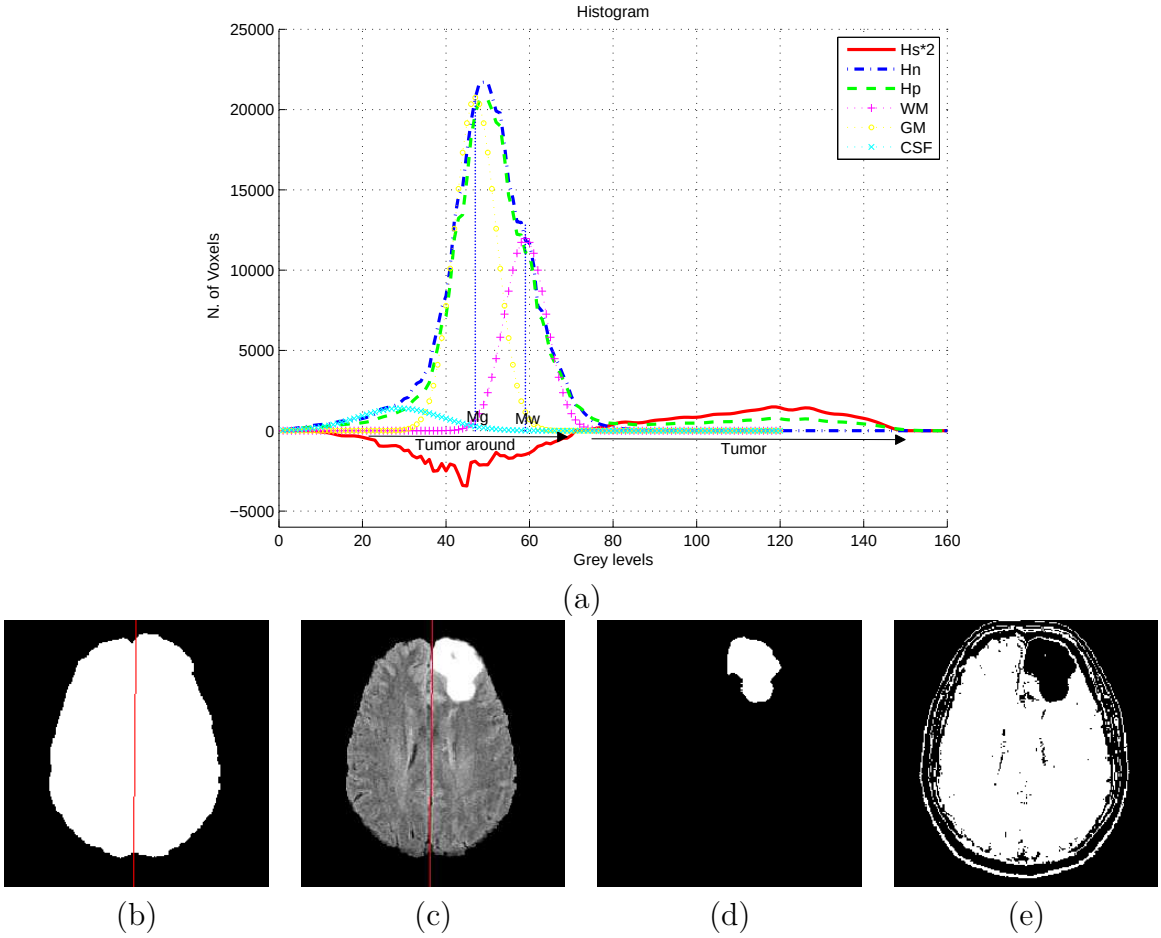

Figure 10: (a) Graphes de $\mathbf{H}_s$, $\mathbf{H}_n$ et $\mathbf{H}_p$ pour une tumeur dans une image FLAIR. (b) Plan de symétrie superposé sur le masque du cerveau. (c) Plan de symétrie superposé sur le cerveau segmenté. (d) Tumeur détectée. (e) Tissus environnants.

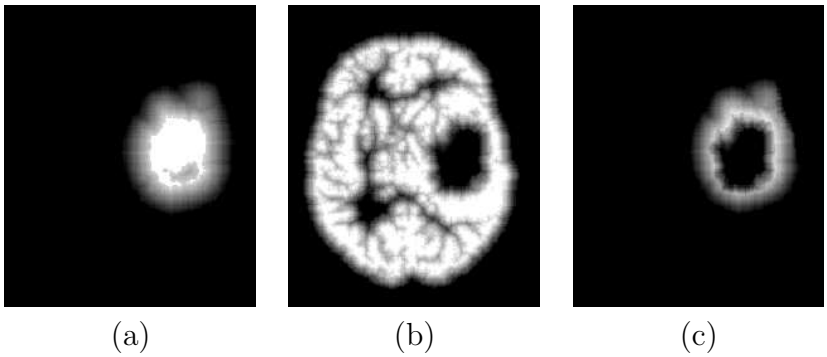

Figure 11: Relations spatiales utilisées pour raffiner la segmentation de la tumeur détectée dans la figure 8 (les valeurs les plus élevées de niveaux gris correspondent aux régions où la relation spatiale est mieux satisfaite). (a) Près de la tumeur. (b) Relation fournie par les tissus environnants de la tumeur. (c) Fusion des deux relations.

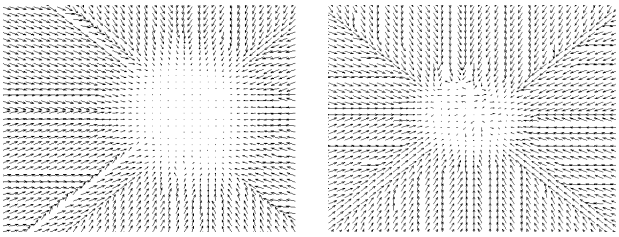

(a) (b)

Figure 12: Force externe $\mathbf{F}_R$ calculée pour un sous-ensemble flou μ_R correspondant à la relation spatiale R. (a) Force $\mathbf{F}_R$ calculée pour μ_R pour la relation "près de la tumeur" (figure 11). (b) Force calculée pour la fusion des deux relations de la figure 11 (pour la visualisation un sous-échantillonnage a été effectué).

médicaux. Nous montrons quelques graphes qui comparent les résultats quantitatifs des méthodes. Le premier graphe (figure 13) montre les moyennes et les écarts-types des métriques de volume et de surface pour 10 tumeurs FEN en CE - T1w. On peut observer que les mesures de volume de segmentation initiale et finale par MPFCM et analyse de symétrie (raffinés par le modèle déformable) sont approximativement égales. En conclusion, on peut observer que les relations spatiales ont le potentiel d' améliorer les résultats. En employant le modèle déformable contraint par des relations spatiales, on améliore les métriques de surface et de volume en comparaison à un modèle déformable simple.

Le deuxième graphe (figure 14) compare les résultats quantitatifs sur les tumeurs NEN en CE-T1w par analyse de symétrie. Là encore on peut observer que le modèle déformable avec et sans des relations spatiales peut améliorer les résultats de la segmentation initiale. La comparaison de ce graphe et du précédent prouve également que la qualité de segmentation pour les tumeurs FEN est meilleure que pour les tumeurs NEN en raison de leurs bords bien définis. L'amélioration de la méthode pour segmenter les tumeurs NEN peut encore être utile.

Le dernier graphe (figure 15) illustre les résultats quantitatifs pour la segmentation de tumeurs sur les images FLAIR. Il prouve que l'amélioration par le modèle déformable ne mène pas à une amélioration considérable des métriques de volume. Il améliore les mesures de surface plus que les mesures de volume.

Pour conclure, nous avons développé une méthode hybride de segmentation qui exploite l'information de contour et de région de l'image pour segmenter la tumeur et ses composantes. Nous avons comparé une méthode de classification floue et une méthode d'analyse de symétrie pour détecter les tumeurs et nous avons employé un modèle déformable contraint par des relations spatiales pour l'amélioration de la segmentation. Ce travail prouve que le plan de symétrie est très utile pour la détection de tumeurs. Nous avons également présenté une nouvelle méthode de classification floue qui peut être employée pour le traitement des images médicales. En comparaison à

d'autres méthodes, notre approche a certains avantages tels que son aspect automatique et son caractère plus général. Notre méthode peut également segmenter les composantes des tumeurs telles que l'œdème et la nécrose. Nous prévoyons également qu'elle sera applicable à n'importe quel type d'image du cerveau comme FLAIR, T2-we ighted, CT, etc.

Une limite de notre approche par symétrie est que l'analyse de symétrie peut échouer dans le cas d'une tumeur symétrique par rapport au plan moyen-sagittal. Cependant ce cas est très rare. Les travaux futurs visent à déterminer le type de tumeur à partir d'une ontologie des tumeurs. Nos résultats peuvent également servir d'étape préliminaire à la segmentation des structures environnantes dans la prochaine section en employant des relations spatiales floues définies selon le type des tumeurs.

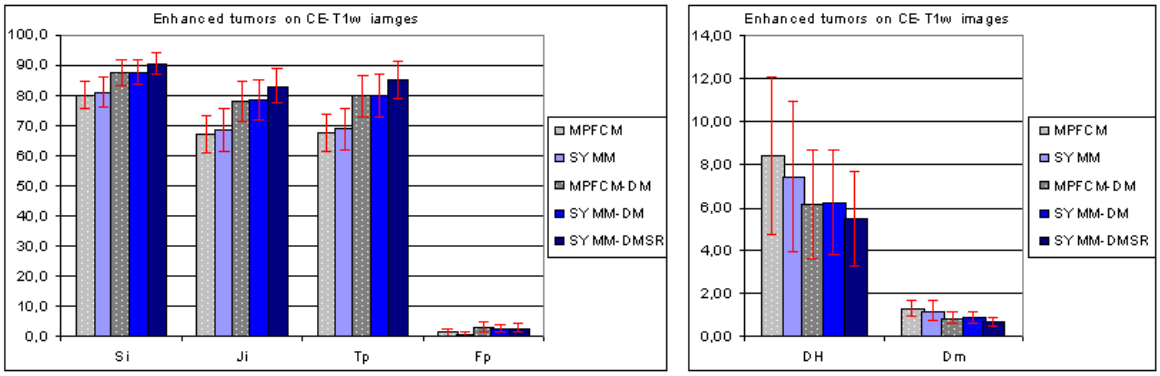

(a) (b)

Figure 13: Graphe des résultats quantitatifs pour les tumeurs FEN sur 10 images CE-T1w. (a) Moyenne et écart-type des mesures de volume. (b) Moyenne et écart-type des mesures de surface. Ici, MPFCM, MPFCM-DM, SYMM, SYMM-DM et SYMM-DMSR désignent respectivement la méthode de MPFCM, MPFCM raffinée par le modèle déformable, la méthode d'analyse de symétrie, l'analyse de symétrie raffinée par le modèle déformable et l'analyse de symétrie raffinée par le modèle déformable avec des relations spatiales.

Segmentation des structures internes en présence d'une pathologie tumorale

Nous présentons dans cette section une extension originale d'un cadre de segmentation, dédié initialement aux structures internes du cerveau normal, aux cas pathologiques. En oncologie du cerveau, il est souhaitable d'avoir un modèle humain descriptif du cerveau qui peut intégrer l'information de tumeur extraite à partir des données IRM telles que sa localisation, son type, sa forme, son positionnement anatomo-fonctionnel, ainsi que son influence sur les structures environnantes du cerveau (par exemple leurs

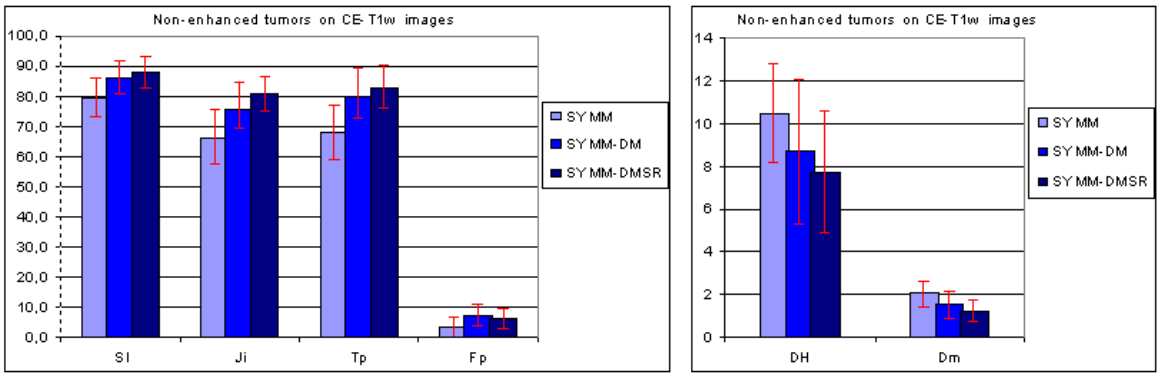

(a) (b)

Figure 14: Graphe des résultats quantitatifs pour les tumeurs NEN sur 10 images CE-T1w. (a) Moyenne et écart-type des mesures de volume. (b) Moyenne et écart-type des mesures de surface. Ici, SYMM, SYMM-DM et SYMM-DMSR désignent respectivement la méthode d'analyse de symétrie, l'analyse de symétrie raffinée par le modèle déformable et l'analyse de symétrie raffinée par le modèle déformable avec des relations spatiales.

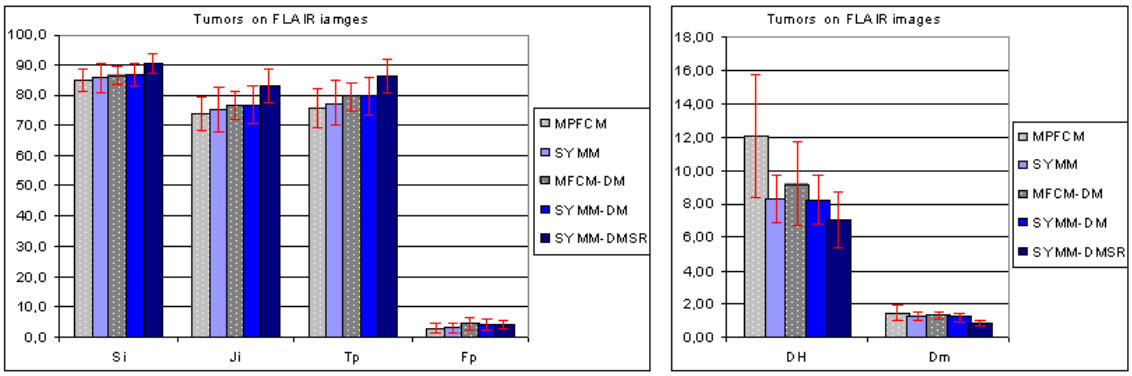

(a) (b)

Figure 15: Graphe des résultats quantitatifs pour les tumeurs NEN sur 10 images FLAIR. (a) Moyenne et écart-type des mesures de volume. (b) Moyenne et écart-type des mesures de surface. Ici, MPFCM, MPFCM-DM, SYMM, SYMM-DM et SYMM-DMSR désignent la méthode de MPFCM, MPFCM raffiné par le modèle déformable, la méthode d'analyse de symétrie, l'analyse de symétrie raffinée par le modèle déformable et l'analyse de symétrie raffinée par le modèle déformable avec des relations spatiales.

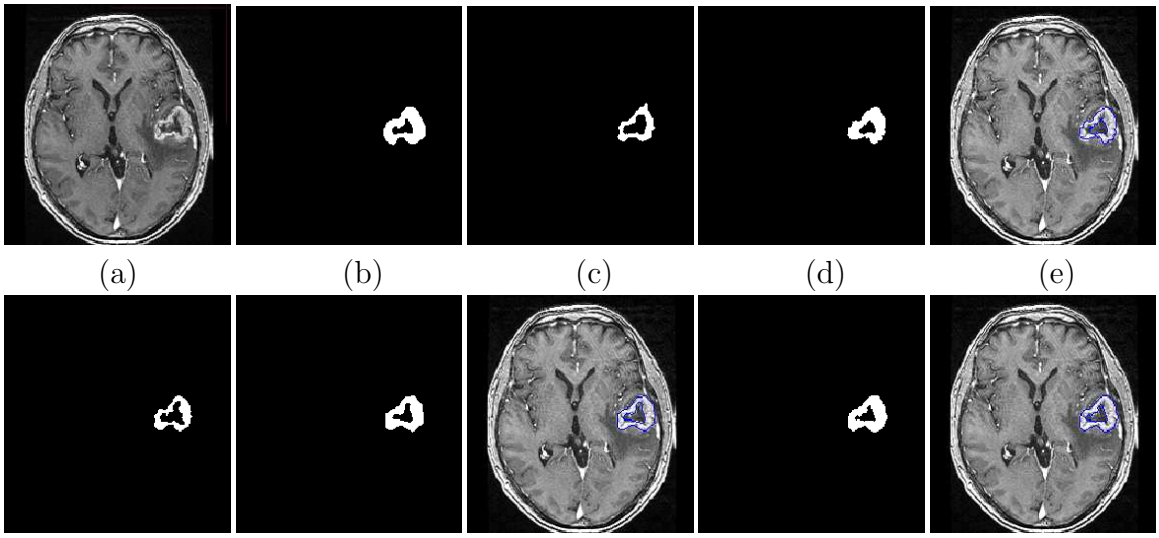

Figure 16: Comparaison des segmentations manuelle et automatique obtenues en utilisant l'analyse de symétrie et MPFCM pour une tumeur REN dans une image CE-T1w. (a) Image originale. (b) Segmentation manuelle. (c) Segmentation initiale par MPFCM. (d) Segmentation raffinée de MPFCM. (e) Résultat superposé à l'image originale. (f) Segmentation initiale par analyse de symétrie. (g) Segmentation raffinée d'analyse de symétrie par le modèle déformable sans relations spatiales. (h) Résultat superposé à l'image originale. (i) Segmentation raffinée d'analyse de symétrie par le modèle déformable avec des relations spatiales. (j) Résultat superposé à l'image originale.

relations spatiales). Il y a une grande littérature rapportant des travaux sur la segmentation des structures cérébrales ou des tumeurs mais rarement de toutes les deux en même temps. Cette thèse essaye de remplir cet espace, en traitant le problème de la segmentation des structures internes du cerveau en présence d'une tumeur.

En raison du manque de bords clairement définis dus à l'hétérogénéité d'intensités, aux effets de volume partiel et au bruit, la segmentation des structures du cerveau est une tâche difficile qui ne sera pas accomplie par les algorithmes qui s'appuient seulement sur l'information présente dans l'image. Par conséquent la plupart des méthodes récentes emploient des informations a priori. Ici nous avons divisé les méthodes existantes fondées sur le type d'information a priori. Nous pouvons distinguer trois types principaux de méthodes : les méthodes utilisant un atlas, les méthodes utilisant des patrons déformables et les méthodes utilisant des relations spatiales.

Peu de méthodes existantes pour la segmentation de structures du cerveau sont adaptées aux cas pathologiques. La plupart des méthodes présentées utilisent un atlas comme information a priori et une technique de recalage [Kyriacou et al., 1999 ;

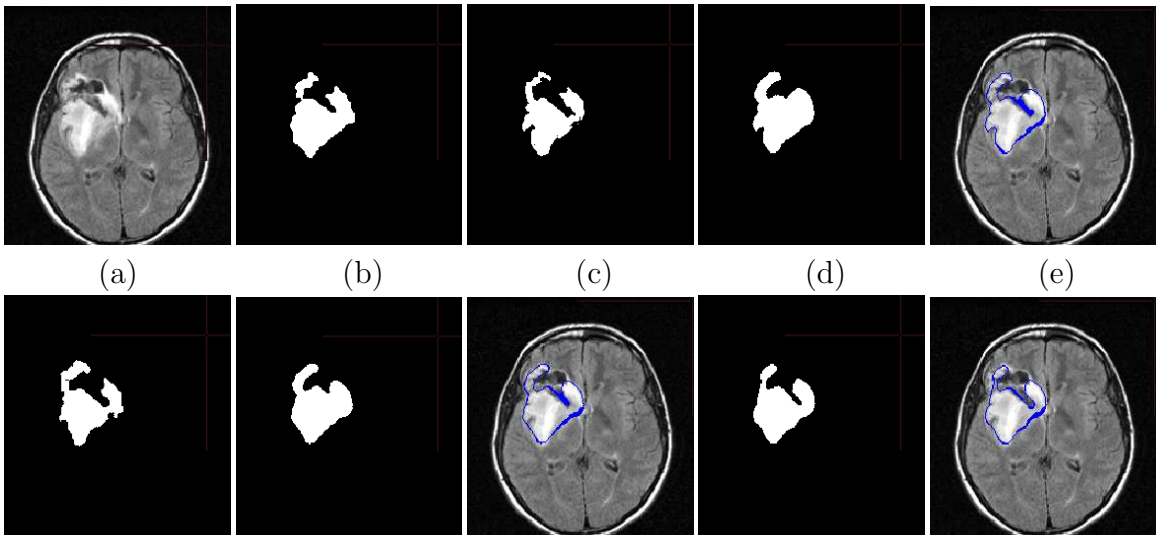

Figure 17: Comparaison des segmentations manuelle et automatique obtenue en utilisant l'analyse de symétrie et MPFCM pour une tumeur dans une image FLAIR. (a) Image originale. (b) Segmentation manuelle. (c) Segmentation initiale par MPFCM. (d) Segmentation raffinée de MPFCM. (e) Résultat superposé à l'image originale. (f) Segmentation initiale par analyse de symétrie. (g) Segmentation raffinée d'analyse de symétrie par le modèle déformable sans relations spatiales. (h) Résultat superposé à l'image originale. (i) Segmentation raffinée d'analyse de symétrie par le modèle déformable avec des relations spatiales. (j) Résultat superposé à l'image originale.

Nowinski and Belov, 2005 ; Bach Cuadra et al., 2004].

Le paradigme computationnel proposé dans notre méthode est fondé sur les travaux précédents [Colliot et al., 2006] en présentant un cadre pour l'intégration des relations spatiales dans un modèle déformable, pour segmenter les structures normales du cerveau dans des données IRM. Les relations spatiales, telles que des directions et des distances, sont représentées par des sous-ensembles flous de l'espace de l'image et incorporées à un modèle déformable en tant que forces externes. Dans cette section nous étendons ce cadre aux cas pathologiques, où la présence d'une tumeur peut induire des changements importants des caractéristiques iconiques et morphométriques des structures environnantes. En analysant le comportement spatial de la tumeur et son incidence sur les structures environnantes (petites ou grandes déformations), nous discutons la conservation de quelques relations spatiales utilisées pour la segmentation.

Comme illustré sur le schéma 18, le cadre proposé repose sur une base de connaissances qui est constituée d'une ontologie de tumeurs, d'une ontologie de l'anatomie du cerveau, d'une ontologie de relations spatiales et des descriptions de structures du cerveau. En utilisant l'information de la tumeur segmentée et de ses composantes,

nous choisissons les relations spatiales correspondant à la structure d'intérêt qui sont valables. Puis la fuzzification et la fusion des relations spatiales choisies, en utilisant le cadre flou proposé par [Bloch, 2005 ; Colliot et al., 2006], sont réalisées. Nous employons alors les relations spatiales fusionnées pour guider la segmentation de la structure par un modèle déformable. Cette procédure peut être répétée pour d'autres structures et finalement les résultats de la segmentation (tumeur et structures) peuvent être intégrés dans un modèle individuel du cerveau.

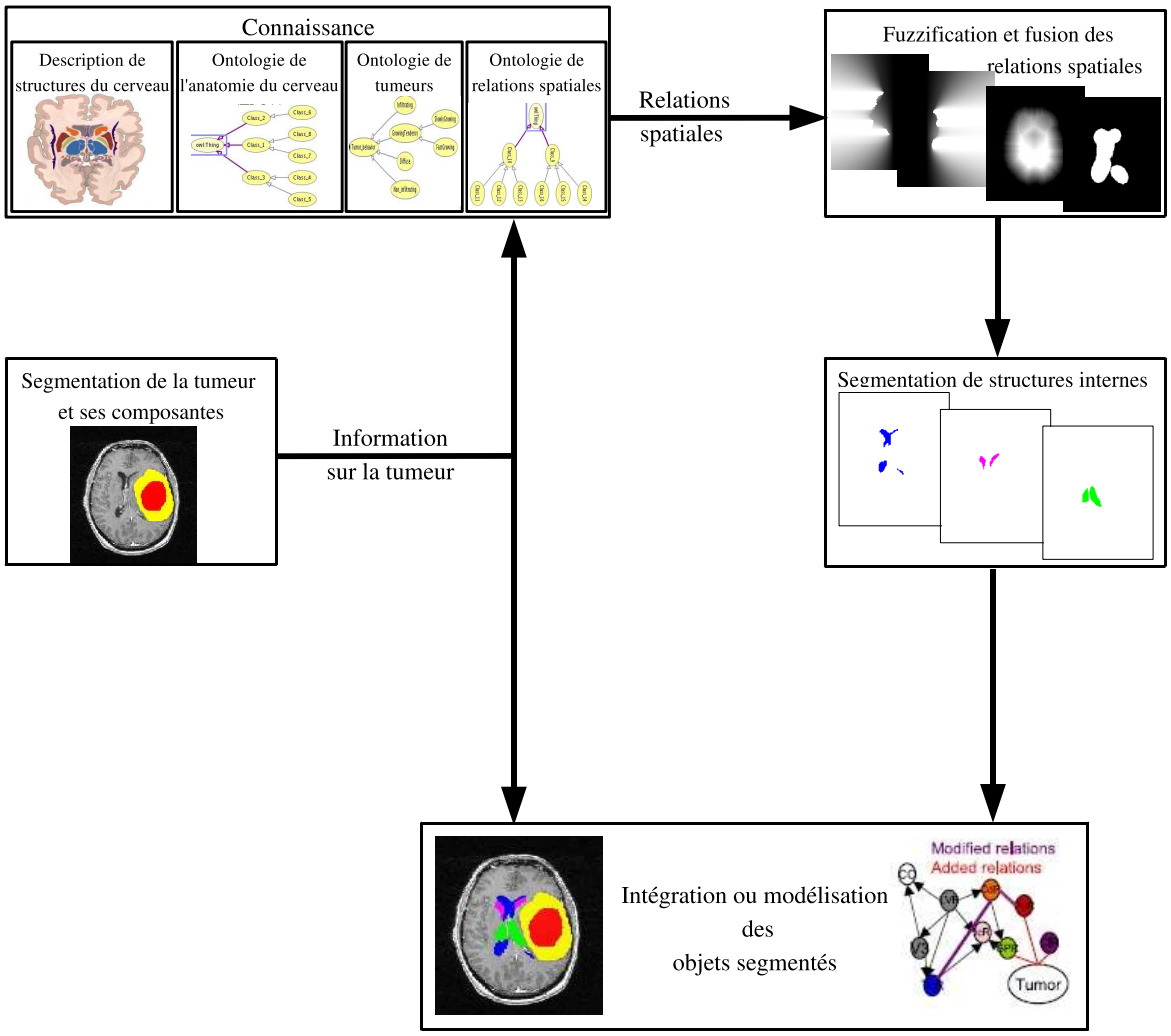

Figure 18: Schéma général de la méthode proposée pour la segmentation de structures internes du cerveau.

Connaissances a priori

Ici notre but est de relier une ontologie contenant la connaissance anatomique avec une ontologie des relations spatiales afin de représenter les relations spatiales entre les

structures anatomiques du cerveau.

Un exemple d'ontologie de référence en informatique biomédicale est le modèle fondamental de l'anatomie (FMA) [Rosse and Mejino, 2003]. Le FMA est concerné par la représentation des entités et des relations nécessaires pour modéliser de manière symbolique des structures du corps humain sous une forme numérique qui est également significative pour des humains. Dans le FMA, les relations spatiales entre les structures anatomiques sont représentées implicitement. Ici nous devons représenter les relations spatiales explicitement. Par conséquent nous représentons d'abord une ontologie des relations spatiales et nous la relions alors au FMA pour représenter les relations spatiales de chaque structure explicitement comme proposé dans [Hudelot et al., 2007]. Récemment notre groupe a développé une ontologie de relations spatiales générique [Hudelot et al., 2007] (figure 19).

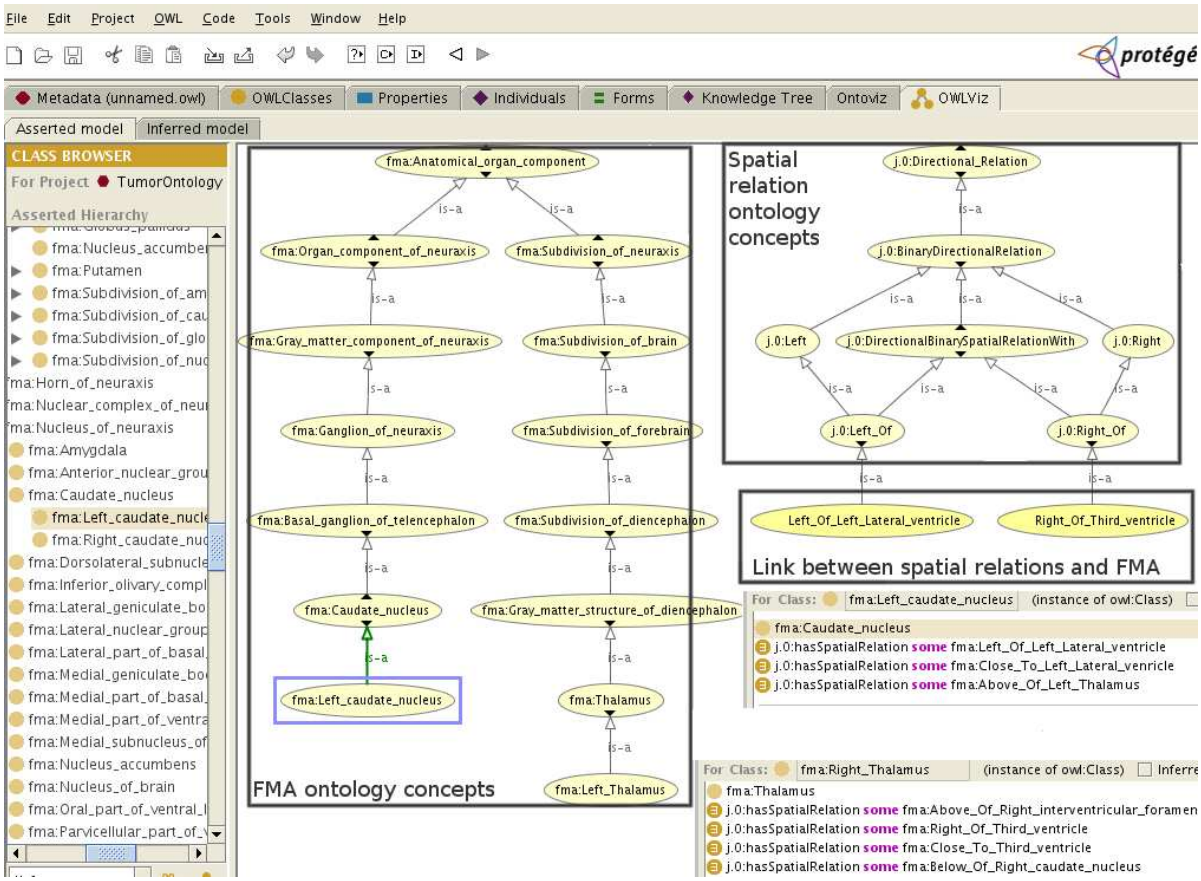

Figure 19: Une partie de l'ontologie du FMA, l'ontologie de relations spatiales et le lien entre elles (visualisées par Protégé [Protégé, 2007].

Représentation des relations spatiales

Notre but ici est d'intégrer les relations spatiales dans un modèle déformable, qui est nécessaire pour fournir une représentation numérique des relations. Ici, nous considérons les relations spatiales qui définissent la position d'un objet cible par rapport à un objet de référence. Les ensembles flous dans le domaine spatial sont appropriés pour ce cas. Dans ce type de représentation, la valeur d'appartenance de chaque point représente le degré avec lequel la relation est satisfaite. La représentation des relations spatiales est fondée sur un cadre présenté par [Bloch, 2005 ; Colliot et al., 2006]. Dans la figure 20 la répresentation de la relation "à droite de" est illustrée.

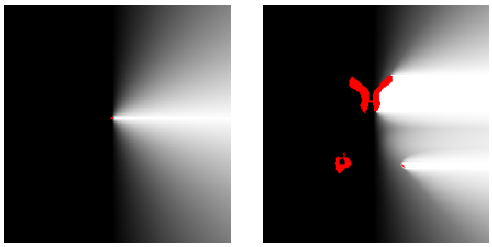

(a) (b)

Figure 20: Représentation d'une relation directionnelle par ensemble flou. (a) Élément structurant flou représentant "à droite de". (b) Dilatation floue du ventricule latéral par l'élément structurant correspondant.

Adaptation aux cas pathologiques

L'adaptation du cadre développé précédemment pour les images normales aux cas pathologiques exige de répondre à la question fondamentale : en présence d'une pathologie, quels types de relations spatiales restent valables ? La réponse dépend du type de tumeur.

Nous considérons dans ce travail une classification des tumeurs du cerveau selon leurs caractéristiques spatiales et la nature des changements potentiels de l'organisation structurelle du cerveau qu'elles induisent. Nous distinguons deux types principaux de tumeurs : peu déformantes et induisant de grandes déformations. L'identification du type de tumeur est fondée sur les résultats de segmentation. Pour réaliser cette classification, nous avons développé une ontologie simple qui classifie la tumeur en utilisant l'information extraite à partir des résultats de segmentation. L'ontologie de la classification de tumeurs a été développée avec Protégé [Protégé, 2007].

Quelques relations spatiales sont plus stables que d'autres en présence d'une tumeur. Intuitivement, les relations topologiques impliquent moins d'instabilité que les relations métriques. Le choix d'écarter ou de maintenir une relation spatiale en présence d'une tumeur est d'abord motivé par les considérations cliniques, à savoir la localisation, la

taille et le type de la tumeur. Le tableau 1 montre notre liste courante de relations spatiales spécifiques à chaque type de tumeurs [Khotanlou et al., 2007a ; Atif et al., 2006a].

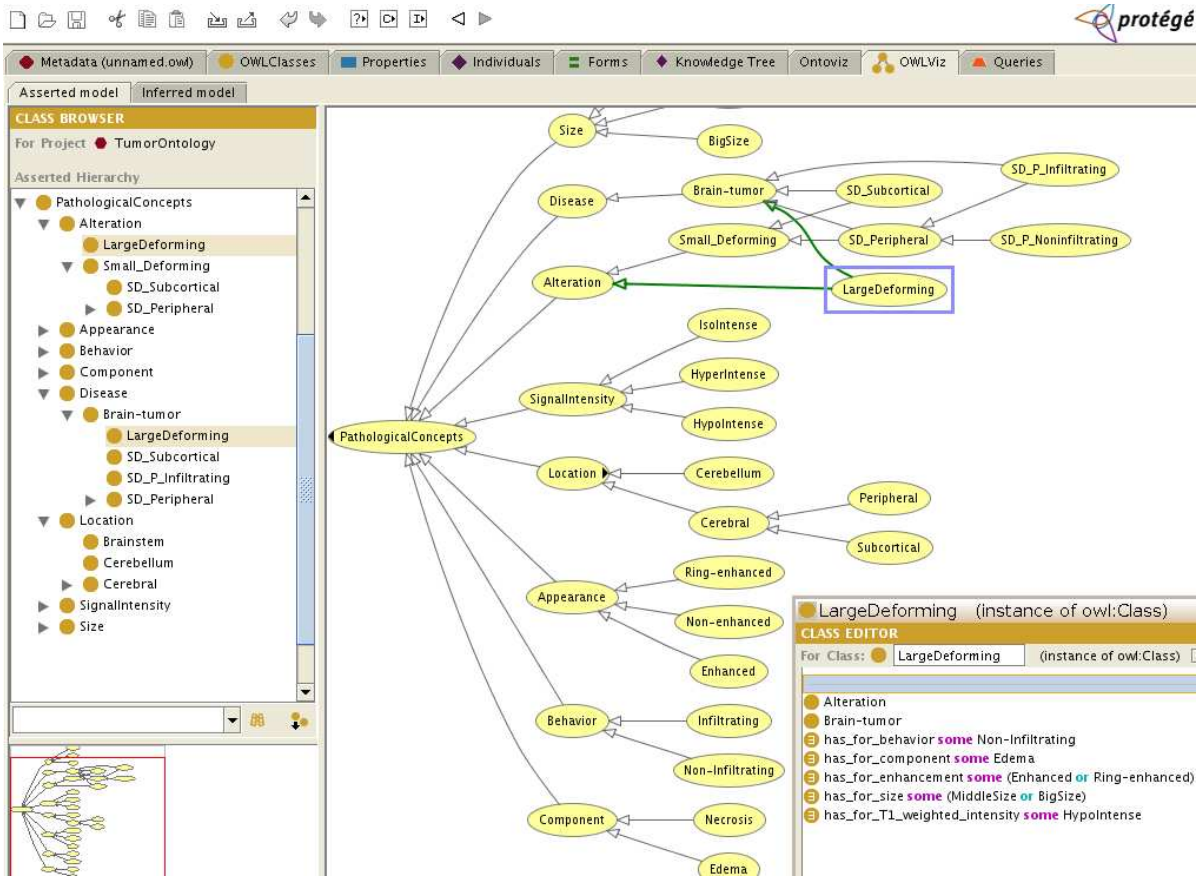

Figure 21: Une partie de l'ontologie de tumeurs visualisée par Protégé [Protégé, 2007].

Caractéristiques spatiales de tumeurs		**Relations spatiales préservées**
Induisant de grandes déformations (LD)		Adjacence, Direction, Distance (loin, près)
Peu déformantes (SD)	Périphériques (SD-P)	Adjacence, Direction, Symétrie, Distance
	Sous-corticales (SD-SC)	Adjacence, Direction, Distance (loin, près)

Table 1: Relations spatiales spécifiques à chaque type de tumeurs.

Algorithme de segmentation

La méthode proposée pour la segmentation de structures internes du cerveau, comme pour les tumeurs, a deux phases : initialisation et raffinement. En d'autres termes, nous segmentons d'abord les tissus du cerveau (comprenant les structures internes du cerveau) et puisque cette segmentation pour les structures internes de cerveau n'est pas assez fine, nous les raffinons alors en employant l'information a priori. Pour exécuter ces deux phases, la procédure de segmentation comprend les étapes suivantes :

1. segmentation initiale du cerveau,
2. requête des relations spatiales que doit satisfaire la structure recherchée par rapport à des structures déjà segmentées et reconnues,
3. sélection des relations spatiales valables,
4. fuzzification et fusion des relations spatiales pour fournir une ROI (region d'intérêt),
5. recherche d'une segmentation initiale d'une structure,
6. raffinement de la segmentation initiale,
7. répétition de l'algorithme pour d'autres structures.

Résultats et conclusion

La méthode proposée a été appliquée sur 10 jeux de données cliniques d'IRM de diverses origines et types pour segmenter les ventricules, les noyaux caudés et les thalami. Nous illustrons les résultats sur quatre cas aux figures 22 et 23. L'évaluation des résultats de segmentation a été réalisée par des comparaisons quantitatives avec les segmentations manuelles, en utilisant des mesures de volume et de surface.

Partant de travaux antérieurs sur la segmentation des structures internes, nous avons montré que la méthode reste adaptée à la présence de pathologies, grâce à l'utilisation de relations spatiales stables. L'introduction de ces relations pour contraindre la segmentation est donc un point fort de la méthodologie. Là encore, de bons résultats ont été obtenus sur des cas très différents, tant par la localisation, la forme et la taille de la tumeur, que par les déformations qu'elle induit sur les structures normales.

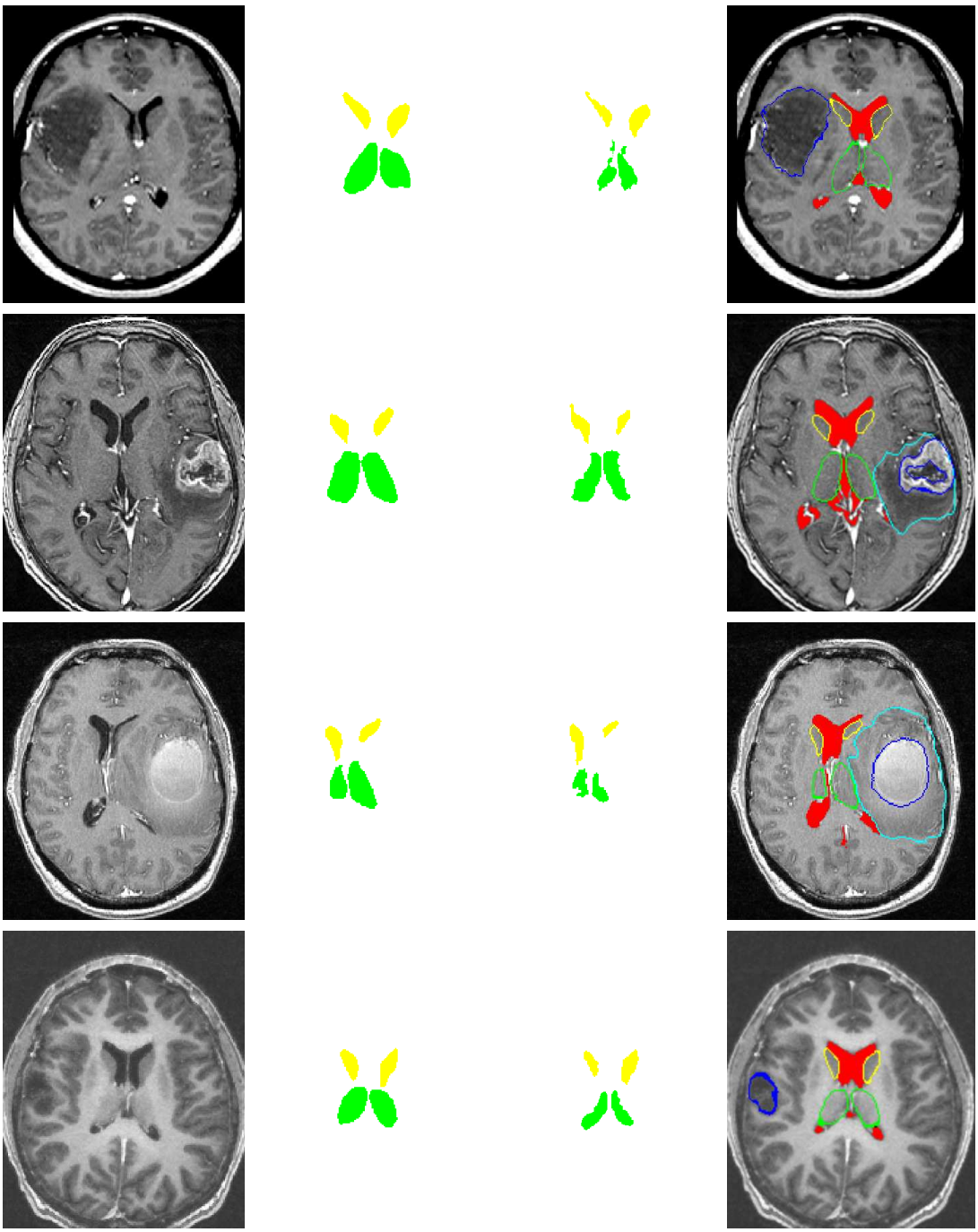

(a) (b) (c) (d)

Figure 22: Résultats de segmentation. (a) Une coupe axiale de l'image originale. (b) Segmentation manuelle. (c) Segmentation initiale. (d) Superposition des résultats sur la coupe axiale.

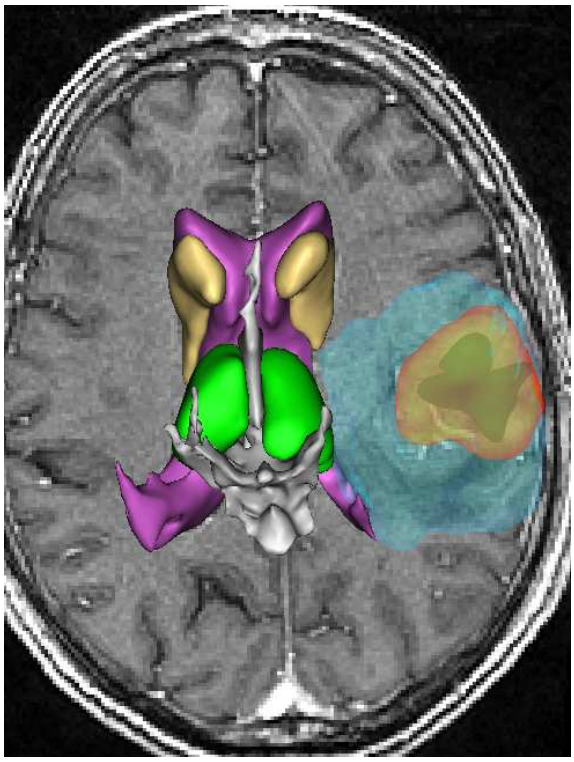

Figure 23: Vue 3D des structures, de la tumeur, de l'œdème et de la nécrose segmentés pour un cas.

Conclusion et perspectives

La méthode proposée pour la segmentation de tumeurs du cerveau utilise une image CE-T1w et une image FLAIR. Elle se compose de deux étapes : prétraitement et segmentation. Dans l'étape de prétraitement, nous avons proposé une nouvelle méthode adaptée aux cas pathologiques pour la segmentation correcte et robuste du cerveau. On a proposé une nouvelle analyse d'histogramme fondée sur la symétrie qui peut détecter automatiquement le type de tumeur et l'hémisphère pathologique. Pour la segmentation, la méthode proposée combine des informations de contours et de régions. L'approche proposée essaye de combiner ces deux types de méthodes pour repousser leurs limites en utilisant les avantages de chacune. La méthode hybride proposée a deux phases principales : initialisation par une méthode de régions et raffinement par une méthode de contours.

Pour l'initialisation nous avons proposé deux méthodes originales et nouvelles. La première est une classification floue non-supervisée. Cette méthode est une approche générale de classification et elle peut être employée afin de détecter et segmenter des tumeurs du cerveau. Cette méthode est une combinaison de FCM, PCM et des contraintes spatiales de régularisation. La seconde méthode se fonde sur l'asymétrie du cerveau pathologique. Nous avons proposé une nouvelle méthode spécifiquement

pour la détection de tumeurs. Elle est fondée sur la détection d'asymétrie dans les histogrammes des hémisphères du cerveau. Elle peut détecter une grande classe de tumeurs dans plusieurs modalités d'imagerie médicale.

La deuxième phase raffine la segmentation initiale en utilisant l'information de contours. Nous employons un modèle classique de modèle déformable 3D qui est initialisé par la surface de la tumeur détectée. Pour résoudre quelques problèmes et guider l'évolution de la surface, nous contraignons le modèle par des relations spatiales entre la tumeur détectée et les tissus environnant la tumeur.

La segmentation de structures internes du cerveau est une autre contribution de cette thèse. La segmentation des structures pathologiques du cerveau est une tâche difficile en raison des différents effets des différentes tumeurs. Nous avons proposé une nouvelle méthode, qui, en plus de l'information de la région et de contours, utilise des informations a priori. Les relations spatiales entre les structures est l'information a priori utilisée dans cette méthode. Ici nous traitons trois problèmes principaux : représentation explicite des relations spatiales pour chaque structure, adaptation des relations spatiales pour des cas pathologiques et méthode de segmentation.

La représentation des relations spatiales en général et leurs représentations explicites pour chaque structure en particulier sont mises en application à l'aide d'outils ontologiques. Un lien entre l'ontologie des relations spatiales et l'ontologie de FMA a fourni une représentation explicite des relations spatiales entre les structures. Pour l'adaptation des relations spatiales pour des cas pathologiques, nous avons employé l'information de la tumeur segmentée. Nous classifions la tumeur en fonction de son influence sur les autres structures. Pour cela nous avons développé une ontologie simple. Nous décidons alors de maintenir ou pas les relations en utilisant cette classification. Pour la segmentation nous avons utilisé une méthode qui intègre une fusion des relations spatiales pour guider la segmentation en phase d'initialisation et de raffinement. C'est une méthode séquentielle et elle est répétée pour toutes les structures dans un ordre défini par l'utilisateur. Cette méthode em ploie les relations spatiales fusionnées (ROI) pour rechercher la segmentation initiale d'une structure et pour guider un modèle déformable pour raffiner cette segmentation initiale.

La comparaison des résultats quantitatifs de la segmentation des tumeurs prouve que la qualité de la segmentation pour les tumeurs FEN est meilleure que pour les tumeurs NEN en raison de leurs contours bien définis. L'amélioration de la méthode pour segmenter les tumeurs NEN peut encore être utile. Une future direction peut employer des cartes de probabilités pour améliorer la méthode de détection de contours, comme proposé dans [Colliot et al., 2006] pour les structures du cerveau. Dans la méthode d'analyse de symétrie nous pouvons adapter un modèle gaussien au pic de la tumeur. Nous pouvons ensuite calculer la carte de probabilités puis calculer la carte de contours de cette carte de probabilités.

Pour l'amélioration de la segmentation par un modèle déformable, le réglage des

paramètres est très important. Notre expérience prouve qu'il y a une relation entre les paramètres et le volume de la segmentation initiale. Comme travaux futurs, définir une relation pour calculer les paramètres peut être utile.

L'interprétation ou la classification des tumeurs établie par l'OMS (Organisation Mondiale de Santé) est importante dans des applications cliniques. A ce moment elle est faite manuellement en utilisant les diagnostics histopathologiques [Julià-Sapé et al., 206]. Comme rapporté dans [Julià-Sapé et al., 206], l'information fournie par l'IRM permet de classer les tumeurs dans les classes de l'OMS avec 90% de bons résultats. En étendant l'ontologie proposée, en employant d'autres informations sur le patient et la segmentation obtenue, il serait donc possible de fournir une méthode automatique pour interpréter et classifier la tumeur détectée et segmentée.

Un avantage des modèles déformables géométriques est la capacité de manipuler automatiquement les changements de topologie. Pour segmenter deux tumeurs ou plus dans un cerveau, il convient d'employer un modèle déformable géométrique pour raffiner la segmentation. Ainsi, développer un modèle déformable géométrique contraint par des relations spatiales, telles que dans [Atif et al., 2006b], pour raffiner la segmentation est une autre future direction. La comparaison entre les résultats du modèle déformable paramétrique et du modèle déformable géométrique peut également être faite.

Nous avons proposé une nouvelle classification des tumeurs fondée sur l'influence de la tumeur et nous choisissons les relations spatiales stables en utilisant cette classification. Pour une future direction nous pouvons la prolonger pour classifier les tumeurs plus précisement.

Dans la méthode proposée, la détermination de la classe de la taille des tumeurs (petit, moyen et grand) et de la classe de la position de la tumeur est encore faite manuellement. Ainsi en prolongeant l'ontologie nous pouvons effectuer la classification automatiquement.

Nous avons employé une méthode simple pour apprendre les paramètres des relations spatiales en utilisant tous les types de tumeurs. Une apprentissage spécifique à chaque type de tumeurs peut être l'objet d'autres travaux futurs.

La recherche des relations spatiales d'une structure est fondée sur le type de tumeur. La méthode proposée peut également être intégrée dans la méthode actuellement développée par [Nempont et al., 2007] pour guider le choix des relations spatiales à employer pour segmenter chaque structure et pour définir des régions d'intérêt, caractérisant la nécessité et la possibilité de position des structures.

La méthode proposée pour la segmentation des structures internes du cerveau est une méthode séquentielle et doit être répétée pour chaque structure. Comme nouvelle méthode nous pouvons segmenter les structures simultanément. Ici nous avons employé les ensembles de niveaux multi-phases comme approche de segmentation

initiale qui peut segmenter plusieurs régions en même temps. Comme un travail futur nous pouvons intégrer des relations spatiales dans les ensembles de niveaux multi-phases pour la segmentation des structures internes simultanément.

Introduction

Tumor is one of the most common brain diseases, so its diagnosis and treatment have a vital importance for more than 400000 persons per year in the world (based on the World Health Organization (WHO) estimates). On the other hand, in recent years, developments in medical imaging techniques allow us to use them in several domains of medicine, for example, computer aided pathologies diagnosis, follow-up of these pathologies, surgical planning, surgical guidance, statistical and time series (longitudinal) analysis. Among all the medical image modalities, Magnetic Resonance Imaging (MRI) is the most frequently used imaging technique in neuroscience and neurosurgery for these applications. MRI creates a 3D image which perfectly visualizes anatomic structures of the brain such as deep structures and tissues of the brain, as well as the pathologies.

Segmentation of objects, mainly anatomical structures and pathologies from MR images is a fundamental task, since the results often become the basis for other applications. Methods for performing segmentation vary widely depending on the specific application and image modality. Moreover, the segmentation of medical images is a challenging task, because they usually involve a large amount of data, they have sometimes some artifacts due to patient's motion or limited acquisition time and soft tissue boundaries are usually not well defined.

When dealing with brain tumors, other problems arise, which make their segmentation more difficult. There is a large class of tumor types which have a variety of shapes and sizes. They may appear at any location and in different image intensities. Some of them may also deform the surrounding structures or may be associated to edema or necrosis that change the image intensities around the tumor. In addition, the existence of several MR acquisition protocols provides different information on the brain. Each image usually highlights a particular region of the tumor. Thus, automated segmentation with prior models or using prior knowledge is difficult to implement.

The accurate segmentation of internal structures of the brain is of great interest for the study and the treatment of tumors. It aims at reducing the mortality and improving the surgical or radiotherapeutic management of tumors. In brain oncology it is also desirable to have a descriptive human brain model that can integrate tumor information extracted from MRI data such as its localization, its type, its shape, its

anatomo-functional positioning, as well as its influence on other brain structures.

Despite numerous efforts and promising results in the medical imaging community, accurate and reproducible segmentation and characterization of abnormalities are still a challenging and difficult task. Existing methods leave significant room for increased automation, applicability and accuracy.

Objectives and contributions In this context, the first aim of this work is to develop a framework for a robust and accurate segmentation of a large class of brain tumors in MR images. Most existing methods are region-based. They have several advantages, but line and edge information in computer vision systems are also important. The proposed method tries to combine region and edge information, thus taking advantage of both approaches while cancelling their drawbacks. 3D contrast enhanced T1-weighted and FLAIR images are the inputs to perform an automatic segmentation of the solid part of tumor and the potential associated edema and necrosis.

For this, we first segment the brain to remove non-brain data. However, in pathological cases, standard segmentation methods fail, in particular when the tumor is located very close to the brain surface. Therefore we propose an improved segmentation method, relying on the approximate symmetry plane. Then we developed two new and original methods to detect and initially segment brain tumors. The first one is a fuzzy classification method which combines membership, typicality and neighborhood information. The second one relies on a symmetry-based histogram analysis. The approximate sagittal symmetry plane is first computed, and the tumor is then extracted by comparing the histograms of the two cerebral hemispheres. To refine the initial segmentation, which is not accurate enough, we use edge information. A deformable model constrained by spatial relations is applied for this purpose.

Segmentation of internal structures of the pathological brain is another aim of this thesis. The use of prior knowledge can guide the segmentation task in medical imaging. Due to the existence of different types of tumors and consequently different effects on the brain structures, segmentation using prior knowledge such as an atlas is a difficult task. In this work we use another type of prior knowledge which preserves its properties in pathological cases.

The prior information used in our method consists of the spatial relationships between structures which are more consistent than properties of the structures themselves (such as size or shape) in the presence of pathologies. To generalize prior information we use ontologies for knowledge representation. Several types of spatial relations are considered to fully assess the structure of a given scene. Based on the tumor type, its location and size, we select the spatial relations which remain consistent. A fusion of these spatial relations provides a region of interest (ROI). In the first step the ROI is used to search the initial segmentation in a globally segmented image. The initial segmentation is not fine enough, so it is then refined using a deformable model which is

constrained by the fused spatial relations. This process is repeated for other structures in a sequential scheme.

Finally, the results of segmentation are integrated as a labeled image or they can be used to make an individual model of the patient.

The general diagram of the proposed methods, summarizing the work developed in this thesis, is shown in Figure 24.

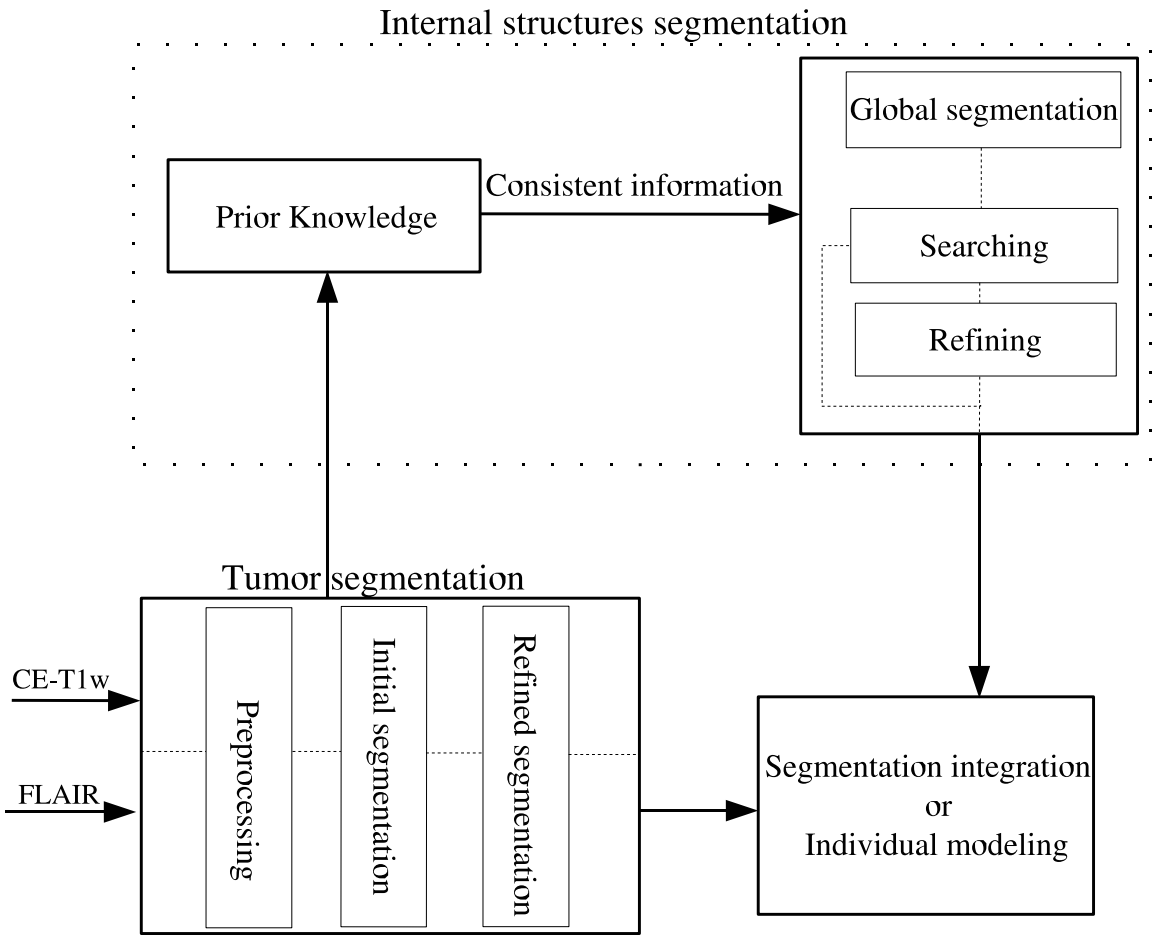

Figure 24: Diagram of the proposed methods for tumor and brain structures segmentation.

Organization of the document This dissertation is organized as follow. Chapter 1 presents the medical and medical imaging background. An overview of the brain anatomy, brain tumors imaging, characteristics and classifications are given in this chapter.

In Chapter 2, we review the existing methods for brain tumor segmentation in three categories, including: region-based, boundary-based and combination of region-

and boundary-based methods.

In Chapter 3 a general framework for brain tumor segmentation is presented. The proposed framework consists of two main parts: preprocessing and segmentation. The preprocessing operations are explained in this chapter.

Chapter 4 presents the second part, i.e. a new segmentation method which combines edge and region information to segment objects. The application of the proposed method for tumor segmentation and its validation are also discussed in this chapter.

The segmentation of brain structures in pathological cases is described in Chapter 5. It consists of a brief survey of existing methods, description of the structure of a priori knowledge using ontologies and the method of segmentation.

Finally, Chapter 6 gives some general conclusions and perspectives for future works.

CHAPTER 1

Brain tumor classification

1.1 Introduction

In this chapter we review some of the brain and tumor characteristics that are useful for the detection, segmentation and interpretation of brain tumors and their surrounding structures in magnetic resonance (MR) images. This chapter starts with an overview of brain anatomy and the magnetic resonance imaging in brain tumors. Section 1.4 gives a definition of brain tumor and its accompanied components. In Section 1.5 brain tumors classification will be presented and Section 1.6 will describe the characteristics of most brain tumors. We will present a classification of tumors based on their location, their radiologic appearance and their alteration on surrounding structures in Sections 1.7, 1.8 and 1.9. Finally in Section 1.11 some conclusions are given.

1.2 Anatomy of the brain

The nervous system is commonly divided into the central nervous system (CNS) and the peripheral nervous system. The CNS is made up of the brain, its cranial nerves and the spinal cord [Waxman, 1999]. In this section we briefly study the cell structures and anatomical components of the brain. The brain consists mainly of two tissue types: gray matter (GM) and white matter (WM) as shown in Figure 1.1. Gray matter is made of neuronal and glial cells, also known as neuroglia or glia that control brain activity, while the cortex is a coat of gray matter that covers the brain and the basal nuclei are the gray matter nuclei located deep within the white matter. The basal nuclei include: caudate nucleus, putamen, pallidum and claustrum (as shown in Figure 1.1). White matter fibers are myelinated axons which connect the cerebral cortex with other brain regions. The corpus callosum, a thick band of white matter fibers, connects the left and right hemispheres of the brain [Waxman, 1999]. The

cerebrospinal fluid (CSF) is also found within the brain and in the spinal cord that surrounds the brain and the spinal cord. The CSF consists of glucose, salts, enzymes and white blood cells. This fluid circulates through channels (ventricles) around the spinal cord and the brain to protect them from injury [T. Woolsey and Gado, 2003]. Between the skull and the brain there is another tissue, that is called the meninges. The meninges consist of three layers that protect the brain and spinal cord.

Anatomically the brain is composed of the cerebrum, the cerebellum and the brainstem (Figure 1.2). The cerebrum, which forms the major part of the brain, is divided into two major parts by the longitudinal fissure: the right and left cerebral hemispheres. Each hemisphere is divided into 4 lobes or areas: the frontal lobe in the front of the brain, the parietal lobe behind the frontal lobe, the temporal lobe on each side of the brain and the occipital lobe at the back of the brain as illustrated in Figure 1.2 [Waxman, 1999].

The cerebellum is located at the back of the brain below the occipital lobes. It is separated from the cerebrum by tentorium (fold of dura). Like the cerebrum, it has a thin outer cortex of gray matter, internal white matter and small, deeply situated masses of gray matter. The brainstem is the lower extension of the brain, located in front of the cerebellum and connected to the spinal cord. It consists of gray matter surrounded by white matter fiber tracts. It has three structures: the midbrain, pons and medulla oblongata. The midbrain is located below the hypothalamus, the pons serves as a bridge between the medulla and midbrain, and the medulla is interconnected with the spinal cord as shown in Figure 1.2.

The central structures of the brain, i.e. the diencephalon, include the thalamus, hypothalamus and pituitary gland. The ventricular system that provides the CSF is divided into four cavities called ventricles, which are connected by a series of holes referred to as foramen, and tubes. Two ventricles enclosed in the cerebral hemispheres are called the lateral ventricles (first and second). They communicate with the third ventricle. The third ventricle is in the center of the brain, and its walls are made up of the thalamus and hypothalamus. The third ventricle connects with the fourth ventricle through a long tube [Waxman, 1999 ; T. Woolsey and Gado, 2003].

1.3 Magnetic resonance imaging (MRI) of brain tumors

For the treatment of patients with brain tumors, imaging of the brain is often indicated at different stages and usually has a significant role in each of them. Several stages of management may be considered:

- detection or confirmation that a structural abnormality is present,

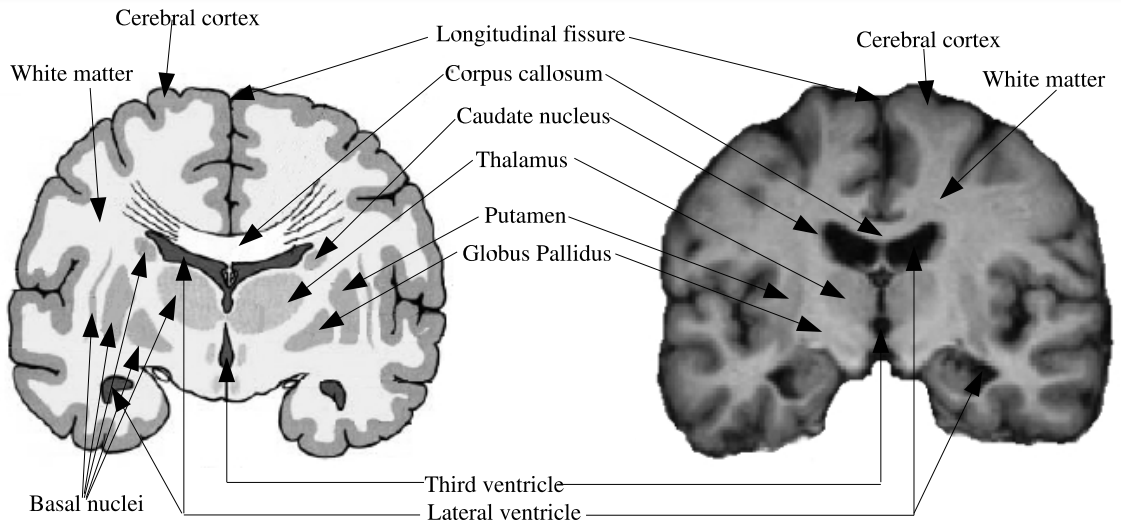

Figure 1.1: Some brain structures illustrated on a schematic drawing (left) and on a slice of a MR image (right) (reproduced from [Marieb, 2000]).

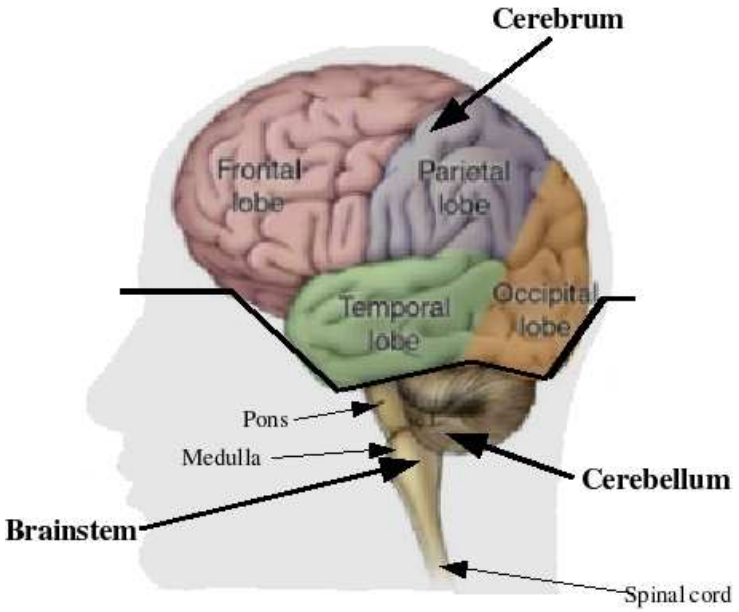

Figure 1.2: Anatomy of the brain (reproduced from [Marieb, 2000]).

- localization and assessment of the extent of any abnormality,
- characterization of the abnormality,

- assessment of the nature of a tumor,
- facilitation of additional diagnosis procedures, and planning for surgery or other types of therapy,
- intraoperative control of rejection progress,
- monitoring of response to therapy.

A variety of imaging techniques are used to study brain tumors, including computed tomography (CT), magnetic resonance (MR) imaging, single photon emission computed tomographic (SPECT) imaging, positron emission tomographic (PET) scanning, and cerebral angiography. At this moment, CT and MR imaging are the most widely used techniques, because of their widespread availability and their ability to produce high resolution images of normal anatomic structures and pathological tissues. CT is the fastest modality, making it the preferred examination for imaging critically ill or medically unstable patients. SPECT and PET imaging serve smaller roles, although their ability to provide information on tissue biology and physiology can be greatly helpful. PET scanning is also used to evaluate tumor grade.

1.3.1 Pros and cons of MRI

MRI is the most frequently used neuroimaging technique for the evaluation and follow-up review of patients with brain tumors for many reasons. It does not use ionizing radiation like CT, SPECT, and PET studies. Its contrast resolution is higher than the other techniques, making it preferable for detecting small lesions and isodense lesions on unenhanced CT. Also, it is more sensitive than CT to detect lesion enhancement. The ability of MRI devices to generate images in the sagittal, axial and coronal planes provides better localization of a lesion in the 3D space of the brain and allows structures involved by the tumor to be more clearly delineated. Finally, MR imaging eliminates the beam-hardening artifact produced by the skull base on CT, making it better for evaluating lesions in the posterior fossa and in the inferior frontal and temporal lobes. In addition to these well-known advantages, the development of MR spectroscopy, MR diffusion imaging, and MR perfusion imaging now permits evaluation of tumor biophysiology with MR scanners. The acquisition of both functional and anatomical information about the tumor during the same scan may be the most important benefit of MR imaging [Ricci and Dungan, 2001].

There are several limitations to MR imaging that must be recognized. Perhaps the most important is a lack of specificity. Multiple pathologic lesions appear hypointense on T1-weighted (T1w) images and hyperintense on T2-weighted (T2w) images. The MRI differential diagnosis for intracranial neoplasms includes infarcts, demyelinating lesions, radiation necrosis, infections, and other inflammatory processes [Kufe et al., 2003]. Although, enhancement does not always correspond to histologic tumor grade,

in general, higher grade tumors will frequently show enhancement on MR imaging. However, an exception to this rule is seen in a very slow-growing tumor such as juvenile pilocytic astrocytoma (JPA), which will frequently show contrast enhancement areas within the tumor. Similarly, some higher grade tumors will not enhance [Kufe et al., 2003]. Hence, although MR features of a lesion can be helpful, but sometimes histologic verification is necessary to establish a diagnosis. MR imaging is also not able to distinguish the edge of a tumor, or determine the full extent of disease. Viable tumor cells are known to exist beyond the borders of abnormal contrast enhancement [Kufe et al., 2003]. Imaging abnormalities seen following treatment are sometimes nonspecific. Radiation injury, including radiation necrosis, is virtually indifferentiable from tumor regrowth. Hence, MRI alone cannot be applied to determine whether tumor is present or not following such a therapy.

In spite of these limitations, MRI remains the standard imaging method in neuro-oncology. Specific imaging characteristics of each tumor type will be presented in the following sections.

1.3.2 MRI physics

Here we do not focus on MRI physics, but in brief, the patient is placed in a strong magnetic field, which causes the protons in the water molecules of the body to align in either a parallel or anti-parallel orientation with the magnetic field. A radiofrequency pulse is introduced, causing the spinning protons to move out of alignment. When the pulse is stopped, the protons realign and emit radiofrequency energy, a signal that is localized by magnetic fields which are spatially varied and rapidly turned on and off. A radio antenna (or coil) within the scanner detects the signal and creates the image. More information about the physics of MRI can be found in [Bushberg et al., 2002], [Brown and Semelka, 2003], [Haacke et al., 1999], [Stark and Bradley, 1999] and [Tofts, 2002].

1.3.3 MRI modalities

The variable behavior of protons within different tissues leads to differences in tissue appearance. The amount of signal produced by specific tissue types is determined by their number of mobile hydrogen protons, the speed at which they are moving, and the tissue's T1 and T2 relaxation times [Armstrong et al., 2004], [Lee et al., 2004] (Table 1.1 summarizes the terms used to describe MRI techniques). As T1 and T2 relaxation times are time dependent, the timing of the RF pulse and the reading of the radiated RF energy change the appearance of the image. The repetition time (TR) describes the time between successive applications of RF pulse sequences. The echo time (TE) describes the delay before the RF energy radiated by the tissue in question is measured. The pulse sequence, which is described by the TR and TE and indicates

the technique used to administer the RF energy, can be chosen to maximize the effect of differences in T1 or T2. This gives rise to the description of an MRI image as T1 or T2 weighted [Stark and Bradley, 1999].

The standard MRI pulse sequence for anatomic and pathologic detail is a spin echo sequence. T1-weighted images (short TR, short TE) provide better anatomic detail, while T2 weighted images (long TR, long TE), which are more sensitive to water content, are more sensitive to pathology. The intermediate or proton density images (long TR, short TE) provide improved contrast between lesions and cerebrospinal fluid.

Fluid-attenuated inversion recovery (FLAIR) image is another pulse sequence that is useful in detecting low contrast lesions. With FLAIR (long T1, long TR, and variable TE), the CSF signal is nulled, enabling pathology adjacent to the CSF to be seen more clearly, i.e. FLAIR sequence produces heavily T2-weighted and CSF-nulled MR image. Many reports confirm the superiority of the FLAIR sequence over conventional spin-echo (SE) sequences with respect to disease [Saleh et al., 2004]. This technique has assumed an important role in routine brain imaging because of its presumed ability to enhance the visibility of brain lesions compared with that of proton density weighted and of T2-weighted spin-echo sequences [Herskovits et al., 2001]. FLAIR images increase detection accuracy for cortical, subcortical and periventricular lesions, and allow more efficient review, compared with T2-weighted images. In FLAIR images, edema is often delineated from tumor, and CSF is distinguished from a cystic or necrotic component, better than T2-weighted and proton density-weighted images [Tsuchiya et al., 1996].

In brain tumors, T1 is proportional to edema. However, a change in oxygen partial pressure is sufficient to alter T1 significantly, hence T1-weighted imaging will not be adequate for accurate quantification of tumor edema. The findings on T2-weighted (also FLAIR) MR images also correlate directly with extracellular water volume and total water content, and inversely with intracellular water content in several tumors. Therefore T2-weighted (also FLAIR) MR images are actually imaging edema [Steen, 1992].

Paramagnetic contrast agents, such as gadolinium, may be administered during MRI acquisitions to highlight regions of abnormality. After injection, the gadolinium remains in the vascular system of the brain, except where the blood-brain barrier has been interrupted. A variety of processes can disrupt the blood-brain barrier, ranging from head trauma to brain tumors [Armstrong et al., 2004]. Certain structures within the brain, such as the pituitary gland, pineal gland, pituitary infundibulum, choroids plexus, and veins, in which the blood-brain barrier is not intact, normally display contrast enhancement. Thus, contrast enhanced T1-weighted (CE-T1w) images provide anatomic details of the brain and distinguish tumor from edema. Figure 1.3 includes an example of T1-weighted, contrast enhanced T1-weighted, FLAIR, and T2-weighted images of a high grade glioma.

Distinguishing low grade from malignant lesions is one of the most important roles of tumor imaging. Unfortunately, something neither MR nor CT does it well [Kufe et al., 2003]. Lesion enhancement by contrast agent is probably the most commonly cited reason for suggesting a tumor is malignant. Histologically, enhancement correlates with areas of increased cellularity and mitotic activity. As a rule, lesions that do not enhance tend to be low grade, whereas enhanced lesions are more likely to be malignant. However, so many exceptions exist (e.g. pilocytic astrocytomas enhance and gliomatosis cerebri often do not), that extreme caution must be exercised when using enhancement as the sole basis for determining the grade of tumors [Ricci and Dungan, 2001].

Term	Description
T1	The time needed for the protons within the tissue to return to their original state of magnetization
T2	The time required for the protons perturbed into coherent oscillation by the radiofrequency pulse to loose this coherence
TR	Repetition time: the time between successive applications of radiofrequency pulse sequences
TE	Echo time: the delay before the radiofrequency energy radiated by the tissue in question is measured
T1-weighted image	Short TR, short TE. Provides better anatomic detail
T2-weighted image	Long TR, short TE. More sensitive to water content and as a result, more sensitive to pathology
FLAIR image	Long TR, short TE. Improved contrast between lesions and cerebrospinal fluid

Table 1.1: Some terms used to describe magnetic resonance imaging techniques [Armstrong et al., 2004].

MRI is evolving rapidly and newer imaging sequences, such as echoplanar MRI, are

being developed, reducing scan times and improving the information obtained from the images [Wen et al., 2001]. Echoplanar MRI can scan images in less than 100 milliseconds and provides information on tumor diffusion and perfusion. Diffusion-weighted MR imaging permits the assessment of the mobility of water molecules and may be useful in helping to distinguish tumor from edema, cystic changes, and normal white matter.

Magnetic resonance spectroscopy (MRS) is a non-invasive method which allows direct investigation of tumor metabolism and provides information on the composition and spatial distribution of cellular metabolites. There is currently a great interest in evaluating the usefulness of MRS for non-invasive diagnosis of tumors, determining tumor grade, and differentiating tumor from radiation effects [Wen et al., 2001].

Functional Magnetic Resonance Imaging (fMRI) is used to visualize brain function by recording changes in the chemical composition of areas of the brain caused by changes in blood flow that occur over intervals of seconds to minutes. This technique, which provides both an anatomic and functional view of the brain, is currently being used for surgical planning for the removal of lesions that impinge on visual or speech areas of the brain [Armstrong et al., 2004].

MR angiography (MRA) provides a means of displaying blood vessels in the brain in a non-invasive manner. It is increasingly being used in preference to conventional angiography, although angiography has better resolution and is still necessary in certain situations [Wen et al., 2001].

Based on this review and our knowledge, it seems that the CE-T1w and FLAIR images are sufficient for detection and segmentation of the majority of brain tumors and its components such as edema and necrosis. Hence in our proposed system for brain tumor segmentation in Chapters 3 and 4, the CE-T1w and FLAIR images are the inputs of the system.

1.4 Brain tumors

A brain tumor is an intracranial mass produced by an uncontrolled growth of cells either normally found in the brain such as neurons, lymphatic tissue, glial cells, blood vessels, pituitary and pineal gland, skull, or spread from cancers primarily located in other organs. Brain tumors are classified based on the type of tissue involved, the location of the tumor, whether it is benign or malignant, and other considerations.

Primary (true) brain tumors are the tumors that originated in the brain and are named for the cell types from which they originated. They can be benign (non cancerous), meaning that they do not spread elsewhere or invade surrounding tissues. They can also be malignant and invasive (spreading to neighboring area). Secondary or

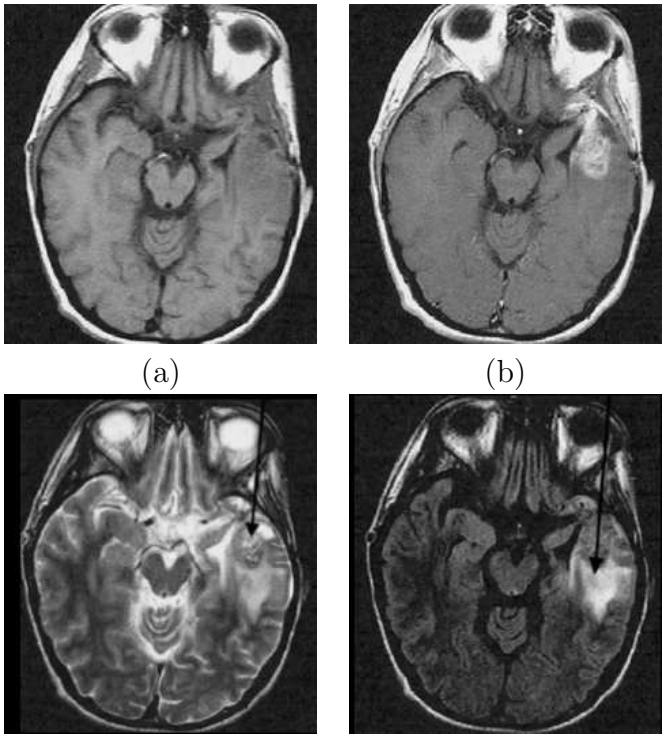

Figure 1.3: MRI of brain. (a) T1-weighted image without contrast enhancement. (b) T1-weighted image with contrast enhancement. (c) T2-weighted image. (d) FLAIR image [Armstrong et al., 2004].

metastasis brain tumors take their origin from tumor cells which spread to the brain from another location in the body. Most often cancers that spread to the brain to cause secondary brain tumors originate in the lumy, breast, kidney or from melanomas in the skin.

Each primary brain tumor, in addition to the solid portion of the tumor, may have other associated parts such as edema and necrosis as in Figures 1.3 and 1.4. Edema is one of the most important factors leading to mortality associated with brain tumors. By definition, brain edema is an increase in brain volume resulting from increased sodium and water content and results from local disruption of the blood brain barrier (BBB). Edema appears around the tumor mainly in white matter regions [Prastawa et al., 2005]. Tumor associated edema is visible in MRI, as either hypointense (darker than brain tissue) or rarely isointense (same intensity as brain tissue) in T1-weighted scans, or hyperintense (brighter than brain tissue) in T2-weighted and FLAIR MRI (Figure 1.4). Necrosis is composed of dead cells in the middle of the brain tumor and are seen hypointense in T1-weighted images (Figure 1.4). A brain tumor may also infiltrate the surrounding tissues or deform the surrounding structures.

In this text we study primary brain tumors and we consider the brain tumor as the primary brain tumor.

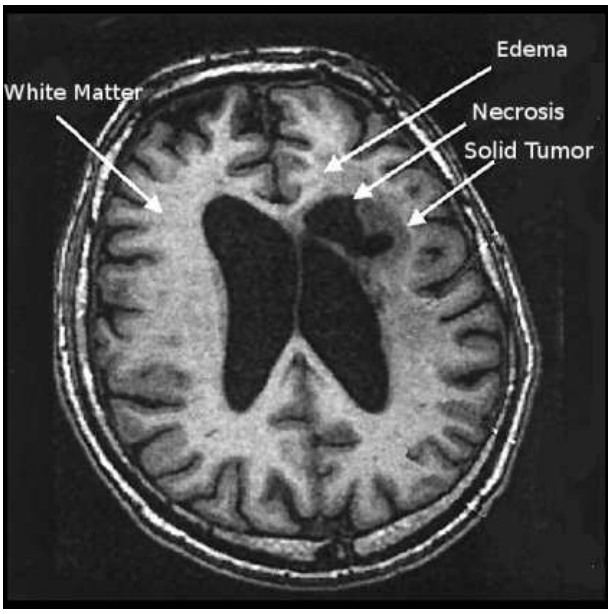

Figure 1.4: One axial slice of a MR image of the brain showing tumor areas [Mahmoud-Ghoneima et al., 2003].

1.5 Classification of brain tumors

The classification of primary brain tumors is usually based on the tissue of origin, and occasionally on tumor location. The degree of tumor malignancy is determined by the tumor's histopathologic features. Because of the substantial variety and unusual biology of brain tumors, it has been extremely difficult to develop a widely accepted histological classification system [Doolittle, 2004].

The earliest brain tumor classifications were provided by Bailey and Cushing in 1926 [Doolittle, 2004]. Their classification scheme proposed 14 brain tumor types, directed important attention to the process of cell differentiation, and dominated views of gliomas until 1949 when a new system was introduced by Kernohan and Sayre [Doolittle, 2004]. Kernohan and Sayre made the important realization that different histopathologic appearances may not represent separate tumor types but rather different degrees of differentiation of one tumor type. They classified tumors into five subtypes: astrocytoma, oligodendroglioma, ependymoma, gangliocytoma, and medulloblastoma and very importantly added a four-level grading system for astrocytomas. The grading system was based on increasing malignancy and decreasing differentiation with increasing tumor grade. The addition of a grading system was a very important advance in classifying brain tumors, and provided information not only regarding tumors' biologic behavior but also information that could be used to guide treatment decisions.

Russell and Rubinstein [Russel and Rubinstein, 1971], Kernohan et al. [Kernohan

et al., 1949], Ringertz [Ringertz, 1950] and Daumas-Duport et al. [Daumas-Duport et al., 200] contributed significantly to the advances in brain tumor classification. Daumas-Duport et al. developed a discrete variable classification system whereby tumors are graded based on the presence or absence of four cellular features: nuclear atypia, mitoses, endothelial cell proliferation, and necrosis. For example, grade I brain tumors have none of the four cellular features, grade II tumors have one of the features, grade III tumors have two features, and grade IV tumors have three or four features. The Daumas-Duport scheme has become known as the St-Anne classification system. Under the supports of the World Health Organization (WHO) (Table 1.2), neuropathologists met in the 1970s to develop a new brain tumor classification system. The WHO system uses a grading system with continuous variables based on survival and histopathological features [Smirniotopoulos, 1999]. The Kernohan [Kernohan et al., 1949], Ringertz [Ringertz, 1950], WHO [Smirniotopoulos, 1999], and St-Anne systems [Daumas-Duport et al., 200] have contributed to advancing the knowledge base and remain widely used brain tumor classification systems internationally.

The classification based on radiologic appearance and location of tumors can also be useful for tumor detection and segmentation, that we will explain in the next section. Based on the alteration of other structures due to the tumor, we will propose another classification of tumors that will be used for the segmentation of the internal brain structures in Chapter 5.

In the next section we review some of WHO system tumors and their radiological characteristics and based on this review, we then classify the tumors based on location, radiological characteristics and effects over other brain structures.

1.6 The tumors of WHO classification

Here we review the properties and characteristics of most common tumors of WHO classification. In this review we focus on the appearance of tumors in MRI images (T1w, CE-T1w, T2w and FLAIR images), the grade of tumors and some general information which will be useful in the detection, segmentation and interpretation of brain tumors in 3D MRI.

1.6.1 Gliomas

A brain tumor that develops from glial cells is called a glioma. About half of all primary brain tumors and one-fifth of all primary spinal cord tumors form from glial cells. Gliomas tend to grow in the cerebral hemispheres, but may also occur in the brain stem, optic nerves, spinal cord, and cerebellum. Gliomas are divided into subgroups depending on the origin of the glial cells. There are several types of gliomas, categorized

Histology	% of Reported Brain Tumors
Tumors of neuroepithelial tissue	**48.1**
Pilocytic astrocytoma	2.1
Diffuse astrocytoma (protoplasmic,fibrillary)	1.0
Anaplastic astrocytoma	3.7
Unique astrocytoma variants	0.5
Astrocytoma, NOS (Not Otherwise Specified)	4.2
Glioblastoma	23.0
Oligodendroglioma	2.9
Anaplastic oligodendroglioma	1.1
Ependymoma/anaplastic ependymoma	1.8
Ependymoma variants	0.4
Mixed glioma	1.0
Glioma malignant, NOS	2.7
Choroid plexus	0.2
Neuroepithelial	0.1
Benign and malignant neuronal/glial	1.3
Pineal parenchyma	0.2
Embryonal/primitive/medulloblastoma	1.9
Tumors of the meninges	**28.7**
Meningioma	27.4
Other mesenchymal, benign, and malignant	0.3
Hemangioblastoma	0.9
Lymphomas and hematopoietic neoplasms	**2.7**
Lymphoma	2.7
Germ cell tumors and cysts	**0.5**
Germ cell tumors, cysts, and heterotopias	0.5
Tumors of the sellar region	**7.4**
Pituitary	6.6
Craniopharyngioma	0.8
Local extensions from regional tumors	**0.2**
Chordoma/chondrosarcoma	0.2
Unclassified tumors	**5.0**
Hemangioma	0.4
Neoplasm, unspecified	4.5
All other	0.1

Table 1.2: Primary (malignant and non-malignant) brain and central nervous system (CNS) tumors (simplified WHO classification) and percent of reported [Doolittle, 2004].

by where they are found, and the type of cells that originated the tumor. Here we review astrocytoma, ganglioglioma, oligodendroglioma and ependymoma that are the most common types of gliomas.

Astrocytoma

Astrocytomas are primary brain tumors derived from connective tissue cells called astrocytes, which are star-shaped glial cell. They are the most common type of the brain tumors and account about 40% of all primary brain tumors. Astrocytomas are included in the category of malignant tumors, WHO and St-Anne grading system grade them based on the appearance of certain characteristics: atypia, mitoses, endothelial proliferation, and necrosis [Daumas-Duport, 1992], [Daumas-Duport et al., 200], [Lopes and Laws, 2002], [Smirniotopoulos, 1999]. These features reflect the malignant potential of the tumor in terms of invasion and growth rate. Tumors without any of these features are grade I, and those with one of these features (usually atypia) are grade II, tumors with 2 criteria and tumors with 3 or 4 criteria are WHO grades III and IV, respectively. Thus, the low grade group of astrocytomas are grades I and II and high grade astrocytomas are grade III and IV.

- Low grade astrocytoma (grades I and II)

  Tumors of this type are well differentiated and grow relatively slow but can spread to neighboring tissue. In general, low grade gliomas cause less mass effect than high grade astrocytomas, because they grow more slowly and incite little vasogenic edema. The location of these tumors is the cerebral hemisphere (occurs often in the frontal region or the subcortical white matter), the cerebellum or brainstem. Most common tumors of this type are pilocytic astrocytoma and diffuse astrocytoma which occur mostly in children and young adults [Henson et al., 2005], [Wen et al., 2001], [Emedicine, 2005]. Both CT scan and MRI can help in the diagnosis of low grade astrocytoma. Generally, MRI is considered the study of choice. In MRI, low grade gliomas show decreased signal relative to surrounding brain on T1 sequences (Figure 1.5). In T2 sequences and FLAIR, higher signal reflects both the tumor and surrounding edema (if exist) (Figure 1.6). Pilocytic astrocytomas are often associated with a cyst, which may be particularly prominent on T2-weighted sequences. There is usually little or no contrast enhancement in MRI (Figure 1.6) [Daumas-Duport, 1992], [Henson et al., 2005], [Kantor et al., 2001], [Wen et al., 2001].

- High grade astrocytoma (grades III and IV)

  Anaplastic astrocytoma and glioblastoma multiform (GBM) are most common tumors of this type and account approximately 30% of all primary brain tumors. These tumors grow more rapidly and infiltrate other nearby healthy cells. They are not well differentiated. Both types of high grade astrocytomas have similar

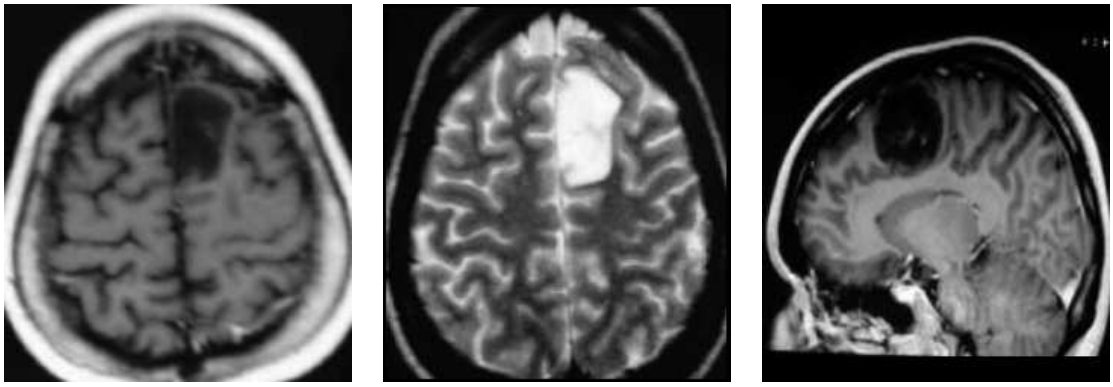

(a) (b) (c)

Figure 1.5: Low grade astrocytoma. a) An axial slice of a T1-weighted image. b) An axial slice of a T2-weighted image. c) A sagittal slice of a contrast enhanced T1-weighted image [Emedicine, 2005].

presentation features. In general they tend to be less circumscribed than low grade astrocytomas and surrounded with more edema. The difference between anaplastic astrocytomas and GBMs is in appearance of necrosis in GBMs. High grade astrocytomas have a variable radiographic appearance. Anaplastic astrocytomas may appear as low density lesions or inhomogeneous lesions, with areas of both high and low density within the same lesion. Unlike low grade lesions, partial contrast enhancement is common. GBM is the most common and most malignant of the glial tumors. Composed of poorly differentiated neoplastic astrocytes, GBMs primarily affect adults, and they are located preferentially in the cerebral hemispheres. Much less commonly, GBMs can affect the brain stem in children and the spinal cord. These tumors may develop from lower-grade astrocytomas (grade II) or anaplastic astrocytomas (grade III) [Mahesh and Tse, 2004], [Wen et al., 2001].

These tumors and surrounding edema have low signal intensity in T1-weighted and high signal intensity in T2-weighted MR images and enhancement is common (Figure 1.7). Hemorrhage may be present but calcification is uncommon unless the tumor arose from a pre-existing lower grade lesion. These tumors tend to infiltrate along white matter tracts (Figure 1.7) and frequently involve and cross the corpus callosum.

GBMs typically have an enhancing ring observed in T1-weighted images (Figure 1.8) and a broad surrounding zone of edema apparent in T2-weighted images. The central hypodense core represents necrosis, the contrast-enhancing ring is composed of highly dense neoplastic cells with abnormal vessels permeable to contrast agents, and the peripheral zone of nonenhancing low attenuation is vasogenic edema containing varying numbers of invasive tumor cells. Several pathological studies have clearly shown that the area of enhancement does not represent the outer tumor border because infiltrating glioma cells can be identified easily within a 2cm margin [Kantor et al., 2001], [Emedicine, 2005].

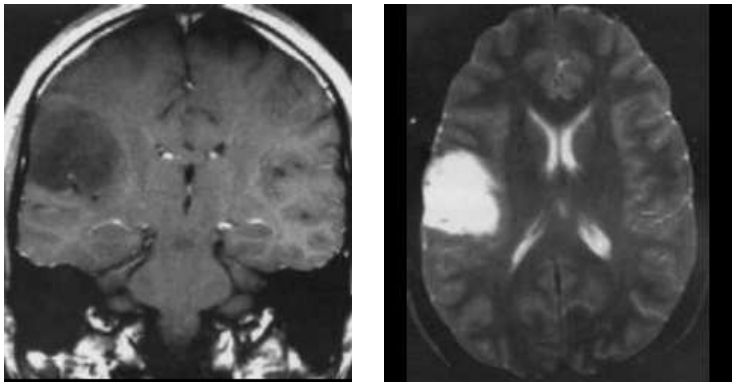

(a) (b)

Figure 1.6: Diffuse low grade astrocytoma (Grade II). a) Coronal slice of contrast enhanced T1-weighted image. No enhancement is present with contrast enhancement. b) Axial slice of T2-weighted image of the same tumor without surrounding edema [Emedicine, 2005].

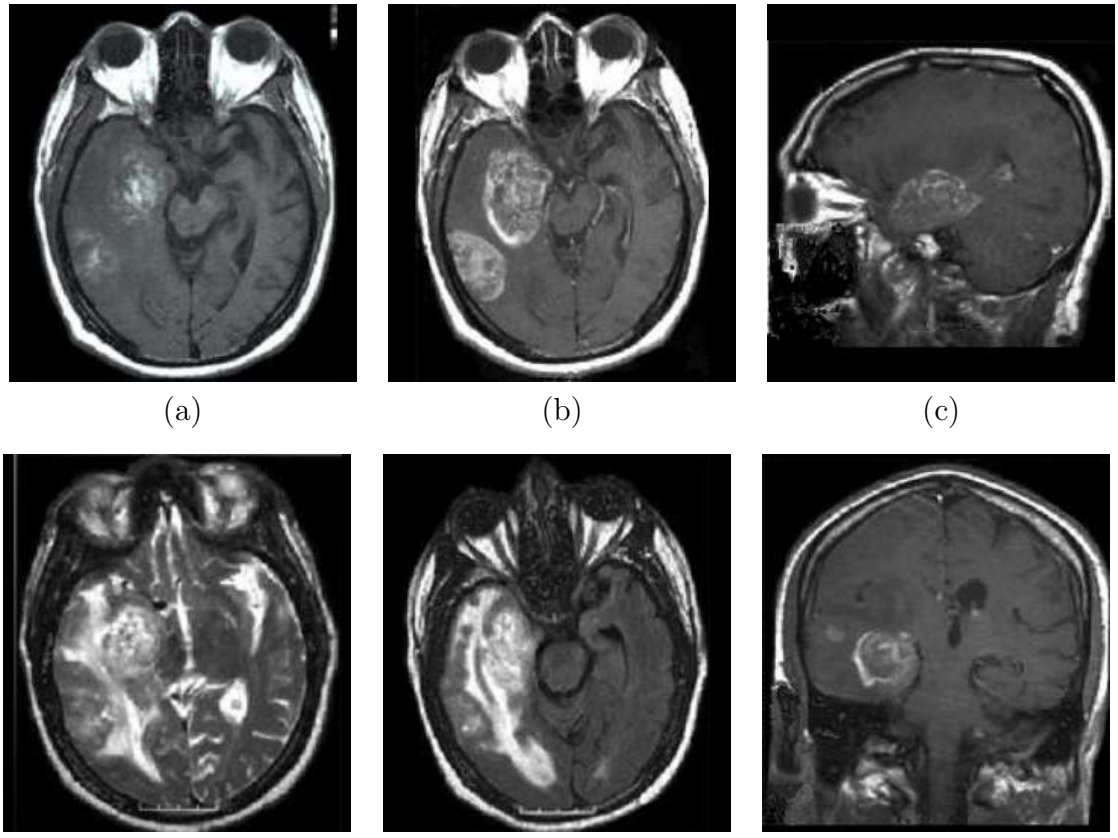

(a) (b) (c)

(d) (e) (f)

Figure 1.7: Glioblastoma multiform. a) Axial slice of T1-weighted image without contrast enhancement. b) Same slice with contrast enhancement. c) Sagittal view of this tumor. d) T2-weighted image of the same tumor with surrounding edema. e) FLAIR image. f) Coronal slice of T1-weighted image [Emedicine, 2005].

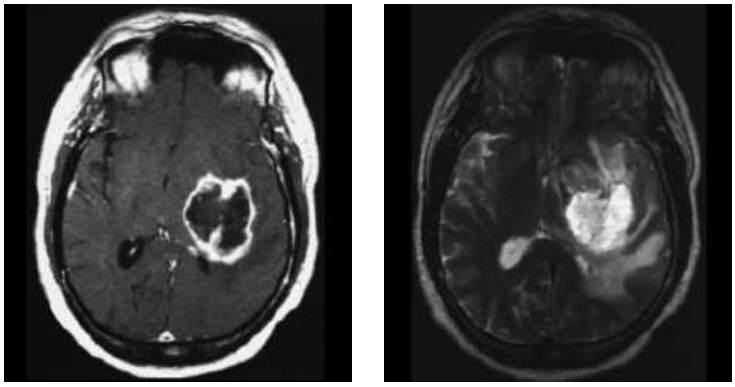

(a) (b)

Figure 1.8: Glioblastoma multiform. a) Contrast enhanced axial T1-weighted of a ring enhanced tumor (necrotic). b) Axial T2-weighted image of the same tumor showing the surrounding edema [Wen et al., 2001].

Ganglioglioma

Gangliogliomas are slowly growing tumors occurring in children and young adults. Temporal lobes and cerebellar hemispheres are the most common locations for this type of tumors. In this type of tumors no surrounding edema is seen (Figure 1.9), but typically they are accompanied with cyst. The radiological appearance is non-specific. The tumors resemble oligodendrogliomas and appear hypointense (darker than GM and brighter than CSF) in T1-weighted images and hyperintense in T2-weighted images with variable enhancement (Figure 1.9) [Wen et al., 2001]. They do not enhance in contrast enhanced T1-weighted images.

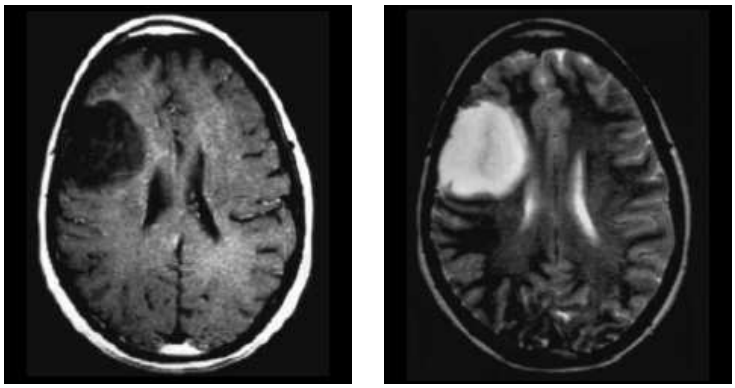

(a) (b)

Figure 1.9: Ganglioglioma. (a) contrast enhanced axial T1-weighted MRI showing non-enhancing hypointense frontal tumor. (b) The same lesion appears hyperintense on T2-weighted MRI [Wen et al., 2001].

Oligodendroglioma

Oligodendrogliomas are the other most common type of glioma, traditionally thought to comprise 2% to 5% of primary brain tumors and 4% to 15% of gliomas. It is believed that, in the past, many tumors that were actually oligodendrogliomas were diagnosed to be various types of astrocytomas. Also, with the improved brain imaging provided by MRI, gliomas are being diagnosed more correctly than in the past. They are generally slowly growing tumors and are frequently located within the frontal, temporal or parietal lobes. Cystic degeneration is common but hemorrhage and edema are uncommon. Oligodendrogliomas are distinctive, consisting of homogeneous, compact, rounded cells with distinct borders and clear cytoplasm surrounding a dense central nucleus, giving them a "fried egg" appearance (Figures 1.10 and 1.11). Within the tumor, branching blood vessels are characteristics and divide the cells into discrete clusters. Based on St-Anne grading system, there are grade A and grade B of these tumors. In grade A contrast enhancement and necrosis can not be seen (Figure 1.10) but in grade B nodular contrast enhancement and necrosis are seen (Figure 1.12). The tumor is typically located in the cortex and white matter, and infiltration of the overlying leptomeninges may be seen [Engelhard et al., 2003].

MRI (with and without gadolinium) is the preferred modality. T1-weighted images generally demonstrate a hypointense mass (Figures 1.10 and 1.11). T2-weighted images show a hyperintense mass with surrounding edema (Figures 1.10 and 1.11).

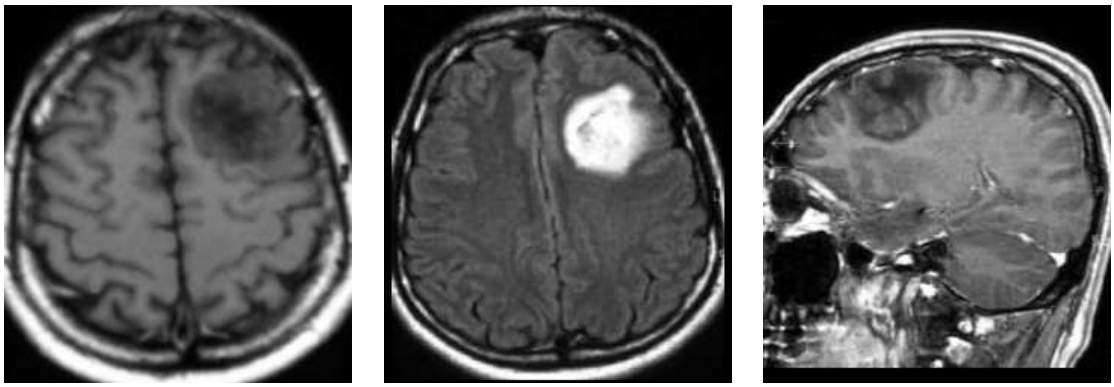

(a) (b) (c)

Figure 1.10: Low grade oligodendroglioma. a) Non enhanced tumor in axial slice of contrast enhanced T1-weighted image. b) Same tumor on FLAIR. c) Sagittal view of the tumor [Emedicine, 2005].

Ependymoma

Ependymomas are glial tumors that arise from ependymal cells within the brain. This tumor is histologically benign but behaves malignantly. Intracranial lesions usually

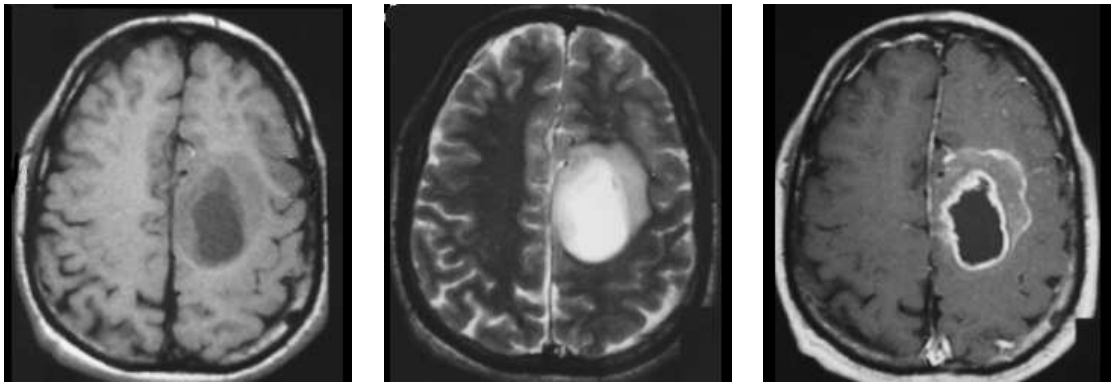

(a) (b) (c)

Figure 1.11: A cystic oligodendroglioma. a) Axial T1-weighted, showing varying degrees of hypointensity. b) T2-weighted image showing hyperintensity, especially of the central cyst. c) Contrast enhanced T1-weighted image showing ring formation at both the tumor-cyst, and tumor-brain interfaces. [Engelhard et al., 2003].

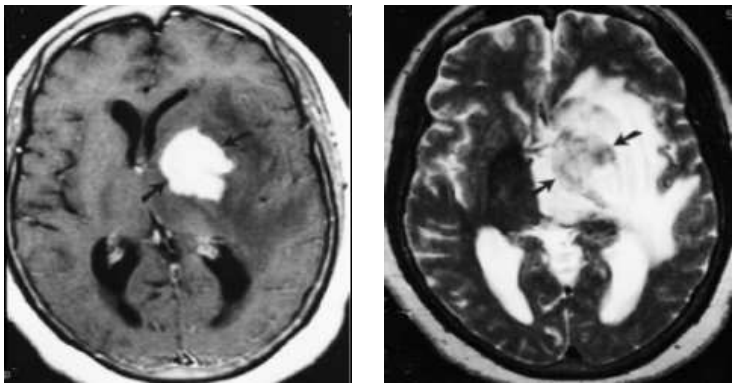

(a) (b)

Figure 1.12: High grade oligodendroglioma. a) Contrast enhanced T1-weighted image. b) T2-weighted image from the same patient, showing isointense to hyperintense appearance of the mass [Engelhard et al., 2003].

arise from the roof of the fourth ventricle in children, while spinal ependymomas typically occur in adults. Here we review the intracranial ependymoma.

The presence of edema is uncommon and polar cysts may be seen. With the administration of contrast material, the tumors usually enhance strongly and homogeneously. Ependymomas appear hypointense in T1-weighted and hyperintense in FLAIR images. Since this tumor is connected to ventricles, to distinguish the tumor from ventricles, FLAIR images are used. Ependymomas are usually hyperintense on T2-weighted sequences. In some cases, contrast enhancement of a cystic ependymoma may be minimal. In these cases, distinguishing these tumors from intramedullary astrocytomas is difficult [Henson et al., 2005], [Wen et al., 2001].

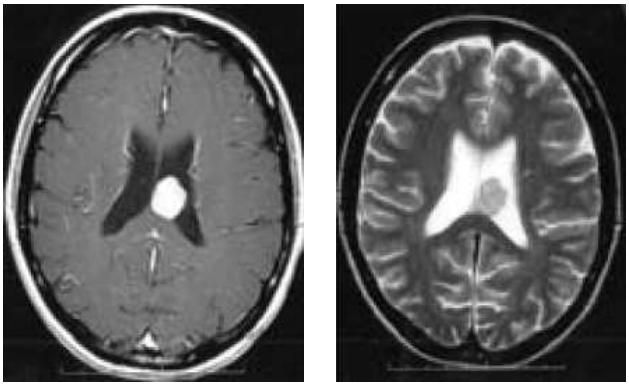

(a) (b)

Figure 1.13: Ependymoma. a) Axial view of contrast enhanced T1-weighted image. b) T2-weighted image of the same tumor [Maksoud et al., 2002].

1.6.2 Medulloblastoma (Primitive Neuroectodermal Tumor (PNET))

In the brain, medulloblastoma most often arises in the posterior fossa. The tumor has the potential of spreading throughout the CNS. Cysts, areas of necrosis, and calcification are rare but edema is common. Adults, more frequently than children, can have the desmoplastic variant of medulloblastoma. This form of the tumor is situated laterally in the hemisphere with indistinct borders and small cystic or necrotic areas [Emedicine, 2005].

MRI with the administration of gadolinium is the diagnosis test of choice for medulloblastoma. Tumors appear hypointense on T1-weighted images, usually seen expanding to the fourth ventricle. The brain stem is compressed and shifted ventrally. By administration of gadolinium in children, homogeneous enhancement commonly occurs, whereas in adults, a more heterogeneous pattern is usually seen (Figure 1.14). T2-weighted and FLAIR images display a hyperintense mass with a surrounding area of edema (Figure 1.14). MRI can help differentiating medulloblastoma from ependymoma: the latter extends further into the lateral recess of the fourth ventricle. MRI can also help distinguishing between medulloblastoma and exophytic brainstem glioma (the latter having a broader attachment to the floor of the fourth ventricle) [Wen et al., 2001].

1.6.3 Lymphoma

Lymphomas typically develop in the subcortical and subependymal white matter. Within the brain substance, the irregular tumor edge extends along perivascular spaces. The spinal cord is frequently affected in secondary lymphoma. Lymphoma tumors are often multiple with central necrosis in AIDS. Tumor lesions can cross the midline and may appear as a butterfly tumor involving both cerebral hemispheres.

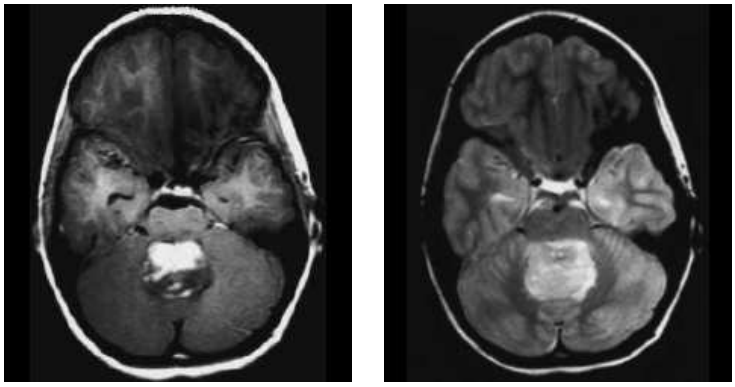

(a) (b)

Figure 1.14: Medulloblastoma. a) Contrast enhanced axial T1-weighted image showing irregularly enhancing tumor in the cerebellar vermis. b) Axial T2-weighted MRI of the same patient showing increased signal in the tumor [Wen et al., 2001].

Involvement of the perivascular spaces with contrast enhancement or of the corpus callosum (glioma or metastatic neoplasm must be differentiated) is strongly suggestive of CNS lymphoma [Plotkin and Batchelor, 2001].

The classic appearance of lymphoma is an hypointense nodule or mass on T1-weighted images and hyperintense on corresponding T2-weighted images. On contrast enhanced T1-weighted MRI, lymphoma tends to enhance intensely and diffusely. A ring like enhancing pattern is seen most often in patients with AIDS (Figure 1.15). Often, little or no surrounding vasogenic edema is demonstrated [Plotkin and Batchelor, 2001], [Wen et al., 2001].

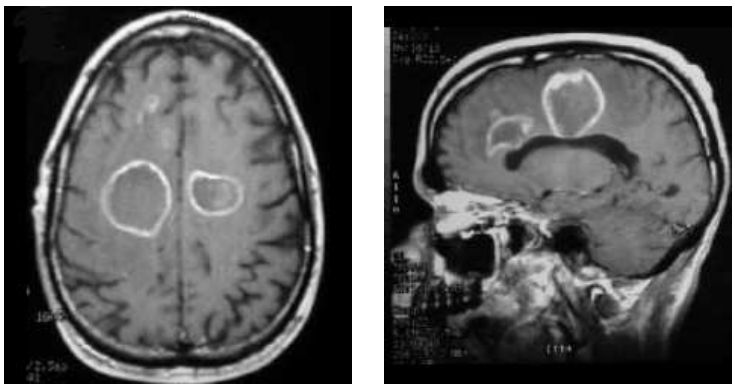

(a) (b)

Figure 1.15: Lymphoma tumor. a) Axial contrast enhanced T1-weighted image shows ring enhanced tumor. b) Sagittal view of the same patient. [Emedicine, 2005].

1.6.4 Meningioma

Meningiomas are the most common benign tumors, accounting for 25-30% of all primary brain tumors. They are most commonly located in the para-sagittal region. They are more common in women (3:1) and occur in middle-aged and elderly patients. Although meningiomas are benign tumors, they are often accompanied by edema [Engelhard, 2001].

On T1-weighted images, most meningiomas are well-circumscribed extra-axial masses, which are usually isointense with gray matter. Other meningiomas are slightly hypointense to gray matter. Because of this, they may be hard to appreciate on T1-weighted images. On T2-weighted images, meningiomas have a more variable appearance (Figure 1.16), which seems to relate to the consistency of the tumor. Rapid growth may cause areas of central necrosis, which are hypointense on T1-weighted and hyperintense on T2-weighted images. Cyst formation and hemorrhage may occur in meningiomas, but are relatively rare [Engelhard, 2001], [Wen et al., 2001].

With gadolinium contrast agent, meningiomas usually show a marked, homogeneous enhancement pattern on T1-weighted images (Figure 1.16). When gadolinium is used, the improved resolution of the newer MR scanners allows better delineation of the extent of tumor spread into dura adjacent to the tumor and the degree of tumor invasion into the dural sinuses. Edema from a meningioma may produce a surrounding lower intensity (darker) signal on T1-weighted images, but is better seen as a higher intensity (whiter) signal on the T2-weighted and FLAIR images. It has been stated that 70% of patients with meningiomas have at least some degree of peritumoral edema. [Lobato et al., 1996] reported that meningiomas located along the frontal convexity or middle third of the falx were most likely to be associated with edema formation. The presence and duration of symptoms, tumor size, and degree of cortical damage (or invasion) are other factors that have been found to correlate with the formation of edema adjacent to meningiomas. FLAIR images can be used to better delineate meningioma from surrounding cerebrospinal fluid [Engelhard, 2001].

1.6.5 Craniopharyngioma

Craniopharyngiomas develop in the area of the brain called the hypothalamus, which is close to the pituitary gland. It is usually found in children or young adults and accounts for around 1% of all brain tumours.

The mixed solid and cystic nature of the tumor is clear on MR images. By MRI examination, the tumor is of variable T1 signal, often hyperintense. The T1 hyperintensity is usually secondary to high protein content in the cyst fluid (Figure 1.17). On T2-weighted sequences, including FLAIR, the solid portion is again usually heterogeneous, whereas the cysts are invariably hyperintense. Following contrast agent,

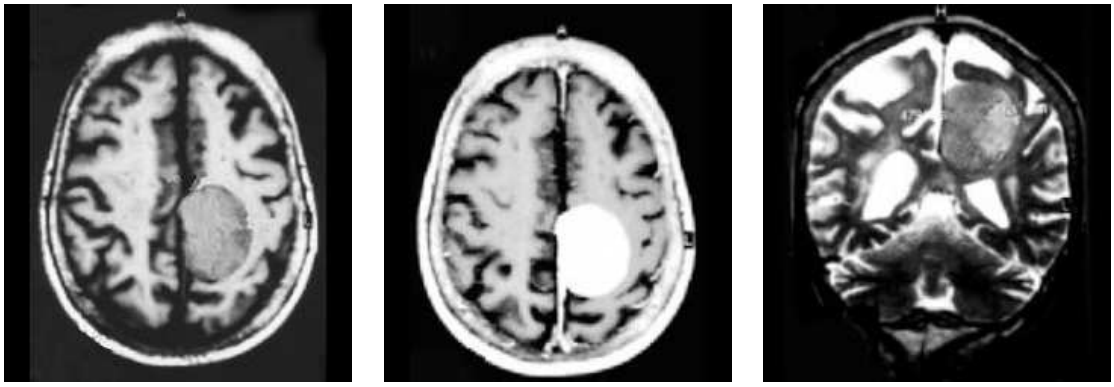

(a) (b) (c)

Figure 1.16: Meningioma tumor. a) Axial slice of T1-weighted image. b) The same tumor on contrast enhanced T1-weighted image. c) Coronal view of T2-weighted image [Emedicine, 2005].

there is almost invariable enhancement of the solid portion and the peripheral rim of the cystic portion on MR image. The enhancement of the solid portion may be either uniform or heterogeneous [Curran and O'connor, 2005].

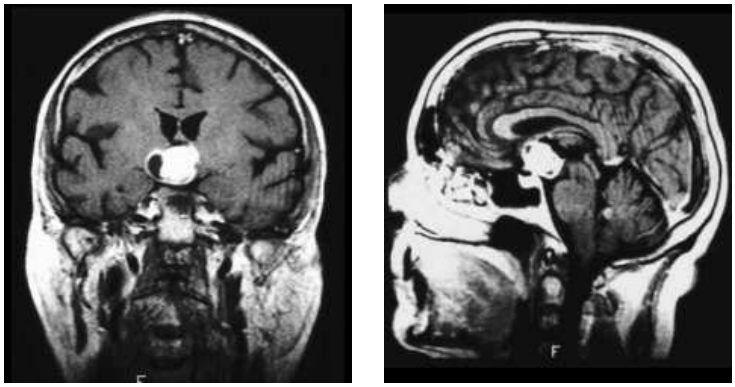

(a) (b)

Figure 1.17: Craniopharyngioma. a) Coronal contrast enhanced T1-weighted image showing an enhanced solid portion of the tumor together with a hypodense cystic component on the right side of the tumor. b) Sagittal view of the same tumor [Wen et al., 2001].

1.6.6 Pituitary adenoma

Pituitary adenomas comprise about 7% of primary brain tumors. They arise from the anterior lobe of the pituitary gland. MRI is the imaging modality of choice. Microadenomas (< 1cm diameter) appear as low intensity lesions on T1-weighted scans. Gadolinium enhances the normal gland adjacent to the adenoma and highlights

the lesion (Figure 1.18). Macroadenomas are usually isointense on T1-weighted images and enhance homogeneously with gadolinium (Figure 1.18). They appear hyperintense in FLAIR and T2-weighted images. The multiplanar capability of MRI enables the full extent of larger lesions to be visualized [Bonneville et al., 2005].

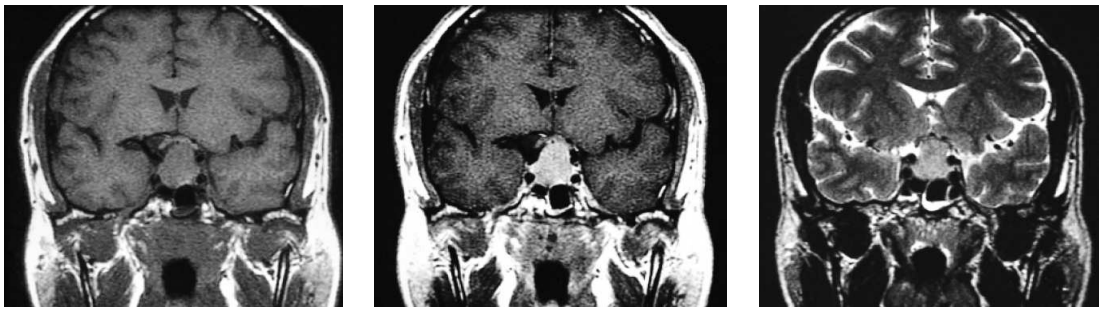

(a) (b) (c)

Figure 1.18: Pituitary adenoma. a) Coronal T1-weighted MRI showing a large pituitary macroadenoma. b) Coronal MRI showing the same tumor enhancing with contrast enhancement. c) T2-weighted image of the same patient [Emedicine, 2005].

1.6.7 Summary

In this section we reviewed some tumors of brain that constitute about 90% of all primary brain tumors. In Table 1.3 we summarize the characteristics of these tumors.

Tumor Name	WHO Grade	T1w App.	FLAIR App.	CE-T1w Enhance	Location	Edema	Necr.	Cyst
Astr.(LG)	I&II	Hypo	Hyper	no	CR,CL,BS	no	no	yes
Astr.(HG)	III	Hypo	Hyper	yes	CR,CL,BS	yes	no	no
Astr.(HG)	IIII	Hypo	Hyper	yes	CR,CL,BS	yes	yes	no
Gang.		Hypo	Hyper	no	CR	no	no	yes
Olig.(LG)	II	Hypo	Hyper	no	CR	no	no	no
Olig.(HG)	III	Hypo	Hyper	yes	CR	yes	yes	yes
Epen.		Hypo	Hyper	yes	CR	no	no	yes
PNET		Hypo	Hyper	yes	CL	yes	no	no
Lymp.		Hypo	Hyper	yes	CR	no	no	no
Meni.		Hypo	Var.	yes	CR	yes	no	no
Cran.		Hypo	Hyper	yes	CR	no	yes	yes
Pitu.		Hypo	Hyper	yes	CR	no	no	no

Table 1.3: Brain tumors properties. Here CR denotes as cerebral hemisphere, CL as cerebellum, BS as brain stem. For the tumor name, the four first characters have been chosen.

1.7 Classification of tumors based on their location

Basically, all brain tumors are considered localized unless they cross the midline or the tentorium or unless they are described as having "drop" metastases in the spinal cord [Seer, 2007]. We can classify tumors by their location into 3 classes: local tumors, regional tumors and distant tumors. Local tumors confined to one hemisphere in one part of brain, meninges and ventricular system as illustrated in Figure 1.19. Regional tumors cross midline or tentorium invades bone, blood vessel, nerves and spinal cord. Distant tumors are extend to nasal cavity, nasopharynx, posterior pharynx and outside the CNS. In this thesis we consider local tumors.

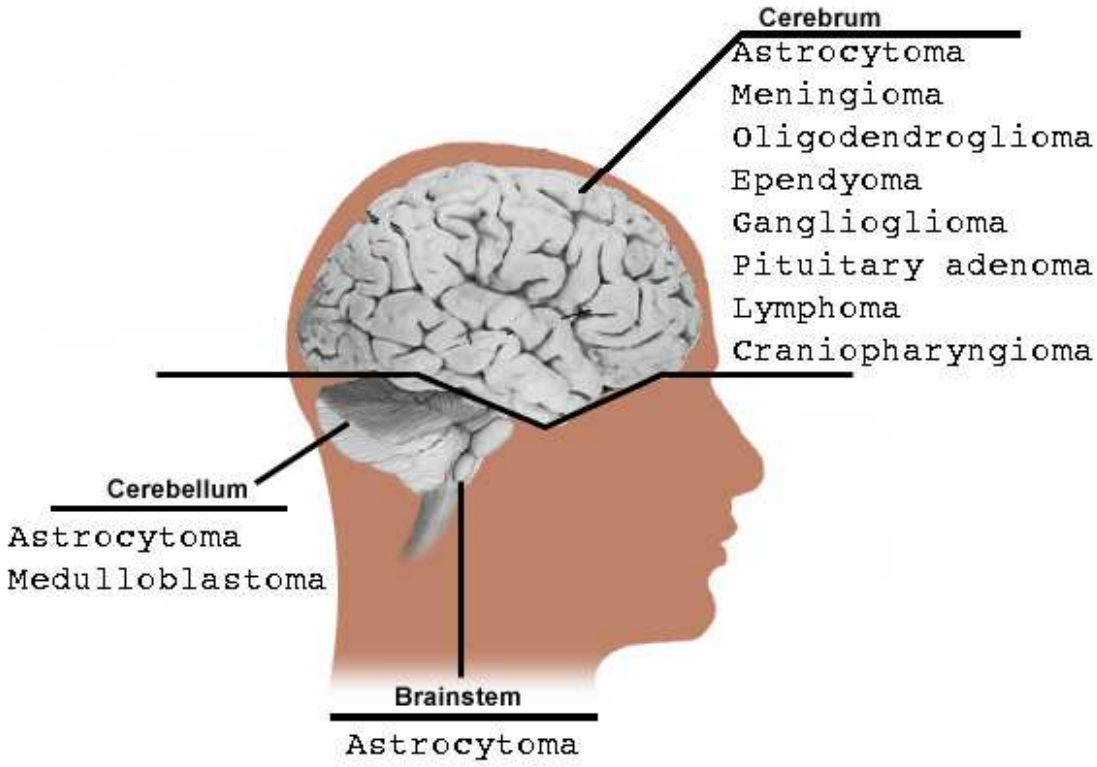

Figure 1.19: Various types of brain tumors in various places in the central nervous system

1.8 Classification of tumors based on their radiologic appearance

Based on radiologic appearance of tumors in contrast enhanced T1-weighted (Table 1.3) and without considering the histology of tumors we can classify the brain tumors into 4 classes: non-enhanced, full-enhanced without edema, full-enhanced with edema and ring-enhanced tumors.

1.8.1 Non-enhanced tumors

The tumors of this type do not take contrast agent and appear hypointense (darker than GM) in contrast enhanced T1-weighted and T1-weighted images (Figure 1.20). They are usually without edema or little edema. In FLAIR and T2-weighted images, they appear as hyperintense (Figure 1.20). Low grade astrocytomas, gangliogliomas and oligodendrogliomas are most common tumors of this type.

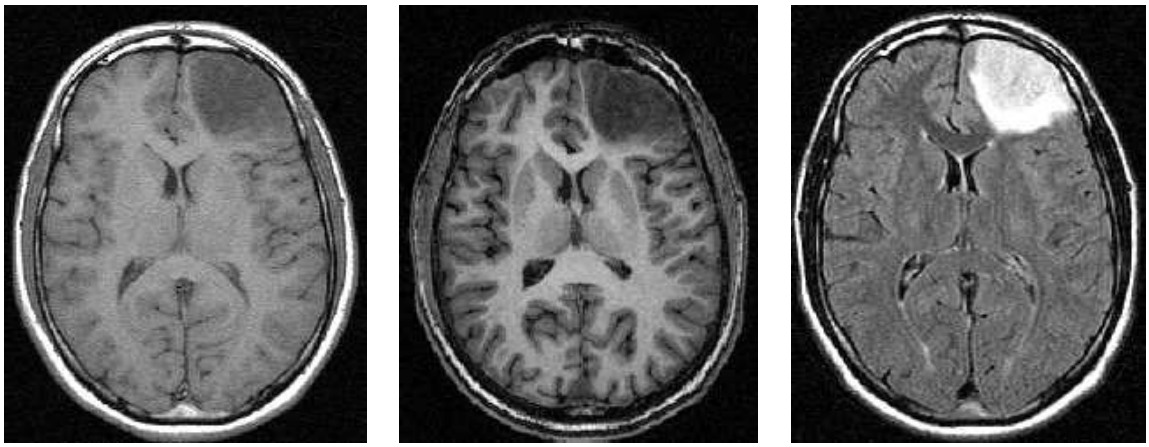

(a) (b) (c)

Figure 1.20: A non-enhanced tumor. a) Axial slice of T1-weighted. b) The same slice of contrast enhanced T1-weighted. c) FLAIR image.

1.8.2 Full-enhanced tumors without edema

These tumors enhance with contrast administration in T1w images and approximately all voxels of the tumor appear hyperintense in CE-T1w (Figure 1.21). These tumors are without edema and appear hypointense in T1-weighted images and hyperintense in T2-weighted and FLAIR images (Figure 1.23). Meningimoas (some types), ependymomas, lymphomas, craniopharyngiomas and pituitary adenomas are in this category.

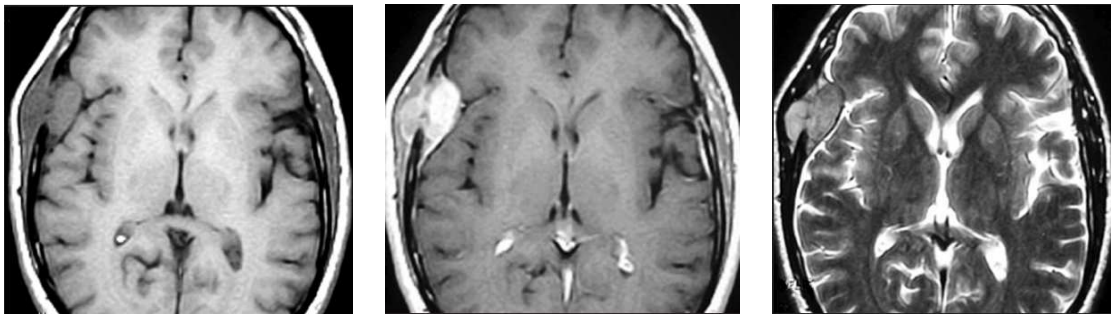

(a) (b) (c)

Figure 1.21: A full-enhanced tumor without edema. a) Axial slice of T1-weighted image. b) The same slice of contrast enhanced T1-weighted image. c) T2-weighted image.

1.8.3 Full-enhanced tumors with edema

These tumors have two sections, the solid section and edema. The solid section takes contrast agent and appears hyperintense in contrast enhanced T1-weighted images and hypointense in T1-weighted images, while the edema appears hypointense in T1-weighted images and contrast enhanced T1-weighted images (Figure 1.22). In FLAIR and T2-weighted images both sections of the tumor appear hyperintense (Figure 1.22). Anaplastic astrocytomas (high grade), high grade oligodendrogliomas, PNETs and some type of meningiomas can be included in this category.

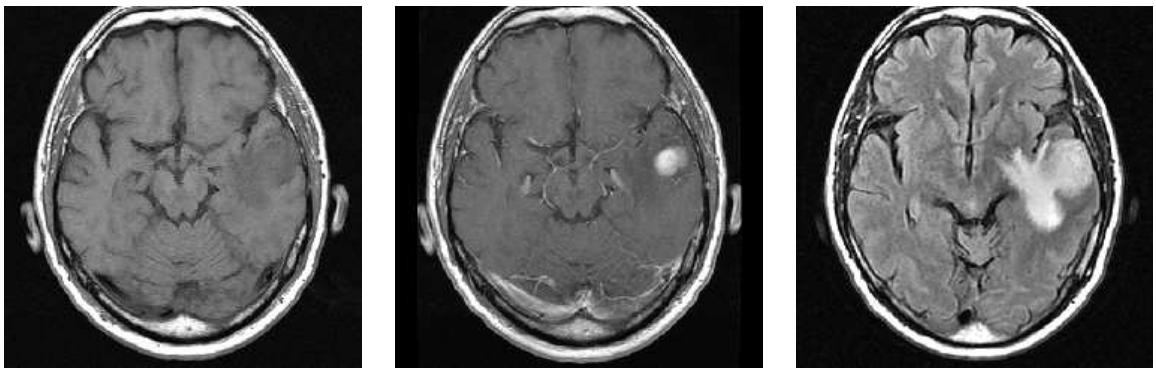

(a) (b) (c)

Figure 1.22: A full-enhanced tumor with edema. a) Axial slice of T1-weighted image. b) The same slice of contrast enhanced T1-weighted image. c) FLAIR image.

1.8.4 Ring-enhanced tumors

These tumors have 3 sections. The central section is necrosis and appears hypointense in contrast enhanced T1-weighted and T1-weighted images. The solid section sur-

rounds the necrosis and takes contrast agent, hence appears hyperintense in contrast enhanced T1-weighted images and hypointense in T1-weighted images (Figure 1.23). The third section is the edema which surrounds the solid section. The edema appears hypointense in both T1-weighted and contrast enhanced T1-weighted images. In T1-weighted images the solid section, edema and necrosis are hypointense, while the necrosis is darker than the other sections. FLAIR images show the edema and solid section as hyperintense signal, while the necrosis section appears hypointense (Figure 1.23). GBMs and high grade oligodendrogliomas have these characteristics.

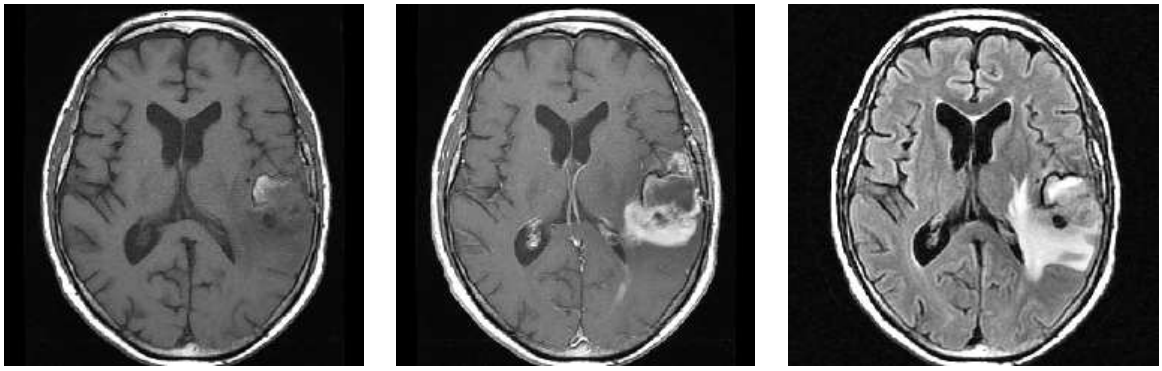

(a) (b) (c)

Figure 1.23: A ring-enhanced tumor. a) Axial slice of T1-weighted image. b) The same slice of contrast enhanced T1-weighted image. c) FLAIR image

1.9 Classification of tumors based on their alterations

As an alternative classification, we consider here a classification of brain tumors according to their spatial characteristics and the nature of the potential alterations of the brain structural organization they induce (location, infiltration, destruction, edema...).

1.9.1 Small deforming tumors (SD)

In this category we include tumors that are principally infiltrating or non-enhanced without necrosis or small necrotic tumors. The whole structural brain arrangement is not significantly altered. A further distinction is made, into subcortical (SD-SC) (Figure 1.24 (b)) or peripheral (SD-P) tumors (Figure 1.24 (a)), according to their sizes, their distance to the inter-hemispheric plane and depending on whether they involve deep gray nuclei or not.

1.9.2 Large deforming tumors (LD)

Tumors and lesions in this class significantly alter the surrounding brain structure arrangement. These tumors are necrotic and can be surrounded by a lot of edema (Figure 1.24 (c)). These tumors usually take contrast agent and are malignant.

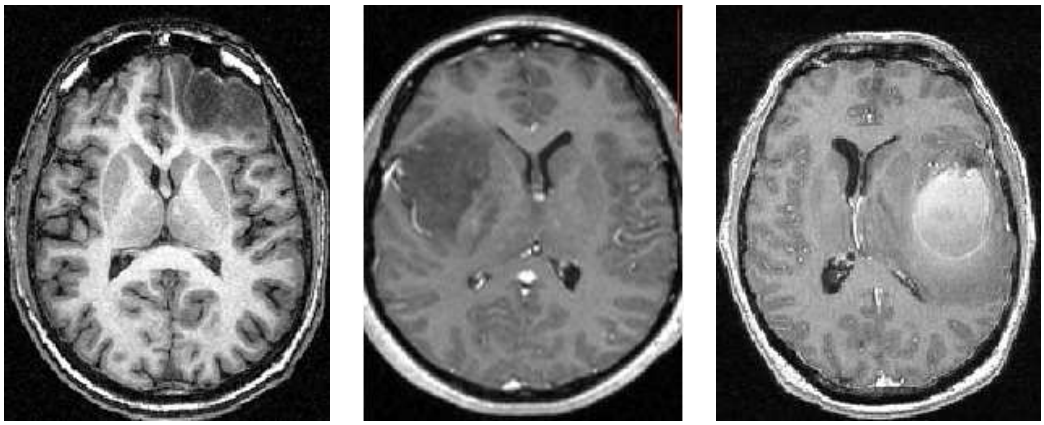

(a) (b) (c)

Figure 1.24: Classification based on the tumor alterations. a) Axial slice of a SD-P tumor. b) SD-SC tumor. c) LD tumor.

1.10 Evaluation data set

In this thesis we use different images to evaluate the proposed approaches. The images were acquired on a 1.5T (General Electric Medical System) scanner (in different hospitals) using an axial 3D IR-SPGR T1w sequence with contrast agent and a FLAIR sequence. These images contain tumors with different sizes, intensities, shapes and locations (10 CE-T1w images with enhanced tumors (full and ring), 10 CE-T1w images with non-enhanced tumors and 14 FLAIR images). The complete specifications of these images are summarized in Tables 1.4 and 1.5.

1.11 Conclusion

In this chapter we first reviewed the anatomy of brain, brain tumor imaging and brain tumor classification. The main result of this section is that the enhancement of tumors in contrast enhanced T1-weighted images is a main parameter for malignant tumors. Also the T1-weighted image is not a proper modality for accurate edema segmentation, while T2-weighted or FLAIR images are more adequate for accurate edema segmentation. Based on these results and tumors characteristics review, we decided to

Data name	Resolution	Voxel size (mm^3)	Hospital	Tumor Type	Ede.	Nec.	FLAIR
TE1	$256 \times 256 \times 124$	$1.02 \times 1.02 \times 1.4$	Val-de-Grâce	Enhan.	Yes	No	No
TE2	$256 \times 256 \times 22$	$1.0 \times 1.0 \times 1.0$	IBSR [1]	Enhan.	No	No	No
TE3	$256 \times 256 \times 124$	$0.94 \times 0.94 \times 0.5$	Salpêtrièr[2]	Enhan.	Yes	No	No
TE4	$256 \times 256 \times 124$	$1.0 \times 1.0 \times 1.1$	Val-de-Grâce	Enhan.	Yes	No	No
TE5	$256 \times 256 \times 124$	$1.0 \times 1.0 \times 1.2$	Val-de-Grâce	Enhan.	Yes	No	No
TR1	$256 \times 256 \times 232$	$0.94 \times 0.94 \times 0.7$	St-Anne	Ring-En.	Yes	Yes	Yes(F12)
TR2	$256 \times 256 \times 232$	$0.94 \times 0.94 \times 0.7$	St-Anne	Ring-En.	Yes	Yes	Yes(F13)
TR3	$256 \times 256 \times 232$	$0.94 \times 0.94 \times 0.7$	St-Anne	Ring-En.	Yes	Yes	Yes(F14)
TR4	$256 \times 256 \times 120$	$1.02 \times 1.02 \times 1.4$	Salpêtrière	Ring-En.	Yes	Yes	No
TR5	$256 \times 256 \times 112$	$1.02 \times 1.02 \times 1.6$	Lariboisière	Ring-En.	Yes	Yes	No
TNE1	$256 \times 256 \times 102$	$0.50 \times 0.65 \times 1.1$	Salpêtrière	Non-En.	No	No	No
TNE2	$256 \times 256 \times 118$	$0.94 \times 0.94 \times 1.5$	Salpêtrière	Non-En.	No	No	Yes(F5)
TNE3	$256 \times 256 \times 116$	$0.94 \times 0.94 \times 1.5$	Salpêtrière	Non-En.	No	No	No
TNE4	$256 \times 256 \times 116$	$0.94 \times 0.94 \times 1.5$	Salpêtrière	Non-En.	No	No	Yes(F6)
TNE5	$256 \times 256 \times 124$	$0.94 \times 0.94 \times 1.5$	Salpêtrière	Non-En.	No	No	Yes(F11)
TNE6	$256 \times 256 \times 116$	$0.94 \times 0.94 \times 1.5$	Salpêtrière	Non-En.	No	No	No
TNE7	$256 \times 256 \times 116$	$0.94 \times 0.94 \times 1.5$	Salpêtrière	Non-En.	No	No	Yes(F8)
TNE8	$256 \times 256 \times 116$	$0.94 \times 0.94 \times 1.5$	Salpêtrière	Non-En.	No	No	Yes(F7)
TNE9	$256 \times 256 \times 116$	$0.94 \times 0.94 \times 1.5$	Salpêtrière	Non-En.	No	No	Yes(F9)
TNE10	$256 \times 256 \times 116$	$0.94 \times 0.94 \times 1.5$	Salpêtrière	Non-En.	No	No	Yes(F10)

Table 1.4: Specifications of the CE-T1w images in our data set (Ede. indicates the presence of edema, and Nec. of a necrotic part).

use the contrast enhanced T1-weighted and FLAIR images for brain tumors detection and segmentation. We then studied the characteristics of brain tumors based on their classification in WHO systems. We summarized the radiological characteristics of tumors to distinguish them in MR images. We then proposed three new classifications of brain tumors based on location, appearance in MR images and alteration of surrounding structures. We will use these classifications to propose a general framework for segmentation of brain tumors and internal brain structures and interpretation of brain tumors.

[1] www.cma.mgh.harvard.edu/ibsr
[2] Pitié-Salpêtrière

Data name	Resolution	Voxel size(mm^3)	Hospital
F1	$512 \times 512 \times 20$	$0.47 \times 0.47 \times 6.45$	Salpêtrière
F2	$512 \times 512 \times 22$	$0.47 \times 0.47 \times 6.49$	Salpêtrière
F3	$256 \times 256 \times 20$	$0.94 \times 0.94 \times 6.5$	St-Anne
F4	$256 \times 256 \times 20$	$0.94 \times 0.94 \times 6.5$	St-Anne
F5	$256 \times 256 \times 20$	$0.94 \times 0.94 \times 6.5$	Salpêtrière
F6	$256 \times 256 \times 20$	$0.94 \times 0.94 \times 6.5$	Salpêtrière
F7	$256 \times 256 \times 20$	$0.94 \times 0.94 \times 6.5$	Salpêtrière
F8	$256 \times 256 \times 20$	$0.94 \times 0.94 \times 6.5$	Salpêtrière
F9	$256 \times 256 \times 20$	$0.94 \times 0.94 \times 6.5$	Salpêtrière
F10	$256 \times 256 \times 20$	$0.94 \times 0.94 \times 6.5$	Salpêtrière
F11	$256 \times 256 \times 20$	$0.94 \times 0.94 \times 6.5$	Salpêtrière
F12	$256 \times 256 \times 20$	$0.94 \times 0.94 \times 6.5$	St-Anne
F13	$256 \times 256 \times 20$	$0.94 \times 0.94 \times 6.5$	St-Anne
F14	$256 \times 256 \times 20$	$0.94 \times 0.94 \times 6.5$	St-Anne

Table 1.5: Specifications of the FLAIR images in our data set.

CHAPTER 2

Tumor segmentation methods: a survey

2.1 Introduction

The most important aim of medical image analysis in general, and brain magnetic resonance image (MRI) analysis in particular, is to extract clinical information that would improve diagnosis and treatment of disease. Brain tumors are one of the most common brain disease, so detection and segmentation of brain tumors in MRI are important in medical diagnosis. The aim is to provide information associated to anatomical structures as well as potential abnormal tissues necessary to treatment planning and patient follow-up. The segmentation of brain tumors can also be helpful for general modeling of pathological brains and the construction of pathological brain atlases [W.Toga et al., 2001].

Despite numerous efforts and promising results in the medical imaging community, accurate and reproducible segmentation and characterization of abnormalities are still a challenging and difficult task because of the variety of the possible shapes, locations and image intensities of various types of tumors. Some of them may also deform the surrounding structures or may be associated to edema or necrosis that change the image intensity around the tumor (see Chapter 1). Existing methods leave significant room for increased automation, applicability and accuracy. In this chapter we classify and study the existing methods for detection and segmentation of brain tumors in MR images.

Conventionally, simple thresholding or morphological techniques have been used on each image to segment the tissue or region of interest for diagnosis, treatment planning, and follow-up of the patients. These methods are unable to exploit all information provided by MRI. Advanced image analysis techniques have been and still are being developed to optimally use MRI data and solve the problems associated with previous

techniques. Most of the methods presented for tumor detection and segmentation have used several techniques and we cannot make a clear division between them but in general, as classically done in image segmentation, we can divide the methods into three groups: region-based, contour-based and fusion of region- and boundary-based method.

Region-based methods seek out clusters of voxels that share some measure of similarity. These methods reduce operator interaction by automating some aspects of applying the low level operations, such as threshold selection, histogram analysis, classification, etc. They can be supervised or non-supervised.

Boundary-based methods rely on the evolution of a curve, based on internal forces (e.g. curvature) and external forces, such as image gradient, to delineate the boundary of brain structure or pathology. These methods can also be supervised or non-supervised. They can be further classified into two classes: (1) parametric deformable model (classical snake) and (2) geometric deformable model (level sets).

The third core class of tumor segmentation methods is the fusion of region- with boundary-based methods. This class has been the most successful, as this technique uses information from two different sources: region and boundary. Due to its large success, it has recently received much attention.

In the remaining of this chapter, we review the existing methods for segmentation of brain tumors in MR images based on the proposed classification as summarized in Figure 2.1 and Tables 2.1 and 2.2.

2.2 Region-based methods

In region-based methods, an algorithm usually searches for connected regions of pixels/voxels with some similar features such as brightness, texture pattern, etc. Thresholding, region growing and classification are the famous algorithms of this type but applying these methods only cannot solve the problem of tumor detection and segmentation. In recent years, researchers have developed advanced and mixed region based methods for tumor detection and segmentation. Here we further classify region-based methods into the following categories: (1) classification-based; (2) clustering-based; (3) morphology-based; (4) atlas-based (5) prior knowledge-based; (6) texture-based; (7) feature extraction-based; (8) fusion-based; (9) neural network-based; (10) fuzzy-based; and (11) fractal-based method.

Sometimes we cannot make a clear division between the methods to classify in these categories, because most of methods have the same nature. To clarify this classification, we present very brief definitions of these distinctive classes.

Classification-based methods are those that assign a pixel to a class and are su-

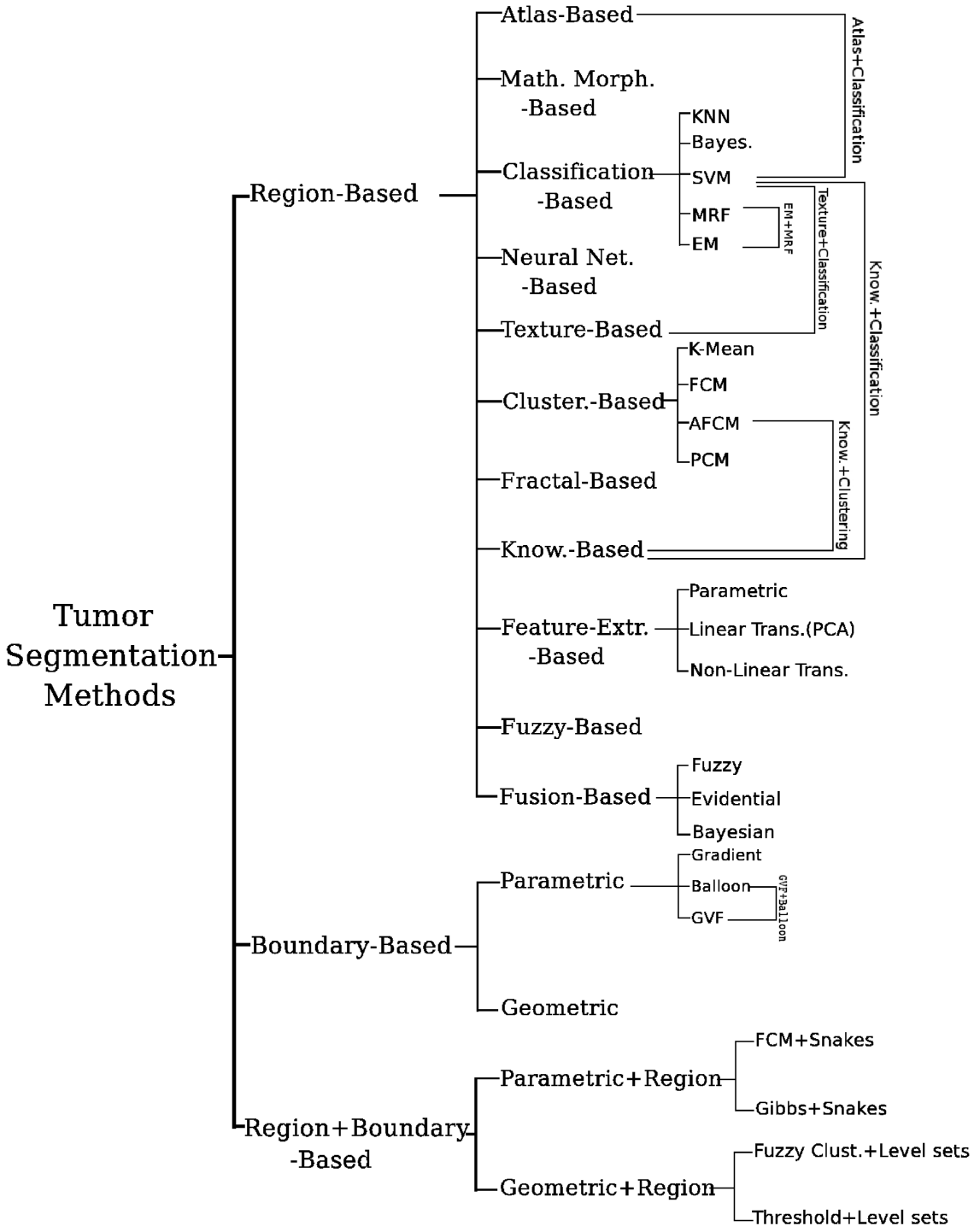

Figure 2.1: Classification of existing tumor segmentation methods.

	Region-based											
Reference	Classifica.	Clustering	Morpholo.	Atlas	Knowledge	Texture	Feature	NeuralNet	Fusion	Fuzzy	Fractal	Subclass
[Vinitski et al., 1997]	x											KNN
[Kaus et al., 1999; 2001]	x											KNN+Regist.
[Warfield et al., 2000]	x											KNN+Regist.
[Corso et al., 2006]	x											Bays.
[Moon et al., 2002]	x											EM+Atlas
[Prastawa et al., 2004]	x											EM+Atlas
[Gering, 2003]	x											MRF+EM
[Solomon et al., 2006]	x											MRF+EM
[Zhang et al., 2004]	x											SVM
[Zhou et al., 2005]	x											SVM
[Ruan et al., 2007]	x											SVM
[Garcia and Moreno, 2004]	x											SVM
[Lee et al., 2005]	x											SVM+MRF
[Phillips et al., 1995]		x										FCM
[Masulli and Schenone, 1999]		x										PNFCM
[Shen et al., 2003]		x										AFCM
[Gibbs et al., 1996]			x									Region grow.
[Letteboer et al., 2004]			x									Watershed
[Mancas and Gosselin, 2004]			x									Watershed
[Rexilius et al., 2007]			x									Region grow.
[Kyriacou et al., 1999]				x								Biomech. model
[Dawant et al., 2002]				x								Optical flow
[Bach Cuadra et al., 2004]				x								Tumor growth
[Clark et al., 1998]					x							FCM+Know.
[Busch, 1997]						x						Text.+Clas.
[Herlidou-Meme et al., 2003]						x						Text.+Clas.
[Zizzari et al., 2001]						x						COM
[Soltanian-Zadeh et al., 1996a]							x					Linear Tran.
[Soltanian-Zadeh et al., 2001]							x					Non-linear Tran.
[Dickson et al., 1997]								x				ANN+Clas.
[Chaplot et al., 2006]								x				ANN+Feau.
[Wasserman et al., 1995]									x			Fuzzy
[Capelle et al., 2004]									x			Belief Func.
[Dou et al., 2007]									x			Fuzzy
[Moonis et al., 2002]										x		Connectedness
[Hata et al., 2005]										x		Connectedness
[Liu et al., 2005]										x		Connectedness
[Uemura et al., 2000]											x	
[Iftekharuddin et al., 2003]											x	

Table 2.1: Region-based methods in the literature.

	Boun.		R.+B.		
Reference	Snakes	LevelSets	Region+Snakes	Region+Levelsets	Subclass
[Luo et al., 2003]	x				GVF+Balloon
[Jiang et al., 2004]	x				Gradient
[Droske et al., 2001]		x			Fast marching
[Lefohn et al., 2003]		x			Threshold speed fun.
[Cates et al., 2004]		x			Threshold speed fun.
[Xie et al., 2005]		x			HLS
[Zhu and Yang, 1997]			x		Sankes+ANN
[Law et al., 2001]			x		FCM+Snakes
[Chen and Metaxas, 2003]			x		Gibbs+Snakes
[Ho et al., 2002]				x	FCM+Level sets
[Taheri et al., 2007]				x	Threshold+Level sets

Table 2.2: Boundary-based and fusion of region- and boundary-based methods in the literature.

pervised. These methods use a statistical-based method. Clustering-based techniques are those that use the fuzzy membership methods for segmenting brain tumors and are unsupervised classification. Mathematical morphology-based methods are those that use the features of mathematical morphology, such as structuring elements (SE) or masks or kernels as templates to convolve with the image, followed by binarisation using a given function or use gradient-dependent diffusion followed by linking. Atlas-based techniques perform the segmentation by registering and deforming the brain atlases over patient images. Prior knowledge-based methods use prior knowledge of different structures, tissues and tumors of the brain to segment tumors. Texture-based techniques use statistical methods to compute textural features to distinguish brain tissues for segmentation of tumors. Feature extraction methods use a technique for extracting other features from patient images and they make a classification based on these features. Neural network-based methods are those that use an artificial neural network (ANN) to learn classification parameters (using test MR data sets), this learned classification is then used to segment the patient images. Fusion-based methods use a fusion technique to combine the information of multimodality images (one device or multiple devices) for classification or clustering. Fuzzy methods are those that use fuzzy logic theory for segmentation. This class may has overlap with other classes and here we consider the fuzzy connectedness methods. Fractal-based methods use fractal concept to detect brain tumors in MR images.

2.2.1 Classification-based

In the image segmentation domain, classification algorithms are either supervised, or unsupervised. A supervised classifier requires input from the user, typically a set of class samples, for determination of the data structures. Unsupervised classification (clustering) on the other hand relies on cluster analysis to drive the natural structures of the data from the data themselves. Here we review tumor segmentation methods based on supervised classification techniques and unsupervised methods will be studied in the clustering-based section. We can distinguish five classes of methods based on supervised classification:

- K-nearest neighbors (KNN),
- Bayesian approach,
- expectation maximization (EM),
- Markov random field,
- support vector machine (SVM).

Here we will briefly explain the fundamentals, advantages and disadvantages of each class of methods specifically for brain tumor segmentation.

Tumor segmentation using K-nearest neighbor (KNN)

There are a number of ways in which training data can be applied in classifier methods. A simple classifier is the KNN classifier, where each pixel or voxel is classified in the same class as the training data with the closest intensity. The KNN classifier is considered a non-parametric classifier since it makes no underlying assumption about the statistical structure of the data.

[Vinitski et al., 1997] have developed a method which used patient-specific training to classify the T1-weighted, T2-weighted and PD-weighted images into 10 tissue classes. The used classifier was a KNN classifier, that assigns labels to pixels based on the most frequent label among the K closest training points under a distance metric applied to the features. The KNN algorithm is a simple and effective method for multi-class classification, that is able to model non-linear distributions. This is the first method which segments all components of the tumor (solid, edema and necrosis sections). This method did not include any spatial regularization, so it is very sensitive to noise and inhomogeneity of tumors.

[Kaus et al., 1999; 2001 ; Warfield et al., 2000] have proposed an automatic method for segmentation of homogeneous brain tumors in MR images that used a manually

segmented atlas as spatial information to correct the KNN classification results. This method incorporated both supervised KNN classification and template registration. The method used the KNN algorithm for classifying an image into different tissue classes based on intensity using the patient-specific training data (the initialization of the classifier is performed by a selection of several points of each tissue by the user). For resolving misclassification problems because of the intensity distributions overlapping of different tissues, a non-linear atlas registration is used. The digital atlas has been manually segmented by an expert. The KNN classification and registration of anatomical brain atlas are then iterated to improve the result of classification. At final, for removing classification artifacts, morphological erosion and dilation were used. This system provides good results for small tumors but in the case of large deformations in the brain it will fail. This method also needs much calculation by repeating the classification and registration, therefore it is relatively slow. This algorithm fails in cases where the intensity distribution in the tumor is highly inhomogeneous and shows large spectral overlap with brain tissues.

In general, disadvantages of the KNN algorithm include the dependence on the parameter K, large storage requirements (for training points), sensitivity to noise in the training data, and the undesirable behavior that can occur in cases where a class is under-represented in the training data, which make it unsuitable for brain tumor segmentation in MRI.

Tumor segmentation using Bayesian approach

In this supervised and parametric approach, the data are assumed to follow a multivariate normal (Gaussian) distribution, where mean and covariance are estimated from the training data set. The goal is to estimate the class labels by maximizing the *a posteriori* probability $P(C|X)$ where X is the observed data and C is the class. Based on the Bayes rule we have: $P(C|X) = \frac{P(X|C)P(C)}{P(X)}$ where $P(X|C)$ is the likelihood function, $P(C)$ is the *a priori* probability of the class C which is computed using the distribution of different tissue types and $P(X)$ is the probability of pixel/voxel.

Recently, [Corso et al., 2006] have proposed a new method based on a combination of Bayesian model and graph-based affinity for segmenting brain tumors and edema. Four classes (non-data, brain matter, tumor and edema) are modeled by Gaussian distributions with full-covariance giving 9 parameters, which are learned from the manually segmented data. The voxels-classes likelihood, $P(X|C)$ are computed directly from these Gaussian models. To integrate the Bayesian model-based into neighborhood voxels affinity, the affinity between two nodes (voxels) has been defined to be the probability $P(X_{uv}|u,v) = \sum_{C_u}\sum_{C_v} P(X_{uv}|u,v,C_u,C_v)P(u|C_u)p(v|C_v)p(C_u,C_v)$ of the binary event X_{uv} between two voxels u and v in the two classes C_u and C_v. Here $P(X_{uv}|u,v,C_u,C_v) = exp(-D(u,v;\theta[C_u,C_v]))$ and is a model-aware affinity, and $\theta[c_u,c_v]$ is defined manually between the classes. Finally a multilevel segmentation al-

gorithm (SWA [Sharon et al., 2001]) was used to segment the image, while in the first level each node is a voxel. This method is applied for segmentation of GBM tumors using T1-weighted, contrast enhanced T1-weighted and FLAIR images.

This method combines a graph-based algorithm and Bayesian model and segments the edema in addition. Also it can be extended to vectorial variables to operate on multi-modality images. But it is relatively slow and can only segment full-enhanced tumors such as GBM. The other problem of this method is the modeling of the tumor by a Gaussian model, since the probability of tumor and edema do not always follow Gaussian distributions.

Tumor segmentation by expectation maximization (EM)

The EM algorithm has been developed by [Moon, 1996] and [Ambroise et al., 1995] and is achieved in two steps iteratively. The expectation (E) step computes the posterior probability $P(C_i|x_j) = \frac{P_i(x_j)P(x_j|C_i)}{\sum_j P_i(x_j)P(x_j|C_i)}$ that the voxel x_j belong to the i'th class and with the latest estimates (from previous repetition or initial values) of $P_i(x_j)$, μ_i and σ_i. In the maximization (M) step, the following parameters are computed: $P_i(x_j) = \frac{1}{N}\sum_j P(C_i|x_j)$, $\mu_i = \frac{1}{NP_i(x_j)}\sum_j P(C_i|x_j)x$ and $\sigma_i^2 = \frac{1}{NP_i(x_j)}\sum_j P(C_i|x_j)(x_j - \mu_i)$. The E and M steps are iterated until the parameter estimates become stable.

[Moon et al., 2002 ; Prastawa et al., 2003] was the first group to adapt the EM algorithm to brain tumor segmentation. This method has been developed based on the work of [Leemput et al., 2001] for normal brain segmentation. The prior probabilities for the normal tissue classes (WM, GM and CSF) are defined by the registered spatial atlas to the patient images and the tumor spatial prior is calculated from the T1-weighted and contrast enhanced T1-weighted difference image (the difference image is converted to probability values through histogram analysis). In this approach the edema class prior has been assumed a fraction of the white matter spatial prior (20%). This method segments only the full-enhanced tumors and in the case of the presence a large deformations in the brain it fails. The deformations of the brain should be small enough so that they are embodied in the probabilistic brain atlas. In the case of edema, the authors have assumed a fraction of white matter probability for edema, although we cannot always consider this fraction. In addition the probability distribution of tumor and edema has been assumed to be a normal distribution and it is not correct in the all cases.

Recently this group has presented a more general approach based on EM algorithm in [Prastawa et al., 2004]. In this approach the abnormal pixels are considered as outliers from three normal classes. This method has 3 steps: first the abnormality region is determined, using the EM algorithm and that the spatial priors for WM, GM, CSF and non-brain classes are corresponding to a registered spatial atlas to patient image. For abnormal class a fraction of the sum of the white matter and the

gray matter probabilities of atlas has been used. Bias correction is also done in this step. Edema is not always present when tumor is present, therefore it is necessary to test the presence of edema. For detecting edema, an unsupervised clustering in the T2-weighted image is done next. Finally a reclassification is performed with spatial and geometric constraints, because of some misclassifications of step 2. Step 1 and 2 rely on intensity information and atlas priors and the final step relies on geometry and spatial information based on prior knowledge about tumor and edema. This method detects edema and does not use contrast enhanced image, but as in the previous method it fails in the case of large deformations. The spatial priors limit the segmentation quality because the segmentation output can not differ greatly from the atlas. Also the method used for detection and segmentation of edema is not robust enough (k-means method).

Tumor segmentation based on Markov random fields

Markov random fields (MRF) models are widely applied to various problems arising in image processing. MRF is a statistical model which can be used within segmentation methods. A natural way to incorporate spatial correlations into a segmentation process is to use Markov random fields [Held et al., 1997] as a priori models. MRF model spatial interactions between neighboring or nearby pixels. These local correlations provide a mechanism for modeling a variety of image properties. In medical imaging, they are typically used to take into account the fact that most pixels belong to the same class as their neighboring pixels.

In the brain tumor segmentation domain, MRFs have been used in some works to refine the results of the EM segmentation such as in [Gering, 2003]. This approach refined the EM results using a MRF, incorporated a structure to boundary constraint using a multi layer MRF, and presented a way to discriminate partial volume pixels from tumor pixels by creating an adaptive spatial prior for pixels that are at the boundaries of normal structures. These three constraint addition to the Expectation Maximization algorithm are combined into a structured Contextual-Dependency Network for the segmentation of brain tumors from T1-weighted images. The multi layer Markov Random Field in particular addressed a major weakness of the Expectation Maximization methods since it allows the identification of tumor structures that have normal intensities but are too thick to be normal. Unfortunately, this is only applicable to tumors that are homogeneous enough to be segmented into a single normal tissue class, and therefore is not generally applicable to heterogeneous tumors.

Recently [Solomon et al., 2006] have proposed a tumor segmentation method using MRF. An additional MRF model (implemented as a Gibbs distribution) has been included into the EM context to improve the segmentation process. This method segments full-enhanced tumors and did not consider other components such as edema and necrosis.

SVM-based tumor segmentation

In the recent years, SVM algorithm has attracted much attention. The SVM is the most recent classifier in machine learning, it was proposed by Vapnik [Vapnik, 1999] and is based on statistical learning theory. The SVM approach is considered as a good candidate due to high generalization performance, especially when the dimension of the feature space is very high. The SVM uses the following idea: it maps the input vector x into a high-dimensional feature space Z through some non-linear mapping, chosen a priori. In this space, an optimal separating hyperplane is constructed. In the pattern recognition cases, SVMs classify two point classes by finding a decision surface determined by certain points of the training set, named support vectors. More information on SVM in classification problem can be found in [Vapnik, 1999 ; Burges, 1998 ; Cortes and Vapnik, 1995].

[Zhang et al., 2004 ; Zhou et al., 2005] proposed a simple system for the segmentation of brain tumors. This approach used a SVM classification to classify the brain into the tumor and non-tumor classes using T1-weighted and contrast enhanced T1-weighted images. Following the classification, some morphological operations have been used to remove the classification errors. This system used patient-specific training and compared two different types of SVM, the standard 2-class method and the more recent 1-class method. However, the advantage of using a 1-class method was a reduction in the manual time needed to perform patient specific training, since only training examples for the tumor class were needed. These methods perform the segmentation in one slice (2D) and cannot segment other components.

[Garcia and Moreno, 2004] proposed another approach for automatic brain tumor segmentation using SVM. This method first performed an initial classification of pixels in 2D slices using patient specific training (by the Adatron algorithm [Anlauf and Biehl, 1989]) and the intensities of the neighbor pixels. The initial classifier is a 2-class SVM. A 1-class SVM has then been used to construct a 3D tumor model from the initial classification of pixels. In fact, in this method the classification is performed in 2D and it does not use the spatial information of pixels in 3D.

Recently [Lee et al., 2005] have used a combination of MRF and SVM for brain tumor segmentation. Since SVM assumes that voxels are independent and identically distributed, it is very sensitive to noise. A combination of SVM and MRF can solve this problem. Their system used T1-weighted, T2-weighted and contrast enhanced T1-weighted images to segment the solid portion and edema of GBM tumors. This system also used a patient-specific training where the training data for the classifier are obtained from the patient images. This group [Schmidt et al., 2005] also proposed a method using SVM and alignment-based features for segmentation of GBM tumors. More recently, [Ruan et al., 2007] proposed a method based on SVM classification from multispectral (T1w, T2w, PDw and FLAIR) MR images. The learning is done on T2 image and to reduce the computation time the SVM classification is performed in two scales. In the low scale a classification is done on the divided image into a set

of windows, and the result is then refined in the high scale (voxel level).

Although the SVM method has the advantage of generalization and working in high dimensional feature space, it assumes that data are independently and identically distributed which is not appropriate for tasks such as segmenting medical images with inhomogeneity and noise and so it must be combined with other methods to consider spatial information. In addition the problem of patient-specific learning and storage must be added to the disadvantage of SVM-based methods.

2.2.2 Clustering-based

Clustering consists of unsupervised classification of patterns (observations, data items, or feature vectors) into groups (clusters).The clustering algorithms essentially work such as classification methods without use of training data set [Jain et al., 1999]. Two commonly used clustering algorithms are the k-means or ISODATA algorithm and the fuzzy c-means (FCM) algorithm. The k-means clustering algorithm clusters data by iteratively computing a mean intensity for each class and segmenting the image by classifying each pixel/voxel in the class with the closest mean. The fuzzy c-means algorithm generalizes the k-means algorithm, allowing for soft segmentations based on fuzzy set theory. It should be mentioned that the membership functions to classes have a counter intuitive shape, which limits their use. This is improved in the possibilistic c-means (PCM) algorithm [Krishnapuram and Keller, 1993].

[Phillips et al., 1995] have used the FCM algorithm for GBM brain tumors segmentation. Their system used T1-weighed, T2-weighted and PD-weighted MRI with a vectorial FCM to segment the pathological brain to WM, GM, CSF, tumor and edema. Although the FCM algorithm is simple, fast and unsupervised, it cannot segment the tumor and edema accurately because of the intensity overlapping of tissues. In addition FCM is very sensitive to noise and initialization values. This method was not validated and only tested for one case.

Another FCM based brain tumor segmentation has been presented in [Masulli and Schenone, 1999]. This possibilistic neuro fuzzy c-means (PNFCM) algorithm combines a bootstrap based on the capture effect model (CENN) [Firenze and Morasso, 1993] with the second version of the PCM-II [Krishnapuram and Keller, 1996]. The CENN avoids the estimation of the fuzzification parameter m and gives a robust estimation of the class numbers c and of their centers. This method has been applied to segment full-enhanced tumors (such as meningioma) using T1-weighted, T2-weighted and PD MR images. Although this method is fast and fully automatic, it is very sensitive to noise and heterogeneity.

In the previous FCM-based methods the spatial information of pixels were not considered, so that they are very sensitive to noise. To solve this problem, [Shen et al., 2003] have proposed a more recent system, which incorporated intensity stan-

dardization (using the pixel histograms) as a preprocessing step, and a modified FCM algorithm which involves dependencies between neighbor pixels. This method is more robust to noise and provides a better segmentation quality in comparison with the other FCM based approaches.

2.2.3 Morphology-based

Mathematical morphology [Serra, 1982] refers to a branch of nonlinear image processing and analysis that concentrates on the geometric structure of objects or regions within images. The basic concept is to search an image with a structuring element and to quantify the manner in which the structuring element fits within the image.

[Gibbs et al., 1996] has presented the first morphology-based approach for the segmentation of full-enhanced brain tumors in T1-weighted post-contrast MR images. This method first applies an intensity threshold (the value of threshold is determined by the user) to a manually selected region of interest (ROI). A region growing algorithm is then used to expand the thresholded regions up to the edges defined by a Sobel filter. The region growing result was refined through iterations of dilation and erosion. These two operations change the labels assigned to individual pixels by examining the labels of neighboring pixels. This method represents an approach for segmenting image objects that are different in intensity from their surrounding tissues. The primary disadvantage is that it requires manual interaction to select the ROI and threshold value. Region growing can also be sensitive to noise, causing extracted regions to have holes or even become disconnected. Also the major problems of the region growing is the leakage of the segmented volume into adjacent structures because of the weak border of tumor.

Recently several works are published in [Letteboer et al., 2004 ; Dam and Letteboer, 2004 ; Mancas and Gosselin, 2004] for brain tumor segmentation based on watershed transform. All of these methods are semi-automatic and a lot of user interactions are needed to have an accurate segmentation. In addition these methods segment only the solid section of the tumor and segmentation of the other components of tumor such as edema and necrosis were not considered.

A recent approach using morphological operations has been presented in [Rexilius et al., 2007]. This method has two steps, in the first step an initial segmentation is performed based on the histogram analysis of multi-spectral images (contrast enhanced T1-weighted, T2-weighted and FLAIR). The histogram analysis is performed by a histogram matching over probabilistic models generated in a multi-spectral histogram feature space. This step is then followed by a local refinement based on a progressive morphological region growing. In this method, in addition to the region growing problems such as leakage to other regions, the histogram model was trained for the full-enhanced tumors and it is very difficult to generalize this model to segment other types of tumors. Also this method needs a lot of user interaction for brain segmentation

and final threshold adaptation in the region growing algorithm.

2.2.4 Atlas-based

In the domain of brain MR image segmentation, one type of prior information which has been largely used is the atlas. This atlas is created by manual segmentation or by other semi-automatic segmentation methods. Atlas can capture spatial, intensity and shape distributions of the anatomical structures of interest. This atlas is then used as a reference frame for segmenting new images. First of all, a global transformation or registration technique is used to align the atlas to the new image that will be segmented and then the atlas information will be applied to refine the segmentation or to detect abnormalities in the image. Therefore these types of segmentation deal also with registration problems and the quality of segmentation depends on the registration method.

In general (in normal and pathological cases), depending on the type of atlas information, there are mainly two classes of atlas driven segmentation methods [Pham et al., 2000],[Pohl et al., 2004], [Grimson and Golland, 2005]. One class of methods uses probabilistic atlases, modeling inter-subject variability. In these methods after aligning the atlas to the new image, the atlas information is used as prior probabilities information, which enables the use of both intensity and spatial information in the segmentation framework. In this type of atlas the appearance and distribution of intensity are an explicit part of the statistical model or atlas. In Section 2.2.1 several methods, which use this type of atlas, were studied [Prastawa et al., 2004 ; Moon et al., 2002 ; Prastawa et al., 2003 ; Kaus et al., 1999; 2001 ; Warfield et al., 2000].

The second class relies on deformable atlases which can be defined by one single individual atlas or by various individual atlases or by an average shape atlas structures [Rohlfing et al., 2004]. In general in this class, an atlas incorporates the locations and shapes of anatomical structures, and the spatial relationships between them in an implicit representation. The methods in this class seek to induce a segmentation of a new image by deforming a given segmented atlas image to the new grayscale image and by mapping its coordinate space to that of the atlas in an anatomically correct way (i.e. a registration process). Labeling an image by mapping it to an atlas is consequently known as atlas-based segmentation, or registration-based segmentation. In the case of the presence of a tumor or lesion, it is segmented after the registration, using a model of tumor growth. This technique converts the segmentation of MR images into a non-rigid registration problem between the MR images of the patient and the MR images used to create the brain atlas. When large space-occupying tumors or lesions alter shape and position of brain structures, these methods have been of limited use. In this section we study the application of this type of approaches to the segmentation of tumors.

The first approach for registering the anatomical atlas to pathological brains was

presented by [Kyriacou et al., 1999]. The proposed method used a biomechanical model of tumor growth and brain. First, an estimate of the anatomy prior to the tumor growth is obtained through a simulated contraction of the tumor region, using finite-elements and knowing the position of the skull, the ventricles, and the falx and tentorium. A normal to normal atlas registration is then applied between an atlas and the estimation of the healthy patient using an elastic deformable model. Finally, the estimation of the tumor growth process is applied to the registered atlas. This method presents good results, but has some drawbacks. The model for tumor growth has a tendency to uniform growth and does not take into account infiltration models. Also, it requires the previous accurate segmentation of many structures in order to perform the linear regression estimation. Finally, it is comparatively slow due to much computational requirements for mesh generation and visualization, so that its implementation in 3D is a very time consuming operation.

Another atlas-based segmentation of pathological brains was introduced by [Dawant et al., 2002]. Their method consists of a simple approach relying on an optical-flow based technique. This registration technique is a modification of the demons algorithm [Thirion, 1998], but introducing a lesion template. This introduction of the new template is completely necessary because the demons algorithm is really useful to warp healthy brains, with the atlas structures overlapped with the same structures in the patient, but not so effective when large anatomical differences exist between the images to match. The demons algorithm works poorly in this case because the assumption of small displacement is violated. Moreover, if a lesion template is not applied into the model, some healthy parts from the brain could warp to the lesion and produce wrong results. The proposed solution is to place a small seed with the same intensity properties as the lesion and then apply the demons algorithm. This method succeeds in lesion growth, but has an important drawback because the seed must has a considerable size to obtain good growth in the tumor. Also, the seed deformation is strongly dependent on both the number of iterations and the elasticity parameters.

[Bach Cuadra et al., 2004] have recently published a new atlas-based segmentation of pathological MR brain images using a new model of lesion growth. Following an affine registration, the registered atlas is seeded manually by selecting a voxel of lesion regions. A non-rigid deformation method at this point is performed in order to match the patient image and seeded atlas. This deformation is performed in two areas, outside of tumor or lesion and inside of tumor or lesion. Outside the lesion, a demons force [Thirion, 1998] is applied and inside the lesion a prior model of tumor growth is used. Finally structures and substructures from the brain atlas are projected onto the patient's image. This method segments only the tumors that have a radial growth model (such as meningioma) and in the case of other types of tumor or infiltration it will fail.

2.2.5 Knowledge based

In the domain of MRI volumes, there are two primary sources of knowledge available. The first is pixel intensity in feature space, which describes tissue characteristics within the MR imaging system and the second is image/anatomical space and includes expected shapes and placements of certain tissues within the MR image [Clark, 1997]. The methods which use this information to build an expert system or knowledge-based (rule-based) system to guide the segmentation process are referred to as knowledge-based methods. For example, [Clark et al., 1998] have proposed an automatic tumor segmentation that used a knowledge-based system for correcting results provided by FCM clustering. First, using a FCM multispectral clustering algorithm, pixels are divided into groups with similar multispectral intensities (contrast enhanced T1-weighted, T2-weighted and PD-weighted images). Then with an expert system which is a set of intensity and anatomical rules, normal clusters are removed. Then the remaining voxels are reclustered and the segmentation is refined using other rules. The system evolves from clustering the entire image to clustering very specific areas, while the rules are used to remove the clusters that do not have tumor properties. [Fletcher-Heath et al., 2001] have later developed this algorithm for segmentation of non-enhanced brain tumors in MRI by changing the rules of the expert system.

One drawback of this type of approach is that the rules may not be robust to non-standard intensity and the errors can propagate if the assumptions of early rules in the sequence are violated. Another disadvantage of this approach is the considerable manual engineering requirement. This is due to the difficulty of translating complex anatomic knowledge and visual analysis into sequential low-level operations and rules. Also in the case of heterogeneous tumor or noise, the rules may not work correctly.

2.2.6 Texture-based

Texture analysis is an important task in image analysis for classification, detection and segmentation of images. Textures are replications, symmetries and combinations of various basic patterns, usually with some random variation. In texture segmentation the goal is to assign an unknown sample image to one of a set of known texture classes [Jiji and Ganesan, 2005]. Texture segmentation process involves two phases: the learning phase and the recognition phase. In the learning phase, the target is to build a model for each the texture content. The texture content of the training images is captured with the chosen texture analysis method, which yields a set of textural features for each image. These features, which can be scalar numbers or discrete histograms or empirical distributions, characterize given textural properties of the images, such as spatial structure, contrast, roughness, orientation, etc. In the recognition phase the texture content of the unknown sample is first described with the same texture analysis method. Then the textural features of the sample are compared to those of the training images with a classification algorithm, and the sample is

assigned to the category with the best match.

In the domain of brain tumor segmentation in MR images using texture analysis, [Lerski et al., 1993 ; Schad et al., 1993 ; Kjaer et al., 1995] have published the first works. These works showed that texture analysis is an interesting tool to characterize brain tissues and tumors such as glioblastoma and metastases in their general aspect (contrast, intensity, homogeneity) or their different constituents (micro or macro textures). These methods used T1w and T2w calculated images (a combined Carr-Purcell/Carr-Purcell-Meiboom-Gill (CP/CPMG) multiecho, multislice sequence was used to measure T1 and T2 in each pixel with an uncertainty not exceeding 10%) of metastases and heterogeneous brain tumors such as glioblastoma.

Recently [Herlidou-Meme et al., 2003] have evaluated the usefulness of texture analysis to characterize healthy and pathologic human brain tissues (white matter, gray matter, cerebrospinal fluid, tumors and edema) in a larger data set. Each selected ROI was characterized by both its mean gray level values and several texture parameters and a multivariate statistical analysis was then applied in order to discriminate each brain tissue type represented by its own set of texture parameters. Four statistical texture analysis methods were used: histogram, co-occurrence matrix, gradient matrix and run-length matrix and they were previously performed on test objects to evaluate the method dependence on acquisition parameters and consequently the interest of a multicenter evaluation. The results show that there is a relatively good discrimination between the tumor and its surrounding edema but no discrimination was made between solid part and cystic or necrotic parts.

[Busch, 1997] presented another texture-based method to segment a specific type of non-enhanced homogeneous tumor (low-grade astrocytomas) in T1-weighted, T2-weighted, and co-registered CT images. This method used five texture extraction methods to compute features. The results of the 5 classifiers were weighted and combined. Finally a knowledge-based post processing using morphological operations was used to remove the misclassified voxels and to refine the result. The use of multiple classifiers allowed a more robust classification than the individual classifiers. Second-order (spatial co-occurrence) textures provided the worst classification performance among the five texture extraction methods.

[Zizzari et al., 2001 ; Mahmoud-Ghoneima et al., 2003] have proposed a new approach of texture analysis using co-occurrence Matrix (COM) for brain tumor detection and segmentation. [Mahmoud-Ghoneima et al., 2003] have extended the 2D method to 3D and showed that 3D-COM method applied on T1-weighted, T2-weighted, and contrast enhanced T1-weighted images can enhance the result of tumor segmentation.

As a result, like supervised methods, texture based methods need a learning procedure and can segment particular types of tumor. Generalization of these methods to more types of tumors is difficult. In addition it seems that these methods cannot segment all components of the tumor and are sensitive to noise and inhomogeneity.

2.2.7 Feature extraction

Quantitative analysis of MRI data is usually done using just the pixel intensities of the acquired images. Features can be pixel intensities themselves, features calculated from the pixel intensities, or edge and texture features. Methods of feature extraction in MRI can be classified into three categories: (1) calculation of tissue parameters; (2) linear transformations (e.g. principal component analysis (PCA)); and (3) non-linear transformation [Soltanian-Zadeh et al., 1996b].

In the domain of brain tumor segmentation in MRI, [Soltanian-Zadeh et al., 1996a] have proposed an optimal linear transformation for feature extraction. This paper presents development and application of a feature extraction method for magnetic resonance imaging (MRI), without explicit calculation of tissue parameters. A three-dimensional (3-D) feature space representation of the data is generated in which normal tissues are clustered around pre-specified target positions and abnormalities are clustered elsewhere. This is accomplished by using a linear minimum mean square error transformation of categorical data to target positions. From the 3-D histogram (cluster plot) of the transformed data, clusters are identified and regions of interest (ROIs) for normal and abnormal tissues are defined. These ROIs are used to estimate signature (feature) vectors for each tissue type which in turn are used to segment the MRI scene. The proposed feature space is compared to those generated tissue-parameter-weighted images, principal component images, and angle images, demonstrating its superiority for feature extraction. The method and its performance are illustrated using MRI images of an egg phantom and a human brain.

[Soltanian-Zadeh et al., 2001] have also published another paper based on transformations. They have presented a non-linear (polynomial) transformation to minimize scattering of data points around normal tissue clusters in a normalized MRI feature space, in which normal tissues are clustered around pre-specified target positions. This transformation is motivated by non-linear relationships between MRI pixel intensities and intrinsic tissue parameters (e.g., T1-weighted, T2-weighted, and PD-weighted). The transformation has been found by minimizing the scattering amount. Then a 3D visualization of the MRI feature space was generated and regions of interest (ROI's) on clusters seen for normal and abnormal tissues were defined. These ROI's were used to estimate signature vectors. Finally, the signature vectors have been used for segmenting and characterizing tissues.

Although the proposed methods reduce the dimensionality of data while improving clustering properties, the quality of the MRI images and the number of images in the sequence affect the results. It is therefore crucial to avoid artifacts, correct for nonuniformities, suppress the noise, and optimize MRI data acquisition protocols, that are very difficult to perform on real data. Another drawback of these methods is that they detect abnormal region from normal tissues and cannot segment the abnormal region into its components. In addition these methods are used to visualize the abnormal region and they are not really a segmentation method.

2.2.8 Neural network-based

Artificial neural networks (ANNs) are massively parallel networks of processing elements or nodes that simulate biological learning. Each node in an ANNs is capable of performing elementary computations. Learning is achieved through the adaptation of weights assigned to the connections between nodes [Pham et al., 2000]. ANNs widely used in medical imaging as a classifier, where the weights are determined using training data [Hall et al., 1992 ; Reddick et al., 1998]. Because of the many interconnections used in neural networks, spatial information can easily be incorporated into its classification procedures.

[Dickson et al., 1997] have developed a method using neural networks to segment acoustic neuromas tumors. Their system has two ANNs. The first one was used to perform an initial segmentation. A database of MR images from 50 patients (with manually labeled of acoustic neuromas) has been provided, and using these data, neural networks (multilayer perceptron (MLP)) have been developed to classify the images at the pixel level. The features used in this system are the pixel and neighboring pixels intensity. The initial pixel level segmentation was then refined by a combined method of edge-region based and morphological operation. The initial segmentation produces clusters of adjacent regions, which are considered to be candidate tumor regions. For each possible combination of these regions, features are measured and presented to a second neural network which has been trained to identify structures corresponding to acoustic neuromas. This system did not use patient-specific training, but it is relatively slow and can segment a specific type of tumors (acoustic neuromas).

Another recent published work using ANN can be found in [Chaplot et al., 2006]. This method used wavelet transform for feature extraction. The result of wavelet transform is the input to a self-organizing map (SOM). SOM is an unsupervised neural network which has advantages over other networks, it can form similarity diagrams automatically, and can produce abstractions. This method was used to classify T2-weighted images into normal and abnormal. A comparison between SVM and ANN has been done that has shown that the SVM provide better results than ANN.

Neural networks perform very well on difficult, multivariate non-linear domains, such as tumor segmentation where it becomes more difficult to use decision trees, or rule-based systems. They also perform slightly better on noisy domains and there is no need to assume an underlying data distribution such as usually done in statistical modeling. But there are several disadvantages in using neural networks for tumor segmentation. Usually they need a patient-specific learning which is a very time consuming process. Another disadvantage is that neural networks do not give explicit knowledge representation in the form of rules, or some other easily interpretable form. The model is implicit, hidden in the network structure and optimized weights, between the nodes (black box).

2.2.9 Fusion-based

Data fusion is a growing research field, and the goal of data fusion is to obtain an information synthesis by combining different data. Data coming from different sources and techniques are usually redundant but also complementary. The usual characteristics of the data is that they are imprecise, uncertain and incomplete. In such a context, the aim of fusion process is to synthesize a more reliable and elaborated information and thus, to improve the decision [Capelle et al., 2004]. Fusion techniques are based on various theories such as probabilistic and Bayesian fusion, fuzzy set theory, possibility and belief functions theory. Since a tumor consists of different biological tissues, one type of MRI cannot give complete information about abnormal tissues. Therefore, different MRI modalities information of a patient is combined to take a decision on the location, extension, prognosis and diagnosis of the tumors [Ruan et al., 2007].

In [Wasserman et al., 1995] the proposed method uses data fusion theory for tumor segmentation. In this algorithm inputs of the system are CT, PET and MR images. Fuzzy edge derived from MRI and CT are fused using a fuzzy method to form an integrated edge map which is employed in conjunction with region based analysis of the PET scan to guide the evolution of tumor segmentation model. The resulting edge map can be used as an external force in deformable models. The authors have compared the result of the fusion technique (MRI, CT and PET) and non fusion technique (PET only) as external force in deformable models and have concluded that the segmentation based on fusion is better than the non-fusion technique. This system uses different images from different machines, therefore it is more expensive than fusion system based on several images from the same acquisition device. Another problem concerns the necessary registration between CT, PET and MR images which is a very difficult task.

Recently [Capelle et al., 2004] have proposed an algorithm for brain tumor segmentation based on data fusion using belief functions. The inputs of the system are multi-echo MR images (such as T1-weighted, T2-weighted and contrast enhanced T1-weighted). First, data are modeled according to an evidential parametric model (Denoeux's model, Shafer's model or Appriou's model). To estimate the parameters of the model, a Gaussian Mixture Model has been used (the parameters of the Gaussian Mixture Model were estimated by EM algorithm). Spatial information (in this case spatial neighborhood information) was then used by a weighted Dempster's combination rule. The authors have concluded that Denoeux's model provides better detection rates and operates better than the other models. Also adding spatial information provides a better segmentation and reduces the sensitivity to noise but it has several problems. The data are modeled using Gaussian distributions, although this assumption does not hold for all type of tumors and edema. This method can be applied for segmentation of homogeneous full enhanced tumors. Another disadvantage is the use of the EM algorithm for estimating the parameters of the Gaussian Mixture Model, while the EM method is very sensitive to initialization.

[Dou et al., 2007] have published a more recent approach for tumor segmentation using fuzzy fusion. By combining information from a priori knowledge (some rules about tumor intensity in MRI modalities) and image intensities, a fuzzy membership function to the tumor is defined for each modality image. A fuzzy fusion using operators such as t-norm or average operators was performed to fuse the membership functions. Finally a fuzzy region growing is used to refine the final result. This method uses the fused information of several MRI types to segment the tumor automatically and is very fast to detect and segment the tumors.

2.2.10 Fuzzy methods

Fuzzy theory and algorithms were used in brain tumor segmentation methods in several published works. Some of them were classified and reviewed in the previous sections, such as FCM algorithm and fuzzy fusion. In this section we review other fuzzy based methods.

One of these methods is the fuzzy connectedness [Udupa and Samarasekera, 1996 ; Saha and Udupa, 2001] which was successfully applied for segmentation of healthy and pathological brain. The authors define a local fuzzy relation k called affinity and the strength of this relation between two pixels c and d denoted by $\mu_k(c, d)$, which is a fuzzy membership function. This function is zero for non adjacent pixels, one for the same pixels and in the other cases, it is calculated based on the intensity of the pixels. A path is simply a sequence of nearby voxels starting from v_1 and ending on v_2. Each path has a strength of connectedness associated with it that is determined by examining successive pairs of voxels along the path. The affinity of each pair of nearby voxels is calculated along the path. The strength assigned to a path is the smallest affinity of pairwise elements along the path. The strength of connectedness between any two elements v_1 and v_2 is the strength of the strongest of all paths between v_1 and v_2. To compute a fuzzy-connected object, the strength of connectedness between all possible pairs of voxels in the image must be determined.

A semiautomatic tumor segmentation by fuzzy connectedness is proposed by [Moonis et al., 2002 ; Hata et al., 2005]. In this algorithm, the user must select the region of the tumor, and the calculation of connectedness is achieved in this region. Then several seed points in the tumor region are specified by the user and the tumor is delineated in 3D as a fuzzy connected 3D object containing the specified seed points. Finally the user deletes the false points and regions from the segmented tumor. T1-weighted, contrast enhanced T1-weighted and FLAIR images are inputs of the system. In this method the user must be an expert because he has to decide about the final result. Also it needs much calculation time for calculating the connectedness of a path and therefore the algorithm is relatively slow. Later [Liu et al., 2005] have developed this system to segment enhanced and non-enhanced tumors and the potential edema. The system has been validated using 10 patient images for its precision, accuracy, and

efficiency.

2.2.11 Fractal-based

The fractal concept developed by Mandelbrot [Mandelbrot, 1982], provides a useful tool for representing a variety of naturally occurring phenomena. A fractal is an irregular geometric object with an infinite nesting of structures at all scales. Some of the most important properties of fractals are self-similarity, chaos, and non-integer fractal dimension (FD). Mathematically, a fractal structure is defined as a set that has a fractal dimension exceeding its topological one. FD serves as an index of the morphometric complexity and variability of the object being studied.

The fractal model has also been proved to be useful in analyzing a wide variety of medical images [Iftekharuddin et al., 2003]. MRI is candidate for characterization using fractal analysis because of its highly complex structure. Although fractal research on the brain MRI has been ongoing, little work has been done on the brain tumor segmentation in MRI.

[Uemura et al., 2000] developed four methods to generate a FD image and have applied them to brain MRI. Conventional count boxing, overlapping, symmetric and folded overlapping methods have been developed to estimate the fractal dimension, where the folded overlapping method is able to detect the edge of narrow regions. They have introduced this method as a new edge enhancing filter which can be used for brain tumor segmentation in T1-weighted images. In [Iftekharuddin et al., 2003] three methods have been improved to estimate FD in the MR images such as piecewise-threshold box-counting (PTBC), piecewise-modified-box-counting (PMBC) and piecewise-triangular-prism-surface-area (PTPSA). In these algorithms, the patient image is first divided into subimages and the FD of each subimage is calculated. Finally the FD of the patient image is compared with the FD of the reference image. If the FD difference between the patient image and difference image is greater than a threshold value, it shows the presence of the tumor and with plotting the FD difference image the location of tumor can be modified. [Zooka and Iftekharuddin, 2005] have recently validated the capability of their method to detect the location of tumors using 80 MR and CT images of patients with tumors.

The proposed methods for tumor detection are in the preliminary steps and there are many problems to be solved in the future. For example the size of sub images is a problem, because different sub image sizes result in different FD. The second problem is the selection of reference images, because the MR images have different sizes and different parameters and for tumor detection it is required to have a reference image similar to the patient image.

2.2.12 Summary of region-based methods

This section surveyed the main region based methods for brain tumor segmentation in MRI. They have been classified into 11 classes, each class has been reviewed in a subsection. Most proposed methods of this type have focused solely on the segmentation of enhanced tumors which is a simpler task than the segmentation of non-enhanced or ring-enhanced tumors. Also, most of these methods focused on the segmentation of the solid section of tumors, only few of them segmented the edema and only one method has segmented the necrosis [Vinitski et al., 1997]. In clinical applications, all of the tumor components are important for diagnosis, treatment and follow-up. Approximately all methods (except the work of [Gering, 2003]) have used the multimodality MRI. It seems that in order to segment accurately all parts of the tumor, it is necessary to use T1-weighted or contrast enhanced T1-weighted images with FLAIR or T2-weighted images. The automation level in these methods is relatively high but in some of the methods the user interaction is needed. Unfortunately there is not a standard method to validate segmentation methods but a few methods have used manual segmentation of tumors to this aim.

The main problem of these methods is the quality of the segmentation in the border of tumors. Due to the partial volume effect the region-based techniques suffer from misclassification of voxels and hence, it is difficult to have a crisp region of tumor. Most of the time, some kind of postprocessing step, such as morphological operations, user interaction and knowledge based operations were used to remove invalid objects or misclassified pixels/voxels from segmentation results but these operations could not solve this problem completely. Another problem is the segmentation of heterogeneous tumors and it remains an unsolved problem in these methods. Finally most of these methods segment a specific type of tumors and generalization of a method to large types of tumor also remains unsolved.

2.3 Boundary-based methods

In order to overcome some of the limitations of region-based methods for segmentation, boundary-based methods are used to look for explicit or implicit boundaries between regions corresponding to different tissue types. In this method an algorithm searches for pixels/voxels with high gradient values that are usually edge pixels/voxels and then tries to connect them to produce a curve which represents a boundary of the object. In the recent years deformable models, one of the most popular boundary-based methods, have been widely used in image segmentation. The idea behind deformable models is quite simple. The user determine an initial guess for the contour, which is then deformed by image driven forces to the boundaries of the desired objects. In these models, two types of forces are considered. The internal forces, defined within the curve, are designed to keep the model smooth during the deformation process. The

external forces, which are computed from the image data, are defined to move the model toward an object boundary.

There are basically two types of deformable models: parametric deformable models, also referred to as snakes, and geometric deformable models. Parametric deformable models represent curves and surfaces explicitly in their parametric forms during deformation. This representation allows a direct interaction with the model and can lead to a compact representation for fast real-time implementations. Adaptation of the model topology during the deformation can be difficult using these models [Xu et al., 2000].

Geometric deformable models also called level sets, on the other hand, can handle topological changes naturally. These models, based on the theory of curve evolution and the level sets method, represent curves and surfaces implicitly as a level set of a higher-dimensional scalar function. Their parameterizations are computed only after complete deformation, thereby allowing topological adaptivity to be easily accommodated. Despite this fundamental difference, the underlying principles of both methods are very similar.

Deformable models have been extensively studied and widely used in medical image segmentation. In the case of pathology segmentation in MRI the literature is poor and only a few papers deal with the segmentation of tumors.

2.3.1 Parametric deformable models (snakes)

The parametric deformable models that have attracted the most attention to date is popularly known as snakes [Kass et al., 1988]. Snakes or active contours is a special case of the general multidimensional deformable model theory presented by [Terzopoulos, 1987]. Mathematically, a deformable contour is a curve X which moves through the spatial domain of an image to minimize this energy function: $E(X) = \mathbf{F}_{int}(\mathbf{X}) + \mathbf{F}_{ext}(\mathbf{X})$ where $\mathbf{F}_{int}$ is the internal force that constrains the regularity of the curve and $\mathbf{F}_{ext}$ is the external force. The internal force is usually defined as: $\mathbf{F}_{int} = \alpha\nabla^2\mathbf{X} - \beta\nabla^2(\nabla^2\mathbf{X})$ where α and β respectively control the curve tension and rigidity.

For the brain tumor segmentation, [Luo et al., 2003] proposed a method which used two external forces in classical snakes. The adaptive balloon force has been used to increase the capture range of gradient vector flow (GVF) [Xu and Prince, 1998]. This balloon force also increases the speed of the model convergence. The initialization of this method is done manually and in the case of 3D application it needs considerable user operation. The input of the system consists of a T1-weighted image and it segments the solid section of tumor.

[Jiang et al., 2004] have published another method for segmentation and quantification of brain tumors. The gradient magnitude is selected as external force that is computed by the derivative of a Gaussian filter. The initial snake or surface is

provided manually by the user inside or outside of the tumor region. This method cannot segment smooth tumors perfectly and in 3D cases a lot of manual operations are needed for determining the initial surface.

Parametric contour based methods detect tumor boundaries better than region-based methods but they have two main limitations. First, when the initial model and the desired object boundary differ largely in size and shape, the model must be re-parameterized to fully recover the object boundary. Methods for re-parameterization require moderate computational time [Niu, 2006]. Hence, in the proposed methods, to have a good initialization, the initial contour has been manually generated, which needs a lot of user interaction. The second limitation with the parametric approach is that it has difficulty dealing with topological adaptation such as splitting or merging model parts [Xu et al., 2000]. Finally, classical snakes that use the gradient magnitude as image force often have the leakage problem when the boundary of the object to be segmented is ill-defined.

2.3.2 Geometric deformable model

Geometric deformable models, proposed independently by [Caselles et al., 1993] and [Malladi et al., 1995] provide a solution to address the limitations of parametric deformable models (especially for topological adaptation). Geometric deformable models are based on the theory of curve evolution and are implemented using the level sets [Osher and Sethian, 1988] numerical method. In particular, curves and surfaces are evolved using only geometric measures, resulting in an evolution that is independent of the parameterization. As in parametric deformable models, the evolution is coupled with the image data to recover object boundaries. Since the evolution is independent of the parameterization, the evolving curves and surfaces can be represented implicitly as a level set of a higher-dimensional function. As a result, topology changes can be handled automatically [Xu et al., 2000]. The mathematical form of level sets scheme is given as: $\frac{\partial \phi}{\partial t} = V(k)|\nabla \phi|$ where $V(k)$ is called speed function, k is curvature and ϕ is the level sets function.

The use of level sets has been widely documented in the medical imaging literature and several works have been published about segmentation of normal brain and pathological brain in MRI. For example, a semi-automatic method based on level sets for segmentation of glioma of grades II and III was proposed in [Droske et al., 2001]. This approach segments the tumor region in each 2D slice independently and finally it renders 2D segmented tumor in each slice to have a 3D result of segmentation. In each slice, the user selects initially the tumor region. A fast marching level set is used to deform the initial segmentation toward the borders of the tumor. The manually segmented region was used to estimate the parameters of the speed function. Finally the user selects correct segmented slices to generate a 3D mesh of the segmented tumor.

Another semiautomatic method based on level sets for brain tumor segmentation is proposed in [Cates et al., 2004 ; Lefohn et al., 2003]. The speed function $D(I) = \epsilon - |I - T|$ was used in level set evolution where I is the intensity value of each point. Here T controls the brightness of the region to be segmented and ϵ controls the range of grayscale values around T that could be considered inside the object. Thus when the model lies on a voxel with a grayscale level between $T - \epsilon$ and $T + \epsilon$, the model expands and otherwise it contracts. To exceed the speed of level set implementation a graphics processing unit (GPU) was designed in this system. To segment a tumor, the user selects a region of tumor in one slice or several slices, and the mean value and variance of this region are calculated. The other parameter ϵ of the speed function is also determined by the user. The level set is initialized by the selected region of tumor. To have a good result, the user can repeat the level set evolution by changing the parameters and selected region. This system was evaluated for tumor segmentation in contrast enhanced T1-weighted image (only the enhanced section of tumor).

Recently another semi-automatic tumor segmentation using levels set was proposed by [Xie et al., 2005]. In this system the initialization is also achieved manually. The method is evaluated by comparing the results of 10 non-enhanced tumors in T1-weighted images with a manual segmentation.

The topological adaptation can be useful in many applications, but it sometimes lead to undesirable results. Geometric deformable models, when applied to noisy images with ill-defined boundary, may produce shapes that have inconsistent topology with respect to the actual object [Xu et al., 2000]. In these cases, the significance of ensuring a correct topology is often a necessary condition for many subsequent applications, while in the case of tumor segmentation it is very difficult or impossible. Another drawback of the level sets is its relatively low speed of computation in 3D processing which makes it unsuitable for real time applications.

2.3.3 Summary of boundary-based methods

This section reviewed methods based on parametric and geometric deformable models to segment brain tumors in MRI. Although deformable methods have been used to overcome some limitations of region-based methods, it is clear that they cannot solve solely brain tumor segmentation problems. The first problem is the automation of methods. All reviewed methods were initialized manually and need a lot of user interaction specially in 3D applications. Hence these methods cannot operate automatically and need to be combined with region-based methods to have this property. Another problem concerns the heterogeneous tumors, noise and segmentation of the other components of tumor.

Some region-based methods are more robust in dealing with noise and heterogeneous tumors and can be combined with deformable models to yield a good result. In the case of a weak border or a gap in the border of the tumor, the contour or surface

may leak to other regions. Using the region information or global information on the tumor may overcome this problem. The next section will survey several methods based on combination of region-based and boundary-based methods.

2.4 Fusion of region and boundary-based methods

Looking at the advantages of boundary-based and region-based methods, the third class of brain tumor segmentation approaches was designed, which is the fusion of region- with boundary-based techniques. This class has been the most successful, as this technique uses information from two different sources: boundary and region. These methods take advantage of the local and global shape information for deforming the boundaries to capture the topology of tumor areas in the parametric or geometric deformable models. Due to its success, it has recently received much attention and here we review this type of methods in two categories: combination of region-based methods with snake and region-based methods with level sets.

2.4.1 Combination of region-based methods with snakes

The first approach of this type was presented in [Zhu and Yang, 1997]. In this work, for providing an initial contour, a slice that has best intensity contrast is selected as the first slice. Then, by thresholding and some morphological operations, the tumor is initially segmented in this slice. The threshold value has been considered above white matter gray level. The boundary of the extracted tumor is considered as the initial contour for this slice. A Hopfield network was designed to solve the energy optimization problem in classical snakes where the image gradient (edge map is calculated by Sobel filter) as external force. The final contour of each slice is considered as initial contour for neighborhood slices. This method is not really a 3D method and segments the tumor in each slice separately. Contrast enhanced T1-weighted image is the input of system, and this system can segment full-enhanced tumors. The region-based method for initial segmentation of tumor is not robust enough and works in the case of homogeneous tumors with a good enhancement in contrast enhanced T1-weighted image. Also because of the slice by slice segmentation, in the case of contour leakage in a slice, this error is propagated to all other remaining slices and the final segmentation will not be correct.

[Law et al., 2001] proposed another method by combining FCM clustering and classical snakes. This method is a semi-automatic method that begins by selecting one of the slices containing the tumor. This 2D slice is clustered by FCM algorithm in two steps, followed by several morphological operations to extract the tumor. This initial segmentation of the tumor is then refined by a parametric deformable model which uses the image gradient (edge map is calculated by derivatives of a Gaussian

filter) as external force. The result of each slice is used as initial contour for neighbor slices in a deformable model. In another work [Law et al., 2002] have used the GVF as external force, which provides better results. This method is not a really 3D method and operates in 2D. FCM is very sensitive to noise and initial values of cluster centers, hence it can detect and initially segment full-enhanced homogeneous tumors.

Recently in [Chen and Metaxas, 2003] a new hybrid framework by integrating Gibbs model, marching cubes and parametric deformable models has been proposed for brain tumor segmentation (as in Figure 2.2). This method used an individual 2D Gibbs prior model with default parameters for each slice to initially segment the tumor. The result is converted to a 3D mesh using the marching cubes algorithm. This initial segmented surface is refined by a parametric deformable model which used GVF and balloon force as external forces. The parameters of Gibbs model are recalculated in the segmented region and the segmentation process is repeated until the segmented region remains stable. The presented method for initial segmentation is more robust in comparison to the earlier methods, but it operates in 2D and does not use all spatial information about the tumor. In this method for each slice a different Gibbs model was used and it is the main drawback of this system. As we know the resolution of images, the size of head and intensity of each slice largely varies in patients and using this method to segment different types of tumors in different types of images is very difficult.

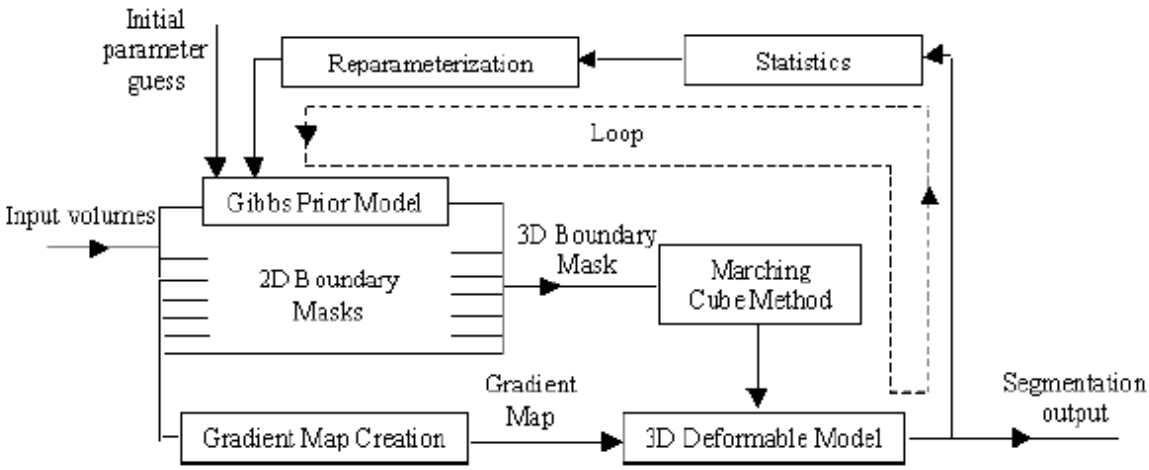

Figure 2.2: Block diagram of the method proposed by [Chen and Metaxas, 2003]

2.4.2 Combination of region-based methods with level sets

[Ho et al., 2002] have proposed a method for automatic 3D segmentation of brain tumors by combining level sets and fuzzy clustering. First a fuzzy clustering method classifies the contrast enhanced T1-weighted with image into tumor and background classes. By calculating the difference image of T1-weighed images with and without contrast enhancement, analyzing of the histogram and using the clustered image, a probability map of tumor is obtained. This initial map is then used to derive an automatic initialization of the surface and to locally guide the level set surface. This initial map prevents the level set from leakage to other regions. Also image forces are balanced with global smoothness constraints to converge stably to a smooth blobby tumor segmentation of arbitrary topology. The method segments enhanced tumors with high accuracy, is full automatic and does not leak to other regions but it has some drawbacks. Because of misclassification in initial clustering, the final segmentation contains the other regions which are enhanced with contrast agent (such as vessels). This method only segments the enhanced section of tumors in contrast enhanced T1-weighted image while a large types of tumors, edema and necrosis remain without enhancement in this type of MRI.

A more recent approach was presented in [Taheri et al., 2007], combining the threshold-based method and level sets. This method is similar to the method of [Chen and Metaxas, 2003] but it works in 3D and uses a threshold method to construct the speed function in level sets. The algorithm is started by selecting one or several ROI in the tumor region. An initial threshold value is calculated using these ROIs and a level set with the proposed threshold-based speed function is deformed using ROI(s) as zero level set. The threshold value is updated by this equation: $T_{i+1} = \mu_i - k\sigma_i$ where μ_i and σ_i are mean and variance values of the segmented region and k is a parameter modified by the user. This process is repeated, upon reaching the tumor boundary. Because of the contrast between tumor and non-tumor intensities, the variation of the threshold declines so that the process stops. Here, authors have assumed that the histogram of tumor and non-tumor regions are slightly overlapped while a few tumors have this condition. Also this method is very sensitive to the initial threshold value which is calculated from selected ROI and the parameter k in threshold updating equation.

2.4.3 Summary of fusion of region and boundary

This section surveyed the methods which combine region and boundary information to segment brain tumors in MRI. Most of these methods are fully automatic because they use region-based methods and the quality of segmentation in the borders of tumor is relatively good because of using boundary information. All proposed methods segment enhanced tumors in contrast enhanced T1-weighted images and segmentation of non-enhanced tumors, edema and necrosis are not achieved with this type of methods.

However it seems that these methods have the ability of solving the problem of tumor segmentation in a large range of tumor types by developing the region based method for initial segmentation, using multimodality images and improving the deformable model method.

2.5 Conclusion

This chapter surveyed existing methods for brain tumor segmentation in MRI. The methods have been reviewed in three core classes: region-based, boundary-based and fusion of region and boundary-based method. The region-based methods segment difficult cases of tumors with high level of automation but they have a main drawback at the boundary of tumors. Due to the partial volume effect the region-based techniques suffer from misclassification of voxels and hence, it is difficult to have a crisp region of tumor. The boundary-based methods were proposed to solve this problem but they also suffer from initialization problems. To obtain a good result they must be well initialized. Initialization has been performed manually which needs a lot of user interaction. The third core class of methods used the advantage of boundary-based and region-based methods to overcome the problems of each type. They have used the capability of automatization of region-based methods to initialize automatically the boundary-based methods and used the good segmentation properties of boundary-based methods to overcome the problem of misclassification at the border of tumors.

Unfortunately, a general framework using combination of boundary and region information has not been presented to segment a large range of tumors (non-enhanced, ring-enhanced and full-enhanced), edema and necrosis. In the next two chapters, a more general method based on combination of region and boundary information to segment a large type of tumors, edema and necrosis will be presented.

CHAPTER 3

Brain tumor segmentation: part I, preprocessing

3.1 Introduction

Despite numerous efforts and promising results in the medical imaging community, accurate and reproducible segmentation and characterization of abnormalities are still a challenging and difficult task because of the variety of the possible shapes, locations and image intensities of various types of tumors. Some of them may also deform the surrounding structures or may be associated to edema or necrosis that change the image intensity around the tumor. As we surveyed in the previous chapter, existing methods leave significant room for increased automation, applicability and accuracy. Most of them are usually dedicated to full-enhanced tumors or specific types of tumors, and do not extent easily to more general types.

The aim of this chapter and the next one is to contribute to this domain, by proposing an original method, which is general enough to address a large class of tumor types. We propose a framework that is a combination of region-based and contour-based paradigms. This framework has two main components as illustrated in Figure 3.1: preprocessing and segmentation. Contrast enhanced T1-weighted (CE-T1w) and FLAIR images, two different modalities of MRI, are inputs of the system. In this chapter we explain the preprocessing section of the framework which performs some preprocessing to reduce the noise, intensity inhomogeneity and interslice intensity variation. Segmentation of the brain to remove non-brain data (skull, fat, skin, muscle) from the image is the next step. However, in pathological cases, standard segmentation methods fail, in particular when the tumor is located very close to the brain surface. Therefore we propose an improved segmentation method, relying on the approximate symmetry plane. To provide some useful information for the next steps and to detect the pathological hemisphere of the brain, we propose a new method relying on a

symmetry-based histogram analysis.

The next chapter will present the segmentation section. Two methods are presented for this aim. The first one is a fuzzy classification method while the second one is based on symmetry analysis. In the segmentation step we first make a decision based on the information that we extracted by the symmetry-based histogram analysis. If the tumor is non-enhanced we continue to initially segment the tumor in FLAIR image by symmetry analysis or using the fuzzy method. Otherwise we initially segment the enhanced section of tumor in the CE-T1w image and edema in the FLAIR image. Also the segmentation of necrosis is done in the CE-T1w and FLAIR images. The initial segmentation of the tumor or its components does not provide an accurate estimation of its boundaries and we therefore propose a refinement step. This is achieved through a parametric deformable model constrained by spatial relations.

This chapter is organized as follows: in Section 3.2 we provide an overview of the proposed system. Section 3.3 describes the segmentation preprocessing operations. Finally in Section 3.4 some conclusions are given.

3.2 Method overview

The automated brain tumor segmentation method that we have developed consists of two main components: preprocessing and segmentation as illustrated in Figure 3.1. The inputs of this system are two different modalities of MR images: CE-T1w and FLAIR that we believe are sufficient for brain tumor segmentation. In the segmentation preprocessing section, operations such as: reduction of intensity inhomogeneity and inter-slice intensity variation of images, spatial registration (alignment) of the input images, segmentation of the brain, computation of the approximate symmetry plane and histogram analysis based on symmetry plane are performed. This section prepares images and some global information on tumor and tumor components to be used in the segmentation section. In the segmentation section, based on the information provided in the preprocessing section, the algorithm is continued in two branches. In the case of a non-enhanced tumor in CE-T1w, the tumor is not accompanied with edema and necrosis and we segment the tumor (in this case tumor is infiltrating) in FLAIR image with a new proposed segmentation method. In the case of a full-enhanced or partially-enhanced tumor, it is with edema and probably with necrosis and we segment them in CE-T1w and FLAIR images with the proposed method. This system can also perform the segmentation using only the CE-T1w image but sometimes (especially for small tumors) user interaction (one click over the tumor) will be required and the quality of segmentation for non-enhanced tumors and edema will be reduced slightly. In the next section the preprocessing operations will be presented.

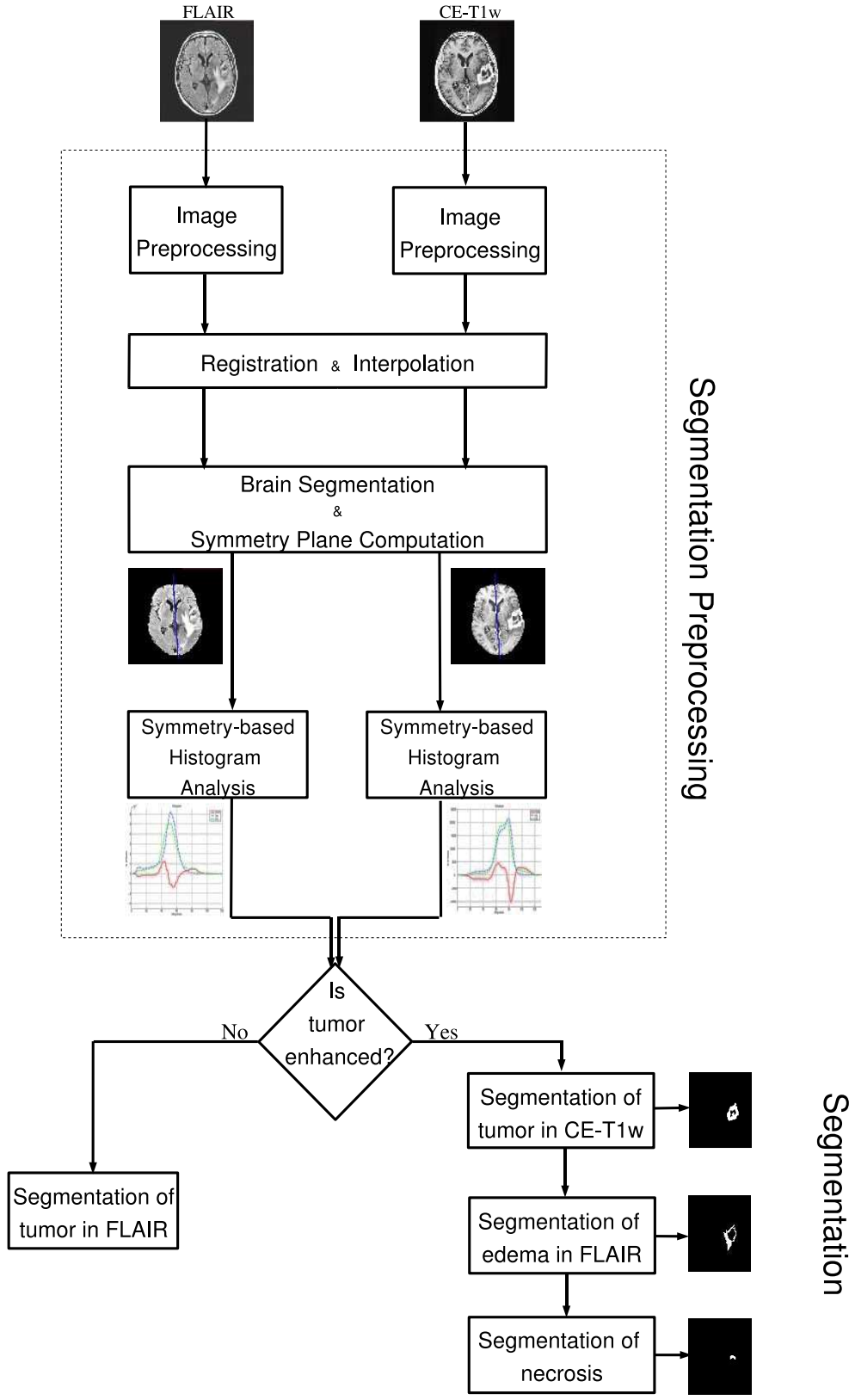

Figure 3.1: Block diagram of the proposed framework for brain tumor segmentation.

3.3 Preprocessing

In the real MRI data there are some problems that have to be first solved before any segmentation operation. Therefore we first try to reduce the intensity inhomogeneity and interslice intensity variations, two main problems of MRI data, in the input images. Our system uses two different modalities of MRI, usually not spatially aligned and often having different resolutions. Hence it is required to add a registration and interpolation step. The brain is then segmented by a combination of histogram analysis, morphological operations and symmetry analysis. In this step we compute the approximate symmetry plane that will be used in the segmentation and sometimes to correct the brain segmentation result. Finally we analyze the histograms of the right and left hemispheres to detect the pathological hemisphere and the type of tumor.

3.3.1 Image preprocessing

Two main problems of MR images are intensity inhomogeneity, or bias field and interslice intensity variation which are caused by the limitations of the current MRI equipments (the main factors are RF excitation field inhomogeneity, non-uniform reception coil sensitivity, eddy currents driven by field gradients, RF penetration and standing wave effects) [Sled and Pike, 1998]. In today MR images, the bias field is not always visible to the human observer, but it causes significant tissue misclassification problems when intensity-based segmentation is used. Therefore, it is required to correct intensity inhomogeneity in the image volume. Here an automatic method based on entropy minimization introduced by [Mangin, 2000] is used (as seen in Figure 3.2). In addition to a smoothly varying field inhomogeneity, two-dimensional multislice sequence MR images, which are acquired in an interleaved way, are typically also corrupted with a slice by slice constant intensity offset. This is usually due to gradient eddy currents and crosstalk between slices. Hence, it is required to normalize interslice intensity to have a correct 3D segmentation. Here a method based on scale-space analysis of histogram, presented in [Dauguet et al., 2004], is used.

3.3.2 Registration and spatial interpolation

Image registration is the operation of aligning images in order to relate corresponding features. For most kinds of image processing on two or more images, it is required that the images are aligned, so that one voxel position represents the same anatomical position in all images. This step allows the use of modalities that are not in perfect alignment.

An image registration program has typically four modules: the transformation model, feature extraction, similarity measure, and an optimization method. In our

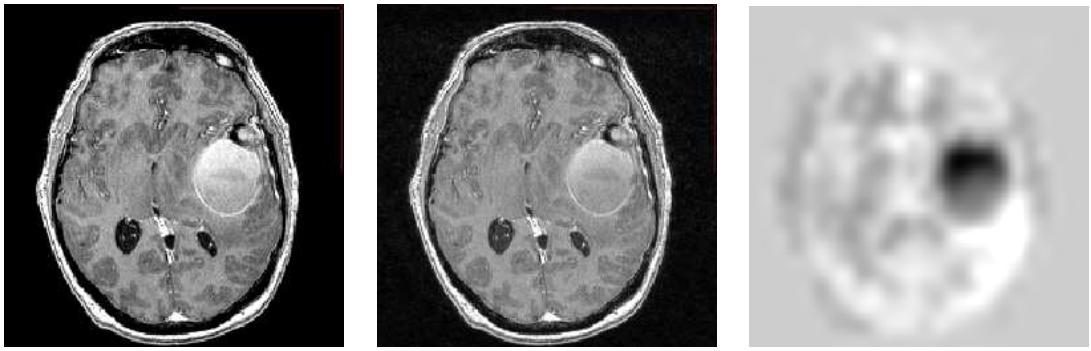

(a) (b) (c)

Figure 3.2: Bias field correction. (a) An axial slice of the original image. (b) Same bias field corrected slice. (c) Applied bias field.

system, the CE-T1w image is used as reference or target image (R) and the FLAIR image as test or source image (T).

Several transformation models can be used to transform the test image T, such as rigid, affine, projection and curved transformations. Here, the registration concerns 3D head images from the same person, which makes it reasonable to assume that the head will not be deformed, and thus can be considered a rigid body. Hence, the rigid transformation model (rotation and translation) is therefore sufficient for our purpose. By using a rigid transformation, we are assuming that the two images can be aligned using a parameterization with 6 degrees of freedom.

Here we restrict ourselves to methods that use directly the intensity images as features, thus avoiding the preliminary extraction of corresponding features in the two images.

To find the transformation parameter that best aligns two images we need a function that measures the similarity between the two images. This measure is a scalar function $S : \mathbb{R}^6 \mapsto \mathbb{R}$ designed so that higher values of S correspond to better matches. Again, since the correct mapping is not known, S can only be a more or less suitable approximation to the true correctness. The registration is performed by finding the parameter vector p that maximizes S. Many similarity measures have been proposed, for example [Woods et al., 1993] generated a ratio image and used the uniformity of the intensity values in this image as a measure of similarity, [Hajnal et al., 1995] used a least-square approach and [Roche et al., 1998] presented correlation ratio as a similarity measure for image registration.

Another similarity measure, that has been applied to both intra- and multi-modality image registration, is mutual information (MI) [Maintz and Viergever, 1998]. MI, or relative entropy is based on the information-theoretic entropy concept and is defined as: $MI(R,T) = H(R) + H(T) - H(R,T)$ where $H(R)$ is the entropy of image R, $H(T)$ is the entropy of image T, and $H(R,T)$ is the joint entropy of corresponding

voxel pairs between the two images. One problem of the Mutual Information metric is that in special cases it can decrease with increasing misalignment when images only partially overlap [Studholme et al., 1998]. In order to overcome this problem, the Normalized Mutual Information (NMI) measure was proposed in [Studholme et al., 1998]: $NMI(R,T) = \frac{H(R)+H(T)}{H(R,T)}$. This measure offers improved results over Mutual Information based registration, and is the measure we use for image registration in our system.

Digital 3D MR images are sampled at discrete grid points, while translating an image causes the transformed image's grid points do not coincide with the original grid points, hence spatial interpolation is applied after linear registration and is used to compute the locations and intensity values of the pixels in the transformed image volume. The choice of an effective interpolation algorithm is important, since some methods will introduce more interpolation artifacts into the image than others. There are many different interpolation methods available, of which four are frequently used in medical image registration, namely trilinear, nearest-neighbor, sinc and β-spline interpolation. As in many other applications, we have to choose between computational speed and accuracy when we decide upon which interpolation method to use. [Meijering, 2002] references a large number of comparative studies of different methods for medical image interpolation. The conclusion drawn based on these evaluations is thatβ-spline kernels are in general the most appropriate interpolator, but it is relatively slow (see Figure 3.3). Therefore, with our experience and based on an objective comparison of results we chose to use a trilinear interpolation which is sufficiently accurate and rapid for our application.

To register the images, we use FSL [Smith et al., 2004] software package, where we choose the rigid six degree transformation, trilinear interpolation and NMI similarity function. The registration tools of this package use a local-global optimization method presented in [Jenkinson et al., 2002]. The results of registration with several methods are shown in Figure 3.3. Here we compared visually the results obtained by correlation ratio, least square, normalized correlation and NMI similarity measure and trilinear, β-spline, cubic lagrangian and sinc windowed interpolation method. The results show that each registered slice by using NMI similarity measure and trilinear interpolation is more similar to the corresponding slice of original FLAIR and T1-weighted image (as seen in the first image of the last row in Figure 3.3 for one slice).

3.3.3 Symmetry plane computation

Normal human brains possess a high degree of bilateral symmetry although they are not perfectly symmetrical. The symmetry plane of the brain is a good approximation of the mid-sagittal plane, which is defined as the plane that best separates the hemispheres. The automatic detection of this plane in brain images is a useful task and here we will use it to segment the brain and to detect the brain tumors. The

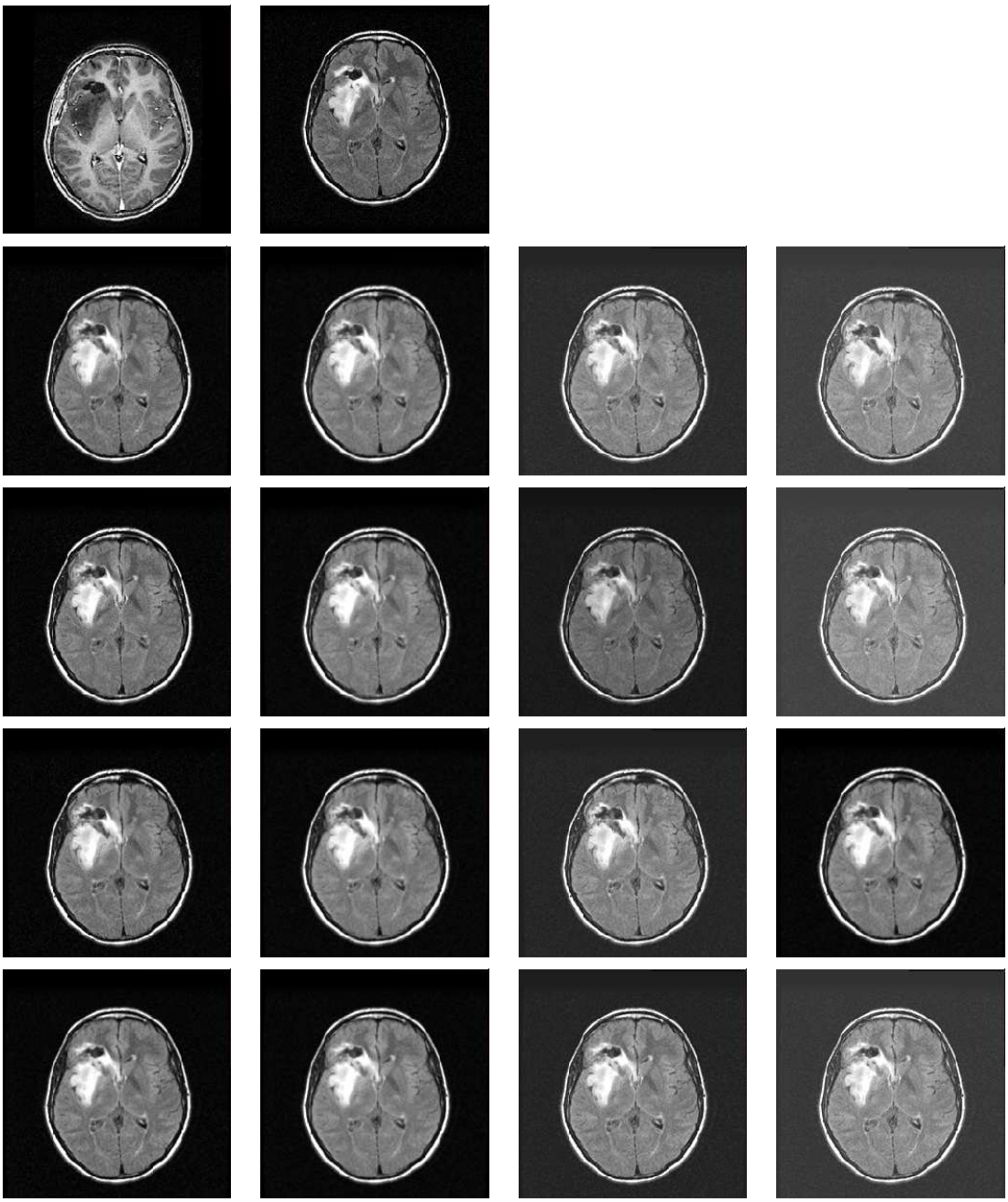

(a) (b) (c) (d)

Figure 3.3: Result of rigid registration methods. First row (a) is one axial slice of the original CE-T1w image and (b) is the corresponding slice of FLAIR image. In 2nd, 3rd, 4th and 5th rows the similarity measures are correlation ratio, least square, normalized correlation and NMI, respectively. In the column (a), (b), (c) and (d) the interpolation methods are trilinear, β-spline, cubic Lagrangian and sinc windowed. The results of the 5th row (NMI) is closer to the original image. The time of registration for the 5th row is 1, 12.5, 1.5 and 4.5 minutes from left to right. By comparing the interpolation results, it seems that NMI with trilinear interpolation is the best choice for our application.

computation of the approximate brain symmetry plane is performed according to a method proposed in [Tuzikov et al., 2003], which is based on the maximization of a symmetry measure. Let us briefly describe it here.

Let $\mathbf{u}$ be a unit vector in $\mathbb{R}^3$ and $\Pi_{\mathbf{u},d}$ a plane in $\mathbb{R}^3$ orthogonal to the vector $\mathbf{u}$ and passing at the distance d from the coordinate origin. We denote by $e_{\mathbf{u},d}(f)$ the reflection of image f with respect to the plane $\Pi_{\mathbf{u},d}$: $e_{\mathbf{u},d}(f)(x,y,z) = f(e_{\mathbf{u},d}(x,y,z))$. An image f is called *reflection symmetrical* if there exists a reflection plane $\Pi_{\mathbf{u},d}$ such that $e_{\mathbf{u},d}(f) = f$. Since there is not an exact symmetry in the brain, we consider a degree of symmetry defined as the similarity between $e_{\mathbf{u},d}(f)$ and f:

$$\mu_{\mathbf{u},d}(f) = 1 - \frac{||f - e_{\mathbf{u},d}(f)||^2}{2||f||^2}.$$

The idea is to compute the symmetry measure $\mu_{\mathbf{u},d}(f)$ of the image f with respect to an arbitrary reflection plane $\Pi_{\mathbf{u},d}$, and to find the plane leading to the maximal symmetry degree and the corresponding value of symmetry measure $\mu(f)$:

$$\mu(f) = \max_{\mathbf{u}\in S^2,\ d\in\mathbb{R}^+} \mu_{\mathbf{u},d}(f). \tag{3.1}$$

First, an initial symmetry plane is estimated based on the ellipsoid of inertia of the image f. The three major planes of the ellipsoid of inertia are computed and the plane for which the symmetry measure is maximum is chosen as an initial plane. Then, the orientation and the position of the plane are improved by optimizing in the 3D space the reflection plane parameters. This leads to an optimum of the proposed similarity measure, and is considered as the approximate symmetry plane.

In the normal brain the symmetry plane of the head in MRI is approximately equal to the symmetry plane of the segmented brain. Although the internal structure of a pathologic brain may depart from its normal bilateral symmetry, the ideal imaginary symmetry plane remains invariant [Liu et al., 1996]. Therefore in the refinement process of the brain segmentation we can use the symmetry plane of the head instead of the symmetry plane of the segmented brain. In the normal brain, it has also been observed that the symmetry plane of the gray level brain image and the one of the segmented brain are approximately equal. Since pathological brains are usually not symmetric when considering the gray level images, we can compute the symmetry plane of the segmented brain, which exhibits more symmetry and the computation time is shorter. Applying this method to images containing tumors provides a good approximation of the mid-sagittal plane, despite the asymmetry induced by the tumors. This is illustrated in Figure 3.4 for a normal brain and for different types of tumors.

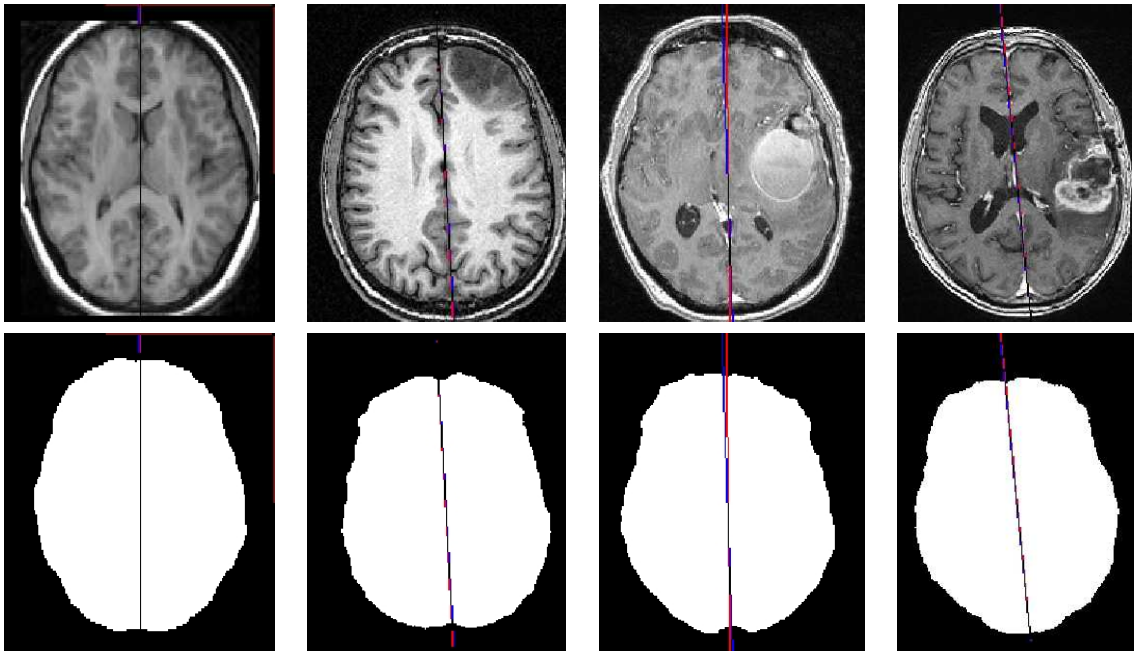

(a) (b) (c) (d)

Figure 3.4: Symmetry plane computation. The first row shows the symmetry plane of the head (red line) and brain (blue line) superimposed on the head image (the symmetry plane is black when they coincide). The second row shows the symmetry plane of the head and brain superimposed on the segmented brain. (a) Normal brain. (b) Non-enhanced tumor. (c) Full-enhanced tumor. (d) Ring-enhanced tumor. These images show that the symmetry plane of the head and segmented brain are approximately equal.

3.3.4 Brain segmentation

The next step of preprocessing consists of brain segmentation. Several methods have been proposed to perform this operation (see e.g. [Mangin et al., 1998 ; Shattuck et al., 2001 ; Smith, 2002]) and some of them are available in softwares such as BrainVisa [Cointepas et al., 2001], FSL [Smith et al., 2001] and Brainsuite [Shattuck and Leahy, 2002]. Unfortunately most of them fail in the case of the presence of a tumor in the brain, especially if located on the border of the brain (Figure 3.5).

To solve this problem, we propose to perform a symmetry analysis, based on the assumption that tumors are generally not symmetrically placed in both hemispheres, while the whole brain is approximately symmetrical.

First we segment the brain using histogram analysis and morphological operations, similarly as in [Mangin et al., 1998]. This leads to a partial segmentation, where a part corresponding to the tumor may be missing. The algorithm summarized in Section 3.3.3 is applied on the gray level image of the head to compute the approximate symmetry plane, because the segmented brain is not symmetric. The computed sym-

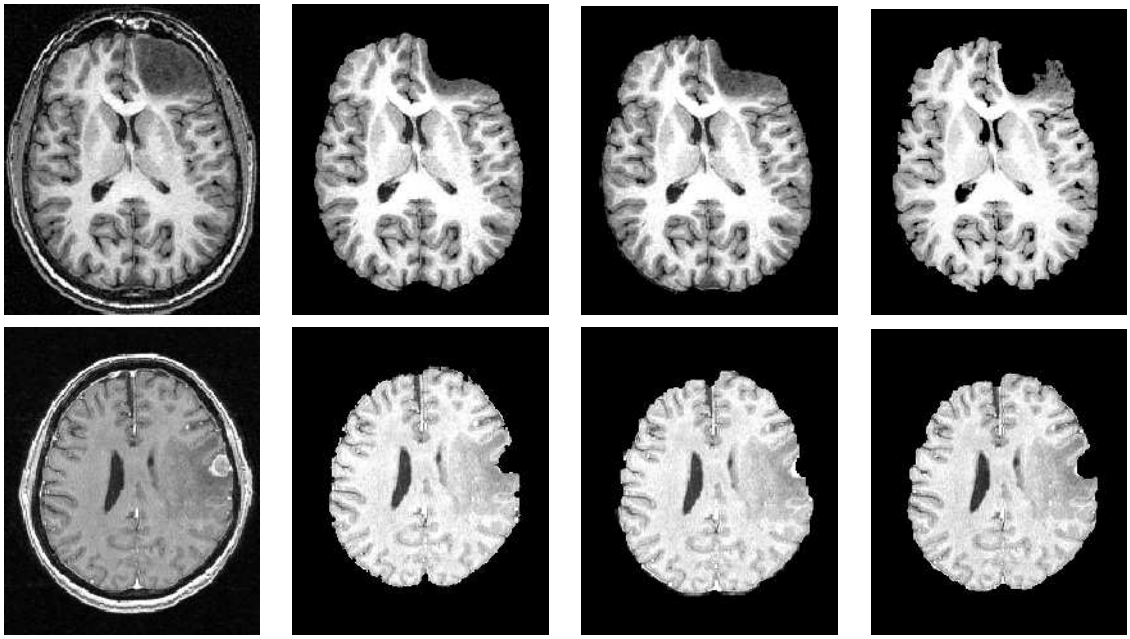

(a) (b) (c) (d)

Figure 3.5: Pathological brain segmentation using existing methods. (a) One slice of the original image on two examples. (b) Segmented brain by histogram analysis and morphological operations [Mangin et al., 1998] using BrainVisa [Cointepas et al., 2001]. (c) Segmented brain by BET [Smith, 2002] using FSL [Smith et al., 2001]. (d) Segmented brain by BSE [Shattuck et al., 2001] using Brainsuite [Shattuck and Leahy, 2002].

metry planes of the head and of the segmented brain in normal cases are approximately equal and this approximation is acceptable in pathological cases for tumor detection purpose. We then compute the reflected brain with respect to the symmetry plane (Figure 3.6). By calculating the difference between the reflected brain mask and the brain mask in the unsigned 8 bit format (the images have two levels 0 and 255 and after subtraction we select the level 255) we obtain an image which contains the removed section of the tumor and other small objects. To select the component which corresponds to the tumor, first we use a morphological opening to disconnect the components. We then select the largest connected component since it corresponds to the removed section of the tumor, as confirmed by all our experiments (in the case of small tumors, a single clicking over the tumor or using the FLAIR image can help to select the tumor component (tumors in the FLAIR images correspond to hyperintense regions)). Here, the elementary neighborhood of the morphological operations corresponds to 6-connectivity. The result can only be considered as an approximation in the tumor area, but it is accurate enough for tumor detection in the next step. Finally we add this result to the segmented brain. The main steps of this method and its results are illustrated on two examples in Figure 3.6. They correspond to the desired whole brain, including the pathological areas.

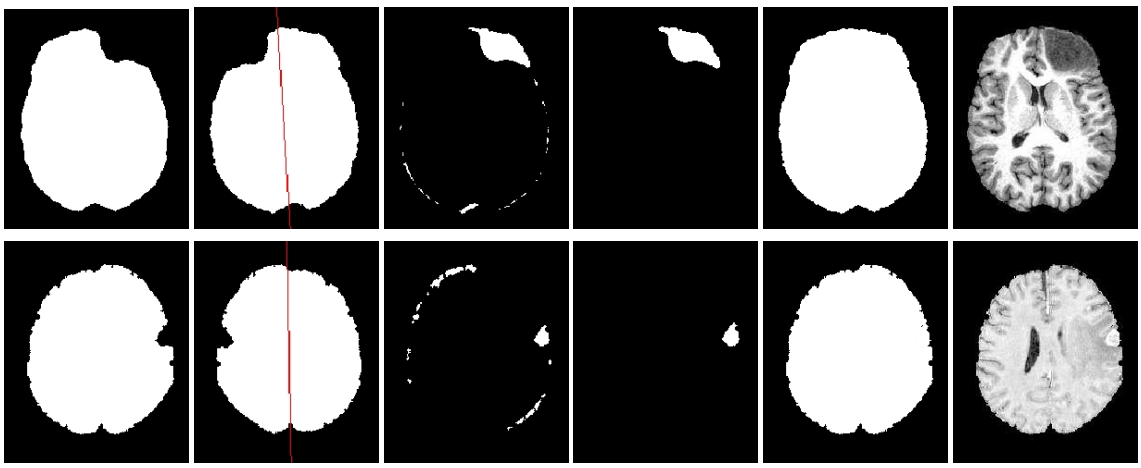

(a) (b) (c) (d) (e) (f)

Figure 3.6: The proposed algorithm for pathological brain segmentation (same examples as in Figure 3.5). (a) Segmented brain by histogram analysis. (b) Reflected brain with respect to the approximate symmetry plane. (c) Difference image of (b) and (a) (bounded difference). (d) Removed section of the tumor obtained by morphological operations from image (c). (e) Final segmented brain. (f) Final gray level segmented brain.

3.3.5 Symmetry-based histogram analysis

In this step we need to extract some information from the brain image histogram which will be needed in the next steps. We first need to find the pathological hemisphere or the hemisphere which has the most part of pathology. Also to decide the type of the segmentation in the next step, it is necessary to know whether the tumor is enhanced or non-enhanced in CE-T1w image.

To extract this information and to provide an initial segmentation of the tumor in the next step, we propose a symmetry-based histogram analysis. As mentioned in Section 3.3.3, since the symmetry plane of the gray level image and the one of the binary mask of the segmented brain in the normal case are approximately equal, to increase the accuracy and to speed-up the algorithm in the pathological case we compute the symmetry plane on the binary mask of the segmented brain (if the symmetry plane has been calculated in the brain segmentation step we use that symmetry plane).

Now the tumor type (enhanced or non-enhanced), tumor global information and the pathological hemisphere can be detected by evaluating this asymmetry with respect to the obtained plane. We assume that tumors are localized in only one hemisphere or are not symmetric. Using the calculated symmetry plane we first obtain the reflection of the brain mask and then provide the intersection of the brain mask and its reflection. This operation is required to equalize the volume of hemispheres. We then calculate

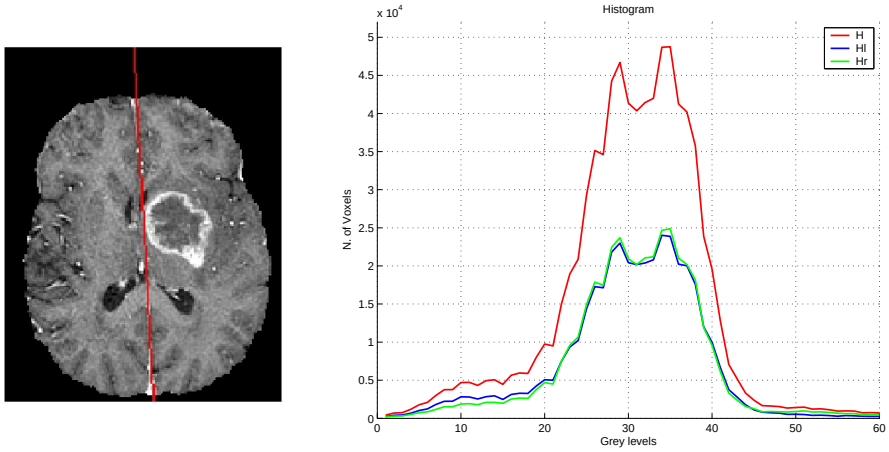

(a) (b)

Figure 3.7: (a) One axial slice of a pathological MR image with symmetry plane. (b) Histograms of the brain ($\mathbf{H}$), right hemisphere ($\mathbf{H}_r$) and left hemisphere ($\mathbf{H}_l$).

the right and left hemispheres of the brain gray level image (which is obtained using the intersection mask). The histograms in the left and right hemispheres are then calculated (as seen in Figure 3.7). To remove noise we filter the histograms with an anisotropic diffusion filter. We then calculate the difference of the right and left histograms and detect its peaks (changes). To analyze and interpret these peaks we estimate the radiometric characteristics of the brain tissues.

Histogram filtering

As seen in Figures 3.7 and 3.9 the histograms are corrupted with different levels of noise. Therefore we first need to achieve a preprocessing step to smooth noise while meaningful structures are preserved. One of the best candidate filters for histogram smoothing is the anisotropic diffusion filter [Perona and Malik, 1990].

By linking the diffusion coefficient $c(x, \sigma)$ of the filter to the gradient $\bigtriangledown I(x, \sigma)$ of the histogram convolved with a Gaussian of variance, the smoothing process could be confined to relatively homogeneous regions, while no smoothing would be carried out in the regions with strong gradients [Aurdal, 1997]. Different functions can be used for c. The two more common choices are $c(x, \sigma) = e^{\left(-(\|\bigtriangledown I\|/K)^2\right)}$ and $c(x, \sigma) = \frac{1}{1+\left(\frac{\|\bigtriangledown I\|}{K}\right)^2}$. The results generated by these two functions are different, the first one privileges high value points over low value ones, the second privileges wide regions over smaller regions.

We have experimented with both coefficient diffusion functions. The second one provides better results for our application. In order to determine the value of K, such that small local differences will be removed while keeping large differences, we

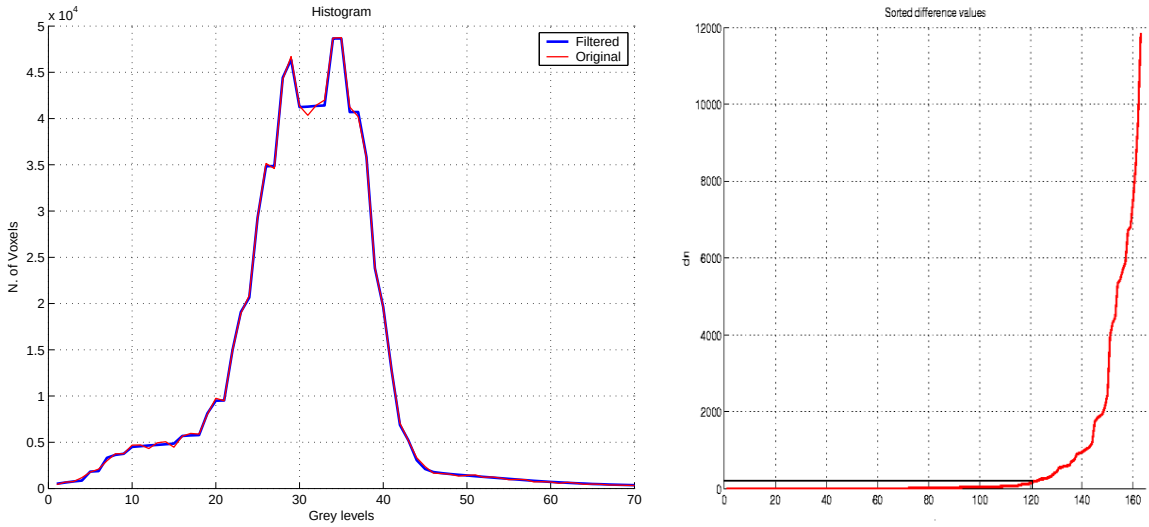

(a) (b)

Figure 3.8: (a) Original and filtered histogram of a pathological MR image with low noise. (b) Plot of sorted difference values of original histogram. Here $K = 120$ was selected based on this sorted list.

calculate the absolute difference values of neighbor gray levels in the original histogram according to: $d_n = |H(n) - H(n+1)|$. We then sort these difference values. In this sorted list, there will be relatively many occurrences of small differences and fewer large differences. Here we choose K as the difference value that corresponds to the median of differences (without zero differences), that satisfy our condition of keeping the meaningful structures in the histogram [Aurdal, 1997]. In Figure 3.8 the result of applying the anisotropic filtering to one of the histograms of Figure 3.7 (a low noisy histogram) and the plot of the sorted difference values are shown. Figure 3.9 illustrates the result of applying the anisotropic filter to a highly noisy histogram.

Peak detection in the difference of histograms

Let $\mathbf{H}(x)$ denote the histogram of gray levels in the whole brain (x denotes the gray level), $\mathbf{H}_l(x)$ the histogram in the left hemisphere and $\mathbf{H}_r(x)$ the histogram in the right hemisphere. The difference of histograms:

$$\mathbf{H}_{srl}(x) = \mathbf{H}_r(x) - \mathbf{H}_l(x) \tag{3.2}$$

provides useful information about new intensity classes induced by the tumor. To extract and analyze this information we first need to detect the peaks (changes) in $\mathbf{H}_{srl}(x)$. The tumor influence over the brain tissues is to decrease the volume of healthy tissues (GM and WM) and increase the volume of gray levels corresponding to the tumor tissue (before GM and after WM) in the pathological hemisphere. Since the volume of tissues in the normal hemisphere remain almost constant, some negative

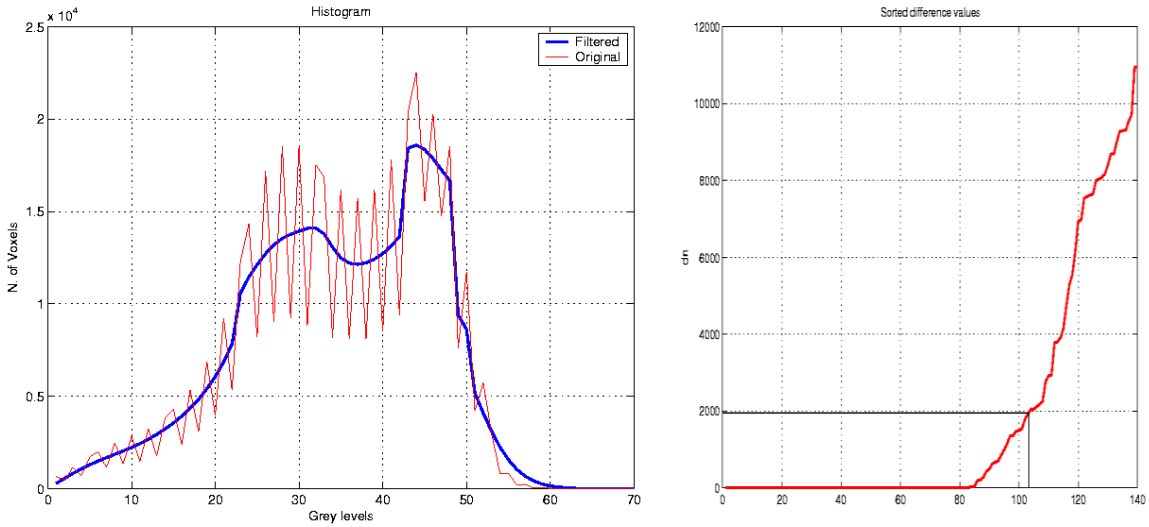

(a) (b)

Figure 3.9: (a) Original and filtered histogram of a pathological MR image with high noise. (b) Plot of sorted difference values of original histogram. Here $K = 1970$ was selected based on this sorted list.

and positive peaks appear in $\mathbf{H}_{srl}(x)$. The zero-crossing of $\mathbf{H}_{srl}(x)$ will indicate the location of the occurred peaks (as seen in Figure 3.10). The following rules are applied to detect the start, end and maximum or minimum of the peaks:

- a zero-crossing to positive values (positive crossover) indicates the start of a positive peak and/or the end of a negative peak,
- a zero-crossing to negative values (negative crossover) indicates the end of a positive peak and/or the start of a negative peak,
- the point at which we have a maximum between a positive and a negative crossover indicates the maximum of a positive peak,
- the point at which we have a minimum between a negative and a positive crossover indicates the maximum of a positive peak,
- the point which divides the number of voxels of a peak by two is the middle of this peak (the occurred peaks have not always a normal distribution).

Therefore each detected peak P_i has 4 values, S_{p_i}, E_{P_i}, M_{P_i} and D_{P_i} which are the start, end, maximum/minimum and middle gray levels respectively and $H(M_{P_i})$ is the maximum/minimum value of the peak P_i. To compute D_{P_i} we minimize the following equation:

$$F(D_{P_i}) = \left| \left(\sum_{j=S_{P_i}}^{D_{P_i}} |H_{srl}(j)| \right) - \left(\sum_{k=D_{P_i}}^{E_{P_i}} |H_{srl}(k)| \right) \right|, S_{P_i} < D_{P_i} < E_{P_i} \tag{3.3}$$

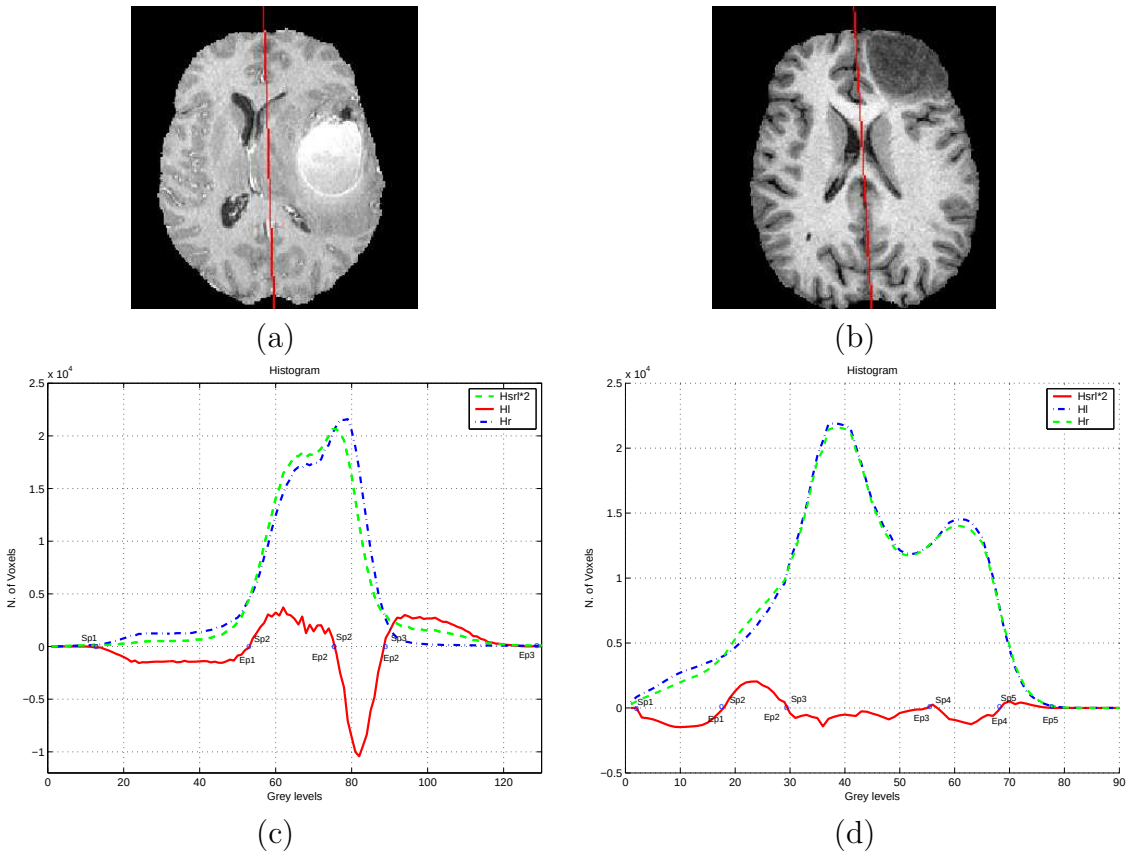

Figure 3.10: Histograms difference. (a),(c) An axial slice of an enhanced tumor and the graph of the right hemisphere histogram, left hemisphere histogram and the difference of histograms (for visualization purposes $\mathbf{H}_{srl}$ is multiplied by 2). (b),(d) An axial slice of a non-enhanced tumor and the graph of the right hemisphere histogram, left hemisphere histogram and difference of histograms.

Estimation of radiometric characteristics of brain tissues

To analyze and interpret the detected peaks in $\mathbf{H}_{srl}(x)$, it is required to find the radiometric characteristics (mean and standard deviation) of brain tissues (CSF, GM and WM). Using these parameters we can determine in which tissue each peak (or change) in $\mathbf{H}_{srl}(x)$ has appeared.

Let M_c and σ_c denote the mean and variance of CSF, M_g and σ_g the mean and variance of GM and M_w and σ_w the mean and variance of WM. To estimate these parameters (or modes of CSF, GM and WM), various approaches have been proposed, including K-means [Kruggel and Lohmann, 1997], fit with a Gaussian mixture model (GMM) [Peng et al., 2005 ; Schroeter et al., 1998], using a priori models [Verard et al., 1997] or based on histogram scale-space analysis [Mangin et al., 1998]. Here, we use the last one which is based on Gaussian scale-space analysis. This method is very fast and robust and we also applied it for brain segmentation in Section 3.3.4. Although this

method has been proposed for normal cases, based on our experience and verification, it correctly operates in tumoral cases (the precision of estimation for our application is sufficient). We apply this method to estimate the modes of CSF, GM and WM before the segmentation of the brain. In Figure 3.11 the extrema of a pathological brain histogram (D_0) and its two first derivatives (D_1 and D_2) in the scale-space are shown. The signatures and scale selections of background, CSF, GM and WM modes for the same histogram are provided in Figure 3.12.

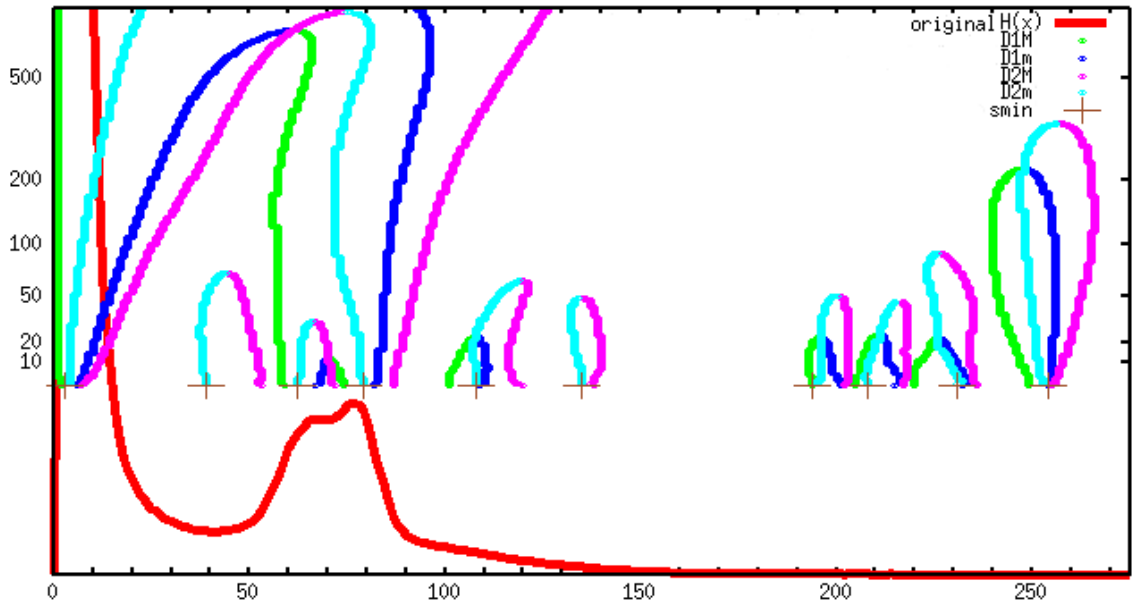

Figure 3.11: The extrema of a pathological brain (Figure 3.10 (a)) histogram (D_0) and its two first derivatives (D_1 and D_2) in the scale-space. D_{iM} denotes a maximum while D_{im} denotes a minimum.

Detection of the tumor type and the pathological hemisphere

Now, using the detected peaks in $H_{srl}(x)$ and the radioparametric characteristics we can determine the type of tumor (enhanced or non-enhanced) and the pathological hemisphere in CE-T1w. We apply the following rules for determining the type of tumor, based on the characteristics of tumors:

- if there is a peak P_i where $D_{P_i} > M_w + 2\sigma_w$ then the tumor is enhanced. If $H_{srl}(M_{P_i})$ is negative then the pathological hemisphere is the left one, else it is the right one,
- if there is a peak P_i where $M_c < D_{P_i} \leq M_g$ and there is not a peak P_j where $D_{P_j} > M_w + 2\sigma_w$ then the tumor is non-enhanced. If $H_{srl}(M_{P_i})$ is negative then the pathological hemisphere is the left one, else it is the right one.

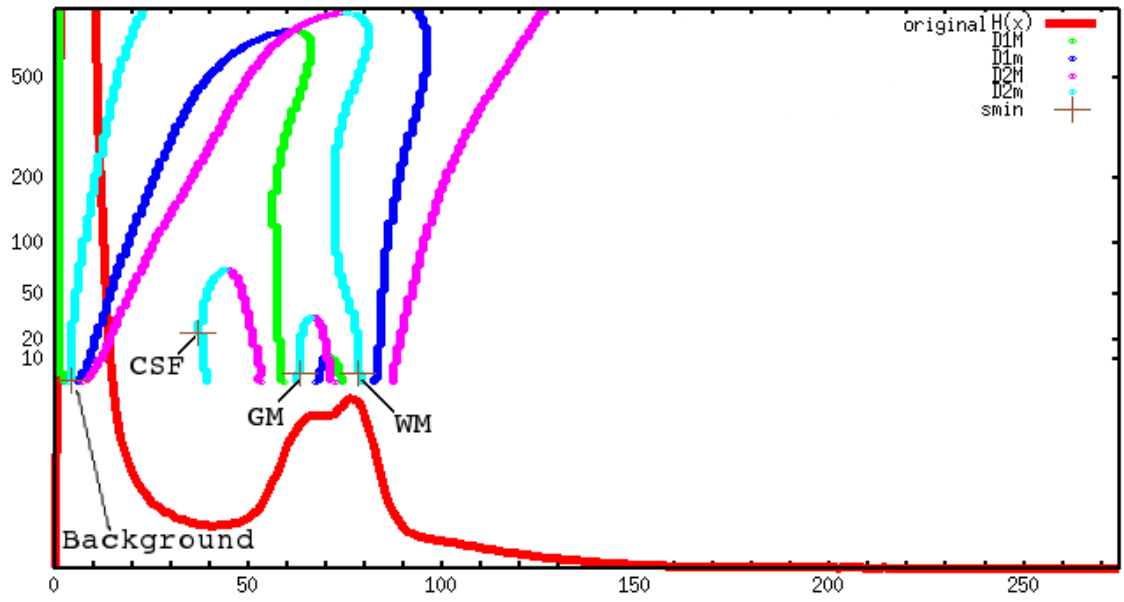

Figure 3.12: The signatures and scale selections of gray and white matter modes for a pathological brain (Figure 3.10 (a)).

To remove the noise effects, we consider the peaks with $N_{P_i} > \epsilon_P$, where N_{p_i} is the number of voxels in P_i and ϵ_P is a user defined constant.

This method can also be applied to detect the pathological hemisphere in FLAIR images (tumor type detection in FLAIR image is not possible because all tumors have hyperintense appearance). We use the following rule to detect the pathological hemisphere:

- if there is a peak P_i where $D_{P_i} > M_w + 2\sigma_w$ then a tumor exists. If $H_{srl}(M_{P_i})$ is negative then the pathological hemisphere is the left one, else it is the right one.

Evaluation

We have applied the proposed method to MR data from 20 patients with cerebral tumors (see Tables 1.4 and 1.5). These images contain tumors with different sizes, intensities, shapes and locations (10 CE-T1w images with enhanced tumors (full and ring) and 10 CE-T1w images with non-enhanced tumors). These images contain tumors with different sizes, intensities, shapes and locations. This allows us to illustrate the large field of application of our method. Two of them are shown in Figures 3.13 and 3.14. The detection results for all cases are also summarized in Table 3.1. In all cases, $\epsilon_p = 500$, hence our method can detect the tumors greater than 500 voxels or about $0.8 \times 0.8 \times 0.8cm$. This table shows that the detection of tumor type and pathological hemisphere in all 20 cases is correct.

We applied the proposed method to detect the pathological hemisphere in 10 FLAIR images. For these images the volume dimension is $256 \times 256 \times 20$ and the voxel size is about $1 \times 1 \times 1 \times 6.5mm^3$. One of them is shown in Figure 3.15 and the detection results for all images are summarized in Table 3.2. This table illustrates that the detection of pathological hemisphere in all cases is correct.

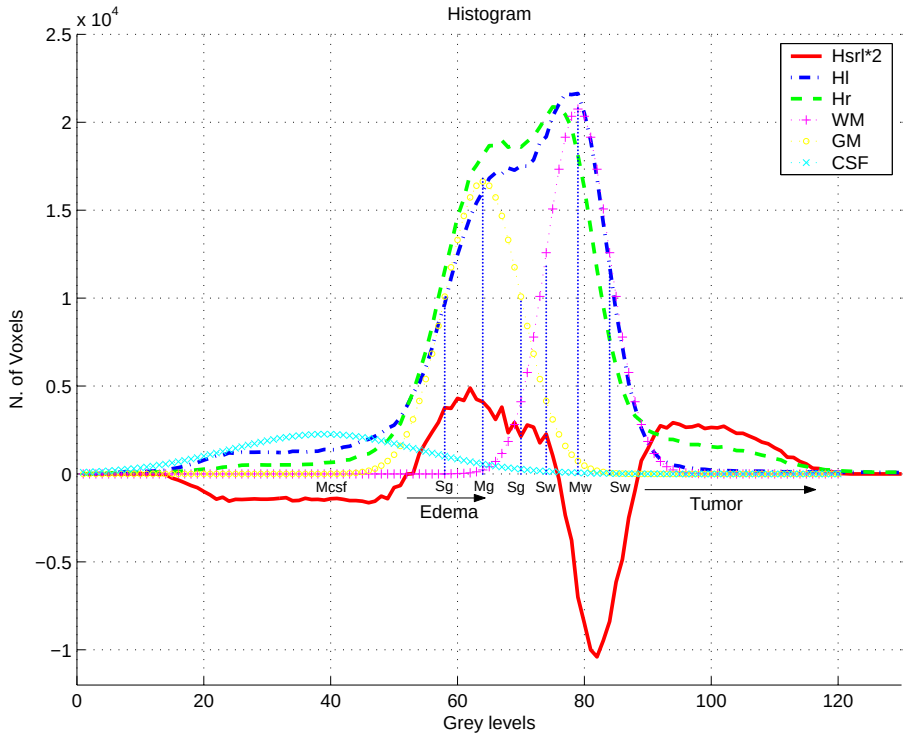

Figure 3.13: Detection of tumor type and pathological hemisphere for an enhanced tumor (Figure 3.10 (a)) in a contrast enhanced T1-weighted image. Here $M_g = 63$, $\sigma_g = 5$, $M_w = 78$, $\sigma_w =$, $S_P = 89$, $E_P = 130$ and $D_P = 102$. The detected tumor type is enhanced and the pathological hemisphere is the right one (for visualization purposes $\mathbf{H}_{slr}$ is multiplied by 2).

3.4 Conclusion

In the preprocessing section we perform some steps which are required before the segmentation. Noise and inhomogeneity reduction, image registration, brain segmentation and tumor type and pathological hemisphere detection are the preprocessing operations in our system.

In this chapter we showed that the sagittal symmetry plane can be helpful in the brain image processing. We proposed a new method for brain segmentation which relies on symmetry plane. In this method we used the symmetry plane to correct the

Data Set	Type	Volume (voxel)	Hem	M_g	σ_g	M_w	σ_w	S_p	E_p	D_p	Type Det.	Hem Det.
TE1	En	10131.6	R	59	5	67	4	80	102	89	En	R
TE2	En	42365.5	R	25	5	35	4	43	65	53	En	R
TE3	En	19248.8	R	36	4	41	4	51	80	62	En	R
TE4	En	39578.5	R	25	8	34	7	45	72	57	En	R
TE5	En	11118.0	R	51	5	68	4	76	125	90	En	R
TE6	En	13629.2	L	31	4	45	4	53	70	61	En	L
TE7	En	5776.1	L	43	5	50	4	55	76	59	EN	L
TE8	En	24550.9	R	28	4	36	4	45	76	57	En	R
TE9	En	2312.0	R	65	7	79	4	83	95	90	En	R
TE10	En	63118.8	R	63	5	78	5	89	130	102	En	R
TNE1	NEn	842823.7	L	56	9	70	8	39	61	50	NEn	L
TNE2	NEn	53885.3	L	38	7	59	6	12	30	21	NEn	L
TNE3	NEn	19472.0	L	24	4	41	4	11	18	15	NEn	L
TNE4	NEn	61121.7	R	38	8	63	6	18	29	25	NEn	R
TNE5	NEn	55248.1	L	33	5	54	5	5	35	19	NEn	L
TNE6	NEN	9554.1	R	31	5	48	5	3	34	19	NEn	R
TNE7	NEn	66221.8	R	39	13	59	11	23	41	34	NEn	R
TNE8	NEn	34021.5	L	38	5	60	5	25	54	34	NEn	L
TNE9	NEn	35763.2	R	44	7	74	7	26	50	42	NEn	R
TNE10	NEn	38672.8	R	41	6	64	4	33	44	38	NEn	R

Table 3.1: Result of tumor type and pathological hemisphere detection in CE-T1w images. Here NEn, En, R and L denote non-enhanced, enhanced, right and left respectively.

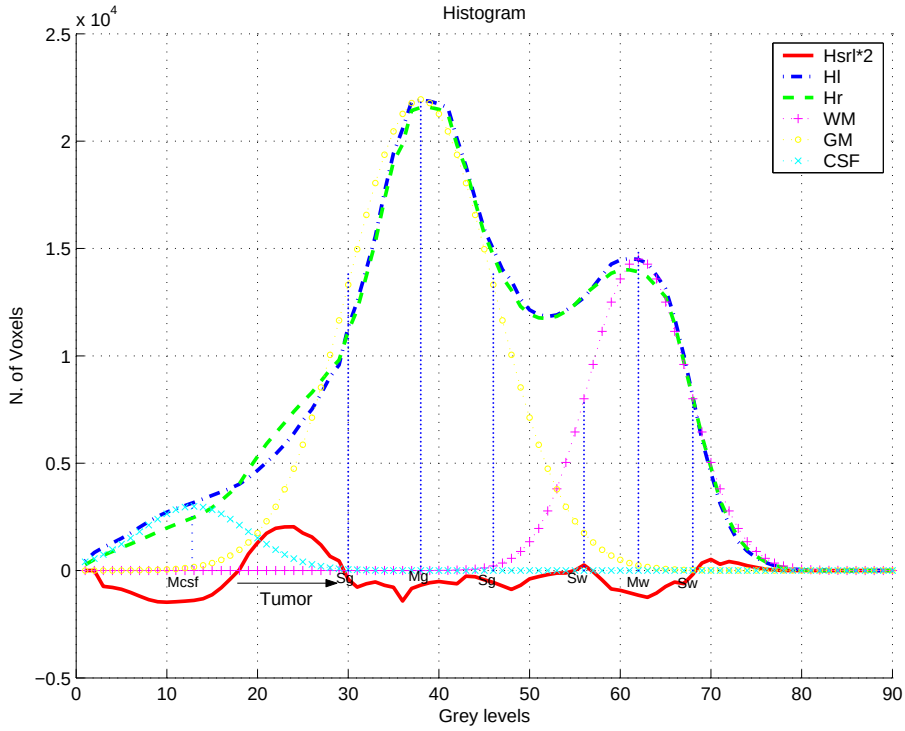

Figure 3.14: Detection of tumor type and pathological hemisphere for a non-enhanced tumor (Figure 3.10 (b)) in a contrast enhanced T1-weighted image. Here $M_g = 38$, $\sigma_g = 8$, $M_w = 63$, $\sigma_w = 6$, $S_P = 19$, $E_P = 29$ and $D_P = 25$. The detected tumor type is non-enhanced and the pathological hemisphere is the right one (for visualization purposes $\mathbf{H}_{slr}$ is multiplied by 2).

brain segmentation in the presence of a tumor especially on the border of the brain. We proposed a new method relying on symmetry analysis for the detection of tumor types and the pathological hemisphere in CE-T1w and FLAIR images. This method can be applied for other types of brain images. We applied the proposed method to 20 CE-T1w and 10 FLAIR images with different tumor sizes, at different locations and with different shapes. In all cases, it detects the tumor type and pathological hemisphere correctly.

Now, the system can use the processed images and the extracted information to segment the tumor and its components. In the next chapter we propose a new method for brain tumor segmentation using region and border information.

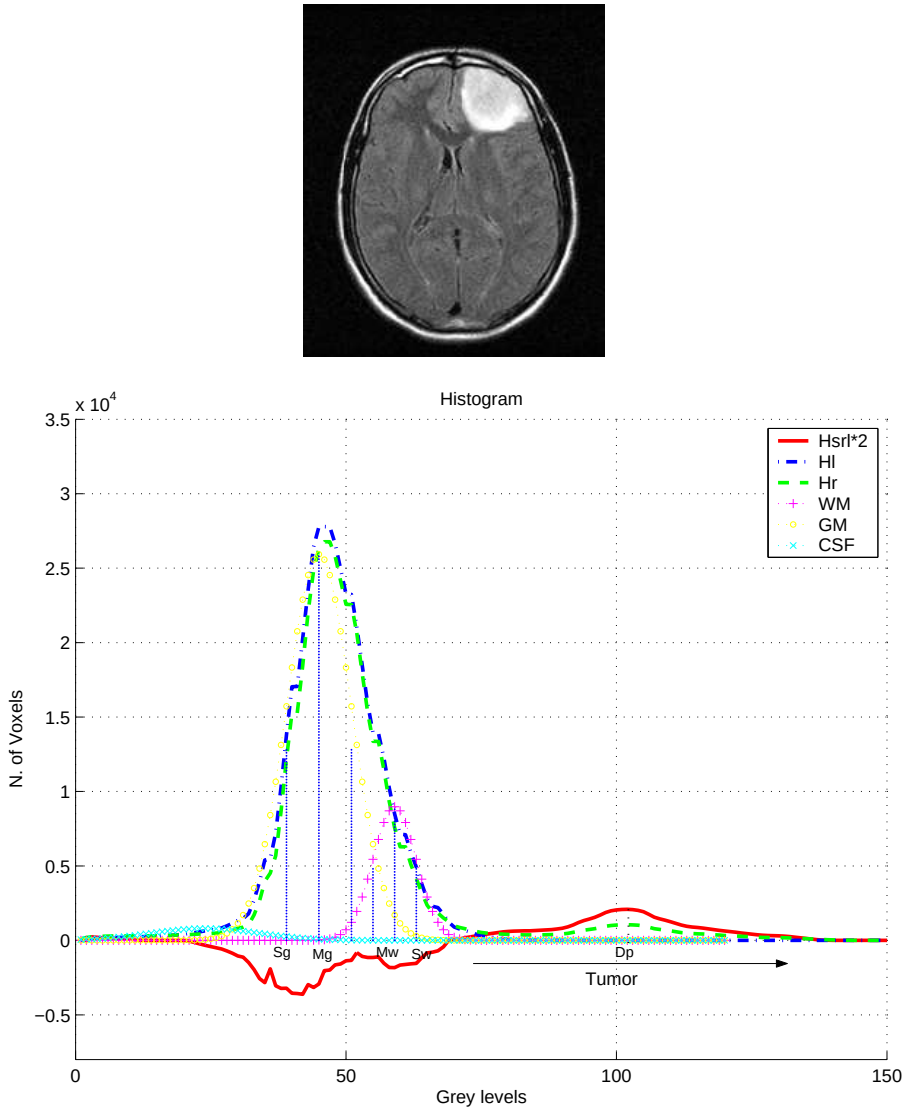

Figure 3.15: Detection of pathological hemisphere in a FLAIR image. Here $M_g = 49$, $\sigma_g = 7$, $M_w = 61$, $\sigma_w = 4$, $S_P = 70$, $E_P = 144$ and $D_P = 104$ (for visualization purposes $\mathbf{H}_{slr}$ is multiplied by 2).

Data Set	Volume (voxel)	Hemi.	M_g	σ_g	M_w	σ_w	S_p	E_p	D_p	Hemi. Detected.
F1	25499.5	R	56	12	67	4	66	151	88	R
F2	17564.8	L	56	9	66	4	73	111	87	L
F3	133545.0	R	52	8	65	7	66	146	83	R
F4	110847.0	R	45	7	55	7	66	108	81	R
F5	53885.2	L	58	5	64	5	91	149	113	L
F6	48046.7	R	49	7	61	4	70	144	104	R
F7	34021.5	L	47	4	55	4	53	130	68	L
F8	76638.8	R	30	8	52	7	72	139	104	R
F9	38672.7	R	56	10	76	8	91	170	136	R
F10	55379.0	R	46	4	61	4	73	151	118	R

Table 3.2: Result of pathological hemisphere detection in FLAIR images. Here R and L denote right and left respectively.

CHAPTER 4

Brain tumor segmentation: part II, segmentation

4.1 Introduction

The second section of our framework is the segmentation. The input consists of the preprocessed images (reduced noise, registered and segmented brain) and some information on the tumor provided by the preprocessing section.

As we surveyed in Chapter 2, region-based methods exploit only local information for each voxel and do not incorporate global shape and boundary constraints. But they have a high level of automation. On the other hand, boundary-based models suffer from the difficulty of determining the initial contour, tuning the parameters and leakage in ill-defined edges. But they perform a good segmentation in the border of objects. In this chapter we propose a method that is a combination of region-based and contour-based paradigms. It works in 3D and is generally enough to segment a large range of tumors in any modality of MR images. To provide an initial detection of the tumor we propose two methods. The first one is a fuzzy classification method that is applicable to hyperintense tumors while the second one is based on symmetry analysis and applies to any type of tumor. The aim of the detection approach is to roughly locate the tumor automatically. This does not provide an accurate estimation of its boundaries and we therefore propose a refinement step. This is achieved through a parametric deformable model constrained by spatial relations.

This chapter is organized as follows: in Section 4.2 we provide an overview of the proposed method. Section 4.3 describes two new methods for detection and initial segmentation of tumors. In Section 4.4 a method to refine the segmentation using edge information and constrained by spatial relations is presented. Segmentation of edema and necrosis are explained in Section 4.5. Section 4.6 presents some results and discussions and finally in Section 4.7 some conclusions are given.

4.2 Method overview

The automated segmentation method that we have developed is composed of two phases: initialization and refinement, as shown in Figure 4.1. In the first phase, we detect and initially segment the tumor or edema. To perform this operation, within the brain, the tumor or edema is detected and initially segmented using a fuzzy classification method or symmetry analysis and some morphological operations. The first method relies on the assumption that the tumor or edema appears in the image with specific gray levels, corresponding to an additional class. The second method relies on the assumption that the brain is roughly symmetrical in shape, and that tumors or edemas can be detected as areas that deviate from the symmetry assumption when looking at gray levels. This detection provides the initialization for a more precise segmentation step, performed in the second stage, using a parametric deformable model constrained by fuzzy spatial relations. This allows representing explicitly relations between the tumor or edema and surrounding tissues, thus reinforcing the robustness of the method.

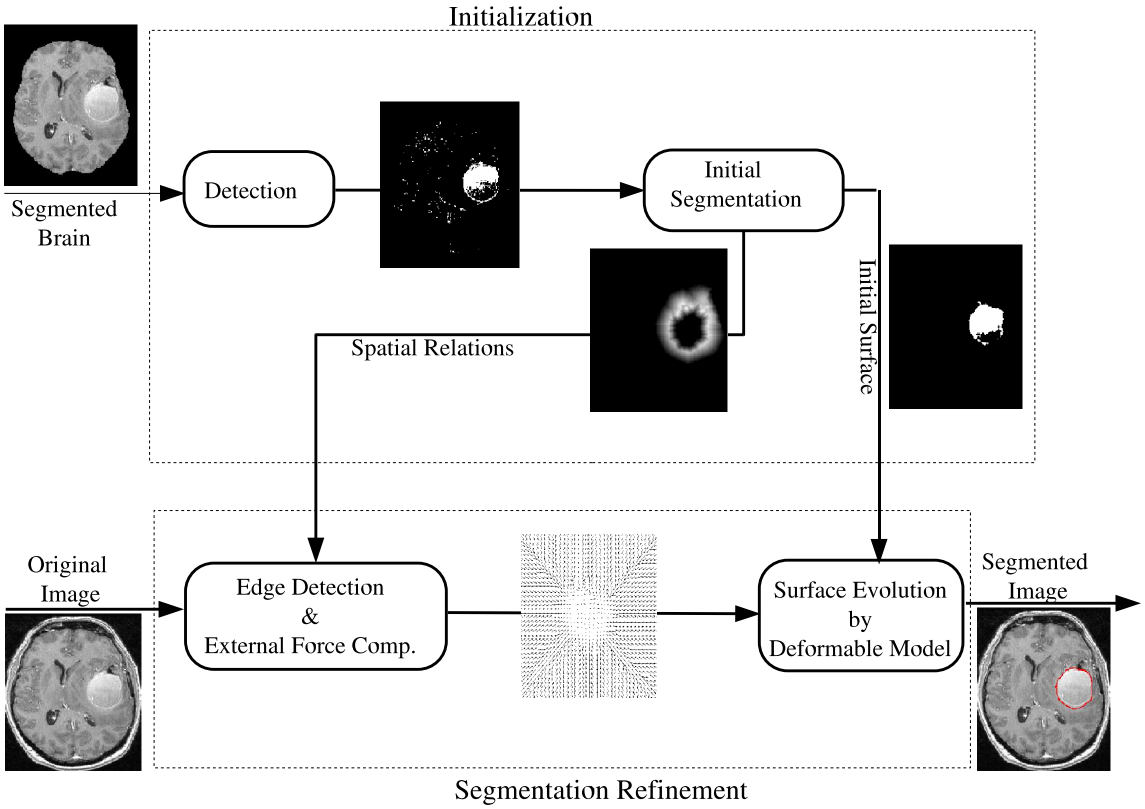

Figure 4.1: The segmentation method diagram.

Several sources of imprecision are taken into account in the proposed method. Imprecision is inherently present in the images, due to the observed phenomenon itself (imprecise limits of pathological areas for instance), to the acquisition system and

the numerical reconstruction process (leading to spatial and intensity imprecisions). Moreover, available knowledge is also prone to imprecision. For instance we exploit the constant order of the gray levels of the main brain tissues, but the exact range of values of each tissue is imprecise. We will also make use of spatial relations, expressed in linguistic form, such as "near the tumor", which cannot be modeled in a precise way. All these reasons justify the use of fuzzy models in several steps of the proposed approach (fuzzy classification based on gray levels, models of spatial relations).

4.3 Detection and initial segmentation

We now describe the initial segmentation of the tumor, for which we propose two methods: the first one relies on a fuzzy classification and the second one is based on symmetry analysis.

4.3.1 Detection by modified PFCM

Here, our aim is to propose an automatic method for detection and initial segmentation of brain tumors. The proposed method is based on an unsupervised classification (clustering), because this type of classification does not require user interaction, learning or prior models and hence it can be automated easily. The proposed method uses membership, possibility (typicality) and neighborhood information to classify each pixel/voxel by combining the fuzzy c-mean (FCM), possibilistic c-mean (PCM) and mean filter algorithms.

Classification by membership and typicality

Clustering is the partitioning of unlabeled data set $X = \{x_1, x_2, ..., x_n\} \subset \mathbb{R}^p$ into $1 < c < n$ classes, by assigning labels to the vectors in X. A c-partition of X is a set of (cn) values u_{ik} that can be represented as a $(c \times n)$ matrix $U = [u_{ik}]$ [Pal et al., 2005]. The value u_{ik} denotes the membership degree of sample x_k to class i.

One of the most widely used clustering methods is the FCM algorithm. The FCM algorithm assigns memberships to x_k which are related to the relative distance of x_k to the c points prototypes $V = \{v_i\}$ that are class centers in the FCM.

FCM algorithm has some problems that have limited its application. The main one is that the membership functions are not decreasing with respect to the distance to the class center. To overcome this problem, a new clustering method named possibilistic c-mean (PCM) was proposed by [Krishnapuram and Keller, 1993]. In this algorithm the objective function is modified and the normalization constraint, $\sum_{i=1}^{c} u_{ik} = 1, \forall k$, is

not considered and each element of k'th column can be any number between 0 and 1 (at least one of them is non zero). The authors named the value u_{ik} as typicality (typicality of x_k relative to cluster i). In fact each row of U is a possibility distribution over X. However this algorithm also has some problems. It is very sensitive to initialization and sometimes coincident clusters will occur. In addition it is very sensitive to additional parameters in this model.

To address the problems of FCM and PCM a new fuzzy possibilistic c-mean (FPCM) algorithm was proposed in [Pal et al., 1997] by combining these two algorithms. In data classification, both membership and typicality are mandatory for data structures interpretation and FPCM computes these two factors simultaneously. FPCM solves the noise sensitivity defect of FCM and overcomes the problem of coincident clusters of PCM. The objective function of FPCM is written as:

$$J_{m,\eta}(U,T,V;X) = \sum_{i=1}^{c}\sum_{k=1}^{n}(u_{ik}^{m} + t_{ik}^{\eta})D_{ik} \tag{4.1}$$

where $m > 1$, $\eta > 1$, $0 \leq u_{ik} \leq 1$, $0 \leq t_{ik} \leq 1$, $\sum_{i=1}^{c} u_{ik} = 1$, $\forall k$, $\sum_{k=1}^{n} t_{ik} = 1$, $\forall i$ and $D_{ik} = \|x_k - v_i\|^2$ ($\|.\|$ is any inner product norm). Here $T = [t_{ik}]$ is the typicality matrix.

Although FPCM is less prone to the problems of FCM and PCM, in the case of a large data set this algorithm does not work properly (it operates such as FCM), because FPCM normalizes the possibility values, so that the sum of typicality of all data points in each row of U is one. Hence the typicality values are very small in large data sets.

PFCM

[Pal et al., 2005] proposed a new algorithm for data clustering that is named possibilistic fuzzy c-mean (PFCM). In this algorithm the constraint of the typicality values ($\sum_{k=1}^{n} t_{ik} = 1$, $\forall i$) has been relaxed to overcome the problem of FPCM. The objective function of PFCM is written as:

$$J_{m,\eta}(U,T,V;X) = \sum_{i=1}^{c}\sum_{k=1}^{n}(au_{ik}^{m} + bt_{ik}^{\eta})D_{ik} + \sum_{i=1}^{c}\gamma_i\sum_{k=1}^{n}(1-t_{ik})^{\eta} \tag{4.2}$$

where $\sum_{i=1}^{c} u_{ik} = 1$, $\forall k$, $0 \leq u_{ik}, t_{ik} \leq 1$ and $a > 0$, $b > 0$, $\gamma_i > 0$, $m > 1$, $\eta > 1$ are user defined constants. The relative importance of fuzzy membership u_{ik} (as in FCM) and typicality t_{ik} (as in PCM) in the objective function are defined by the constants a and b. If $a = 1$, $b = 0$ and $\gamma_i = 0, \forall i$, PFCM reduces to FCM and if $a = 0$ and $b = 1$, it reduces to PCM. In [Krishnapuram and Keller, 1993] the following equation is suggested to compute γ_i:

$$\gamma_i = K \frac{\sum_{k=1}^{n} D_{ik}}{\sum_{k=1}^{n} u_{ik}^m}, K > 1 \tag{4.3}$$

PFCM algorithm overcomes the problems of PCM and FCM and functions properly on large data sets. It can easily be seen from Equation (4.2) that the objective function of PFCM does not take into account any spatial information. Hence, it is sensitive to noise and intensity inhomogeneity, and its application for real MR image classification is very limited.

MPFCM

Recently, approaches have been proposed by modifying the objective function to increase the robustness of FCM to noise [Liew and H. Yan, 2003], [Pham, 2001], [Ma and Staunton, 2007], [Ahmed et al., 2002], [Feng and Chen, 2004] and [Shen et al., 2005].

In [Liew and H. Yan, 2003] the distance is weighted by a term based on the difference between the membership values of pixels in the neighborhood of the pixel. [Pham, 2001] modified the objective function to discourage undesirable configurations according to the neighborhood of the pixels. In [Ahmed et al., 2002], [Shen et al., 2005] and [Ma and Staunton, 2007] a term is added to the objective function that allows the labeling of a pixel to be influenced by the labels in its immediate neighborhood. In the proposed methods the objective function is modified to make the algorithm to be indirectly similar to the Markov random field (MRF). [Feng and Chen, 2004] proposed a modified FCM based on Markov and Gibbs random field theory. A spatial context constraint based on Gibbs random field is added to the objective function.

Here we propose a new algorithm (modified PFCM (MPFCM)) which uses both the information of voxels and their neighborhoods (inspired from Markov Random Fields (MRF)), membership and typicality for classification. We modify Equation (4.2) by adding a term that allows the labeling of a data point being influenced by its immediate neighborhood. The added neighborhood term is similar to the one which is used in modified FCM (MFCM) [Ahmed et al., 2002] to incorporate the neighborhood effects in the classic FCM (similar terms are also used in [Ma and Staunton, 2007] and [Shen et al., 2005]):

$$\sum_{i=1}^{c} \sum_{k=1}^{n} (a u_{ik}^m + b t_{ik}^\eta) S_{ik} \tag{4.4}$$

Here $S_{ik} = \sum_{w=1}^{n_w} \|x_w - v_i\|^2$ where x_w is a neighbor pixel/voxel of x_k in a window around x_k and n_w is the number of neighbors in this window.

The sum of Equations (4.2) and (4.4) is the objective function of the proposed method:

$$J_{m,\eta}(U,T,V;X)=\sum_{i=1}^{c}\sum_{k=1}^{n}(au_{ik}^{m}+bt_{ik}^{\eta})D_{ik}+\sum_{i=1}^{c}\gamma_i\sum_{k=1}^{n}(1-t_{ik})^{\eta}+\beta\sum_{i=1}^{c}\sum_{k=1}^{n}(au_{ik}^{m}+bt_{ik}^{\eta})S_{ik} \tag{4.5}$$

The relative importance of the added term (neighborhood effect) is controlled by β (β can be written as $\frac{\alpha}{n_w}$). If $m>1$ and $\eta>1$ then the objective function will be minimized for (the proof can be found in Appendix A):

$$u_{ik}=\sum_{j=1}^{c}\left(\frac{D_{ik}+\beta S_{ik}}{D_{jk}+\beta S_{jk}}\right)^{\frac{1}{1-m}},1\leq i\leq c,1\leq k\leq n \tag{4.6}$$

$$t_{ik}=\frac{1}{1+\left(\frac{b}{\gamma_i}D_{ik}+\beta S_{ik}\right)^{1/(\eta-1)}},1\leq i\leq c,1\leq k\leq n \tag{4.7}$$

$$v_i=\frac{\sum_{k=1}^{n}\left(au_{ik}^{m}+bt_{ik}^{\eta}\right)\left(x_k+\beta R_k\right)}{(1+\alpha)\sum_{k=1}^{n}\left(au_{ik}^{m}+bt_{ik}^{\eta}\right)},1\leq i\leq c \tag{4.8}$$

where $R_k=\sum_{w=1}^{n_w}x_w$.

In summary, the MPFCM algorithm can be written as:

1. select initial prototypes $V=\{v_i\}_{i=1}^{c}$
2. update the membership matrix using Equation (4.6).
3. update $\Gamma=\{\gamma_i\}_{i=1}^{c}$ using Equation (4.3).
4. update the typicality matrix using Equation (4.7).
5. update the prototypes using Equation (4.8).
6. repeat 2-5 until termination. The termination criterion is as follows:

$$\|V_{new}-V_{old}<\|\epsilon \tag{4.9}$$

where $\|.\|$ is the Euclidean distance norm and ϵ is a small number, to be set by the user.

Evaluation of MPFCM

We have applied the proposed method to 3D simulated T1-weighted MR data with different levels of Gaussian noise [Cocosco et al., 1997]. The volume dimension is $181 \times 217 \times 181$ and the voxel size is $1 \times 1 \times 1 mm^3$.

The classification results into 4 classes (background, CSF, WM, GM) obtained by FCM, FPCM, PFCM, MFCM (the neighborhood term is added to FCM [Ahmed et al., 2002]) and the proposed MPFCM are shown in Figure 4.2. The used image was corrupted with 9% Gaussian noise. The results can be compared with the reference segmented image that was obtained from a non noise corrupted image. In all algorithms, the initial values of prototypes are the same. These images show that the proposed method removes the noise and classifies the voxels correctly. In comparison with MFCM, our algorithm performs better, especially at the border of tissues.

The evaluation of the classification results was performed through a quantitative comparison with the results of the reference segmented image. We used the classification accuracy measure to evaluate the results, which is:

$$C_A = \frac{Nc}{N_t} \times 100\% \tag{4.10}$$

where N_c is the number of correct classified voxels and N_t is the total number of voxels.

The quantitative results obtained with different algorithms are provided in Table 4.1 for four images with different levels of Gaussian noise. As seen in Table 4.1 and Figure 4.3 when the noise is low, the difference between the classification accuracies of the algorithms is low. When the noise increases, the difference between classification accuracies is increased, and the MFCM and MPFCM perform better than the other algorithms. For example the difference between the C_A of FCM and MPFCM in the image with 3% noise is about 1, while for the image with 9% noise, it is about 10. Also when the noise is increased MPFCM performs better than MFCM. This shows that in addition to membership and neighborhood information, the typicality is also important and can improve the accuracy of classification.

Figure 4.4 shows the comparison of iteration convergence of FCM, MFCM and MPFCM. It shows that MFCM converges faster than FCM because of neighborhood information and MPFCM converges faster than these two algorithms because of the typicality and neighborhood information. The computation time for segmentation of a 3D simulated image for FCM, MFCM and MPFCM algorithms is about 30 second, 11 minutes and 6.5 minutes respectively (on a PC Pentium IV 2 MHz). If we change the initialization method, for example by using the final result of FCM or by predicting the class centers by histogram analysis, the computation time will be decreased to about 1 minute for MPFCM algorithm.

Setting the parameters of MPFCM (a, b, β) with proper values is important. The parameter β controls the neighborhood effect and it should be selected high enough

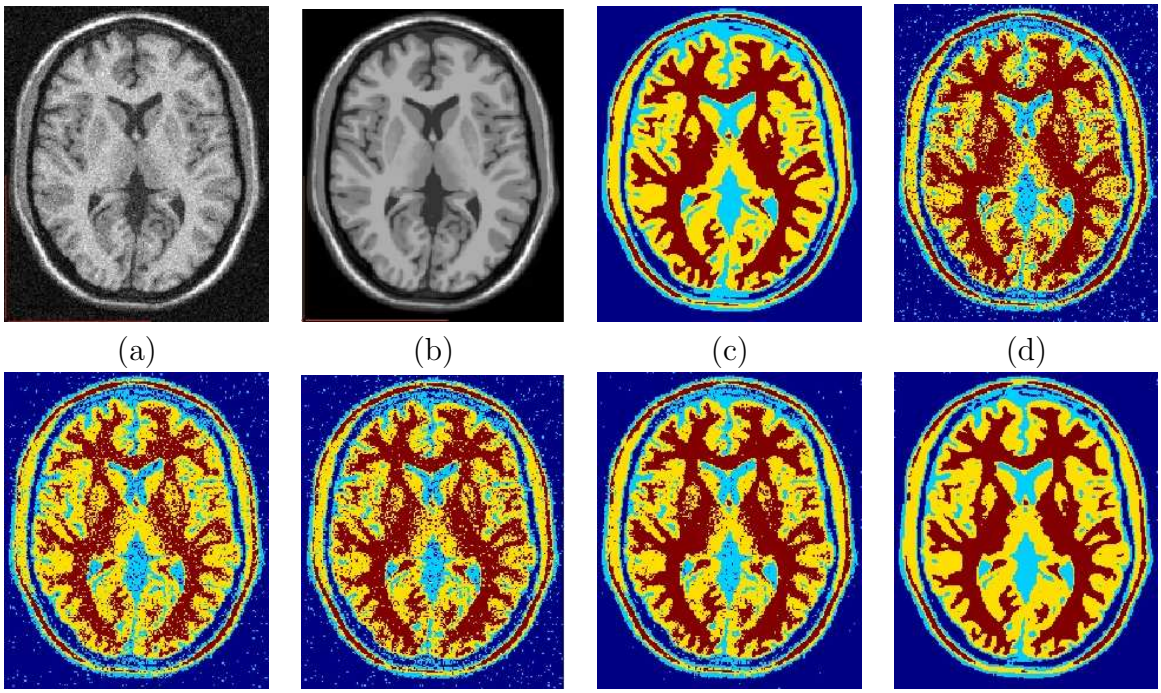

Figure 4.2: Comparison of classification results (into 4 classes) on a 3D simulated MR image corrupted with 9% Gaussian noise. (a) One axial slice of the original image with 9% Gaussian noise. (b) Original image without noise. (c) Reference segmented image. (d) Result of the FCM algorithm. (e) Result of FPCM. (f) Result of PFCM classification. (g) Classification by MFCM. (h) Result of proposed MPFCM algorithm. Here we set the parameters $\alpha = 0.85$ (such as in [Ahmed et al., 2002]), $m = 1.5$ and $n_w = 27$ for MFCM algorithm and $a = 5$, $b = 3$, $\beta = \frac{\alpha}{n_w} = 0.1$, $m = 1.5$ and $\eta = 2$ for MPFCM algorithm. All algorithms were initialized with the same class centers.

for very noisy images. A small value of β converts the MPFCM algorithm to PFCM algorithm. Here we obtained the best results with $\beta = 0.2$ for T1-weighted images and $\beta = 0.1$ for FLAIR images. The parameter a controls the effect of membership and b the effect of typicality. Setting these parameters depends on the type of images and the number of classes. Setting b with a high value compared to a causes the centroid be more influenced by the typicality values than the membership values and a coincidence problem may occur. Conversely using a high value of a with a high value compared to b causes the centroids be more influenced by membership values and it may generate the FCM problems (for the parameters m and η similar effects can also be obtained). In the classification of medical images (T1-weighted and FLAIR) into 5 and 6 classes with $a = 5$ and $b = 3$ we obtained the best results and in the all cases the algorithm converged, but further investigation is required for other images and different numbers of classes.

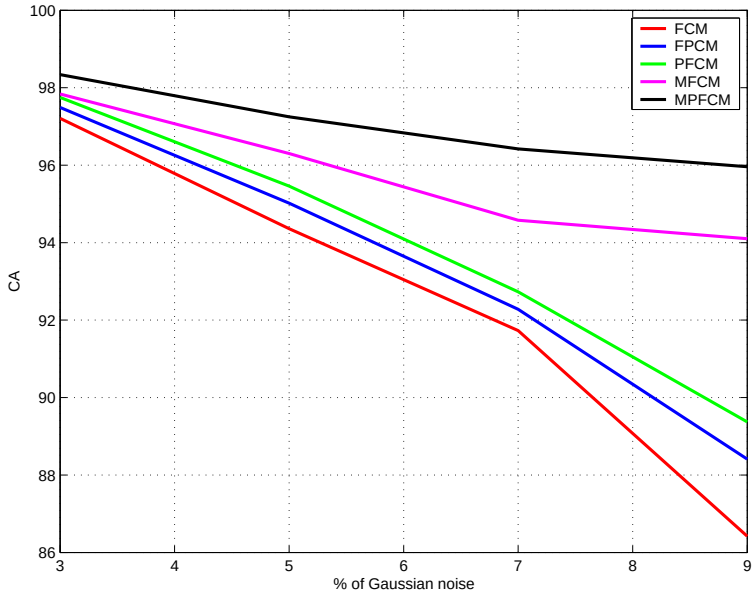

Figure 4.3: Comparison of classification accuracy (C_A) of algorithms.

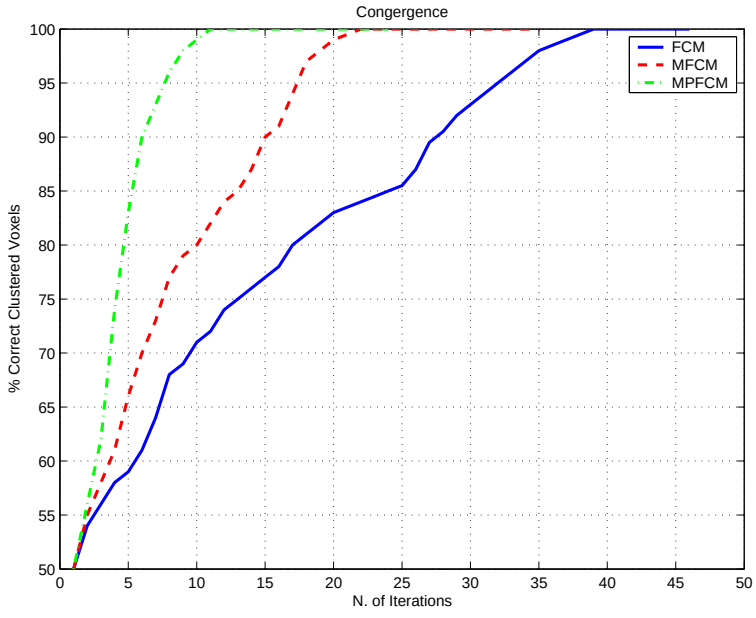

Figure 4.4: Comparison of the convergence of classification algorithms when applied to the simulated 3D MR image without noise (all algorithms were initialized with the same class centers).

Algorithm	Gaussian noise			
	3%	5%	7%	9%
FCM	97.21	94.36	91.73	86.42
FPCM	97.49	95.02	92.28	88.41
PFCM	97.75	95.26	92.53	88.67
MFCM	97.84	96.30	94.78	93.78
MPFCM	98.34	97.25	96.42	95.96

Table 4.1: Quantitative comparison of classification results obtained by different algorithms. The values in the table are the ratio of correct classified voxels (C_A) in 3D simulated MR images with different levels of Gaussian noise.

In summary we have developed a new method for classification of MR images that uses the membership, typicality and neighborhood information. The results show that this method performs better than the other fuzzy clustering algorithms such as FCM, FPCM, PFCM and MFCM and can be a good candidate for detection and initial segmentation of brain tumors in MR images. In the next section we describe how we use this method towards this aim.

MPFCM and tumor detection

To detect tumors, we consider two types of tumors on contrast enhanced T1-weighted images: enhanced (full-enhanced with and without edema and ring-enhanced) and non-enhanced tumors.

In the case of an enhanced tumor we classify the extracted brain into six classes: CSF, WM, GM, edema, tumor and background. To obtain the initial values of the class centers, we use the results of the histogram analysis [Mangin et al., 1998] in the brain extraction step: we define them as the average gray level values of the CSF, WM and GM ($\mathbf{m_C}$, $\mathbf{m_W}$ and $\mathbf{m_G}$, respectively). For the background, the value zero is used. To select the tumor class we assume that the tumor has the highest intensity among the five classes and for edema classes we select a value between CSF and GM (usually edema is hypointense, darker than WM and brighter than CSF) [Khotanlou et al., 2005]. Our proposed method is not very sensitive to initial values and selecting good values for class centers will reduce the computation time.

We applied the MPFCM method to classify contrast enhanced T1-weighted images with enhanced tumor at different locations, with different sizes and shapes. In Figure 4.5, the classification result (into 6 classes) obtained by MPFCM for a relatively large

tumor is compared with FCM, FPCM and MFCM results. In Figure 4.6 and Figure 4.7 the results for a relatively small tumor and a ring enhanced tumor are shown.

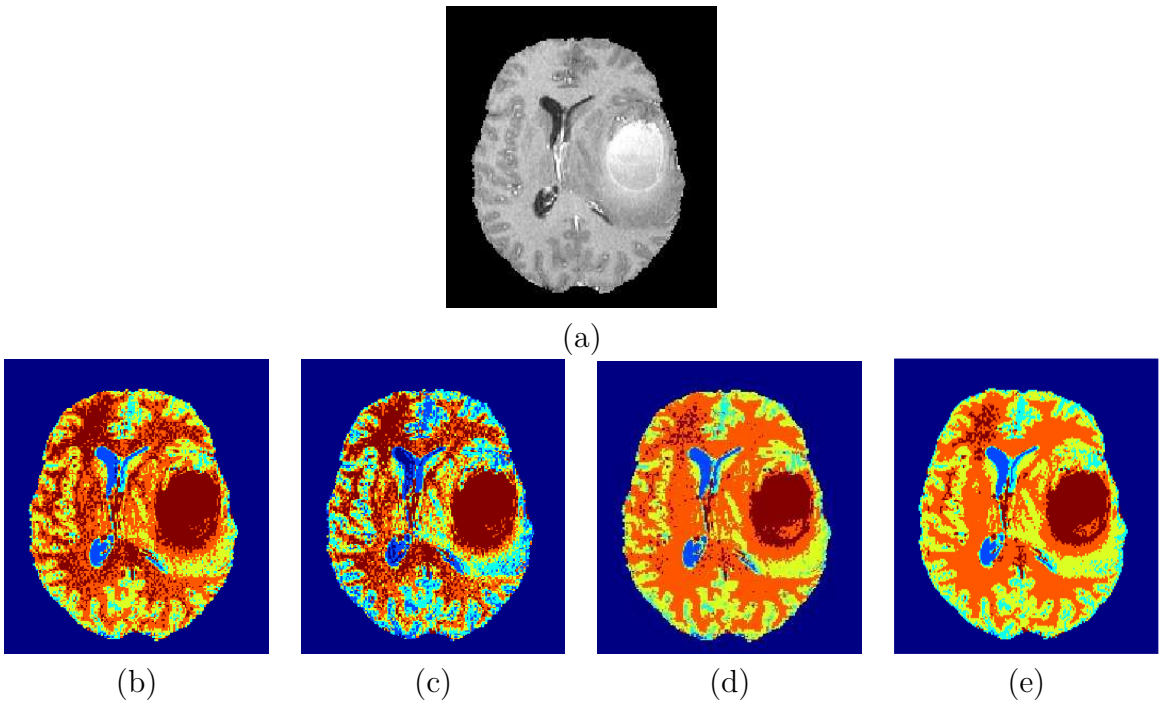

(a) (b) (c) (d) (e)

Figure 4.5: Comparison of classification results (6 classes) obtained by FCM, FPCM, MFCM and MPFCM for a large full-enhanced tumor. (a) One axial slice of the original contrast enhanced T1-weighted image. (b) Result of FCM classification. (c) Result of FPCM. (d) Result of MFCM. (e) Result of MPFCM. Here $a = 5$, $b = 3$, $\beta = 0.2$ and $n_w = 27$ for the MPFCM algorithm.

Because of some classification errors (some other components of brain may take contrast agent (such as vessels) and be seen as hyperintense structures on contrast enhanced T1-weighted images), there are undesired additional voxels in the tumor class. To remove these missclassified components, a connected component analysis is performed, using the 6-connectivity. In the case of a large tumor, the largest component is the tumor but in the case of a small tumor the largest component is not always the tumor. To address this problem, we use the FLAIR image when it is available. Since all tumors appear as hyperintense structures on FLAIR images and other components, which take contrast agent, appear as hypointense ones, we can detect the tumor among the components with a simple comparison with corresponding components in the FLAIR image. In this case we select the regions corresponding to the components from the FLAIR image and calculate the mean intensity of each region. The region which has the maximum mean intensity corresponds to the tumor.

In the case of a non-enhanced tumor, because of a large overlapping between tumor and brain tissues, a correct detection of the tumor is a difficult task. As seen in Figure

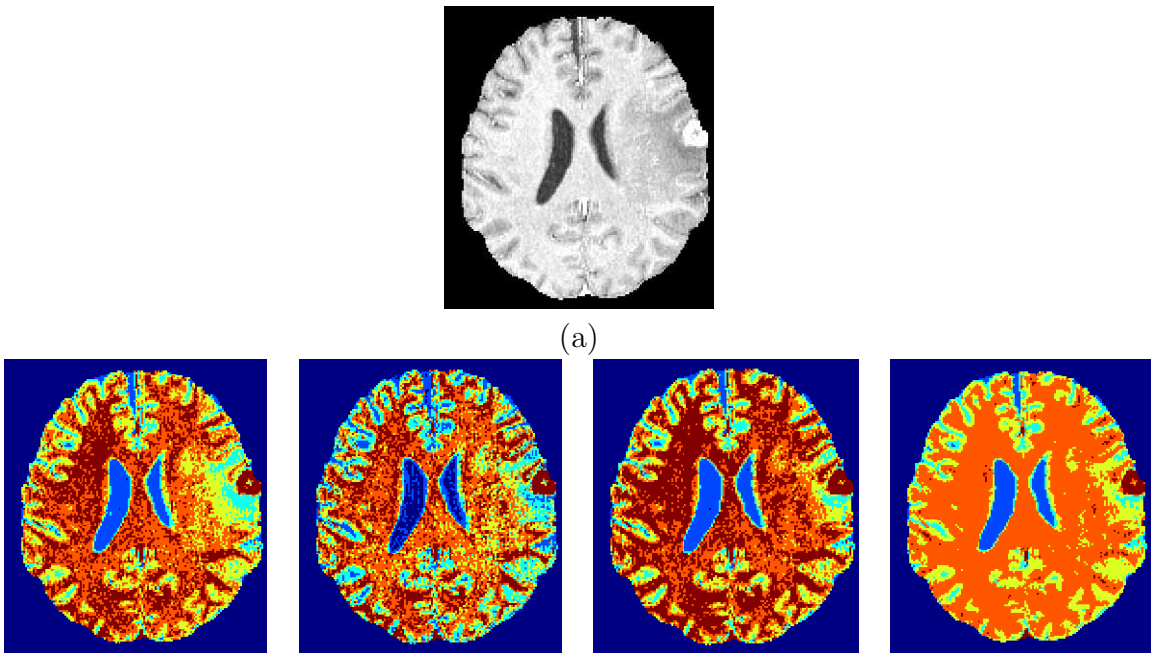

(a) (b) (c) (d) (e)

Figure 4.6: Comparison of classification results obtained by FCM, FPCM, MFCM and MPFCM for a small tumor. (a) One axial slice of the original contrast enhanced T1-weighted image. (b) Result of FCM classification. (c) Result of FPCM. (d) Result of MFCM. (e) MPFCM result. Here $a = 5$, $b = 3$, $\beta = 0.2$ and $n_w = 27$ for the MPFCM algorithm.

4.8 the tumor class has a large overlap with GM and CSF classes even with the MPFCM classification method (note that this image is a good image with low noise). To overcome this problem we can use the FLAIR image. Since non-enhanced tumors have hyperintense appearance on FLAIR images and they have no other components (such as edema and necrosis), we perform the detection step on FLAIR images if available. We classify the FLAIR image into 5 classes (background, CSF, GM, WM and tumor). To initialize the MPFCM algorithm we use the final result of FPCM. In Figure 4.9 a comparison of classification results in a FLAIR image obtained by FCM, FPCM, MFCM and MPFCM is shown. These results show that the MPFCM algorithm can be a good candidate for FLAIR image classification.

Such as in enhanced tumor detection, because of some classification errors there are undesired additional voxels in the tumor class. Again a connected component analysis allows removing these voxels. In the FLAIR image the tumor is large enough and we select the largest component which always coresponds to the tumor.

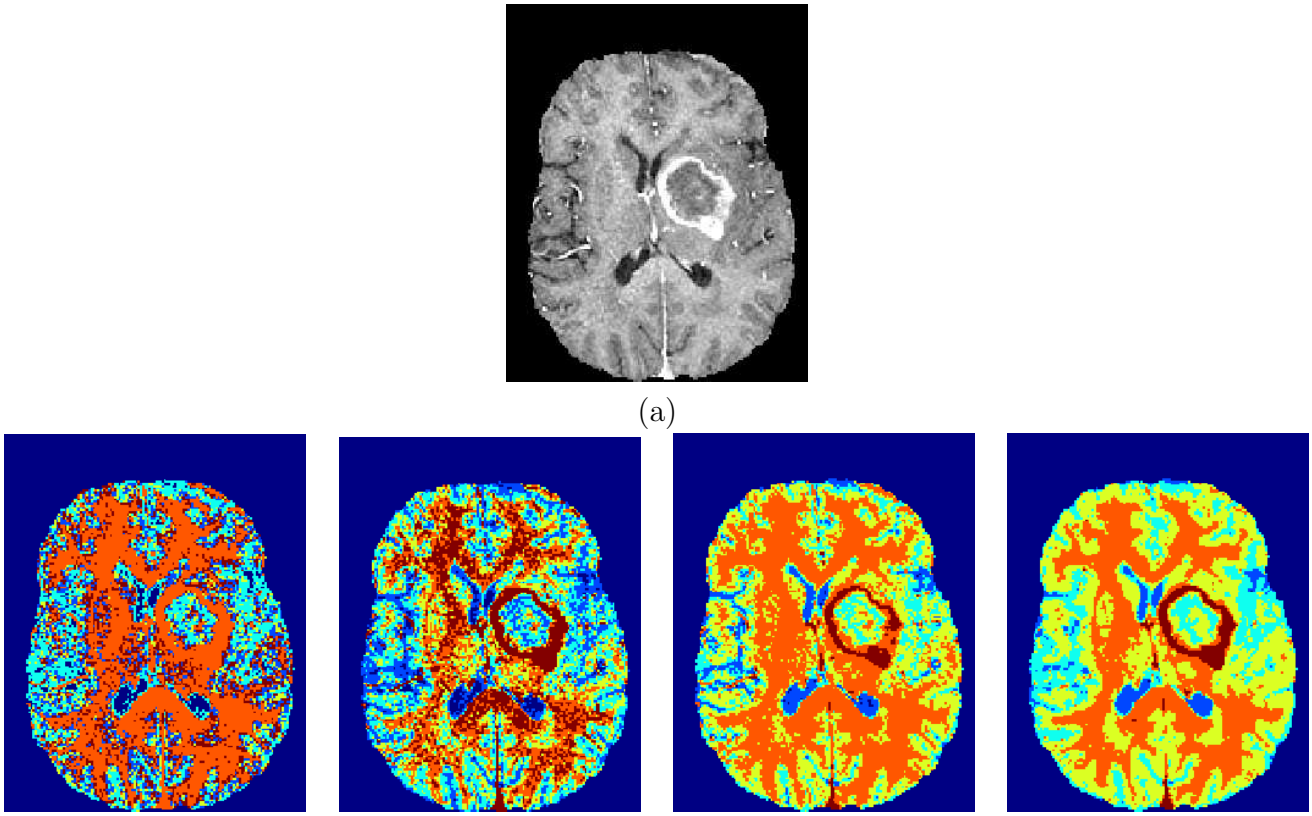

(a) (b) (c) (d) (e)

Figure 4.7: Comparison of classification results (6 classes) obtained by FCM, FPCM, MFCM and MPFCM for a ring-enhanced tumor. (a) One axial slice of the original contrast enhanced T1-weighted image. (b) Result of FCM classification. (c) Result of FPCM. (d) Result of MFCM. (e) Result of MPFCM. Here $a = 5$, $b = 3$, $\beta = 0.2$ and $n_w = 27$ for the MPFCM algorithm.

Evaluation of tumor detection

We have applied this method to 10 3D contrast enhanced T1-weighted images with enhanced tumor at different locations and with different sizes and shapes. The results for 3 images are shown in Figures 4.10, 4.11 and 4.12.

The evaluation of the initial segmentation results was performed through a quantitative comparison with the results of a manual segmentation. Let us denote by M the manually segmented tumor and A the segmented tumor by our method. We used five measures to evaluate the results which are:

- ratio of correct detection: $T_p = \frac{N_{T_p}}{N_M} * 100\%$, where N_{T_p} is the number of true positive voxels and N_M is the cardinality of M;

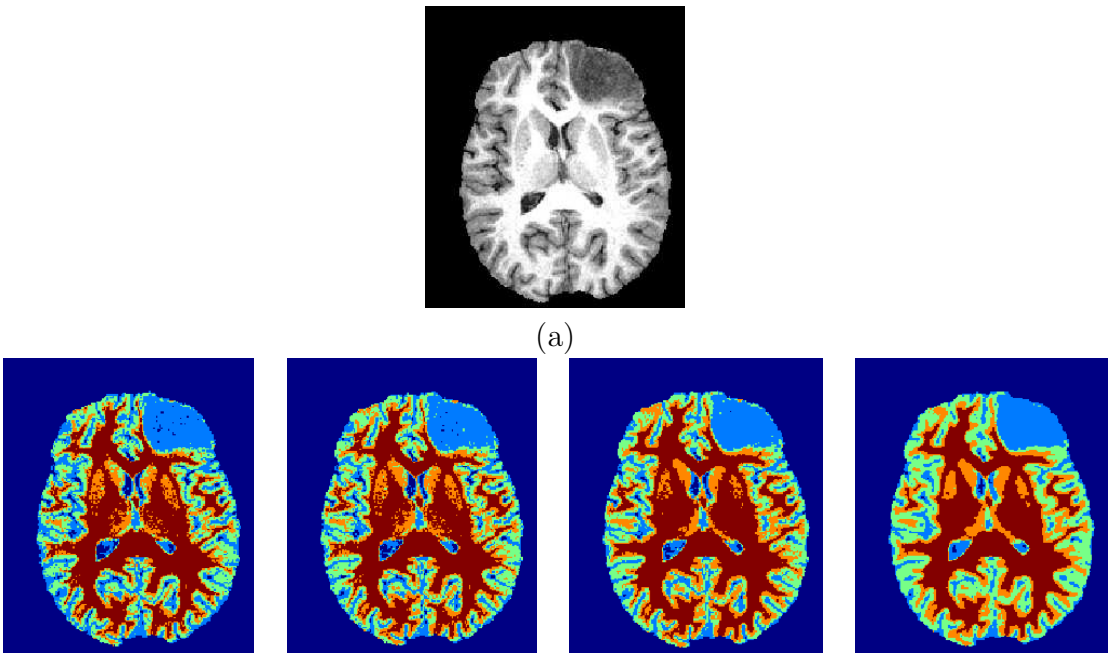

(a) (b) (c) (d) (e)

Figure 4.8: Comparison of classification results obtained by FCM, FPCM, MFCM and MPFCM for a non-enhanced tumor on contrast enhanced T1-weighted image. (a) One axial slice of the original contrast enhanced T1-weighted image. (b) Result of FCM classification into 5 classes. (c) Result of FPCM. (d) Result of MFCM. (e) Result of MPFCM. Here $a = 5$, $b = 3$, $\beta = 0.2$ and $n_w = 27$ for the MPFCM algorithm.

- ratio of false detection: $F_p = \frac{N_{F_p}}{N_A} * 100\%$, where N_{F_p} is the number of false positive and N_A is the cardinality of A;
- similarity index: $S_i = \frac{2N_{T_p}}{N_M + N_A} * 100\%$;
- Jaccard index: $J_i = \frac{N_{T_p}}{N_A + N_M + N_{T_p}} * 100\%$;
- Hausdorff distance between A and M, defined as $D_H = \max(h(M, A), h(A, M))$ where $h(M, A) = \max_{m \in M} \min_{a \in A} d(m, a)$, and $d(m, a)$ denotes the Euclidean distance between m and a (m and a are points of M and A respectively);
- average distance (D_m) between the surfaces of M and A.

The T_p value indicates how much of the actual tumor has been correctly detected, while F_p indicates how much of the detected tumor is wrong. The similarity index S_i and Jaccard index are more sensitive to differences in location. For example, if region A completely includes region M, while M is one half of A, then the T_p value is 100% while the S_i value is 67% an J_i is 50%. Since usually most errors are located at the boundary of the segmented regions, small regions will have smaller S and T_p values than large

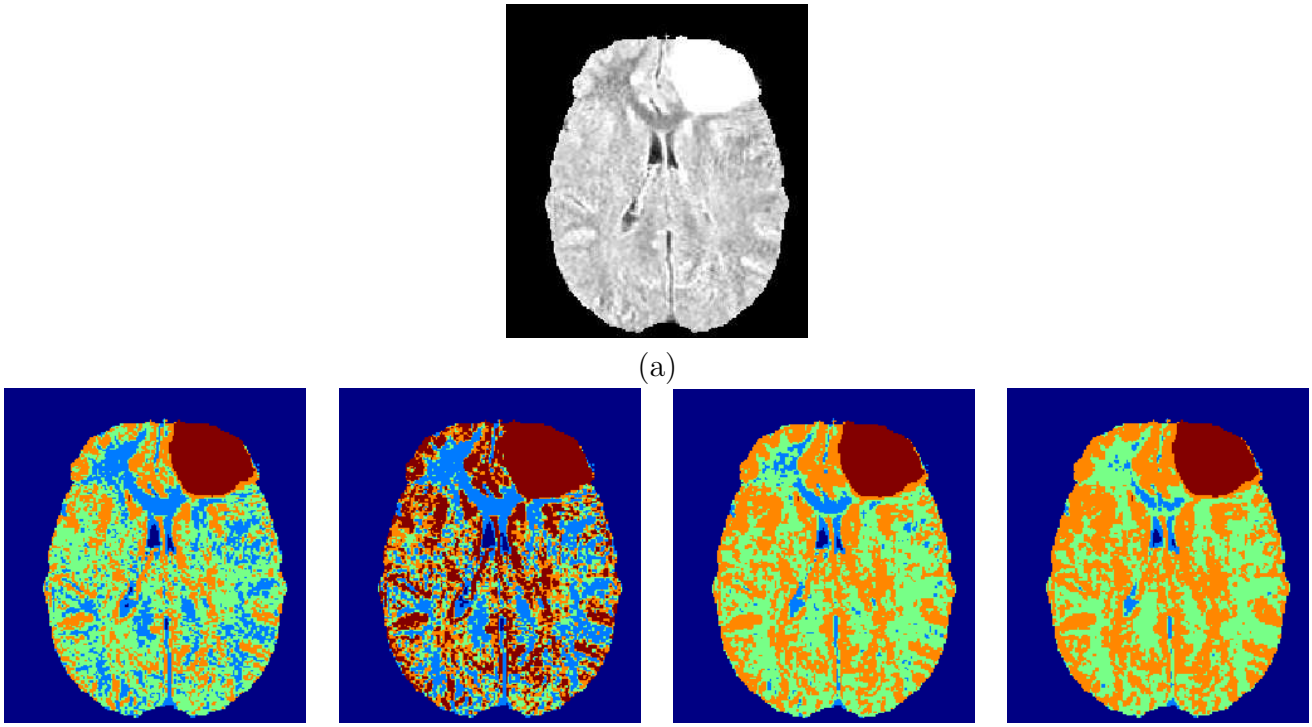

(a) (b) (c) (d) (e)

Figure 4.9: Comparison of classification results obtained by FCM, FPCM, MFCM and MPFCM for a non-enhanced tumor on FLAIR image. (a) One axial slice of the original FLAIR image. (b) Result of FCM classification into 5 classes. (c) Result of FPCM. (d) Result MFCM. (e) Result of MPFCM. Here $a = 5$, $b = 3$, $\beta = 0.1$ and $n_w = 27$ for the MPFCM algorithm.

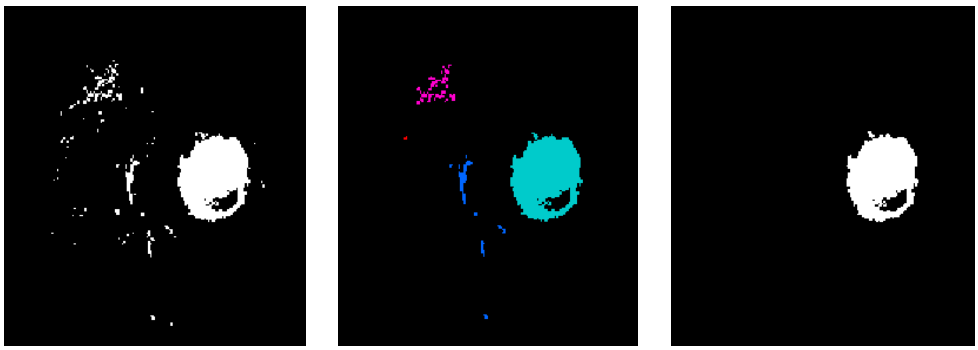

(a) (b) (c)

Figure 4.10: Tumor detection result for a relatively large full-enhanced tumor (Figure 4.5). (a) One axial slice of the selected tumor class. (b) Connected components of the tumor class (the tumor is the largest component). (c) Detected tumor.

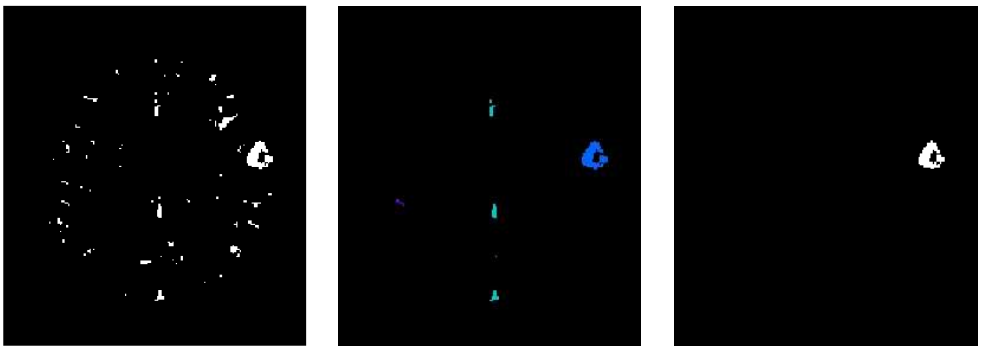

(a) (b) (c)

Figure 4.11: Tumor detection result for a small full-enhanced tumor (Figure 4.6). (a) One axial slice of the selected tumor class. (b) Connected components of the tumor class (here the tumor is the second largest component). (c) Detected tumor.

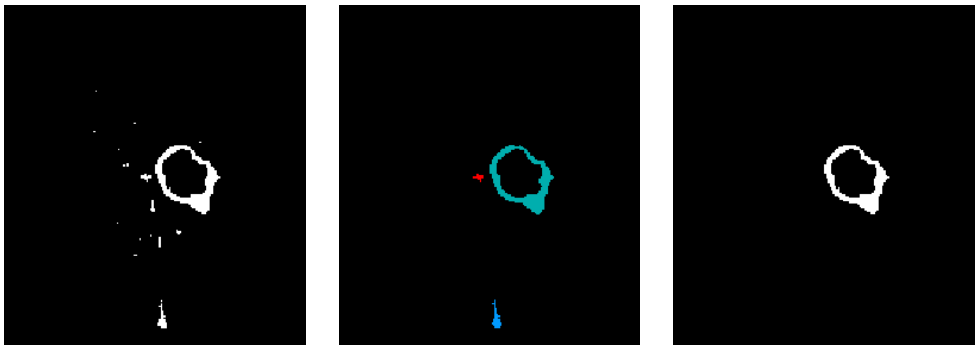

(a) (b) (c)

Figure 4.12: Tumor detection result for a ring-enhanced tumor (Figure 4.7. (a) One axial slice of the selected tumor class. (b) Connected components of the tumor class (here the tumor is the largest component). (c) Detected tumor.

regions. Therefore we also use the average distance and the Hausdorff distance that do not depend on the region size. More details about comparative measures can be found in Appendix B.

The quantitative results obtained by comparing the automatic segmentations with the available manual segmentations are provided in Table 4.2 for 10 cases with enhanced tumor (5 ring-enhanced and 5 full-enhanced). As seen in Table 4.2, the tumor size varies from 2366 mm^3 to 65864 mm^3. The similarity index varies from 75% to 87% with a mean of 80%. The Jaccard index varies from 60% to 78% with a mean of 67% and the correct detection ratio is between 62%-78% with a mean of 68%. The false detection ratio ranges between 0% and 4.7% with an average of 1.3%. To compare the results with other methods, there is not a gold standard, however in comparison with recent works such as [Dou et al., 2007], [Corso et al., 2006], [Prastawa et al., 2004] and

[Cai et al., 2007], where a quantitative evaluation has been done, our results are better than or equal to the ones reported in these works. The false detection ratio illustrates that approximately all of the detected tumor is located within the true tumor and on the other hand the correct detection ratio shows that about 30% of the tumor volume has been not detected. Therefore we can improve the results with deforming the detected tumor toward the true borders of the tumor. This deformation will also improve the surface measures that depend on the quality of the segmentation at the borders. The Hausdorff distance, that is a maximum distance and therefore a particularly severe evaluation, varies from 4.5 mm to 17.4 mm with a mean of 8.1 mm. The mean value of the average distance is about 1.27 mm which is about one voxel.

In the comparison between the full-enhanced and ring-enhanced tumors, it can be observed that the results of full-enhanced tumors are better, because the ring-enhanced tumors have two surfaces (external and internal) and the errors are summed over the two borders.

We believe that the result of initial segmentations can be improved by using a boundary-based method, which will be discussed in the next sections.

(a) (b) (c)

Figure 4.13: Tumor detection result for a non-enhanced tumor in a FLAIR image (Figure 4.9). (a) One axial slice of the selected tumor class. (b) Connected components of the tumor class (the tumor is the largest component). (c) Detected tumor.

We applied the MPFCM algorithm to 10 FLAIR images (with a non-enhanced tumor on CE-T1w image). One of them is illustrated in Figure 4.13. For the FLAIR images the quantitative results also obtained by comparing the automatic segmentations with the available manual segmentations are provided in Table 4.3 for 10 cases. This table shows good results especially in volume metrics but the surface metrics values show that the border of segmentation requires to be improved.

Tumor type	M mm^3	S_i %	J_i %	T_p %	F_p %	D_H mm	D_m mm
TE1	10518.7	84.0	72.2	72.5	0.3	9.24	1.60
TE2	11524.0	87.3	77.5	77.5	0.0	5.83	0.91
TE3	4643.6	75.1	60.1	62.0	4.7	7.61	0.94
TE4	2366.1	76.2	61.6	62.1	1.4	4.56	1.16
TE5	65846.4	84.6	73.3	74.5	2.1	17.37	2.03
Ave.	18979.8	81.5	69.0	69.7	1.7	8.32	1.32
TRE1	43259.5	77.9	63.8	64.1	0.7	10.50	1.35
TRE2	19437.1	75.1	60.2	60.6	1.1	8.50	1.53
TRE3	41833.4	76.7	62.2	62.4	0.5	8.87	1.28
TRE4	13629.2	80.1	67.4	67.8	0.8	5.13	1.12
TRE5	26777.3	83.8	72.1	73.0	1.6	6.60	1.03
Ave.	28987.3	78.7	65.1	65.6	0.9	7.92	1.26
Ave. total	23983.6	80.1	67.1	67.7	1.3	8.12	1.29

Table 4.2: Evaluation of the initial segmentation results of enhanced tumors (full and ring) by MPFCM on a few 3D CE-T1w images for which a manual segmentation was available (M denotes the manually segmented tumor, TE the full-enhanced and TRE the ring-enhanced tumor).

Summary

Here we proposed a new and automatic method for classification and segmentation of medical images relying on fuzzy sets theory which uses membership, typicality and neighborhood information. We then applied it to detect and segment tumors on CE-T1w and FLAIR images. The quantitative results illustrate that this method performs relatively well, but it can be improved by refining the results at the border of the segmented objects. In the next section we present a boundary based method to improve and refine the results.

Tumor type	M mm^3	S_i %	J_i %	T_p %	F_p %	D_H mm	D_m mm
F1	22851.7	79.5	65.9	67.0	2.3	8.00	0.90
F2	25499.5	81.7	69.1	70.2	2.2	7.76	1.00
F3	110338.0	82.8	70.6	71.3	1.3	18.00	2.28
F4	119415.6	82.8	70.7	71.7	2.0	14.03	1.53
F5	57634.7	84.7	73.5	77.0	5.9	10.87	1.40
F6	47342.3	87.4	77.6	80.7	4.6	13.44	1.53
F7	41378.0	92.1	85.4	89.8	5.4	6.50	0.80
F8	78887.0	84.0	72.4	74.5	3.7	14.04	1.66
F9	37971.4	86.3	75.9	77.2	2.1	13.19	1.73
F10	57769.2	87.9	78.5	78.8	0.6	14.74	1.65
Ave.	59908.8	85.0	74.0	75.8	3.0	14.51	1.45

Table 4.3: Evaluation of the segmentation results of tumors by MPFCM on a few 3D FLAIR images for which a manual segmentation was available (M denotes the manually segmented tumor).

4.3.2 Tumor detection by symmetry analysis

To overcome the lack of generality of the previous method in tumor segmentation, we suggest another approach, using the approximate symmetry plane [Khotanlou et al., 2007b;c]. In Section 3.3.5 we used this method to extract some information on image and tumor, here we use it to detect and segment tumors in any type of MR image modalities. First of all we explain the method for detection on contrast enhanced T1-weighted images and we will then extend it to other types of images.

Let $\mathbf{H}_n(x)$ denote the histogram of gray levels in the normal hemisphere and $\mathbf{H}_p(x)$ the histogram in the pathological hemisphere. The histogram difference $\mathbf{H}_s(x) = \mathbf{H}_p(x) - \mathbf{H}_n(x)$ provides useful information about new intensity classes induced by the tumor. By detecting, analyzing and interpreting the occurred peaks in $\mathbf{H}_s(x)$ we can extract the tumor from the brain.

To detect the peaks we apply the algorithm presented in Section 4.3.2 and to analyze and interpret the peaks, we consider the proposed classification of tumors in Chapter 1: non-enhanced tumors, full-enhanced tumors without edema, full-enhanced

tumors with edema and ring enhanced tumors.

Non-enhanced tumors

In the case of a non-enhanced tumor (as in Figures 4.14 and 4.15) a positive peak can be observed between CSF and GM in $\mathbf{H}_s(x)$ that shows the tumor intensity range. In this case the tumor naturally decreases the volume of the GM and WM, hence a negative peak can be seen after the tumor peak. When the tumor moves the ventricles toward the normal hemisphere or is located in the border of the brain, a negative peak will be observed before the tumor peak (in CSF), as illustrated in Figure 4.15. To extract the tumor from the brain we use a simple thresholding. We set the low value of threshold to $T_l = S_{P_t}$ and the high value to $T_h = E_{P_t}$, where P_t represents the tumor peak. When an overlap exists between the tumor peak and the GM mode or CSF mode, i.e $E_{P_t} > M_g - \frac{1}{2}\sigma_g$ or $S_{P_t} < M_c + \frac{1}{2}\sigma_c$, the extraction will be difficult. To address this problem we limit the threshold values according to:

- if $E_{P_t} > M_g$ then $T_h = M_g - (\frac{1}{2}\sigma_g)$
- if $S_{P_t} < M_c$ then $T_l = M_c + (\frac{1}{2}\sigma_c)$

These limitations may cause some tumor voxels be removed but in the refinement step they will be added again.

To illustrate the influence of a non-enhanced tumor on the histogram of the normal hemisphere, pathological hemisphere and the difference of histograms, we added a simulated tumor in the right hemisphere of a normal image. Figure 4.14 shows the result for this simulation.

The negative peak can also provide some information about the tumor which can be used in the segmentation process. Since the presence of a tumor decreases the volume of tissues in which the tumor is located, hence the negative peak illustrates the tissues which surround the tumor. Thus with a thresholding we can obtain the tissues around the tumor as seen in Figure 4.15.

Full-enhanced tumors without edema

In this case a peak appears after the WM mode. The tumor usually decreases the WM and GM volumes and consequently a negative peak will appear within the WM and GM modes. When the tumor deforms the structures largely and moves the ventricles or appears at the border of the brain, a negative peak will also be created in the CSF mode. To extract the tumor from the brain, a thresholding, with $T_l = S_{P_t}$ and $T_h = E_{P_t}$, is used. An overlap between the tumor peak and the WM mode can be

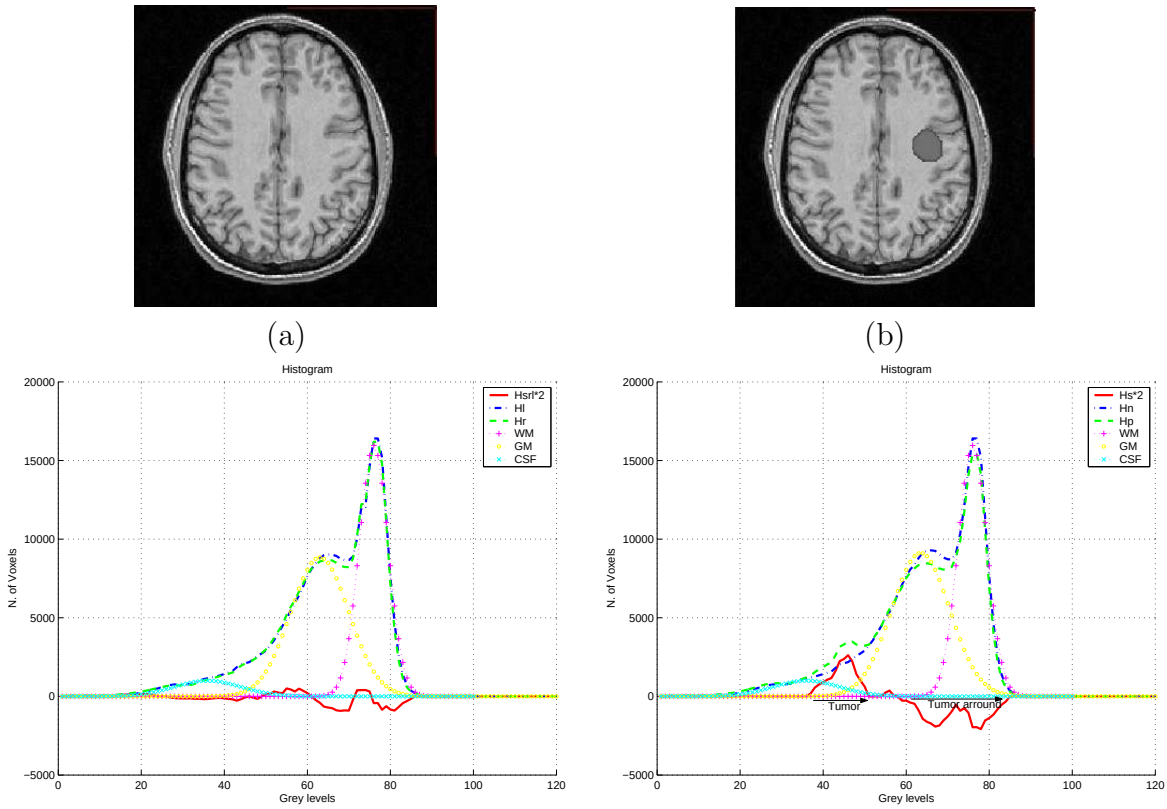

Figure 4.14: (a),(c) A normal image and the graph of $\mathbf{H}_{srl}$, $\mathbf{H}_l$, $\mathbf{H}_r$, WM, GM and CSF for this image. (b),(d) A pathological image (a non enhanced tumor about 8000 voxels ($2 \times 2 \times 2 \times cm$), which has a normal distribution of gray levels (45 ± 4), has been added to the normal image) and the graph of $\mathbf{H}_s$, $\mathbf{H}_n$, $\mathbf{H}_p$, WM, GM and CSF for

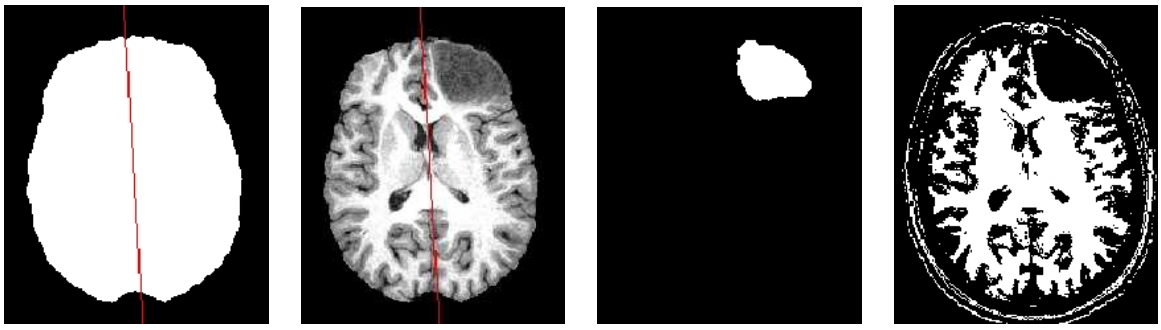

Figure 4.15: (a) Symmetry plane superimposed on the brain mask. (b) Symmetry plane superimposed on the segmented brain. (c) Extracted tumor after morphological operations. (d) Tissues around the tumor (graph of $\mathbf{H}_s$, $\mathbf{H}_n$ and $\mathbf{H}_p$ are shown in Figure 3.14).

observed. Although this rarely occurs, to overcome this problem we apply the following limitation:

- if $S_{P_t} < M_w + 2\sigma_w$ then $T_l = M_w + 2\sigma_w$

We also threshold the negative peak gray levels range to extract the tissues around the tumor.

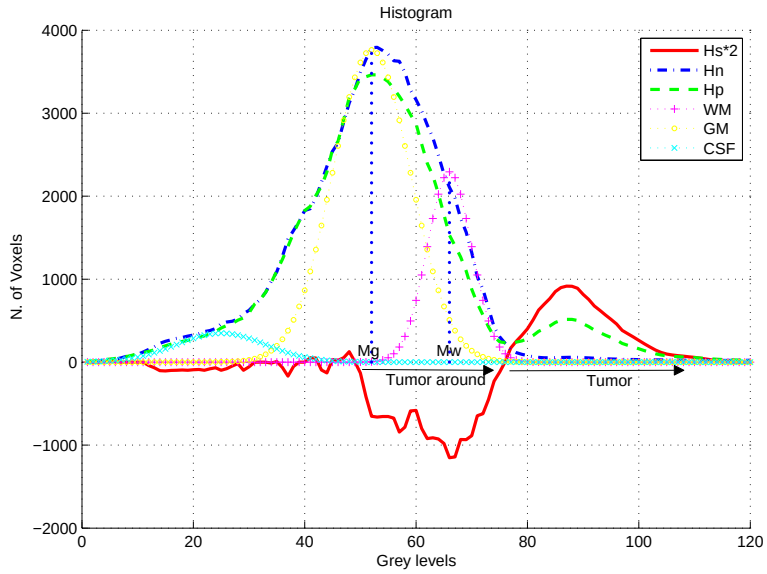

(a)

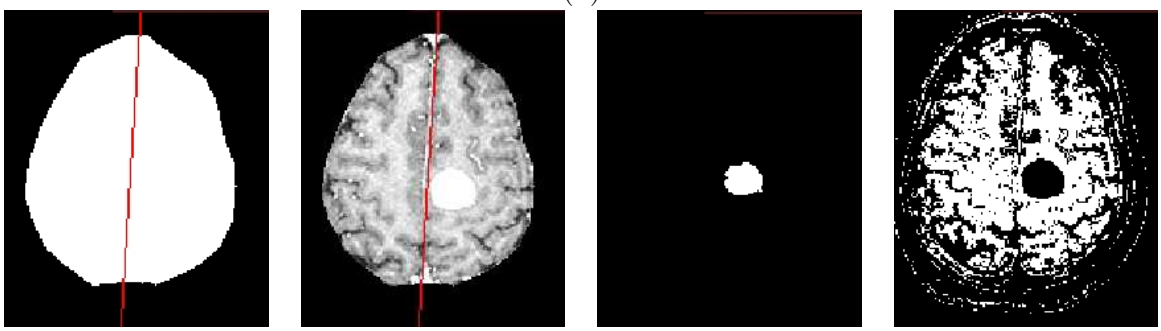

(b) (c) (d) (e)

Figure 4.16: (a) Graph of $\mathbf{H}_s$, $\mathbf{H}_n$ and $\mathbf{H}_p$ for a full-enhanced tumor without edema. (b) Symmetry plane superimposed on the brain mask. (c) Symmetry plane superimposed on the segmented brain. (d) Extracted tumor after morphological operations. (e) Tissues around the tumor.

Ring enhanced and full-enhanced tumors with edema

When a full-enhanced tumor with edema (as in Figure 4.17 for a simulated tumor and Figure 4.18 for a real tumor) or ring enhanced tumor (as in Figure 4.19) exists

in the image, we have two positive peaks in $\mathbf{H}_s(x)$, where the first peak shows the edema intensity range and the second one shows the tumor intensity range, because the intensity of edema is always between CSF and GM. Since these types of tumors usually deform the brain structures and move the ventricles toward the normal hemisphere, a negative peak can be observed in the range of the CSF mode (as in Figures 4.18 and 4.19).

To demonstrate the effects of a full-enhanced tumor on the histograms of the normal and pathological hemispheres and the difference of histograms, we added a simulated tumor in the right hemisphere of a normal image. Figure 4.17 shows the result for this simulation.

The extraction of the tumor is the same as for the full-enhanced tumors without edema. Since in these cases edema surrounds the tumor, to obtain the surrounding tissues, we apply a thresholding using the range of the edema peak.

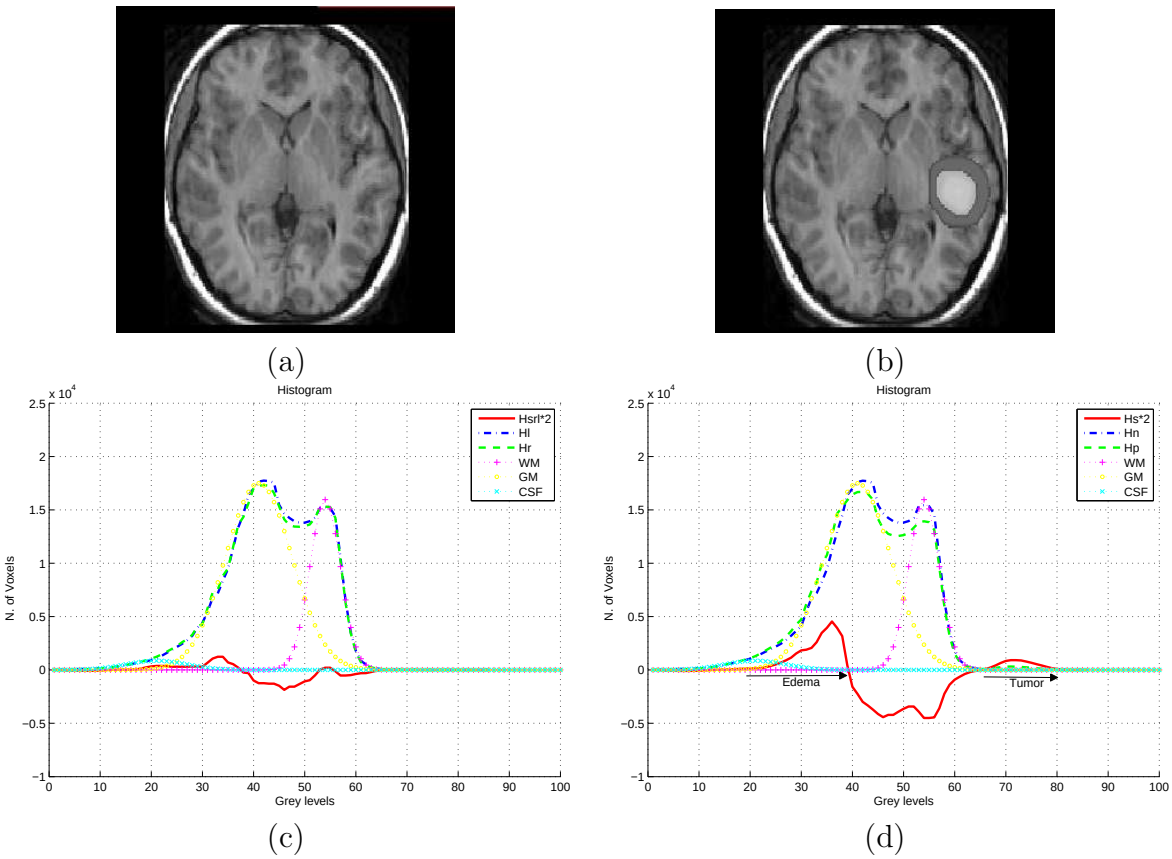

Figure 4.17: (a),(c) A normal image and the graph of $\mathbf{H}_{srl}$, $\mathbf{H}_l$, $\mathbf{H}_r$, WM, GM and CSF for this image. (b),(d) A pathological image (a full-enhanced tumor (about 6000 voxels) with edema (about 12000 voxels) which has a normal distribution of gray levels (75 ± 5 for tumor and 38 ± 5 for the edema), has been added to the normal image) and the graph of $\mathbf{H}_s$, $\mathbf{H}_n$, $\mathbf{H}_p$, WM, GM and CSF for this image.

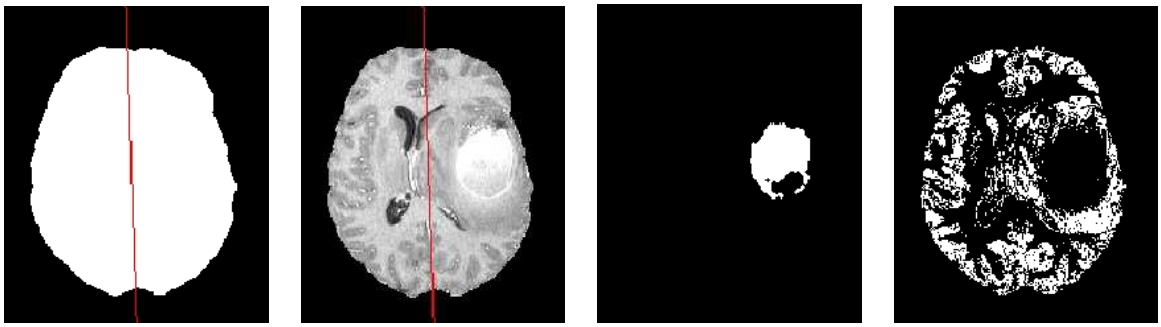

(a) (b) (c) (d)

Figure 4.18: a) Symmetry plane superimposed on the brain mask. (b) Symmetry plane superimposed on the segmented brain. (c) Extracted tumor after morphological operations. (d) Tissues around the tumor (graph of $\mathbf{H}_s$, $\mathbf{H}_n$ and $\mathbf{H}_p$ are shown in Figure 3.13).

Extraction of tumors on FLAIR images

We can apply this method to detect and extract anomalies in all types of brain images such as T2-weighted, PD-weighted, CT and PET images. Here we use this method to detect and extract tumors on FLAIR images. Since tumors on FLAIR images appear as hyperintense tissues a positive peak, which corresponds to the tumor, will occur in $H_s(x)$ after the WM mode as illustrated in Figure 4.20. Due to the tumor influence over the WM and GM tissues, a negative peak can be seen in the range of WM and GM gray levels in $H_s(x)$. To extract the tumor we make a threshold in the range of $T_l = S_{P_t}$ and $T_h = E_{P_t}$. When the tumor peak and WM mode overlap, we use the same limitation as for the enhanced tumors.

Initial segmentation

To extract the tumor we first use a thresholding with tumor peak range values. Some misclassified voxels are removed using morphological operations. An opening is first used to disconnect the components. The largest connected component is then selected since it corresponds to the tumor (as seen in Figures 4.15, 4.16, 4.18 and 4.19). In some cases on CE-T1w images the largest components may not correspond to the tumor (especially for small tumors). In these cases when the FLAIR image exists, it helps us to detect the component which corresponds to the tumor (as we explained in Section 3.3.4), otherwise with a simple click by the user the tumor component can be detected.

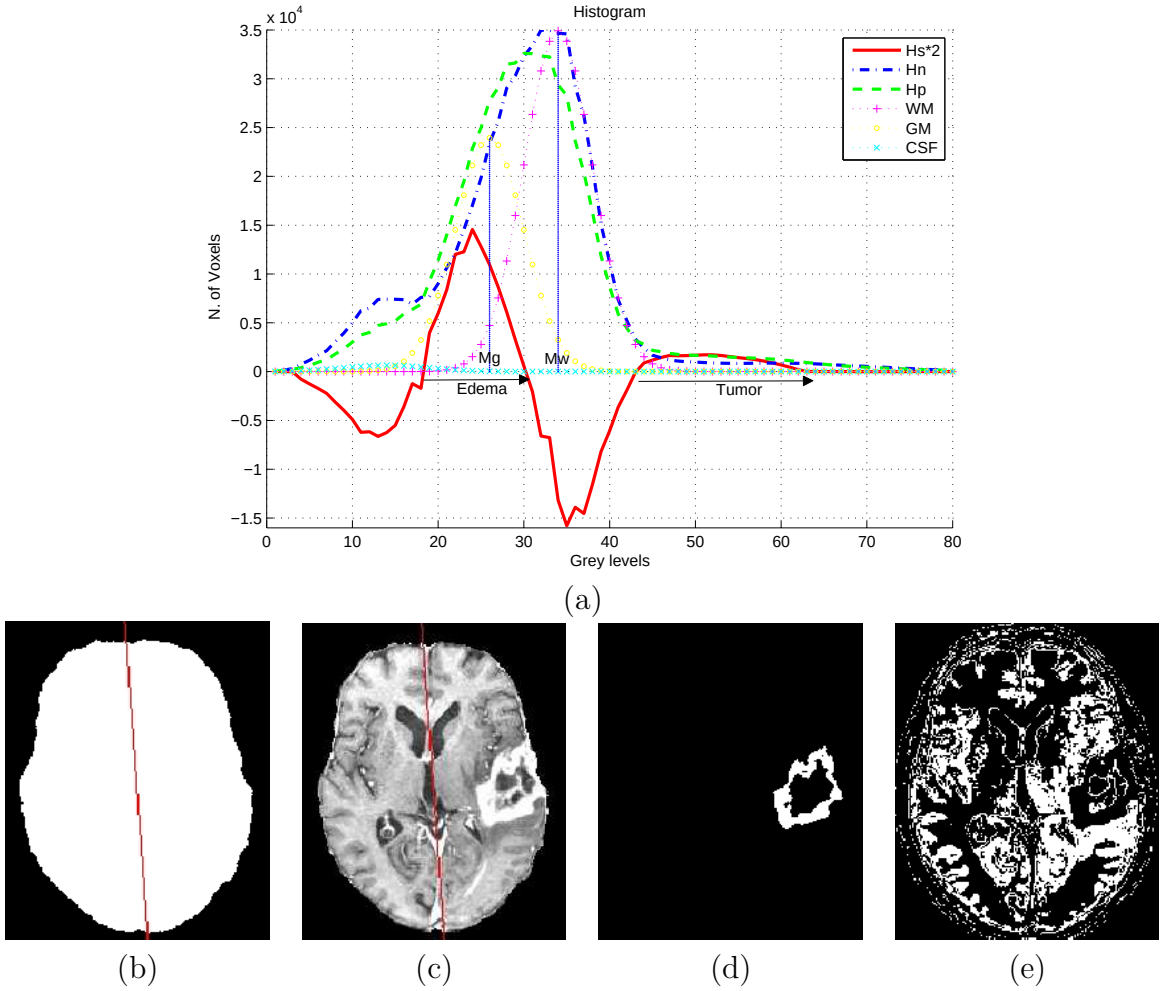

Figure 4.19: (a) Graph of $\mathbf{H}_s$, $\mathbf{H}_n$ and $\mathbf{H}_p$ for a ring-enhanced tumor with edema (image (c)) (for visualization purposes $\mathbf{H}_s$ is multiplied by 2). (b) Symmetry plane superimposed on the brain mask. (c) Symmetry plane superimposed on the segmented brain. (d) Extracted tumor after morphological operations. (e) Tissues around the tumor.

Evaluation

We applied the method to 20 cases with different tumor types, at different locations and with different intensities on CE-T1w images and 10 cases on FLAIR images. In all cases it detects and initially segments the tumors as illustrated for 5 cases in Figures 4.15, 4.16, 4.18, 4.19 and 4.20.

In Table 4.4 the quantitative results are obtained by comparing the automatic segmentations with the available manual segmentations for 20 cases (10 enhanced and 10 non-enhanced tumors) on CE-T1w images. As observed in Table 4.4, for enhanced tumors, the similarity index varies from 74% to 87% with a mean of 81% and the Jaccard index and correct detection ratio are between 60%-78% with a mean of 69%.

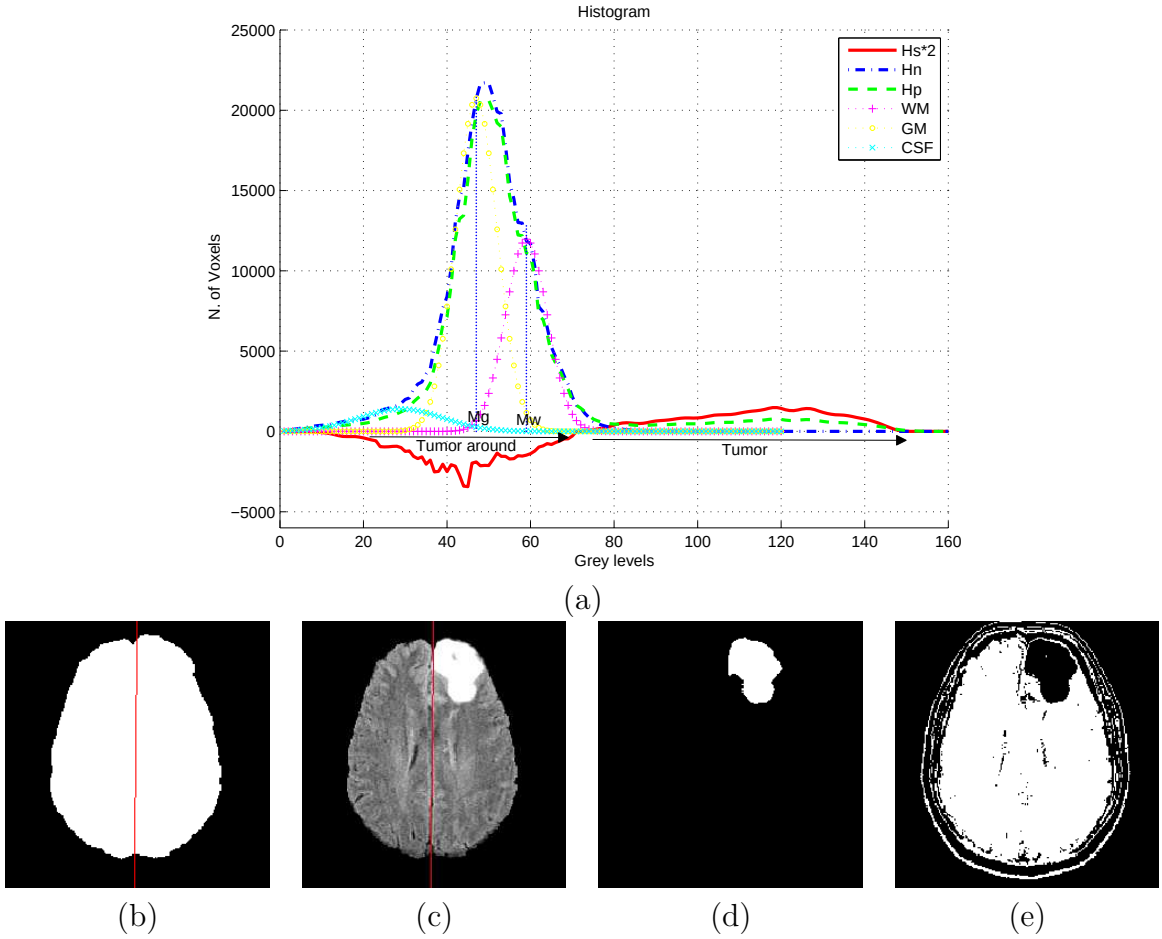

Figure 4.20: (a) Graph of $\mathbf{H}_s$, $\mathbf{H}_n$ and $\mathbf{H}_p$ for a non-enhanced tumor in a FLAIR image (image (c)) (for visualization purposes $\mathbf{H}_s$ is multiplied by 2). (b) Symmetry plane superimposed on the brain mask. (c) Symmetry plane superimposed on the segmented brain. (d) Extracted tumor after morphological operations. (e) Tissues around the tumor.

The false detection ratio has also a mean about 0.6%. In comparison with the MPFCM method, the results are very close and we obtain approximately the same results. As in the MPFCM method, the false detection ratio is very small since all voxels of the segmented tumor are located within the true tumor. Thus we can deform this initial segmented tumor toward the true border of the tumor to improve the quality of segmentation.

Analyzing the results of Table 4.4 for the non-enhanced tumors gives the same results as for the enhanced tumors on volume metrics. But the surface measures show that the segmentation quality of the non-enhanced tumors is worse than the one of enhanced tumors due to ill-defined borders.

Table 4.5 represents the quantitative results obtained on FLAIR images. The similarity index, which varies from 75% to 93% with a mean of 86%, and correct detection

ratio, which varies from 62% to 89% with a mean of 77%, show a good matching between volumes of automatic and manual segmentation. The surface metrics also illustrate a relatively good segmentation, but the results can be improved on the borders. These results also illustrate that the initial segmentation on FLAIR images is better than on CE-T1w images due to well-distinguished intensity of tumors on FLAIR images.

Summary

Here we developed a new and general method for detection and initial segmentation of brain tumors that can be used in any type of brain images. We applied successfully this method to detect and segment tumors on CE-T1w and FLAIR images. The volume metrics of the quantitative evaluation show that it performs a good segmentation but the surface metrics illustrate that the borders of the segmented objects should be improved. In the next section we present a boundary-based method to improve the results of the initial segmentation.

4.4 Segmentation refinement

The result of tumor segmentation by symmetry analysis and MPFCM classification is not accurate enough especially at the border of tumors, therefore we need a method to refine the segmentation. To obtain an accurate segmentation, a parametric deformable model, that has been applied successfully to segment the internal brain structures [Colliot et al., 2006], is used.

4.4.1 Deformable model

The segmentation obtained from the previous processing is transformed into a triangulation using an isosurface algorithm [Piquet et al., 1996] based on tetrahedra and is decimated and converted into a simplex mesh, denoted by $\mathbf{X}$ [Delingette, 1999].

The evolution of our deformable model is described by the following usual dynamic force equation [Kass et al., 1988 ; Xu et al., 2000]:

$$\gamma \frac{\partial \mathbf{X}}{\partial t} = \mathbf{F}_{int}(\mathbf{X}) + \mathbf{F}_{ext}(\mathbf{X}),$$

where $\mathbf{X}$ is the deformable surface, $\mathbf{F}_{int} = \alpha\nabla^2\mathbf{X} - \beta\nabla^2(\nabla^2\mathbf{X})$ is the internal force that constrains the regularity of the surface and $\mathbf{F}_{ext}$ is the external force. In our case, the external force is composed of two terms. The first one is classically derived from

Tumor type	M mm^3	S_i %	J_i %	T_p %	F_p %	D_H mm	D_m mm
TE1	10518.7	82.9	70.8	70.8	0.1	5.36	1.25
TE2	11524.0	86.7	76.5	76.5	0.0	5.83	0.93
TE3	4643.6	83.5	71.6	72.1	0.8	7.55	0.70
TE4	2366.1	87.8	78.2	78.8	0.8	2.57	0.65
TE5	65846.4	77.5	63.2	63.8	1.4	15.93	2.26
Ave.	18979.8	83.7	72.1	72.4	0.6	7.44	1.15
TRE1	43259.5	75.4	60.5	60.9	0.9	9.64	1.48
TRE2	19437.1	75.5	60.6	60.7	0.2	8.07	1.18
TRE3	41833.4	82.7	70.5	70.5	0.0	7.44	1.16
TRE4	13629.2	74.3	59.2	59.3	0.3	5.74	1.33
TRE5	26777.3	83.7	72.1	72.9	1.5	6.28	1.02
Ave.	28987.3	78.3	64.6	64.9	0.6	7.43	1.23
Ave.	23983.5	81.0	68.4	68.7	0.6	7.44	1.19
TNE1	107177.1	79.3	65.6	66.4	0.2	13.69	3.00
TNE2	50870.2	72.4	56.7	56.8	0.2	10.78	2.49
TNE3	15285.9	89.4	80.9	83.1	3.2	8.59	0.97
TNE4	50093.7	81.2	68.3	69.3	2.1	8.94	2.07
TNE5	59990.6	84.8	73.6	75.5	3.3	10.00	1.65
TNE6	14355.6	72.5	56.9	60.5	9.5	13.51	2.24
TNE7	74292.2	70.4	54.3	57.3	8.7	13.18	2.56
TNE8	16635.1	82.9	70.8	71.3	1.0	6.88	1.39
TNE9	38380.1	85.5	74.6	77.6	5.0	8.65	1.55
TNE10	60652.4	76.8	62.3	63.0	1.5	10.75	2.49
Ave.	48773.3	79.5	66.4	68.1	3.5	10.50	2.04
Ave. total	36378.5	80.3	67.4	68.4	2.1	8.97	1.62

Table 4.4: Evaluation of the initial segmentation results of enhanced and non-enhanced tumors by symmetry analysis on a few 3D CE-T1w images for which a manual segmentation was available (M denotes the manually segmented tumor).

Tumor type	M mm^3	S_i %	J_i %	T_p %	F_p %	D_H mm	D_m mm
F1	22851.7	75.1	60.1	62.0	4.6	8.38	1.20
F2	25499.5	85.8	75.1	77.6	4.0	7.32	0.73
F3	110338.2	91.1	83.7	86.0	3.1	8.0	1.10
F4	119415.6	84.4	73.0	74.1	2.0	9.60	1.40
F5	57634.7	83.3	71.4	75.3	6.7	10.30	1.45
F6	47342.3	85.0	73.9	74.0	0.2	6.80	1.77
F7	41378.0	84.7	73.5	74.1	1.2	6.0	1.43
F8	78887.9	87.3	77.5	79.5	3.1	7.47	1.39
F9	37971.4	88.9	80.0	82.4	3.4	9.51	1.23
F10	57769.2	92.6	86.2	89.1	3.6	9.50	1.05
Ave.	59908.8	85.8	75.4	77.4	3.2	8.29	1.27

Table 4.5: Evaluation of the initial segmentation results of tumors by symmetry analysis on a few 3D FLAIR images for which a manual segmentation was available (M denotes the manually segmented tumor).

image edges, and is denoted by $\mathbf{F}_C$. It can be written as:

$$\mathbf{F}_C = v(x, y, z)$$

where v is a Generalized Gradient Vector Flow (GGVF) field introduced by Xu et al. [Xu and Prince, 1998]. A GGVF field v is computed by diffusion of the gradient vector of a given edge map and is defined as the equilibrium solution of the following diffusion equation:

$$\frac{\partial v}{\partial t} = g(\|\nabla f\|)\nabla^2 v - h(\|\nabla f\|)(v - \nabla f) \quad (4.11)$$

$$v(x, y, z, 0) = \nabla f(x, y, z) \quad (4.12)$$

where f is an edge map and the functions g and h are weighting functions which can be chosen as follows:

$$\begin{cases} g(r) = e^{-\frac{r}{\kappa}^2} \\ h(r) = 1 - g(r) \end{cases} \quad (4.13)$$

To compute the edge map, we applied the Canny-Deriche edge detector.

The second term of $\mathbf{F}_{ext}$ is derived from spatial relations and is described next.

We applied this approach to refine the results of initial segmentation by MPFCM and symmetry analysis on CE-T1w images. In all cases we set k=0.01. Properly setting the parameters of the internal force, i.e. α and β, in this model is very important. Unfortunately there is not a general rule to set these parameters. We believe that a relation between the initial surface and these parameters can be established that could be done in future works. Here we set α and β with 3 different values: 0.2 for large volume ($> 30000mm^3$), 0.1 for middle volume (between 10000-30000mm^3) and 0.05 for small volume ($< 10000mm^3$). It should be noted that the results with these values are not the optimum for some cases and by changing the parameters it is possible to obtain better results. The results of 7 cases are shown in Figures 4.29-4.35.

The quantitative results obtained by comparing the refined segmentation with manual segmentation on CE-T1w images are provided in Tables 4.6 and 4.7. By comparing Table 4.6 with 4.2 and Table 4.7 with Table 4.4, it can be observed that the refinement step improves the segmentation quality. For example for the MPFCM method, it increases the average of S_i about 7, J_i about 11 and T_p about 13 unit. It also improves the surface metrics by reducing the average of D_H by about 2 mm and D_m by about 0.5 mm. On the other hand, the average of F_p (error) was increased about 1.5 unit, which is a small value, compared with other metrics improvement is a small value. For the symmetry analysis method the refinement results are approximately the same as for the MPFCM method.

We also refined the initial segmentation on FLAIR images by this model. Since the resolution of FLAIR images (about 20 slices and the thickness of each slice is about 6.5mm) is usually lower than CE-T1w images (about 120 slices and the thickness of each slice is about 1.3mm), the neighborhood slices are very different. Hence applying a 3D deformable model on FLAIR images will not give a good result. To address this problem when the CE-T1w image exists we register the FLAIR image with it, else we increase the number of slices to about 120 and then interpolate the gray level values by a trilinear method. The results of the segmentation refinement for 2 cases are shown in Figures 4.36 and 4.37. We also provide the quantitative results in Tables 4.8 and 4.9. The comparison of these results with the initial segmentation shows that the refinement phase improves the volume and surface metrics. But the improvement is smaller than the one observed on CE-T1w images, because the initial segmentation on FLAIR images is already better than in CE-T1w images due to their well-distinguished boundaries and the low inhomogeneity.

4.4.2 Deformable model constrained by spatial relations

Spatial relations are useful to guide the recognition of objects in images since they provide an important information about the spatial organization of these objects. Two main classes of spatial relations can be considered: topological relations, such as inclusion, exclusion and adjacency, and metric relations such as distances and orientations.

Tumor type	M mm^3	S_i %	J_i %	T_p %	F_p %	D_H mm	D_m mm
TE1	10518.7	92.1	85.4	87.0	2.1	3.14	0.62
TE2	11524.0	92.4	86.0	86.3	0.5	5.19	0.55
TE3	4643.6	84.2	72.8	76.5	6.3	6.07	0.69
TE4	2366.1	91.0	83.4	85.6	2.9	2.48	0.49
TE5	65846.4	93.3	87.5	90.7	3.9	6.00	0.92
Ave.	18979.8	90.5	83.7	86.3	3.4	4.58	0.65
TRE1	43259.5	85.2	74.2	75.0	1.4	10.79	1.29
TRE2	19437.1	84.3	72.9	75.5	4.6	8.50	0.75
TRE3	41833.4	83.0	70.9	72.0	1.9	8.06	1.13
TRE4	13629.2	82.5	70.2	71.8	3.1	6.55	1.05
TRE5	26777.3	86.4	76.0	77.7	2.7	4.80	0.85
Ave.	28987.3	84.3	72.9	74.4	2.7	7.74	1.01
Ave. total	23983.6	87.4	78.3	80.4	3.0	6.16	0.83

Table 4.6: Evaluation of the refined segmentation results by deformable model which is initialized by the MPFCM method on a few CE-T1w images.

Here we use a combination of topological and distance information. The evolution process of the deformable model can be guided by a combination of such relations, via information fusion tools.

In the case of tumor detection by symmetry analysis, two types of information are available: the initial detection and the surrounding tissues. Therefore we use (i) the distance from the initial segmented tumor, and (ii) the tissues around the tumor which were obtained in the previous step (as in Figure 4.22). The idea is that the contour of the tumor should be situated somewhere in between the boundary of the initial detection and the boundary of the tumor around tissues (excluding the background). This constraint also prevents the deformable model from leakage in the weak boundaries.

For distance relations such as "near the initial segmented tumor", we define a fuzzy interval f of trapezoidal shape on the set of distances $\mathbb{R}^+$ (Figure 4.21). The kernel of f is defined as $[0, n_1]$ and its support as $[n_1, n_2]$. Here n_1 and n_2 are defined according to the largest distance between the initial segmentation of the tumor and its surrounding tissues. To obtain a fuzzy subset of the image space, f is combined with a distance map d_A to the reference object A: $d(P) = f(d_A(P))$ where P is a point of

Tumor type	M mm^3	S_i %	j_i %	T_p %	F_p %	D_H mm	D_m mm
TE1	10518.7	91.9	85.0	86.6	2.1	3.04	0.65
TE2	11524.0	91.8	84.8	85.0	0.2	4.89	0.62
TE3	4643.6	85.5	74.9	76.3	2.4	6.76	0.69
TE4	2366.1	92.8	86.7	90.0	3.8	2.41	0.38
TE5	65846.4	92.9	86.5	89.2	3.3	6.50	0.96
Ave.	18979.8	91.0	83.6	85.4	2.36	4.72	0.66
TRE1	43259.5	84.6	73.3	74.2	1.6	10.6	1.25
TRE2	19437.1	83.4	71.4	73.5	3.8	8.28	0.91
TRE3	41833.4	87.1	77.1	79.2	3.3	6.62	0.92
TRE4	13629.2	82.4	70.0	71.0	1.8	7.86	1.25
TRE5	26777.3	85.3	74.1	75.6	2.2	5.31	0.88
Ave.	28987.3	84.6	73.2	74.7	2.5	7.73	1.04
Ave.	23983.6	87.8	78.4	80.1	2.4	6.23	0.85
TNE1	107177.1	82.1	70.1	71.9	4.2	12.45	2.51
TNE2	50870.2	82.3	70.0	72.1	4.0	10.81	1.72
TNE3	15285.9	93.8	88.4	93.4	5.6	3.04	0.56
TNE4	50093.7	90.7	83.0	87.1	5.3	9.37	1.13
TNE5	59990.6	91.3	84.4	90.7	7.5	6.67	0.97
TNE6	14355.6	80.2	66.9	70.0	6.1	9.60	1.51
TNE7	74292.2	75.2	60.2	69.1	17.6	13.01	2.27
TNE8	16635.1	90.7	82.9	88.4	6.8	4.51	0.84
TNE9	38380.1	87.0	77.0	81.8	7.1	7.70	1.49
TNE10	60652.4	83.3	71.3	74.7	5.9	11.76	2.00
Ave.	48773.3	85.7	75.4	80.0	7.0	8.69	1.50
Ave. total	36378.5	86.8	76.9	80.1	4.7	7.46	1.17

Table 4.7: Evaluation of the refined segmentation results by deformable model which is initialized by the symmetry analysis method on a few CE-T1w images.

Tumor type	M mm^3	S_i %	J_i %	T_p %	F_p %	D_H mm	D_m mm
F1	22851.7	81.3	68.4	71.6	6.0	7.90	0.85
F2	25499.5	85.1	74.0	77.3	5.3	7.40	1.12
F3	110338.0	91.0	83.5	85.6	2.9	13.72	1.14
F4	119415.6	84.6	73.3	75.1	3.1	12.20	1.41
F5	57634.7	87.7	78.1	84.5	8.8	7.50	1.21
F6	47342.3	86.9	76.8	78.1	2.0	7.82	1.60
F7	41378.0	85.9	75.3	78.6	5.3	5.93	1.38
F8	78887.9	86.1	75.6	78.5	4.6	9.56	1.56
F9	37971.4	90.0	81.8	84.7	4.0	11.78	1.27
F10	57769.2	89.2	80.5	81.8	1.9	8.13	1.38
Ave.	59908.8	86.8	76.7	79.6	4.4	9.19	1.29

Table 4.8: Evaluation of the refined segmentation results by deformable model which is initialized by the MPFCM method on a few 3D FLAIR images.

the space.

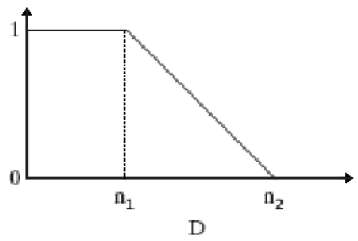

Figure 4.21: Fuzzy interval on the set of distances corresponding to the relation "near".

The relation "near the tissues surrounding the tumor" is modeled in a similar way. These two relations are represented as fuzzy sets in the image space (as shown in Figure 4.22).

These relations are combined using a conjunctive fusion operator (a t-norm such as minimum), leading to a fuzzy set μ_R. The resulting fuzzy set provides high values in the region where both relations are satisfied, and lower elsewhere. As shown in Figure 4.22, this result is a good region of interest for the contour to be detected.

Tumor type	M mm^3	S_i %	J_i %	T_p %	F_p %	D_H mm	D_m mm
F1	22851.7	78.1	64.0	65.5	3.3	7.58	0.95
F2	25499.5	85.9	75.3	77.5	3.7	7.44	0.81
F3	110338.0	91.8	84.9	87.1	3.0	8.58	1.05
F4	119415.6	86.2	75.8	77.9	3.5	8.74	1.31
F5	57634.7	87.0	77.0	82.7	8.2	8.43	1.24
F6	47342.3	88.6	79.6	81.1	2.3	6.98	1.32
F7	41378.0	83.0	71.0	74.2	5.8	9.09	1.66
F8	78887.9	87.9	78.4	81.8	5.0	7.59	1.33
F9	37971.4	90.1	82.0	85.4	4.7	11.59	1.12
F10	57769.2	90.0	81.8	83.2	2.0	6.50	1.38
Ave.	59908.8	86.9	77.0	79.7	4.2	7.95	1.21

Table 4.9: Evaluation of the refined segmentation results which is initialized by the symmetry analysis method on a few 3D FLAIR images.

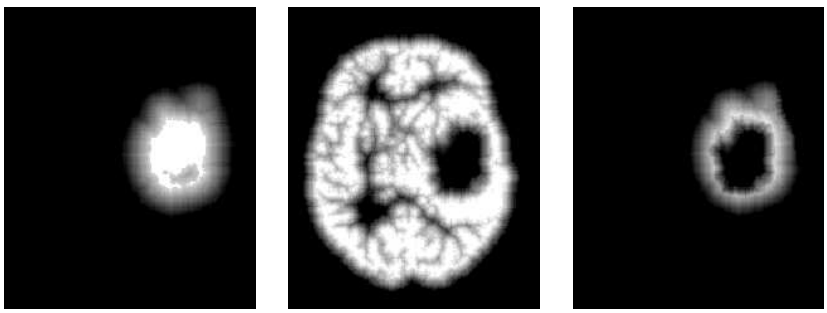

(a) (b) (c)

Figure 4.22: Spatial relations used for segmenting the tumor detected in Figure 4.18 (highest gray level values correspond to regions where the spatial relation is best satisfied). (a) Near the tumor. (b) Relation provided by the tissues surrounding the tumor. (c) Fusion of the two relations.

In [Colliot et al., 2006], several methods to compute the force from a fuzzy set μ_R were proposed. For instance, if $\mu_R(x)$ denotes the degree of satisfaction of the fuzzy relation at point x, and $supp(R)$ the support of μ_R, then we can derive the following potential:

$$P_R(x) = 1 - \mu_R(x) + d_{supp(R)}(x),$$

where $d_{supp(R)}$ is the distance to the support of μ_R, used to have a non-zero force outside the support. The force $\mathbf{F}_R$ associated with the potential P_R is derived as follows:

$$\mathbf{F}_R(x) = -(1 - \mu_R(x)) \frac{\nabla P_R(x)}{\|\nabla P_R(x)\|}.$$

This force is combined to the classical external force derived from edge information $\mathbf{F}_C$:

$$\mathbf{F}_{ext} = \lambda \mathbf{F}_C + \nu \mathbf{F}_R \tag{4.14}$$

where λ and ν are weighting coefficients. The role of $\mathbf{F}_R$ is to force the deformable model to stay within regions where specific spatial relations are fulfilled. Figure 4.23 shows examples of two spatial relations and their corresponding forces.

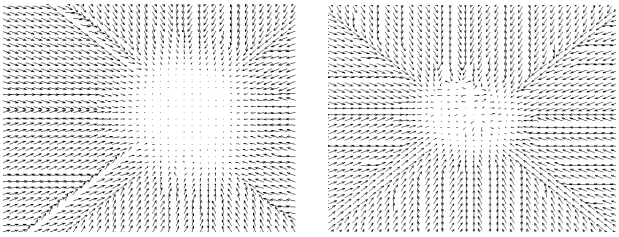

(a) (b)

Figure 4.23: External force $\mathbf{F}_R$ computed from a fuzzy subset μ_R corresponding to a spatial relation R. (a) The force $\mathbf{F}_R$ computed from μ_R for the relation "near the tumor" in Figure 4.22(a). (b) The force computed from the fusion of the two relations of Figure 4.22(c) (for visualization purposes an under-sampling has been performed).

This model is applied to refine the initial segmentation of tumors by symmetry analysis on CE-T1w images, 7 of them being shown in Figures 4.29-4.35. The parameters λ and ν are set to one and the other parameters are set to the previous values. The quantitative results are provided in Table 4.10. This table illustrates that constraining deformable model with spatial relations improves the correct detection ratio and reduce the false detection voxels. This model also improves the quality of the segmentation at the border of the tumor by decreasing surface metrics.

We applied this model to refine the results of segmentation on FLAIR images. Two of them are illustrated in Figures 4.36 and 4.37. The provided quantitative results in Table 4.11 illustrate that the usage of spatial relations can also improve the results of segmentation on FLAIR images. This model has increased the average values of S_i, J_i and T_p about 4, 5 and 5 units without increasing the value of F_p in comparison with the model without spatial relations.

Tumor type	M mm^3	S_i %	j_i %	T_p %	F_p %	D_H mm	D_m mm
TE1	10518.7	93.3	87.4	89.8	3.1	2.80	0.59
TE2	11524.0	92.7	86.4	87.0	0.8	4.89	0.53
TE3	4643.6	90.4	82.5	82.8	0.5	6.70	0.47
TE4	2366.1	94.3	89.3	94.2	5.5	1.49	0.32
TE5	65846.4	96.1	92.4	95.2	3.0	7.00	0.60
Ave.	18979.8	93.4	87.6	89.8	2.6	4.58	0.50
TRE1	43259.5	86.7	76.5	77.4	1.5	8.49	1.08
TRE2	19437.1	88.6	80.0	81.9	3.5	8.01	0.69
TRE3	41833.4	90.2	82.1	83.8	2.4	5.87	0.75
TRE4	13629.2	85.8	75.2	77.9	4.1	5.26	0.88
TRE5	26777.3	88.1	78.7	80.0	1.7	4.28	0.78
Ave.	28987.3	87.9	78.5	80.2	2.6	6.38	0.83
Ave.	23983.6	90.7	83.1	85.0	2.6	5.48	0.67
TNE1	107177.1	86.5	76.2	78.9	2.7	13.33	1.94
TNE2	50870.2	87.4	77.6	79.7	3.1	8.79	1.20
TNE3	15285.9	94.5	89.7	94.1	5.0	3.86	0.48
TNE4	50093.7	92.2	85.6	88.2	3.3	6.50	0.95
TNE5	59990.6	91.8	84.8	89.7	5.9	6.40	0.93
TNE6	14355.6	82.1	70.0	76.5	11.2	6.23	1.26
TNE7	74292.2	78.5	64.6	71.0	12.2	11.18	2.05
TNE8	16635.1	91.7	84.7	89.9	6.3	5.22	0.76
TNE9	38380.1	88.1	78.7	83.5	6.8	6.64	1.38
TNE10	60652.4	86.3	76.0	79.4	5.3	9.12	1.69
Ave.	48773.3	87.9	80.8	83.1	6.2	7.72	1.26
Ave. total	36378.5	89.3	82.0	84.1	4.4	6.6	0.97

Table 4.10: Evaluation of the refined segmentation results of enhanced and non-enhanced tumors by deformable model constrained by spatial relations (initialized by symmetry analysis) on a few 3D CE-T1w images.

Tumor type	M mm^3	S_i %	J_i %	T_p %	F_p %	D_H mm	D_m mm
F1	22851.7	82.0	69.5	72.5	5.6	7.58	0.77
F2	25499.5	90.3	82.3	87.0	6.1	6.55	0.46
F3	110338.2	92.1	85.4	87.3	2.5	8.08	1.00
F4	119415.6	91.3	84.0	87.3	4.3	8.45	0.90
F5	57634.7	89.6	81.2	84.5	4.6	7.70	1.00
F6	47342.3	94.3	89.2	90.5	1.5	4.28	0.73
F7	41378.0	91.0	83.5	85.5	2.7	4.92	0.96
F8	78887.9	90.6	82.8	86.5	4.9	7.13	1.07
F9	37971.4	92.5	86.0	90.0	4.8	10.00	0.95
F10	57769.2	93.4	87.6	92.2	5.3	6.00	0.86
Ave.	599908.8	90.7	83.2	86.3	4.2	7.07	0.87

Table 4.11: Evaluation of the refined segmentation results of tumors by deformable model constrained by spatial relations (initialized by symmetry analysis) on a few 3D FLAIR images.

4.5 Segmentation of edema and necrosis

The segmentation of edema and necrosis is important in the treatment of tumors. As we surveyed in Chapter 2, a few methods segment tumor, edema and necrosis altogether.

To segment edema in a CE-T1w image we use the symmetry analysis method. As commented in Chapter 1, edema appears in the case of enhanced tumors. Hence a positive peak is observed in $\mathbf{H}_p$ between GM and CSF which corresponds to the gray levels range of edema (as seen in Figures 4.17 and 4.19). Because edema is usually darker than GM and brighter than CSF. Therefore, the procedure of non-enhanced tumor segmentation can be applied to segment edema. We first apply a threshold in the range of $T_l = S_{P_e}$ and $T_h = E_{P_e}$, where P_e represents the edema peak. When an overlap exists between the edema peak and the GM mode or CSF mode we use the same limitation as for the non-enhanced tumor (see Section 4.3.2). An opening is used to disconnect the components and the largest connected component is then selected as the initial segmentation. Some times because of overlapping between edema and

GM tissues, disconnecting edema from GM tissues by morphological operation is not possible. Hence we disconnect non-edema components manually. Finally we refine the initial segmentation by a deformable model constrained by spatial relations.

Segmentation of edema on FLAIR image can be performed automatically by both proposed algorithms (MPFCM and symmetry analysis). We can use the same procedure as for the non-enhanced tumor segmentation on FLAIR images to segment edema (for both methods).

Figures 4.24 and 4.25 show the results of edema segmentation on CE-T1w and FLAIR images for two cases. To evaluate the method, we provide quantitative results in Table 4.12 by comparing the results with manual segmentation. It can be observed that the segmentation of edema on FLAIR images is more accurate. The false detection ratio is about 2 times less than on CE-T1w image. This is because edema tissues are well-distinguished on FLAIR images and have little overlapping with other tissues.

Necrosis is the central section of tumors which appears darker than edema. Here to obtain the necrosis in the case of a ring enhanced tumor we select the connected component in the complement of the tumor which is inside the tumor (as illustrated in Figures 4.24 and 4.25).

Tumor type	M mm^3	S_i %	J_i %	T_p %	F_p %	D_H mm	D_m mm
ET1	81680.2	87.8	78.3	86.5	10.7	9.38	1.65
EF1	81680.2	91.0	83.5	86.4	3.8	7.83	1.10
ET2	104146.2	88.2	78.9	86.4	10.0	9.00	1.81
EF2	104146.2	91.6	84.5	91.0	8.5	9.83	1.21
Ave.ET	92913.2	88.0	78.6	86.5	10.35	9.19	1.73
Ave.EF	92913.2	91.3	84.0	88.7	6.1	8.83	1.15

Table 4.12: Evaluation of the segmentation results of edema on two FLAIR and CE-T1w images. The FLAIR image is registerd to CE-T1w image. Here ET and EF represent edema on CE-T1w and edema on FLAIR image.

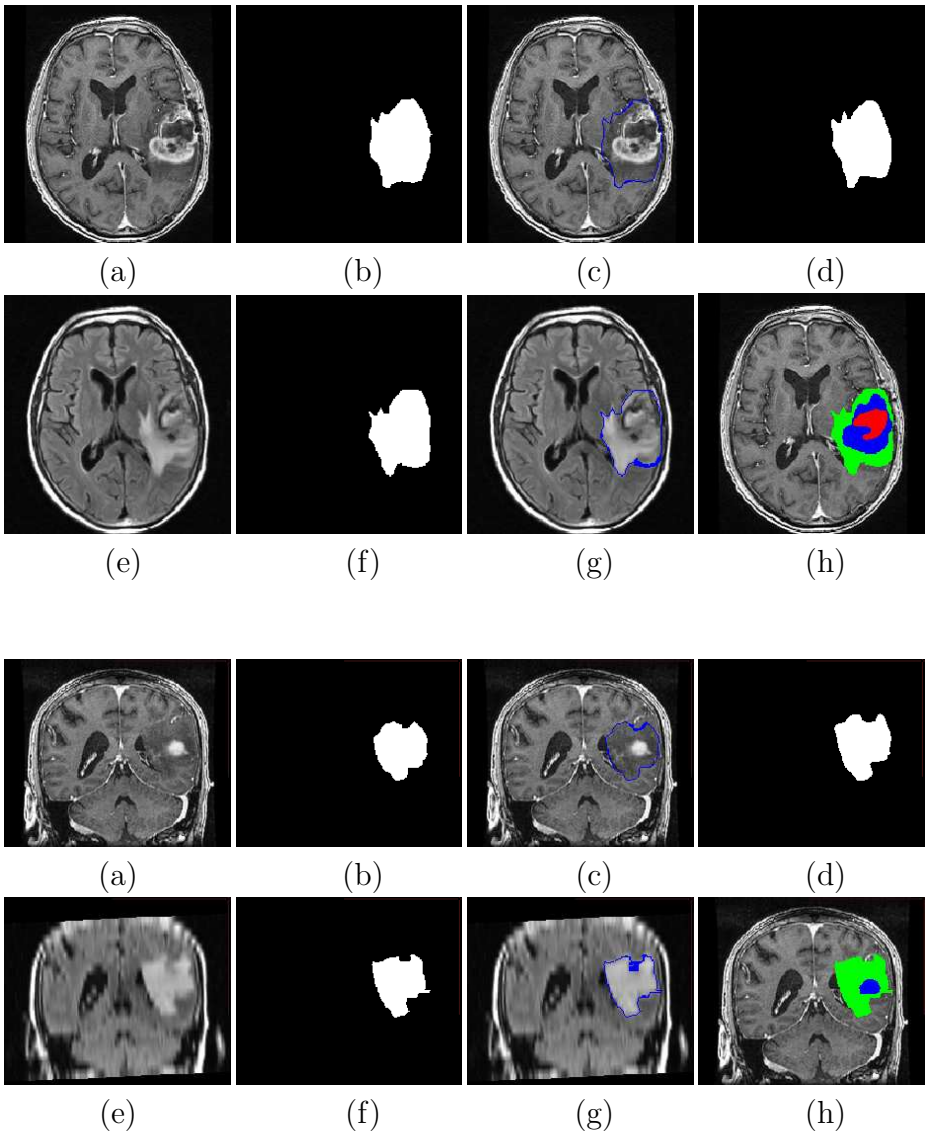

Figure 4.24: Segmentation of edema (an axial and a coronal slice). (a) Original CE-T1w image. (b) Segmented edema on the CE-T1w image. (c) Result superimposed on the original image. (d) Manually segmented edema. (e) Original FLAIR image. (f) Segmented edema on the FLAIR image. (g) Result superimposed on the original image. (h) Result of the tumor, edema and necrosis segmentation superimposed on the original image. Red, blue and green area represent necrosis, tumor and edema repectively.

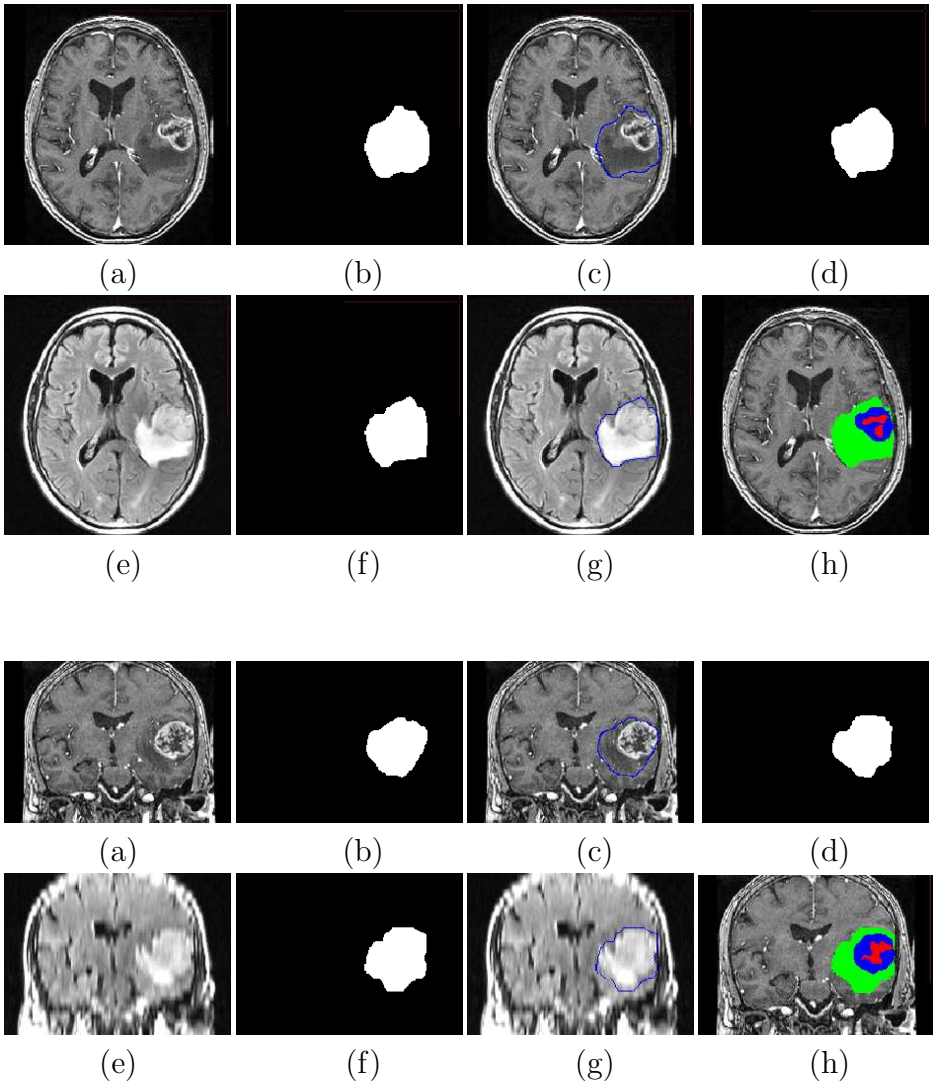

Figure 4.25: Segmentation of edema (an axial and a coronal slice). (a) Original CE-T1w image. (b) Segmented edema on the CE-T1w image. (c) Result superimposed on the original image. (d) Manually segmented edema. (e) Original FLAIR image. (f) Segmented edema on the FLAIR image. (g) Result superimposed on the original image. (h) Result of the tumor, edema and necrosis segmentation superimposed on the original image. Red, blue and green area represent necrosis, tumor and edema repectively.

4.6 Results and discussion

We have applied the proposed methods to 30 MR data with cerebral tumors (see Tables 1.4 and 1.5 for specifications). The segmentation results for 9 cases which are initially segmented by symmetry analysis and refined by deformable model and constrained deformable model are shown in Figures 4.29-4.40. The results can be compared with manually segmented tumors. The 5 first figures are full- and ring-enhanced tumors

while the 4 last tumors are non-enhanced tumors on CE-T1w and FLAIR images. In all cases, the initial detection based on symmetry analysis or MPFCM only provides a part of the tumor. The whole tumor is successfully recovered by the second segmentation step using the deformable model and the spatial relations.

To evaluate the methods we have provided quantitative results for each method by comparing the segmentation results with manual segmentations. The manual segmentations are provided by medical experts.

We provide some graphs which compare the quantitative results of the methods. The first graph (Figure 4.26) shows the averages and standard deviations of volume and surface metrics for 10 enhanced tumors on CE-T1w image. It can be observed that the volume measures of initial and final segmentation by MPFCM and symmetry analysis (refined by deformable model) are approximately equal. Symmetry analysis has better surface measures in initial segmentation but the results of refined segmentation for the both method are approximately equal. This comparison shows that the MPFCM and symmetry analysis methods (refined by deformable model) segment enhanced tumors approximately equally well. Finally, it can be observed that the spatial relations have the potential of improving the results. Refinement using the deformable model constrained by spatial relations improves the surface and volume metrics in comparison with a simple deformable model.

The second graph (Figure 4.27) compares the quantitative results on non-enhanced tumors on CE-T1w images by symmetry analysis. Again it can be observed that the deformable model with and without spatial relations can improve the results of the initial segmentation. Although the deformable model ameliorates the volume and surface metrics, on the other hand it increases the false detection ratio due to ill defined borders. But the use of spatial relations reduces the ratio of false detection, because they prevent the leakage of contours in the ill defined borders.

The comparison of this graph and the previous one also shows that the quality of the segmention for enhanced tumors is better than for the non-enhanced tumors because of their well-defined boundaries. Improvement of the method for segmenting non-enhanced tumors could still be useful.

The last graph (Figure 4.28) illustrates the quantitative results for non-enhanced tumor segmentation on FLAIR images. It shows that the refinement by deformable model does not lead to a considerable improvement of volume metrics. It ameliorates the surface measures more than volume measures. This graph shows that the deformable model does not increase the false detection ratio, because on the FLAIR images the borders are often well-defined.

Unfortunately there is not a gold standard to compare quantitatively the method with existing methods. In comparison with recent works, such as Dou et al. [Dou et al., 2007] (reported F_p=5% an T_p=96% for 4 cases), Corso et al. [Corso et al., 2006] (reported J_i=56% for 30 cases) and Prastawa et al. [Prastawa et al., 2004] (reported

S_i=73% and D_H=15 mm for 4 cases), our results are better than or equal to the ones reported in these works.

The computation time for segmenting (preprocessing and segmenting) a tumor by MPFCM method on a standard computer (Pentium IV 2GHz) is about 4.5 minutes, by symmetry analysis method without spatial relations it is about 2.5 minutes and with spatial relations it is about 3 minutes.

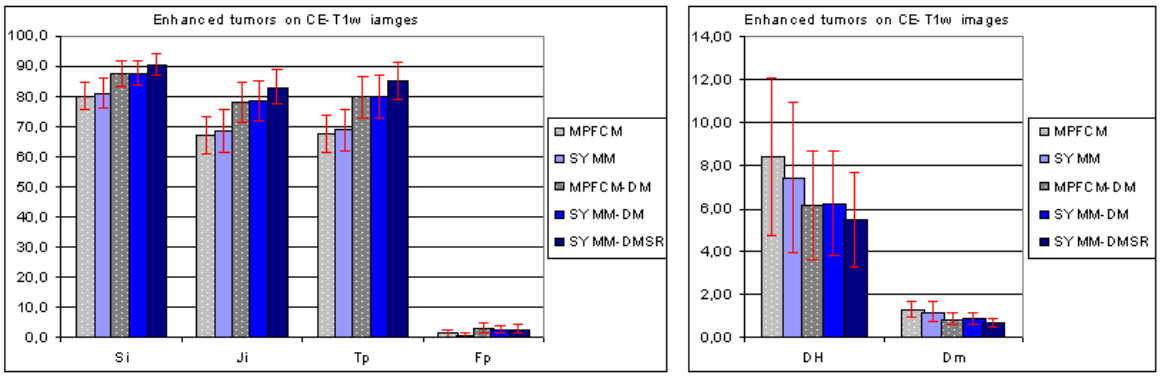

(a) (b)

Figure 4.26: Graph of the quantitative results for enhanced tumors on 10 CE-T1w images. (a) Average and standard deviation of volume measures. (b) Average and standard deviation of surface measures. Here, MPFCM, MPFCM-DM, SYMM, SYMM-DM and SYMM-DMSR denote the MPFCM method, MPFCM refined by deformable model, the symmetry analysis method, symmetry analysis refined by deformable model and symmetry analysis refined by deformable model with spatial relations respectively.

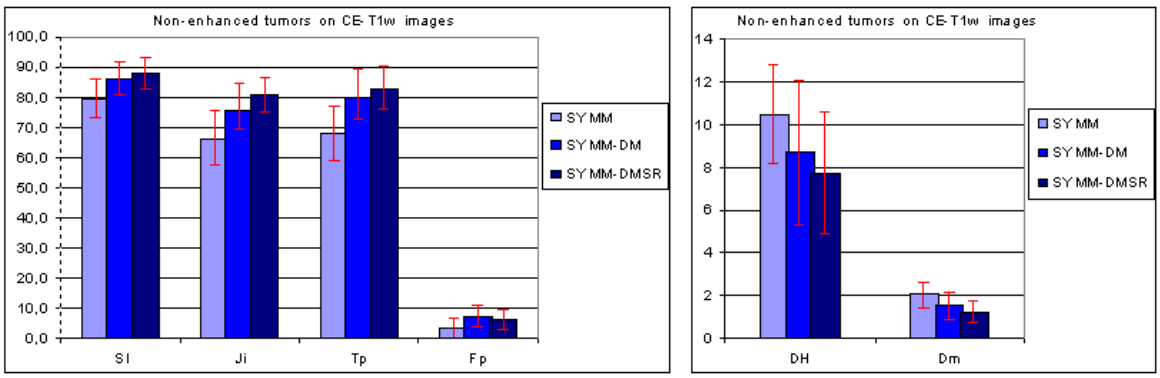

(a) (b)

Figure 4.27: Graph of the quantitative results for non-enhanced tumors on 10 CE-T1w images. (a) Average value of volume measures. (b) Average value of surface measures. Here, SYMM, SYMM-DM and SYMM-DMSR denote the symmetry analysis method, symmetry analysis refined by deformable model and symmetry analysis refined by deformable model with spatial relations respectively.

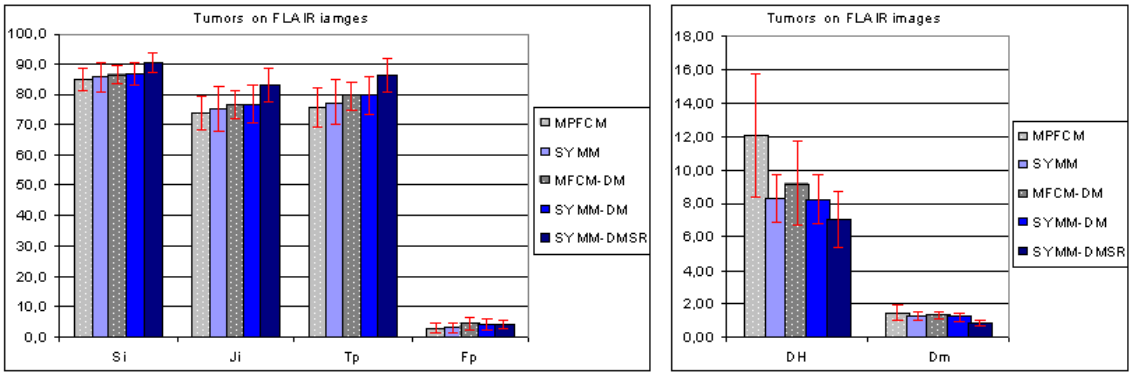

(a) (b)

Figure 4.28: Graph of the quantitative results for non-enhanced tumors on 10 FLAIR images. (a) Average value of volume measures. (b) Average value of surface measures. Here, MPFCM, MPFCM-DM, SYMM, SYMM-DM and SYMM-DMSR denote the MPFCM method, MPFCM refined by deformable model, the symmetry analysis method, symmetry analysis refined by deformable model and symmetry analysis defined by deformable model with spatial relations respectively.

4.7 Conclusion

We have developed a hybrid segmentation method that uses both region and boundary information of the image to segment the tumor and its components. We compared a fuzzy classification method and a symmetry analysis method to detect the tumors and we have used a deformable model constrained by spatial relations for segmentation refinement. This work shows that the symmetry plane is a useful feature for tumor detection. We also presented a new fuzzy classification method which can be used in medical imaging applications. In comparison with other methods, our approach has some advantages such as automation and more generality with respect to the wide range of tumors. Our method can also segment the tumor components such as edema and necrosis. We also anticipate that it is applicable to any type of image such as T2-weighted, PD, etc.

A limit of our symmetry based approach is that the symmetry analysis may fail in the case of a symmetrical tumor across the mid-sagittal plane. However this case is very rare.

Future work aims at determining the type of tumor based on an ontology of tumors. Our results can also serve as a preliminary step for segmenting surrounding structures in the next chapter by using fuzzy spatial relations defined according to the type of the tumors.

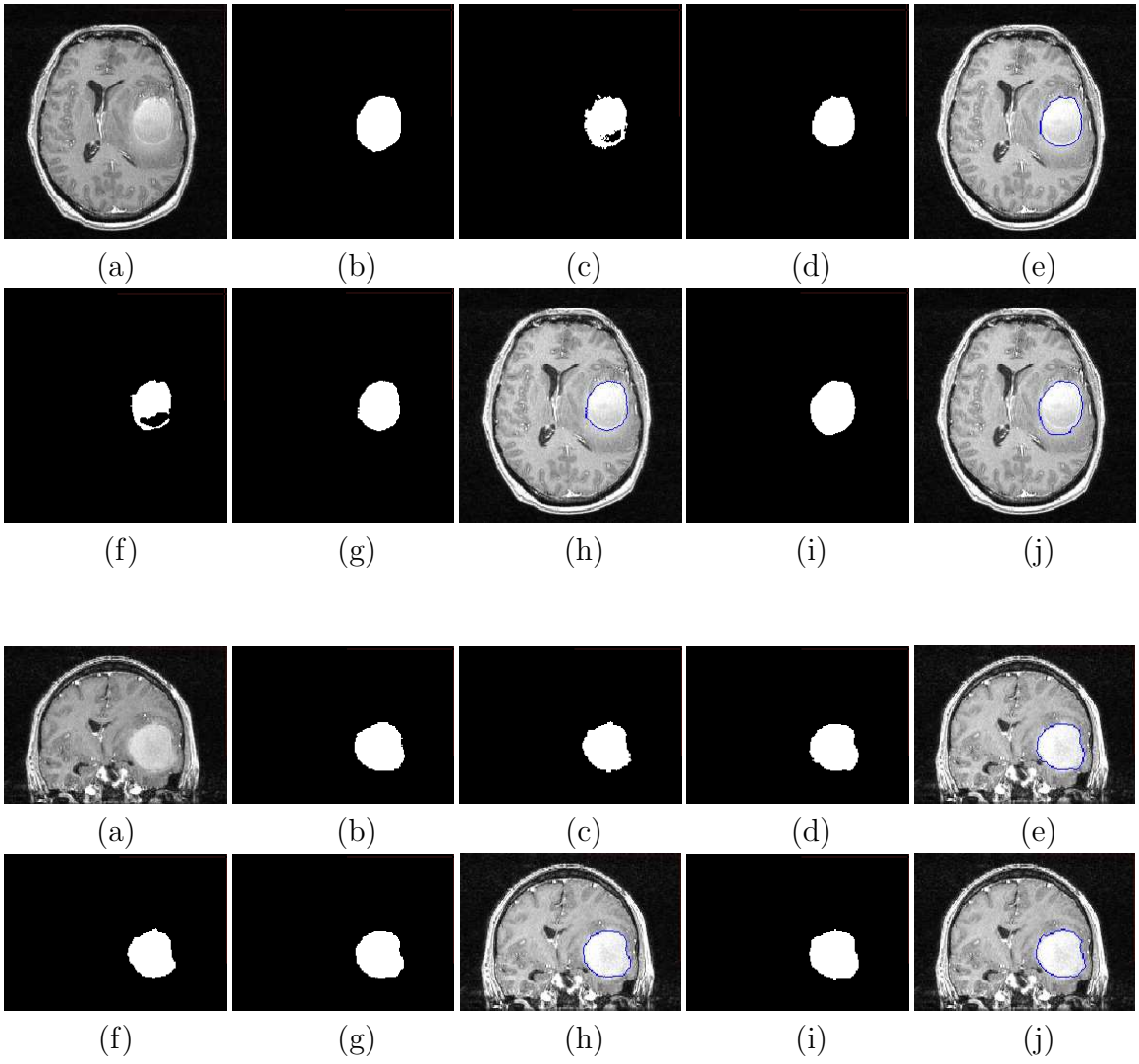

Figure 4.29: Comparison of manual and automatic segmentation results using symmetry analysis and MPFCM for a relatively large full-enhanced tumor on a CE-T1w image (an axial and a coronal slice). (a) Original image. (b) Manual segmentation. (c) Initial segmentation by MPFCM. (d) Refined segmentation of MPFCM. (e) Result superimposed on the original image. (f) Initial segmentation by symmetry analysis. (g) Refined segmentation of symmetry analysis by deformable model without spatial relations. (h) Result superimposed on the original image. (i) Refined segmentation of symmetry analysis by deformable model with spatial relations. (j) Result superimposed on the original image.

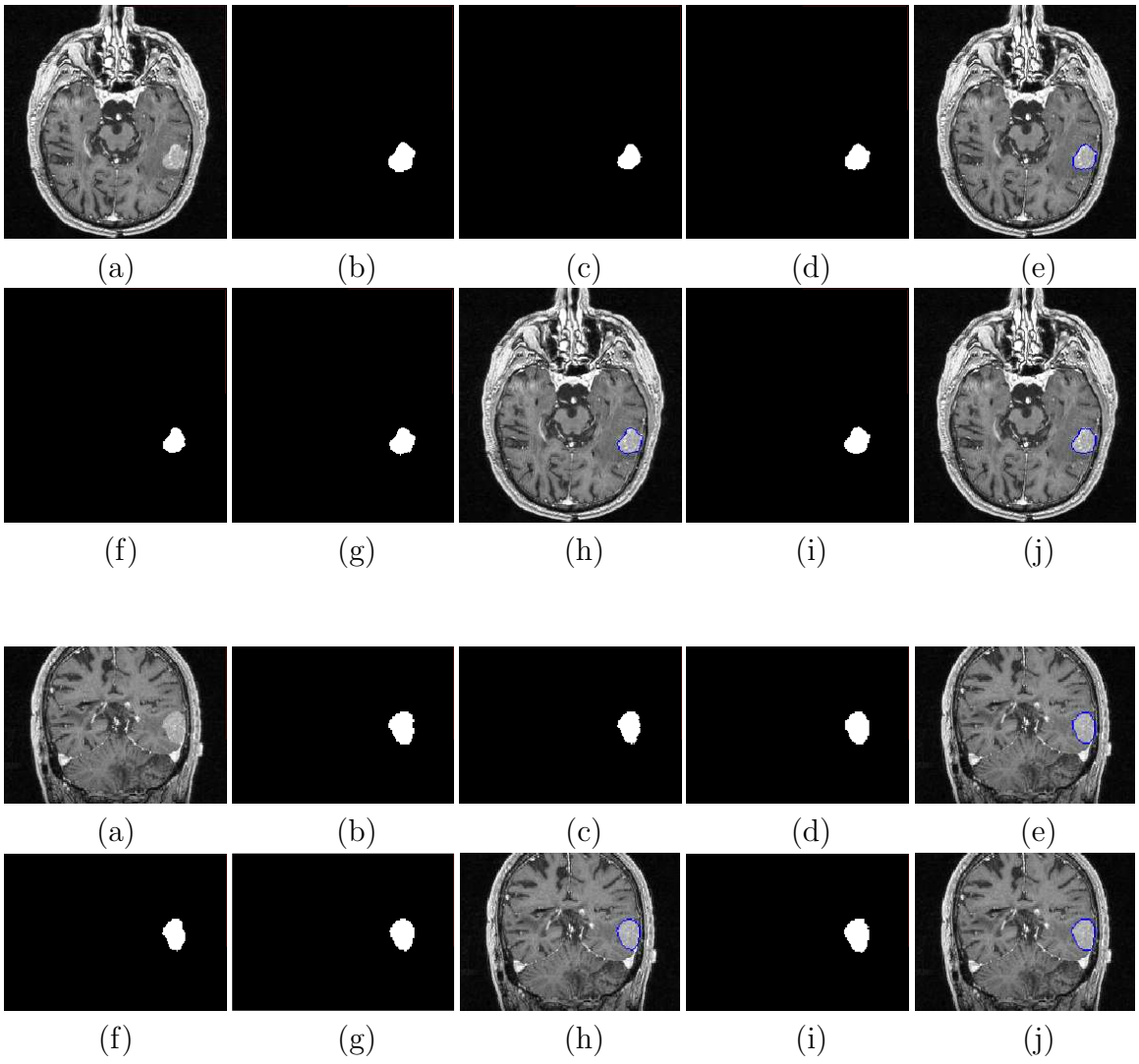

Figure 4.30: Comparison of manual and automatic segmentation results using symmetry analysis and MPFCM for a relatively medium full-enhanced tumor on a CE-T1w image (an axial and a coronal slice). (a) Original image. (b) Manual segmentation. (c) Initial segmentation by MPFCM. (d) Refined segmentation of MPFCM. (e) Result superimposed on the original image.(f) Initial segmentation by symmetry analysis. (g) Refined segmentation of symmetry analysis by deformable model without spatial relations. (h) Result superimposed on the original image. (i) Refined segmentation of symmetry analysis by deformable model with spatial relations. (j) Result superimposed on the original image.

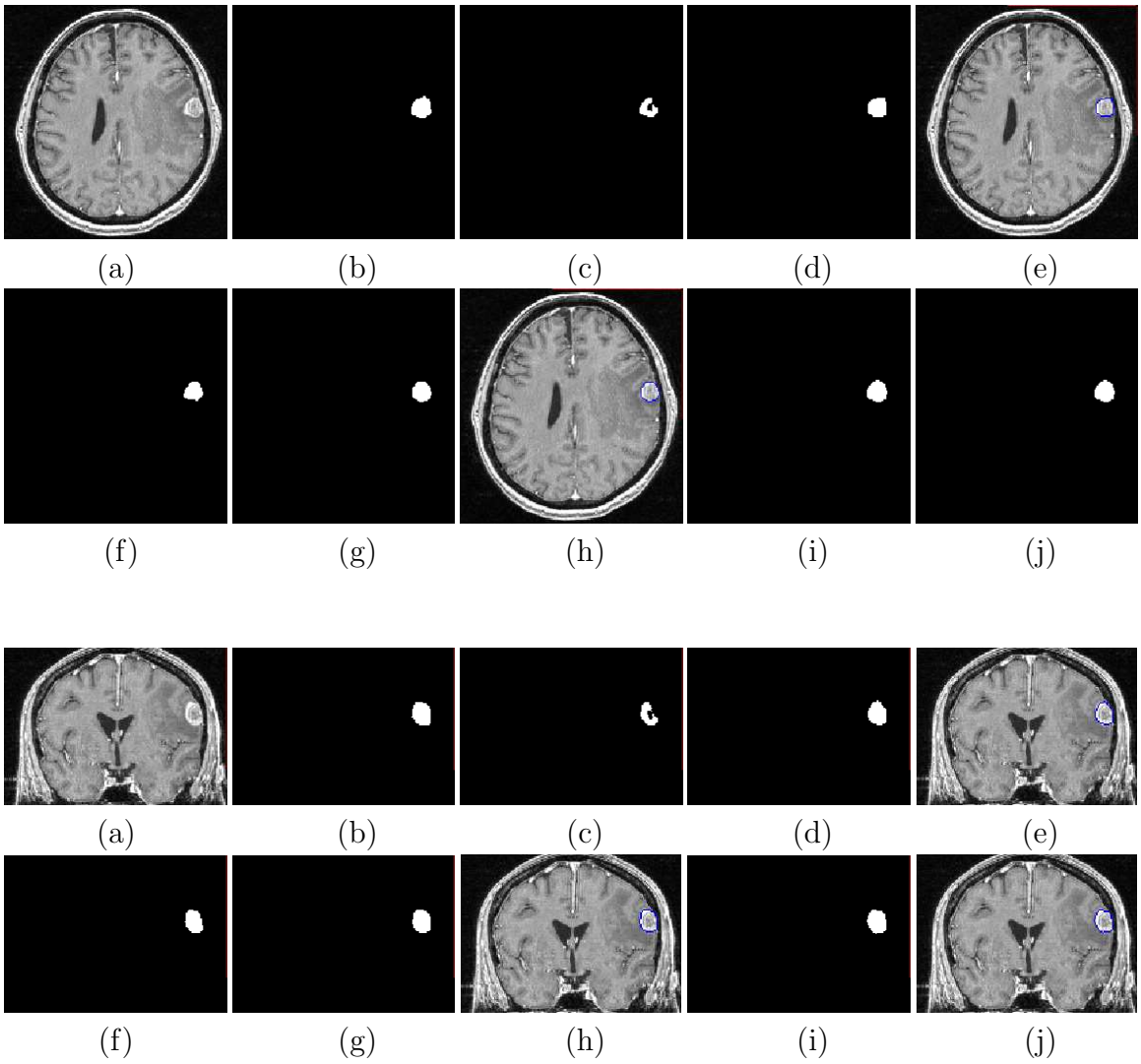

Figure 4.31: Comparison of manual and automatic segmentation results using symmetry analysis and MPFCM for a relatively small full-enhanced tumor on a CE-T1w image (an axial and a coronal slice). (a) Original image. (b) Manual segmentation. (c) Initial segmentation by MPFCM. (d) Refined segmentation of MPFCM. (e) Result superimposed on the original image. (f) Initial segmentation by symmetry analysis. (g) Refined segmentation of symmetry analysis by deformable model without spatial relations. (h) Result superimposed on the original image. (i) Refined segmentation of symmetry analysis by deformable model with spatial relations. (j) Result superimposed on the original image.

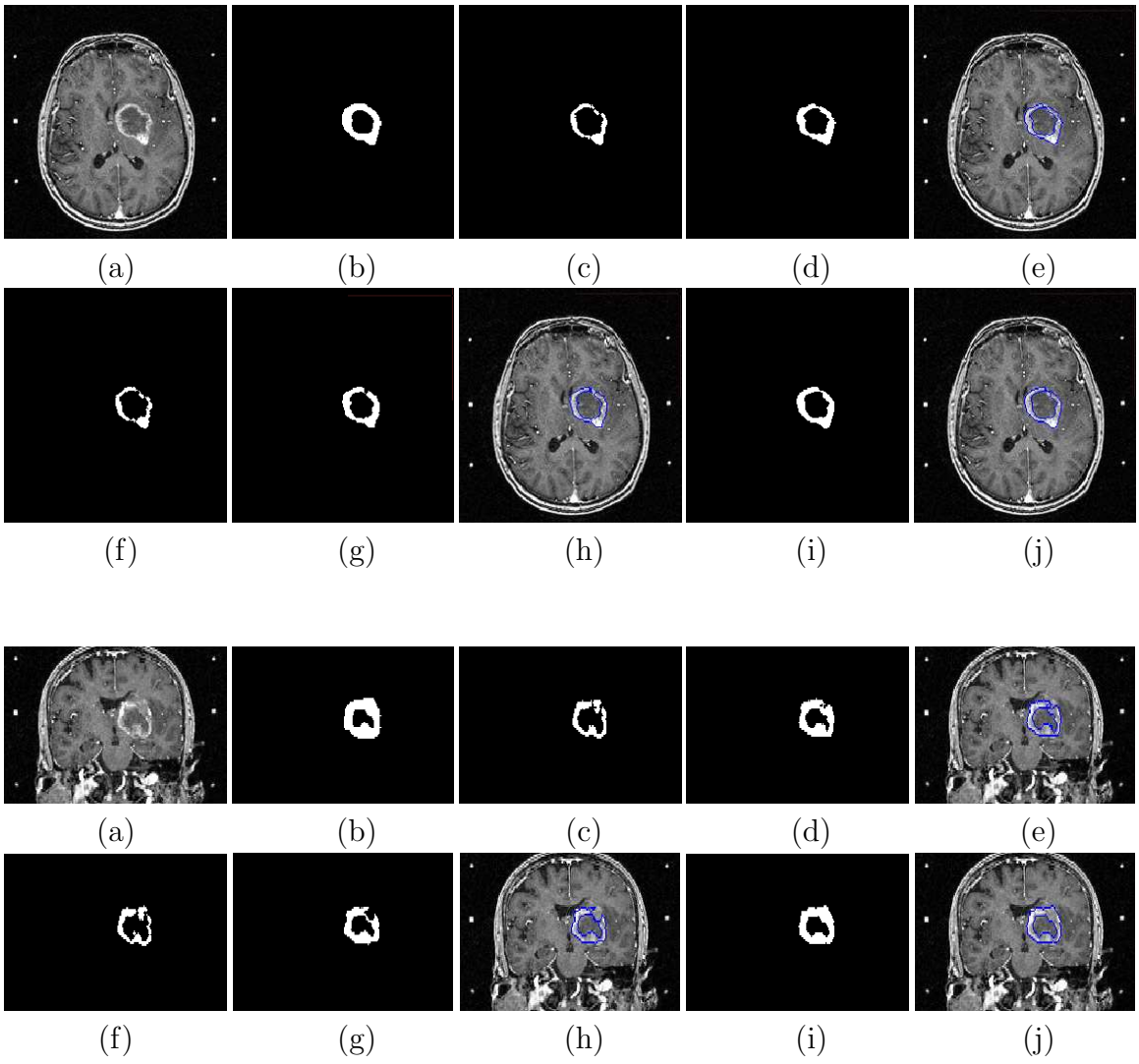

Figure 4.32: Comparison of manual and automatic segmentation results using symmetry analysis and MPFCM for a ring-enhanced tumor on a CE-T1w image (an axial and a coronal slice). (a) Original image. (b) Manual segmentation. (c) Initial segmentation by MPFCM. (d) Refined segmentation of MPFCM. (e) Result superimposed on the original image. (f) Initial segmentation by symmetry analysis. (g) Refined segmentation of symmetry analysis by deformable model without spatial relations. (h) Result superimposed on the original image. (i) Refined segmentation of symmetry analysis by deformable model with spatial relations. (j) Result superimposed on the original image.

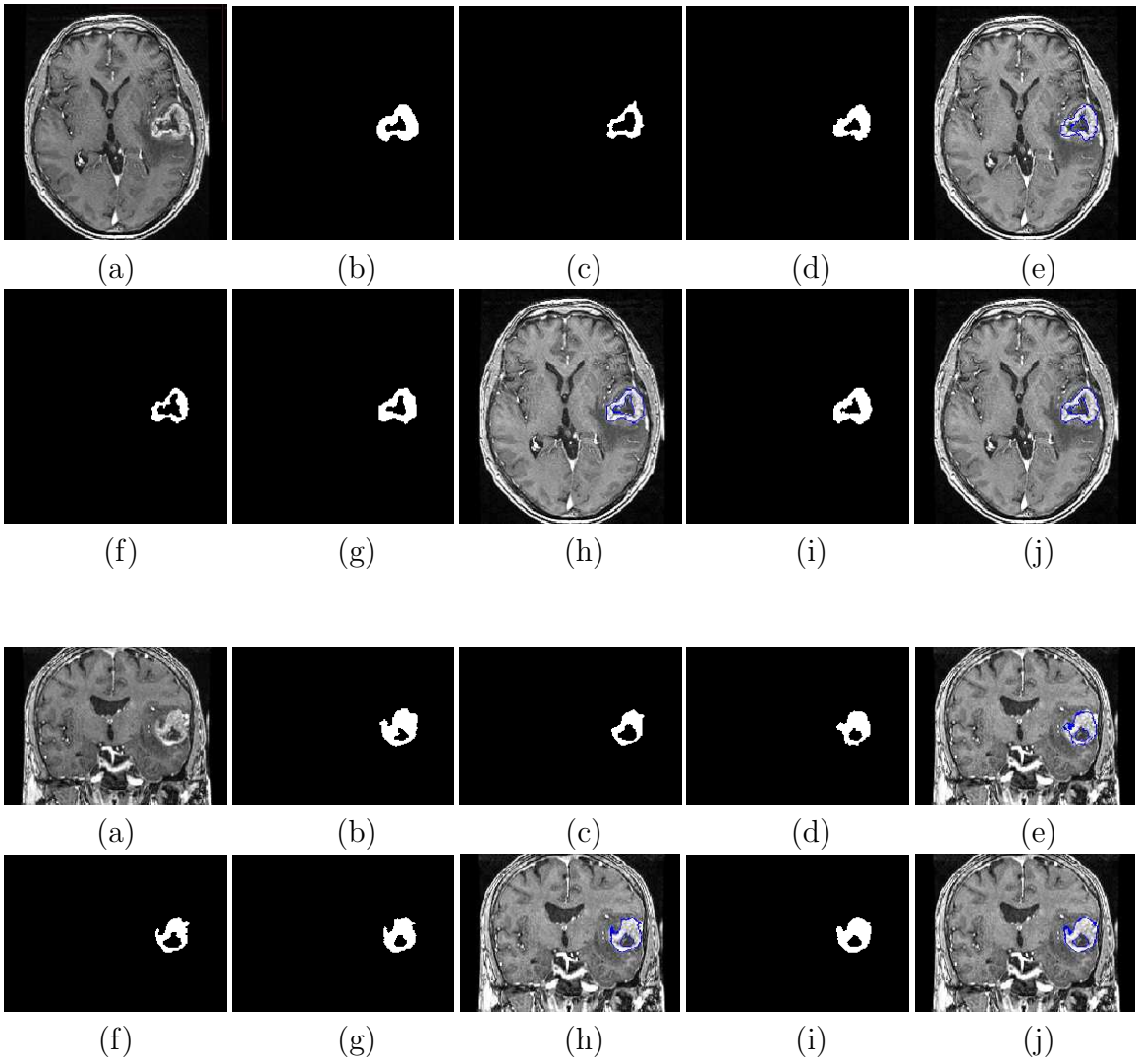

Figure 4.33: Comparison of manual and automatic segmentation results using symmetry analysis and MPFCM for a ring-enhanced tumor on a CE-T1w image (an axial and a coronal slice). (a) Original image. (b) Manual segmentation. (c) Initial segmentation by MPFCM. (d) Refined segmentation of MPFCM. (e) Result superimposed on the original image. (f) Initial segmentation by symmetry analysis. (g) Refined segmentation of symmetry analysis by deformable model without spatial relations. (h) Result superimposed on the original image. (i) Refined segmentation of symmetry analysis by deformable model with spatial relations. (j) Result superimposed on the original image.

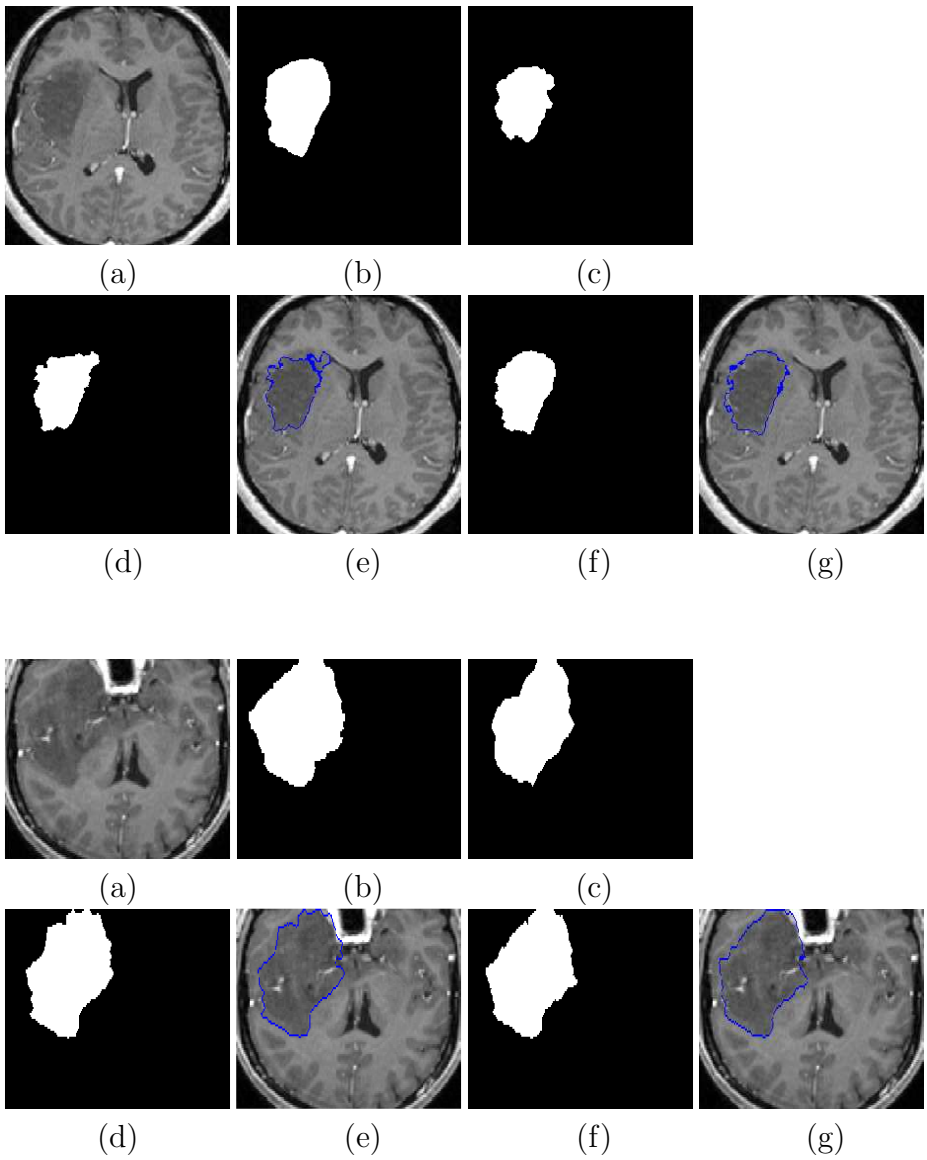

Figure 4.34: Comparison of manual and automatic segmentation results using symmetry analysis for a non-enhanced tumor on a CE-T1w image (an axial and a coronal slice). (a) Original image. (b) Manual segmentation. (c) Initial segmentation by symmetry analysis. (d) Refined segmentation of symmetry analysis by deformable model without spatial relations. (e) Result superimposed on the original image. (f) Refined segmentation of symmetry analysis by deformable model with spatial relations. (g) Result superimposed on the original image.

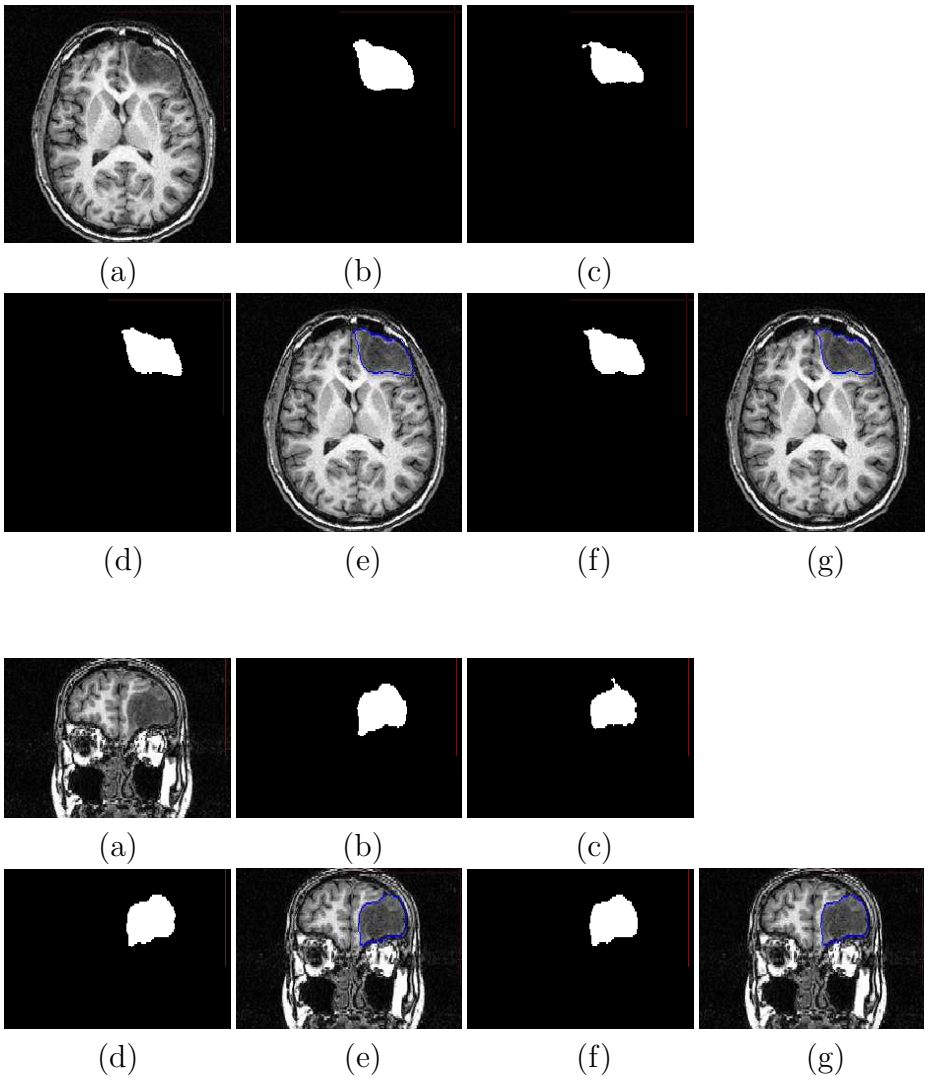

Figure 4.35: Comparison of manual and automatic segmentation results using symmetry analysis for a non-enhanced tumor on a CE-T1w image (an axial and a coronal slice). (a) Original image. (b) Manual segmentation. (c) Initial segmentation by symmetry analysis. (d) Refined segmentation of symmetry analysis by deformable model without spatial relations. (e) Result superimposed on the original image. (f) Refined segmentation of symmetry analysis by deformable model with spatial relations. (g) Result superimposed on the original image.

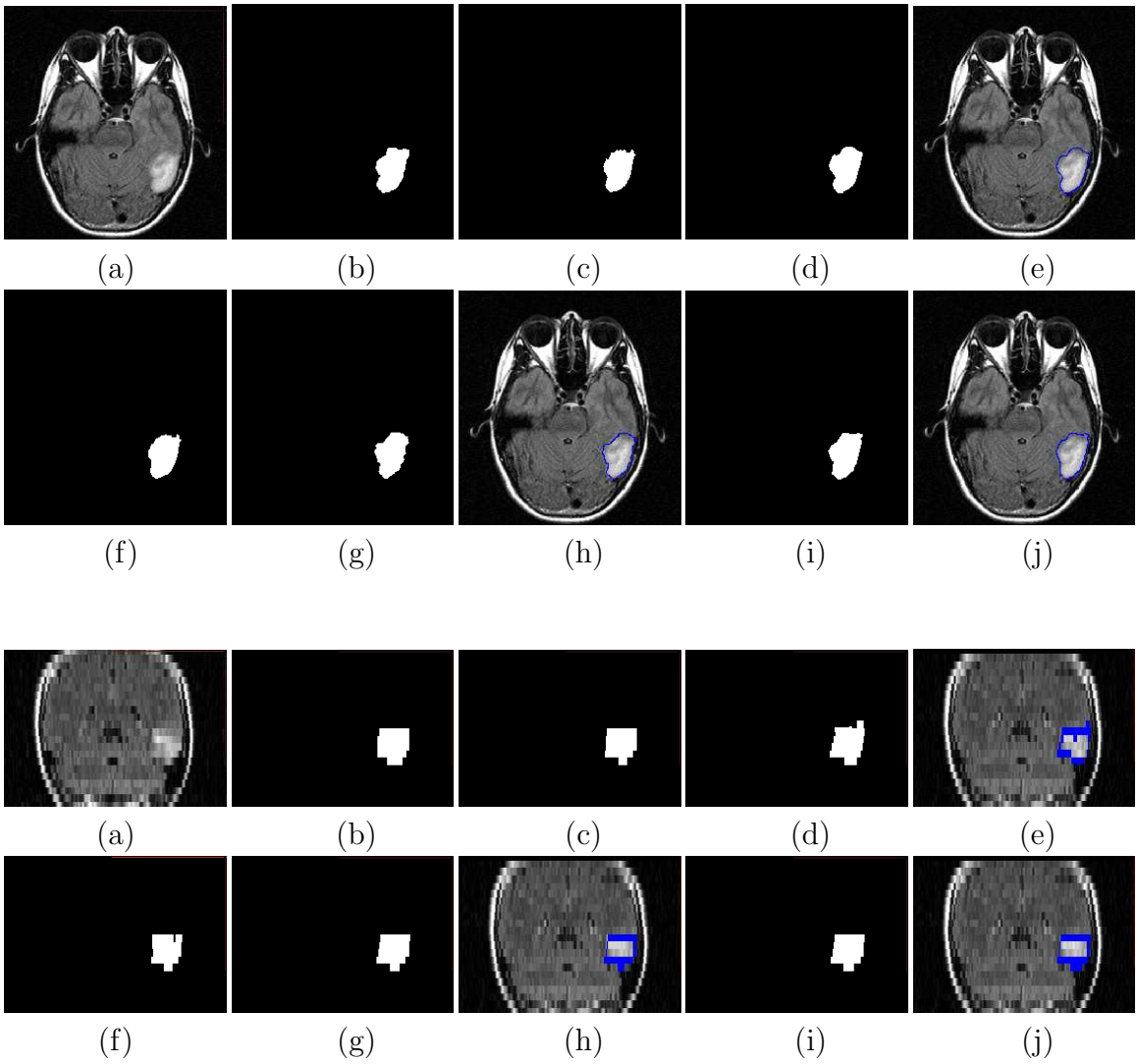

Figure 4.36: Comparison of manual and automatic segmentation results using symmetry analysis and MPFCM for a tumor on a FLAIR image (an axial and a coronal slice). (a) Original image. (b) Manual segmentation. (c) Initial segmentation by MPFCM. (d) Refined segmentation of MPFCM. (e) Result superimposed on the original image. (f) Initial segmentation by symmetry analysis. (g) Refined segmentation of symmetry analysis by deformable model without spatial relations. (h) Result superimposed on the original image. (i) Refined segmentation of symmetry analysis by deformable model with spatial relations. (j) Result superimposed on the original image.

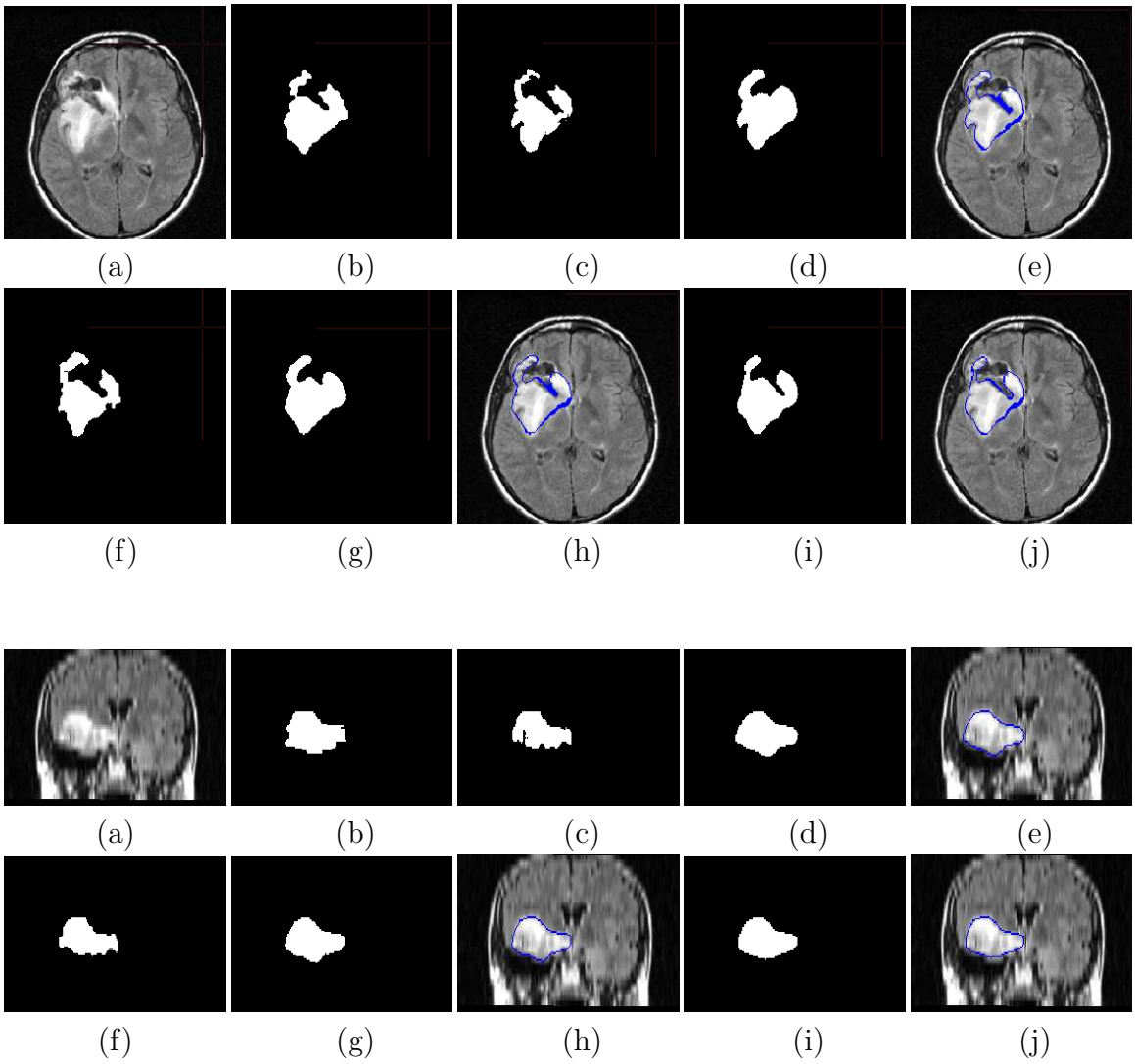

Figure 4.37: Comparison of manual and automatic segmentation results using symmetry analysis and MPFCM for a tumor on a FLAIR image (an axial and a coronal slice). (a) Original image. (b) Manual segmentation. (c) Initial segmentation by MPFCM. (d) Refined segmentation of MPFCM. (e) Result superimposed on the original image. (f) Initial segmentation by symmetry analysis. (g) Refined segmentation of symmetry analysis by deformable model without spatial relations. (h) Result superimposed on the original image. (i) Refined segmentation of symmetry analysis by deformable model with spatial relations. (j) Result superimposed on the original image.

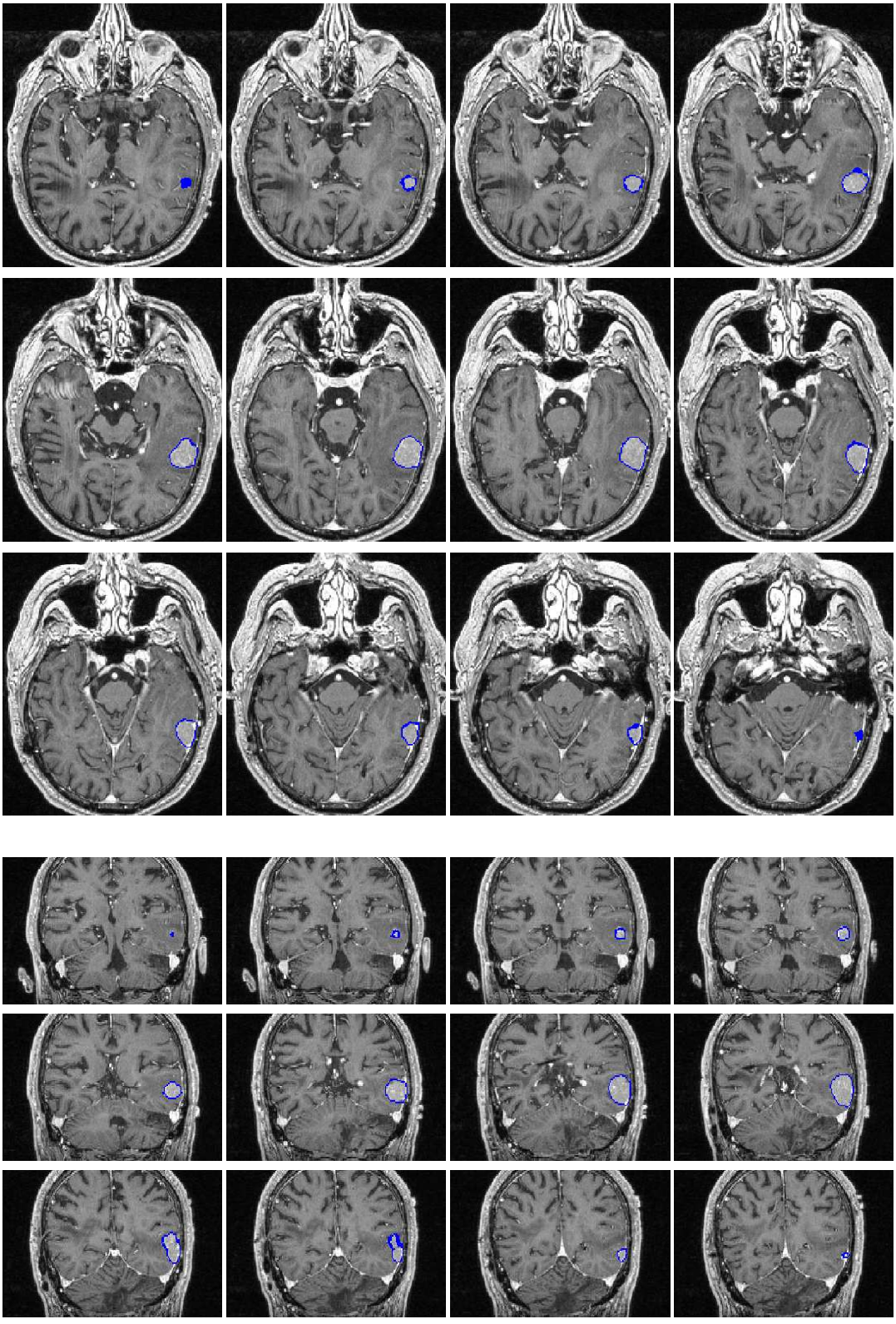

Figure 4.38: Axial and coronal slices of a segmented tumor (full-enhanced) in a CE-T1w image by symmetry analysis and deformable model constrained by spatial relations.

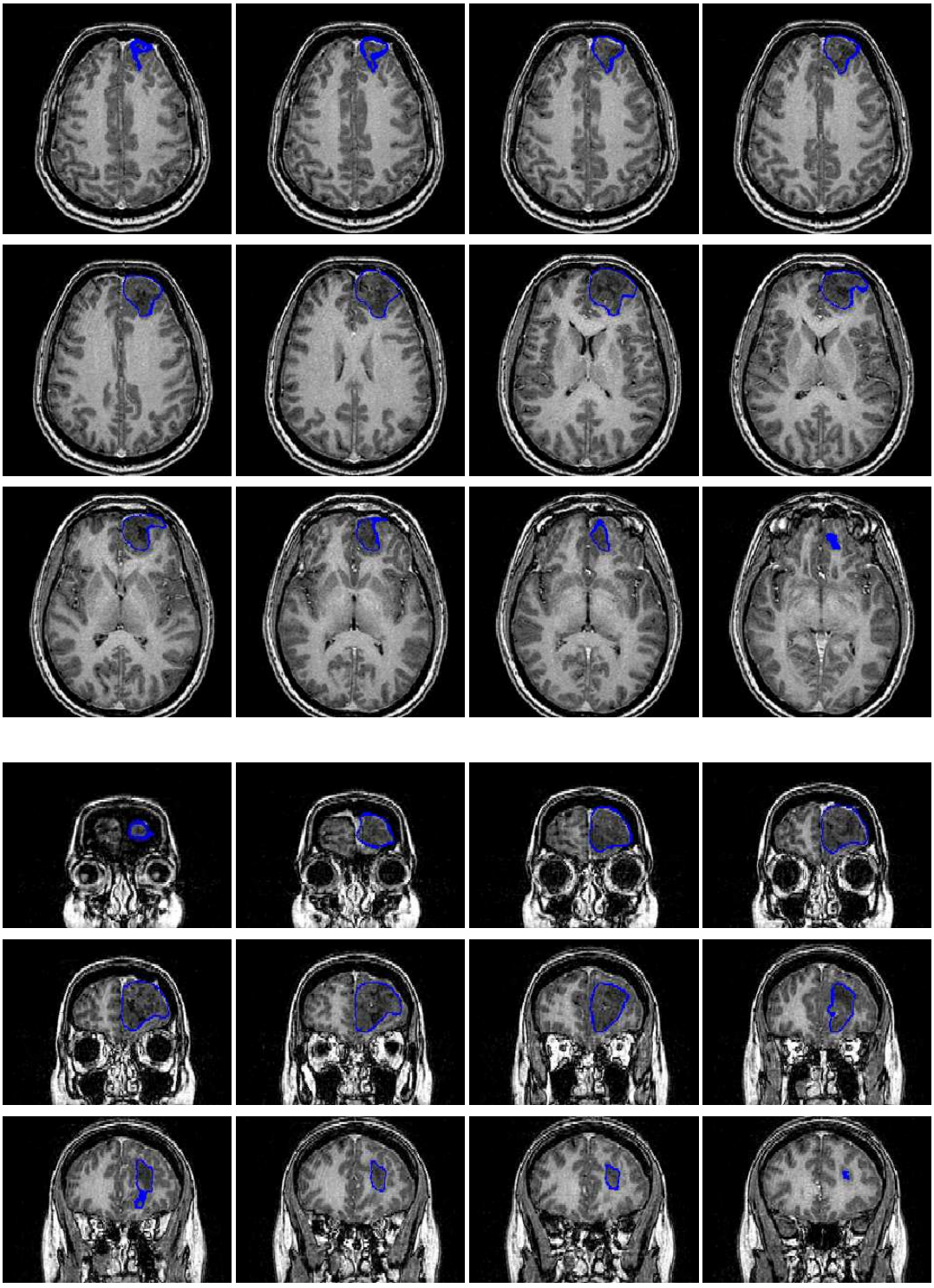

Figure 4.39: Axial and coronal slices of a segmented tumor (non-enhanced) in a CE-T1w image by symmetry analysis and deformable model constrained by spatial relations.

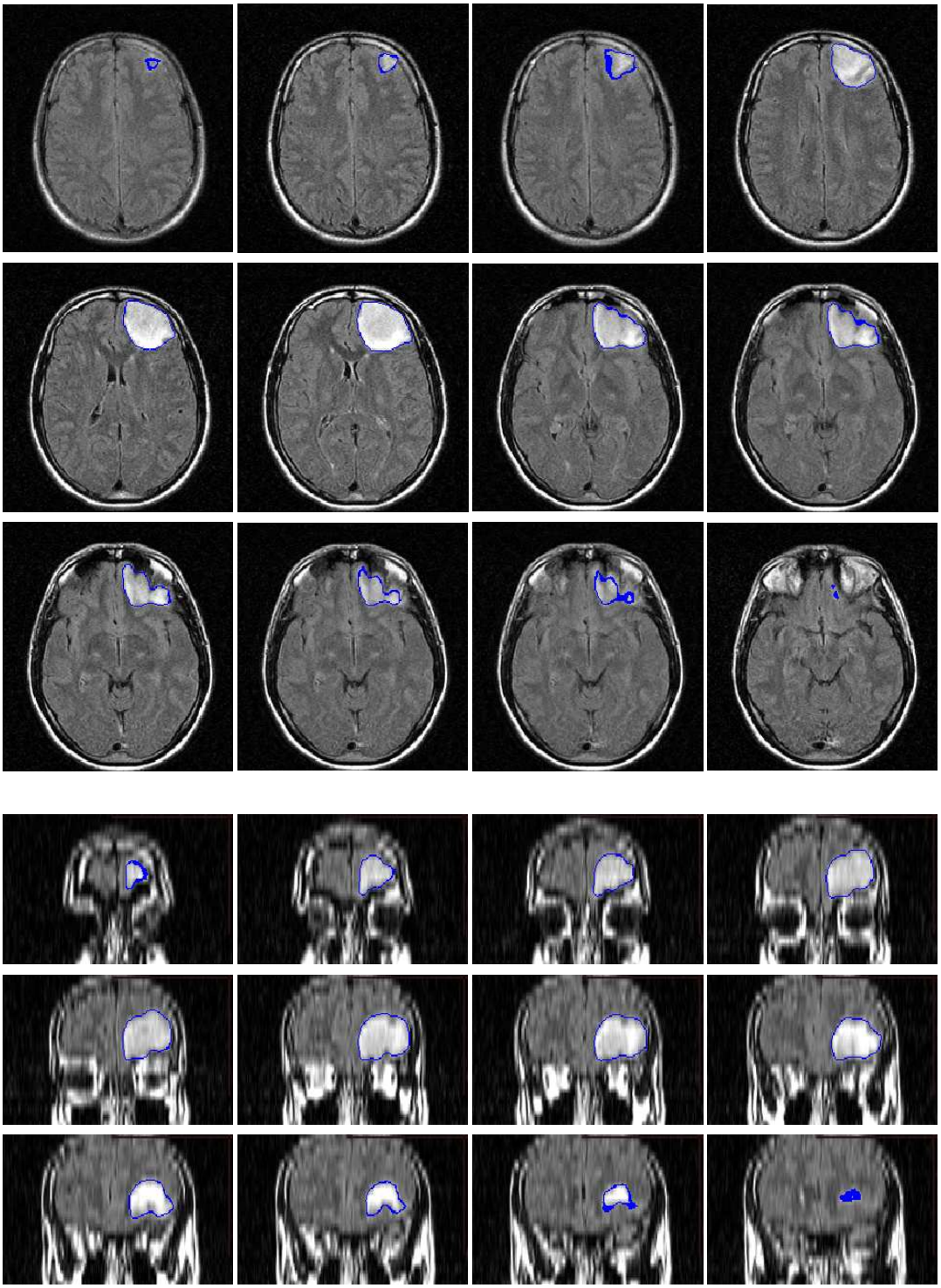

Figure 4.40: Axial and coronal slices of a segmented tumor in a FLAIR image by symmetry analysis and deformable model constrained by spatial relations.

CHAPTER 5

Segmentation of Internal Brain Structures

5.1 Introduction

We present in this chapter an original extension of a segmentation framework based on prior spatial relations, initially derived for normal internal brain structures, to cases with brain tumors. In brain oncology, especially when dealing with brain tumors, it is desirable to have a descriptive human brain model that can integrate tumor information extracted from MRI data such as its localization, its type, its shape, its anatomo-functional positioning, as well as its influence over the surrounding brain structures (through their spatial relations for example). There is a large literature reporting works on segmentation of either cerebral structures or tumors but rarely both at the same time. This chapter tries to fill this gap, by addressing the problem of segmenting internal brain structures in the presence of a tumor, via the modeling of its influence on the spatial relations between surrounding structures.

This chapter is organized as follows: in Section 5.2 we briefly review the presented methods for brain structures segmentation in normal and pathological cases. Section 5.3 provides an overview of the proposed method. In Section 5.4 we describe the structure of a priori knowledge which is used in our system. Fuzzification of spatial relations are presented in Section 5.5. In Section 5.6 we describe how to classify the tumors and determine the spatial relations that remain useful for each class of tumors. Section 5.7 describes the segmentation method. In Section 5.8 evaluation and results are presented. Finally in Section 5.9 some conclusions are given.

5.2 Brain structures segmentation: a survey

As we surveyed in Chapter 2, a large amount of methods have been proposed for brain tumor segmentation. In the literature a lot of approaches have been also introduced for segmenting the brain structures. But only a few methods have been proposed for segmenting both at the same time. In this section we briefly review the existing methods for segmentation of brain structures in normal cases and we then survey the methods for pathological cases.

Because of the lack of clearly defined edges due to intensity inhomogeneity, partial volume effects and noise, the brain structures segmentation is a challenging task that will not be accomplished by algorithms that rely solely on information present in the image. Hence most recent methods use prior information and we restrict our presentation to these approaches. This prior information can be explicit or implicit. Here we partition the existing methods based on the type of prior information. We can distinguish three main types of methods: atlas based, template based and spatial relation based.

Atlas based

Atlas information is an important type of prior information which is widely used in brain MRI segmentation. In Section 2.2.4 we presented the principal and different types of atlas-based segmentation and here we review the existing methods for the brain structures segmentation.

[Collins, 1994] used a non-linear registration relying on the local correlation of gradients. The atlas is created from the mean of 305 brain images. [Iosifescu et al., 1997] performed tissue classification by separating voxels into white matter, cerebrospinal fluid, subcortical and non-subcortical gray matter. A manually delineated digital atlas was then warped to the classified image using an inelastic registration followed by an elastic registration. This method was applied to segment the thalamus, caudate and putamen. [Geraud, 1998] presented another method using sequential registration. First, one of the structures whose segmentation is easy (for example lateral ventricle) is segmented. The deformation field between the atlas and the target image is then calculated by registering the segmented structure and its corresponding structure in the atlas. Using the information of atlas (anatomical and morphological) and the radiometric characteristics, a new interesting structure is segmented in its ROI. The ROI is obtained by dilating the corresponding structure in the atlas on the image space. The deformation field is then updated. This procedure is repeated for other structures.

A global-local registration procedure was proposed by [Dawant et al., 1999a]. A global registration using mutual information maximization and a local non-linear registration with demons method [Thirion, 1998] are used to match the structures of atlas

and target image. [Bach Cuadra et al., 2001] proposed a similar method using an optical flow algorithm for local deformations. A level sets method which is initialized by an atlas (the atlas is registered by a dense registration to the target image) was proposed by [Baillard et al., 2001]. This method was then extended by [Ciofolo et al., 2004] with an automated tuning of the parameters using a fuzzy control approach. [Xue et al., 2001] used the Talairach stereotaxic atlas registration followed by a genetic algorithm to label the brain structures. [Magnotta et al., 2003] proposed a registration method which uses 35 identified cortical and cerebellar landmarks by experts, subcortical and cerebellar structures defined semi-automatically by an artificial neural network, classified images (generated using a discriminant analysis of T1, T2, and PD images to distinguish the main tissues) and an intensity normalized image. These four groups are co-registered to the target image by inverse-consistent linear elastic registration. [Linguraru et al., 2007] proposed an approach which is a combination of rigid, affine and non-rigid registration, segmentation of the key anatomical landmarks and propagation of the information of the atlas to detect the internal brain structures.

These methods have typically a high level of automation and provide a good quality of segmentation. The main drawback is the computation time which limits their application domain. Another problem is the segmentation of small structures. In these methods the accuracy of segmentation for small structures is lower and often a little deformation in the brain structures will lead to a wrong result. The adaptation of these methods to segment pathological brains is also very difficult, because a large deformation of the brain due to a pathology influences the segmentation which may then fail.

Template based

These methods use a deformable model while a priori knowledge about the shape, the location or the appearance of the target structure can be used to guide the deformation process. They differ in the type of deformable model, the parameters of the shape model and the learning method of the parameters. Based on the type of knowledge, the methods can be partitioned into explicit or implicit ones.

[Poupon et al., 1998] proposed the use of 3D moment invariants as a way to embed shape distribution in deformable templates. Their approach is able to deal with several simultaneously deforming templates. The aim of the method is dedicated to the segmentation of the brain deep nuclei in normal 3D MR images.

[Cootes et al., 1995] developed active shape models which restrict the possible deformations using the statistics of training samples. Object shapes are described by the point distribution model (PDM) which represents the object outline by a subset of boundary points and a series of relationships established between these points from different instances of the training set. The basis for the statistical analysis of the object shape deformations is provided by normalization with respect to size, orientation, and

position. The variation modes and positions of mean point are used to constrain the object deformations to an acceptable linear subspace of the complete parameter space. To characterize the anatomical shape variability, principal component analysis (PCA) has also been used. Many variants of active shape models have been presented in the literature. For example [Duta and Sonka, 1998] used the intensity, contours and mean position to describe the objects. The shape statistics are learned from 8 images. [Kelemen et al., 1999] used a hierarchical parametric object description by a series of spherical harmonics rather than a point distribution model. [Nain et al., 2007] proposed a similar method using a spherical wavelet shape representation. [Shen et al., 2001] attached an attribute vector to each point of the model to incorporate geometric as well as statistical information about the shapes of interest. It is used to characterize the geometric structure of the model around that point, from a local to a global scale.

In [Pitiot et al., 2002] a template is modeled by using a parameterized curve whose coefficients are iteratively updated to minimize an objective function. The match between the deformed template and a modified edge image, and the elastic deformation energy (required in the warping process) are measured by this function.

[Belitz et al., 2006] proposed an approach which combines a deformable model using topological constraints for automated segmentation of subcortical structures. A coarse shape description generated from a digital atlas is used in this approach.

In [Yang et al., 2004] a 3D segmentation method with joint shape-intensity prior models using level sets is developed. These models are based on the maximum a posteriori (MAP) estimation whose accuracy depends on the chosen probability density function, and the shape-model parameters are optimized using a gradient descent search algorithm.

[Hu and Collins, 2007] developed similar work which handles topological changes during the level set curve evolution and takes advantage of intensity and texture information using prior training data. The actual segmentation is controlled by a set of model parameters, adjusted during a search optimization procedure, that minimizes the difference between any test image and the one synthesized from the shape and appearance modeling.

[Taron et al., 2005a] introduced a new technique using higher order implicit polynomials to represent shapes. First uncertainties on the registered shapes are estimated according to the covariance matrix of the correspondences at the zero isosurface. These measures are then used with a variable bandwidth kernel-based nonparametric density estimation process to model prior knowledge about the object of interest. Such a nonlinear model is integrated with an adaptive visual-driven data term to segment the object of interest. This method was then applied for the segmentation of the corpus callosum in MR mid-sagittal brain slices [Taron et al., 2005b].

Although these methods take into account the variability of anatomical structures,

their adaptation to pathological cases is still difficult. The learning of the shape parameters is another problem of these methods. This phase usually needs a segmentation by experts and takes a lot of time.

Spatial relation based

This category includes the methods which use spatial relations to guide the recognition and segmentation process. Spatial relations constitute the basic elements contained in linguistic descriptions of spatial configurations and describe the organization of the different objects in an image. These relations are usually classified into different types including topological, distance and directional relations [Freeman, 1975]. These relations provide structural knowledge in image analysis. Their ability to describe scenes makes them potentially useful for a wide range of imaging applications.

The idea of using spatial relations for brain structures segmentation is first introduced by [Geraud, 1998 ; Bloch et al., 2003]. [Bloch, 2005 ; Colliot et al., 2006] proposed a fuzzy framework to model the spatial relations. Since they correspond to linguistic propositions, spatial relations are often intrinsically imprecise and fuzzy sets allow modeling this imprecision . The satisfaction of a given relation will be defined as a matter of degree rather than in an "all-or-nothing" manner. Moreover, fuzzy sets provide a common framework to represent different types of individual spatial relations and the relations can be easily combined using fuzzy fusion operators [Bloch, 2005].

[Geraud, 1998] proposed a method for cerebral structures segmentation which combines the spatial relations to a possibilistic clustering approach using a fusion framework. This method uses spatial relations for high-level tasks (recognition) and is not directly integrated in the segmentation itself which is based only on image characteristics. However, spatial relations could be helpful to find the contours of poorly contrasted objects, with ill-defined boundaries or sharing similar intensities with their neighbors.

Several segmentation approaches implicitly integrate the spatial relationships between the objects of a scene. [Barra and Boire, 2001] used a similar method to segment the brain structures. In this method the relations are solely fused with the results of a possibilistic classification.

Recently [Colliot et al., 2006] have developed a new method which combines spatial relations and deformable models for pattern recognition purposes. Although in some methods in atlas based category such as [Dawant et al., 1999a] and in template based methods such as [Cootes et al., 1995] (and the variants of these methods) spatial relations are used, in these approaches the spatial relations are defined implicitly in either the template or the training set and are not specified individually. The method of [Colliot et al., 2006] integrates explicitly individual spatial relations in the segmentation process. This allows to model more directly expert knowledge expressed

as linguistic descriptions and to explicitly choose the constraints which will be included in the segmentation, for example keeping only the relations which are anatomically meaningful. This method provides very good and precise results for the segmentation of the internal structures in normal case.

Our proposed method for segmentation of brain structures in the presence of a tumor is based on the method of [Colliot et al., 2006] and we will explain this approach in more details in the next sections [Khotanlou et al., 2006; 2007a].

Other methods

In addition to the three reviewed categories, there are some other methods which use a priori information for segmentation.

[Worth et al., 1998 ; Fischl et al., 2002] proposed histogram-based methods to segment the brain structures. The former method involves choosing intensity thresholds by using anatomical information and by locating peaks in histograms. The later method uses a space-varying classification procedure (class statistics are tabulated regionally throughout an atlas space by a linear registration) and prior probabilities which are computed via a frequency histogram in the atlas space for segmentation. Because of intensity overlapping between brain structures in real images, generalization of these methods is very difficult. In addition, in pathological cases the histogram will be modified and the segmentation procedure will fail.

[Sonka et al., 1996] proposed a method based on a hypothesize-and-verify principle. The method begins with a primary segmentation step that divides the image into a large number of primary regions. A primary region adjacency graph is then constructed that describes the properties of each primary region. Finally a genetic algorithm is applied to generate a population of image interpretation hypotheses. It then decides to retain good hypotheses and eliminate poor hypotheses so that over a series of iterations the process converges to the optimal image interpretation. This method requires a learning procedure and can perform a segmentation in normal cases.

[Algorri and Flores-Mangas, 2004] presented an algorithm which uses a knowledge base taken from a small subset of semi-automatically classified images and a set of fuzzy indices. The fuzzy indices are tissue and position specific, in order to consider the biological variations in the tissues and the acquisition inhomogeneities through the image set. The algorithm uses low-level image processing techniques on a pixel basis for the segmentation, then corrects the segmentation by the set of fuzzy indices.

Several methods are proposed based on neural networks. For example [Shichun et al., 2005] used a fuzzy multi-layer perceptron (MLP) which allows to learn anatomical knowledge from a sample of brain scans. [Powell et al., 2008] performed a direct comparison between template, probability, artificial neural network and support vec-

tor machine (SVM) based segmentation methods. In addition to known problems of ANN, their adaptation to pathological cases is very difficult.

These methods are presented for segmentation in normal cases and most of them are validated on simulated images. Extractions to real images and especially pathological cases require to consider a lot of parameters and variables. Hence, application of these methods to pathological cases is difficult.

Pathological brain structures segmentation

A few of existing methods for brain structures segmentation are adapted to pathological cases. We have surveyed some of them in Section 2.2.4 when dealing with tumor segmentation. Here we briefly study them with respect to brain structures segmentation. All presented methods use the atlas prior information and a registration technique.

One of the first methods was proposed by [Kyriacou et al., 1999] in 2D. A biomechanical model of the brain is presented, using a finite-element formulation. The soft-tissue deformations induced by the growth of tumors is modeled and the model is applied to the registration of anatomical atlases with images from patients. First, based on the tumor growth model an estimate of the anatomy is obtained. A normal atlas registration to this estimated without-tumor anatomy is then applied. Finally the registered atlas is modified by applying the deformation from the tumor growth model. The resulting atlas is then fully registered to the patient image. The tumor growth is modeled in a non-linear optimization framework, which is driven by anatomical features such as boundaries of brain structures. The deformation of the surrounding tissues is estimated using a nonlinear elastic model of soft tissues under boundary conditions imposed by the skull, ventricles, and the falx and tentorium. This method was later improved by [Mohamed et al., 2005] for 3D cases by optimizing the computation time.

This method has several limitations. The biomechanical characteristics of normal tissues are required for the modeling step while they are unknown for an actual patient. In addition, mechanical properties of the tumors are generally unknown, and we cannot measure them for the patient. The second drawback comes from the fact that the method has not accounted for tumor infiltration and edema. This method is designed for mass-effect tumors. The factors that are not mechanical in nature (tumor infiltration and edema spread), may also play a role in determining the tumor shape and may cause it to deviate from radial symmetry. Another complication associated with the deformable registration is the significant signal changes associated with edema in MR images. Edema typically causes hypointensity changes in T1-weighted images, which makes it difficult to discern cortical sulci in the affected brain regions. It is therefore not possible to obtain an accurate deformable registration in these regions based on image matching alone. Finally, calculations may take a few hours depending on reso-

lution and accuracy without a guarantee for the algorithm convergence [Nowinski and Belov, 2005].

[Dawant et al., 1999b; 2002] adapted their method for normal cases [Dawant et al., 1999a] to pathological brains by adding the seeded atlas deformation (SAD) technique. In this method after the global registration, the user places a small seed in the lesion region with the same intensity. Then the demons algorithm is applied to deform the seed toward the boundary of the lesion. This approach has some limitations. First, the consistency of the deformation field is controlled by a smoothing filter, and if it is not chosen correctly, the resulting transformation can be wrong. The lack of an explicit underlying mathematical model is also the potential weakness of this approach. As for the previous method, this approach performs well in the cases of mass-effect tumors. In the presence of a large deformation of brain structures, it will also fail. Finally, it requires to use a large seed that masks atlas structures, potentially leading to wrong results.

Based on the method of [Dawant et al., 1999a] several approaches are presented. [Bach Cuadra et al., 2004] and [Pollo et al., 2005] developed a method using an a priori model of tumor growth inside the tumor area (which assumes that the tumor has grown radially from a single voxel seed) instead of applying the nonlinear registration algorithm to the whole image. Compared to the previous approach, this minimizes the amount of atlas information that is masked by the tumor seed. An explicit model of tumor growth (MLG) into the seeded atlas deformation (SAD) algorithm is introduced.

The main limitation of this method is the assumption of radially expansion of the lesion, while only a few classes of tumors have a radial expansion. The deformation accuracy of surrounding brain structures depends on the placement of the tumor seeding point. Generalization of this method is impossible because considering all the possible space-occupying lesions in a unified framework is almost impossible. Here also the infiltration and edema have not been considered and computation time is also relatively high.

[Nowinski and Belov, 2005] presented a fast method that uses a region growing method for tumor segmentation. First the Talairach landmarks are set in the image and the standard Talairach transformation is performed. The tumor is then segmented based on its radiological (intensity) characteristics by a region growing algorithm (it requires a click over the tumor). Finally it warps the atlas against the tumor nonlinearly.

The advantage of this approach is that it warps the atlas non-linearly in three dimensions very fast. But this method has also several limitations. First of all the accuracy of tumor segmentation depends on the position of the selected point. The region growing can segment only homogeneous tumors. Finally, the effect of edema and infiltration over the structures is not taken into account.

In summary, a few methods have been proposed for segmentation of tumor and

brain structures simultaneously, all based on atlas registration and implicitly use the spatial relations between the structures. These methods have several common limitation. In all of them, edema and infiltrating tumors have been not considered, hence the segmentation of the structures around the tumor will not be correct. Another problem is the computation time. Registration and modeling the tumor both require a large amount of computation, therefore their application is limited. Finally, in the case of a large deformation of the brain structures these methods do not perform correctly.

In the remaining of this chapter we propose a method for segmentation of the brain structures which uses the spatial relations between the structures in an explicit form.

5.3 Method overview

The computational paradigm proposed in our method is based on previous work by [Colliot et al., 2006] introducing a framework for the integration of spatial relations into a deformable model, to segment normal brain structures in MRI data. Spatial relations, such as directions and distances, were represented as fuzzy subsets of the image space and incorporated into a deformable model as external forces. In this chapter we extend this framework to pathological cases, where the presence of a tumor may induce important alterations of the iconic and morphometric characteristics of the surrounding structures. By understanding the spatial behavior of the tumor and its incidence on the surrounding structures (small or large deformations), we discuss the preservation of some spatial relations used for recognition and segmentation tasks.

As illustrated in Figure 5.1, the proposed framework relies on a knowledge base that is constituted of a tumor ontology, a brain anatomy ontology, a spatial relation ontology and brain structures descriptions. Using the information on the segmented tumor and its components we select the spatial relations corresponding to the structure of interest which have remained consistent. In the next step the fuzzification and fusion of the selected spatial relations, using the fuzzy framework proposed by [Bloch, 2005 ; Colliot et al., 2006], are performed. We then use the fused spatial relation to guide the segmentation of the interesting structure by a deformable model. This procedure can be repeated for other structures and finally we integrate or model the results of the segmentation (tumor and structures). This part of our work has been developed in collaboration with Jamal Atif and Céline Hudelot during their post doctoral stay at ENST.

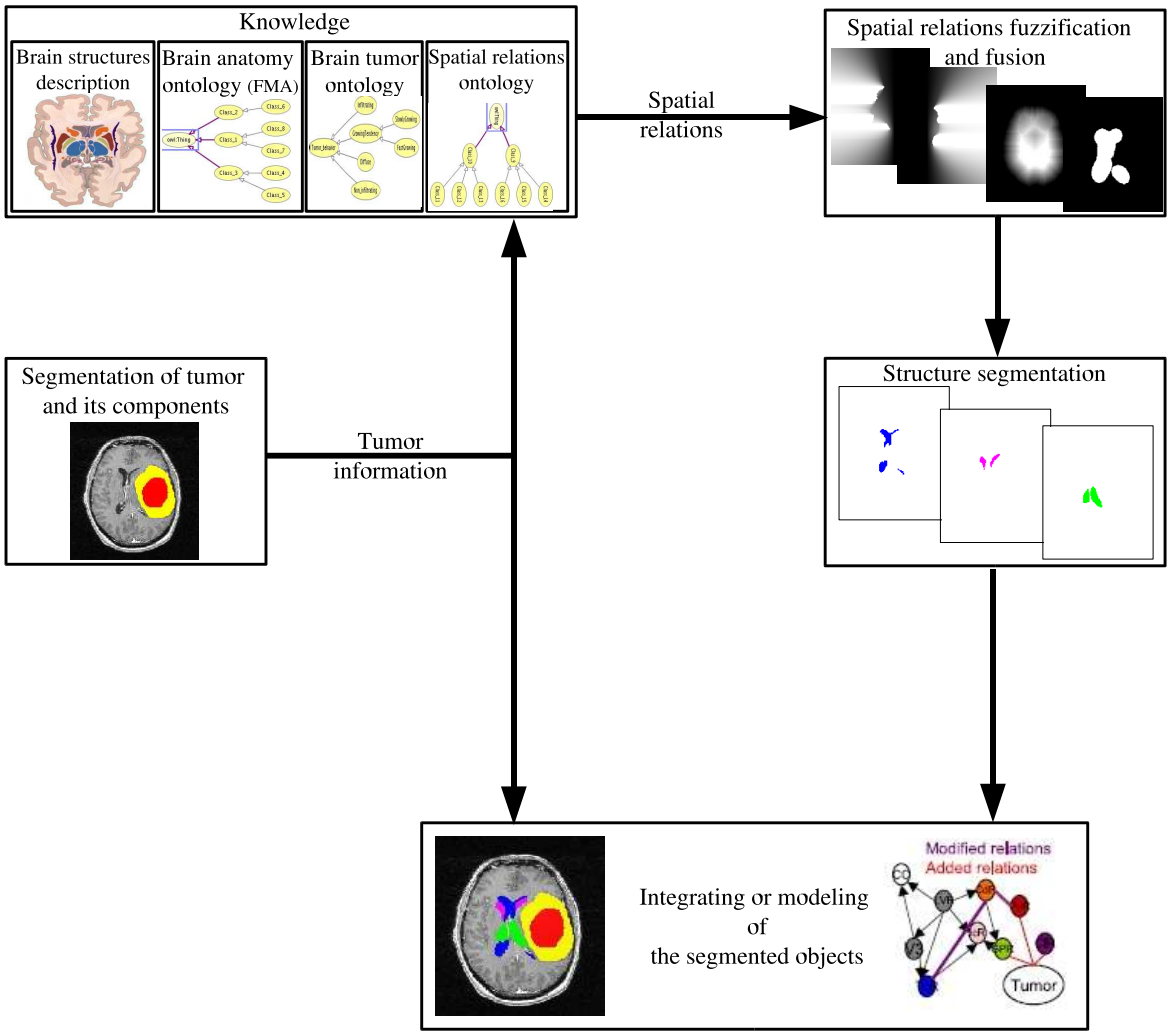

Figure 5.1: The segmentation method diagram.

5.4 A priori knowledge

5.4.1 Ontological engineering

The idea of representing knowledge in a structured manner is at least as old as Aristole, who tried in a systematic method to represent the structure of reality. In recent years ontology has become a common systematic method to represent knowledge. Within the artificial intelligence domain, [Gruber, 1993] has given the first definition of the notion ontology as: "an ontology is an explicit specification of a conceptualization". An ontology is a representation of concepts and relations between them. Ontology engineering is a set of operations that concern the ontology development process, the ontology life cycle, the methods for building ontologies, and the tools and languages that support them [Gomez-Perez et al., 2004]. Here we do not focus on the ontology

engineering and more information can be found in [Gomez-Perez et al., 2004 ; Cristani and Cuel, 2005 ; Corcho et al., 2003].

Ontologies have some advantages which make them interesting in knowledge representation. Sharing common understanding of the structure of information, enabling reuse of domain knowledge, making explicit domain assumption and separating the domain knowledge from the operational knowledge are some of these advantages. In recent years, ontologies have been widely used in several domains for knowledge representation. In the medical domain, for formalization of anatomical or pathological knowledge, several works can be found in [Dameron et al., 2004 ; Donnelly et al., 2006 ; Schulz et al., 2000 ; Marquet et al., 2007 ; Tolksdorf and Bontas, 2004]. Some interesting works on spatial ontologies can also be found in Geographic Information Systems (GIS) [Casati et al., 2003 ; Klien and Lutz, 2005] and in robotics [Dominey et al., 2004].

In the domain of image analysis and pattern recognition, ontologies are increasingly used. For example [Dasiopoulou et al., 2005] proposed an approach for video object detection based on a multimedia ontology. In this method semantic concepts in the context of the examined domain are defined in an ontology with qualitative attributes (color homogeneity), low-level features (color model components distribution), object spatial relations, and multimedia processing methods. [Han et al., 2005] developed a generic ontology of objects. Objects are represented as sets of functional features and their spatial relations. They have also developed a generic geometric shape based object recognition. [Maillot and Thonnat, 2007] proposed an ontology-based object recognition which uses a priori knowledge consisting of a visual concept ontology, a texture concept ontology, a color concept ontology and a spatial relation concept ontology. [Nientiedt, 2007] presented a framework to examine the semantics of land-use and land-cover change. The proposed method uses the semantic description of spatial entities as well as the entity of change. A multi-level concept of action-driven ontologies and notions from an image ontology were adapted to the use case of land-use pattern change. Recently [Hudelot et al., 2007] presented a fuzzy spatial relation ontology for medical image segmentation.

Here our aim is to link an ontology containing anatomical knowledge with an ontology of spatial relations in order to represent the spatial relationships of each anatomical structure of the brain to other ones. In the next section we explain the anatomical and spatial relation ontologies in our prior knowledge representation system.

5.4.2 The reference ontology for biomedical informatics (FMA)

Domain reference ontologies represent knowledge about a particular part of the world in a way that is independent from specific objectives, through a theory of the domain [Burgun, 2006]. An example of the reference ontology in biomedical informatics is the Foundational Model of Anatomy (FMA) [Rosse and Mejino, 2003]. The FMA

is concerned with the representation of entities and relationships necessary for the symbolic modeling of the structure of the human body in a numerical form that is also meaningful for humans. The FMA includes an anatomy taxonomy, which specifies the subsumption relationships of anatomical entities, and an anatomical structural abstraction, which specifies the spatial relationships of the anatomical entities. The ontology is implemented in a frame-based system and is stored in a relational database. The FMA is intended as a reusable and generalizable resource of deep anatomical knowledge, which can be filtered to meet the needs of any knowledge-based application that requires structural information. It is distinct from application ontologies in that it is not intended as an end-user application and does not target the needs of any particular user group. Figure 5.2 illustrates a part of the FMA which was visualized by Protégé [Protégé, 2007].

In the FMA, spatial relations between anatomical structures are represented implicitly. Here we need to represent the spatial relations explicitly. Hence we first represent a spatial relation ontology and we then link it to the FMA to represent the spatial relations of each structure explicitly as proposed in [Hudelot et al., 2007].

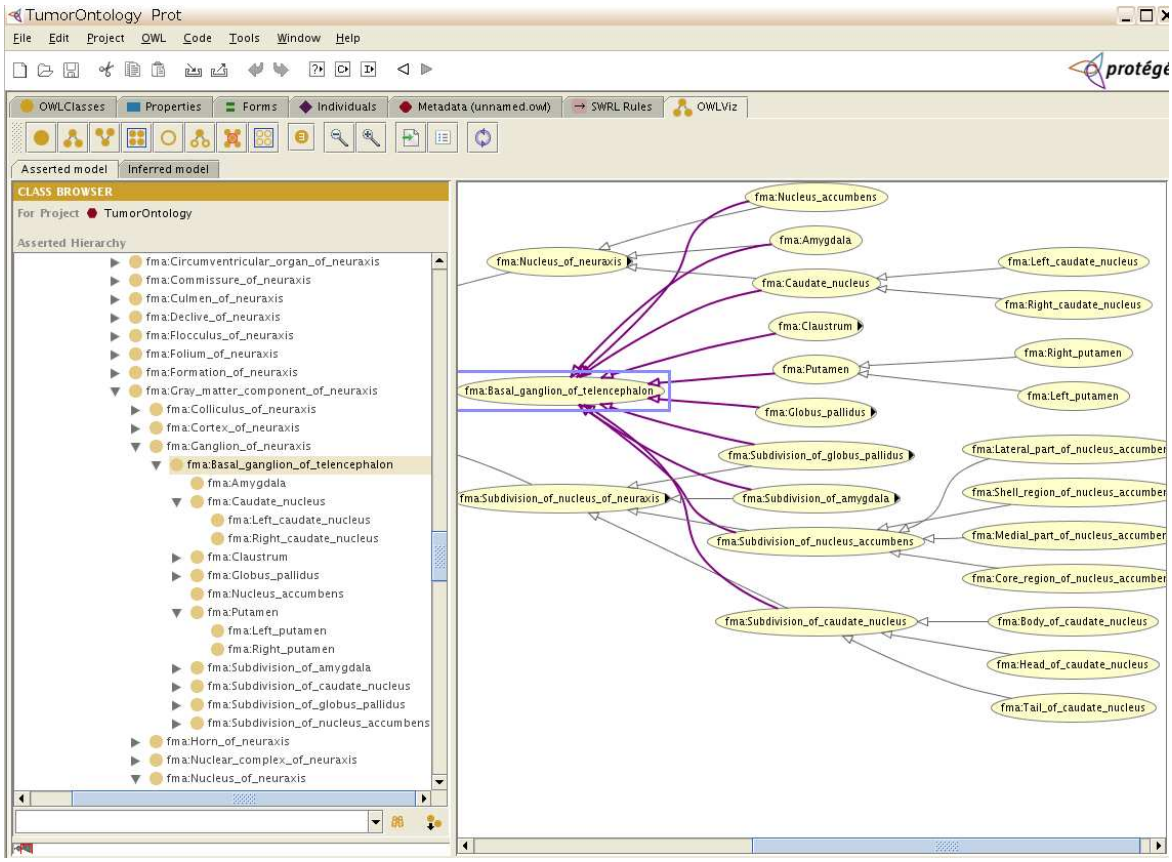

Figure 5.2: A part of the FMA ontology [Rosse and Mejino, 2003] visualized by Protégé [Protégé, 2007].

5.4.3 Spatial relation ontology

Spatial relations between objects play a main role for analysis and recognition in a scene or image, especially in a complex environment like in medical images. To represent explicitly the spatial relations of an anatomical structure we need to integrate an ontology of spatial relations into the FMA. Recently our group has developed a generic spatial relation ontology [Hudelot et al., 2007]. It is a spatial ontology which represents topological and metric relations based on a reference object. An excerpt of the hierarchical organization of spatial relations is illustrated in Figure 5.3.

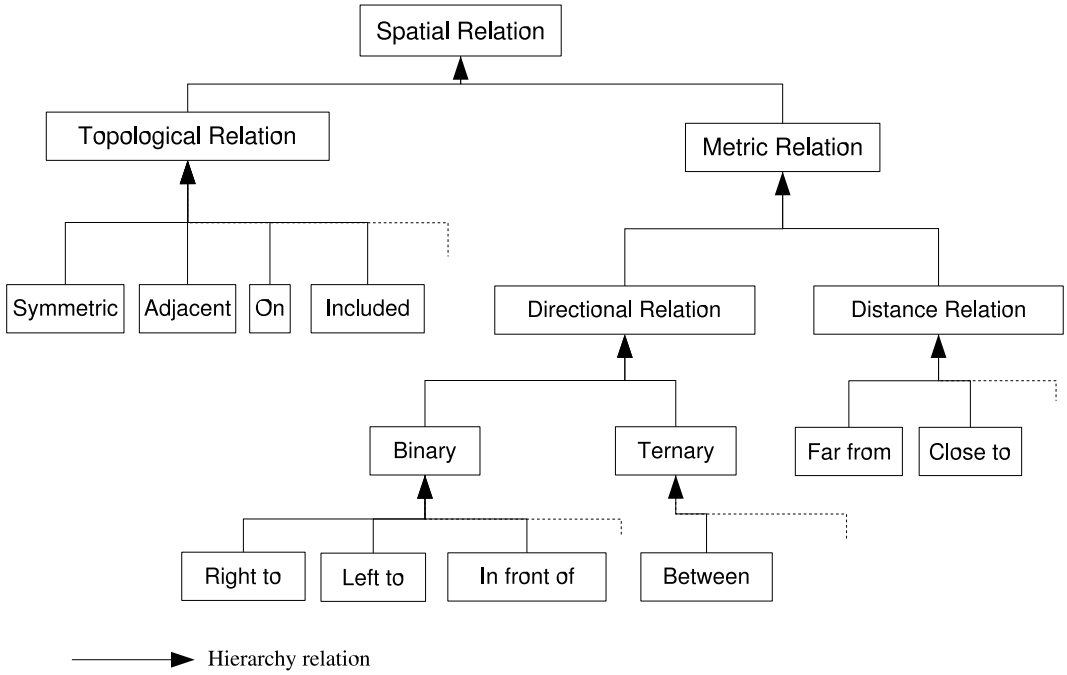

Figure 5.3: Excerpt of the hierarchical organization of spatial relations in the ontology of spatial relations. Regenerated from [Hudelot et al., 2007].

The ontology of spatial relations has been developed with the software Protégé OWL and has the following entities (illustrated in Figure 5.4 as a Venn diagram) :

- ***SpatialObject*** is the main entity of the ontology and refers to the set of spatial objects.
- ***SpatialRelation*** is subsumed by the general concept ***Relation***. It is defined according to a ***ReferenceSystem***. In this ontology a spatial relation is not considered as a role (property) between two spatial objects but as a concept on its own (***SpatialRelation***).
- ***SpatialRelationWith*** refers to the set of spatial relations which are defined according to at least one or more reference spatial objects.

- ***SpatiallyRelatedObject*** refers to the set of spatial objects which have at least one spatial relation with another spatial object.
- ***DefinedSpatialRelation*** represents the set of spatial relations for which target and reference objects are defined.

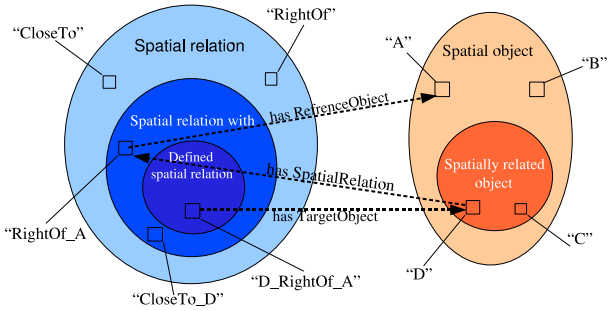

Figure 5.4: Main concepts of the spatial relation ontology. This diagram represent the main concepts and their relations. For example "A" is a ***SpatialObject***, it is the ***ReferenceObject*** of the ***SpatialRelationWith*** concept "RightOf_A". "D" is a ***SpatialObject*** which has the property of having as ***SpatialRelation*** the relation "RightOf_A" [Hudelot et al., 2007].

To link the FMA with the spatial relation ontology, we consider that each physical anatomical component is a spatial object. Spatial relations between these different spatial objects are then described by using the spatial relation ontology. One example of this link for the left caudate nucleus and the right thalamus is illustrated in Figure 5.5.

5.5 Spatial relations representation

Our aim here is to integrate spatial relations in a deformable model, so it requires to provide a computational representation of the relations. As seen in Section 5.4.3 making spatial relations explicit, in particular metric relations, requires a reference system. So, we consider spatial relations that define the position of a target object with respect to a reference object. Fuzzy sets in the spatial domain are appropriate for this case. In these representations, the membership value at each point represents the degree to which the relation is satisfied. The following representations of spatial relations are based on a framework presented by [Bloch, 2005 ; Colliot et al., 2006].

A spatial fuzzy set is a fuzzy set defined on the image space, denoted by $\mathcal{S}$, $\mathcal{S}$ being $\mathbb{Z}^2$ or $\mathbb{Z}^3$ for 2D or 3D images. Its membership function μ (defined from $\mathcal{S}$ into $[0, 1]$) represents the imprecision on the spatial definition of the object (its position, size, shape, boundaries, etc.). For each point P of $\mathcal{S}$ (pixel or voxel), $\mu(P)$ represents

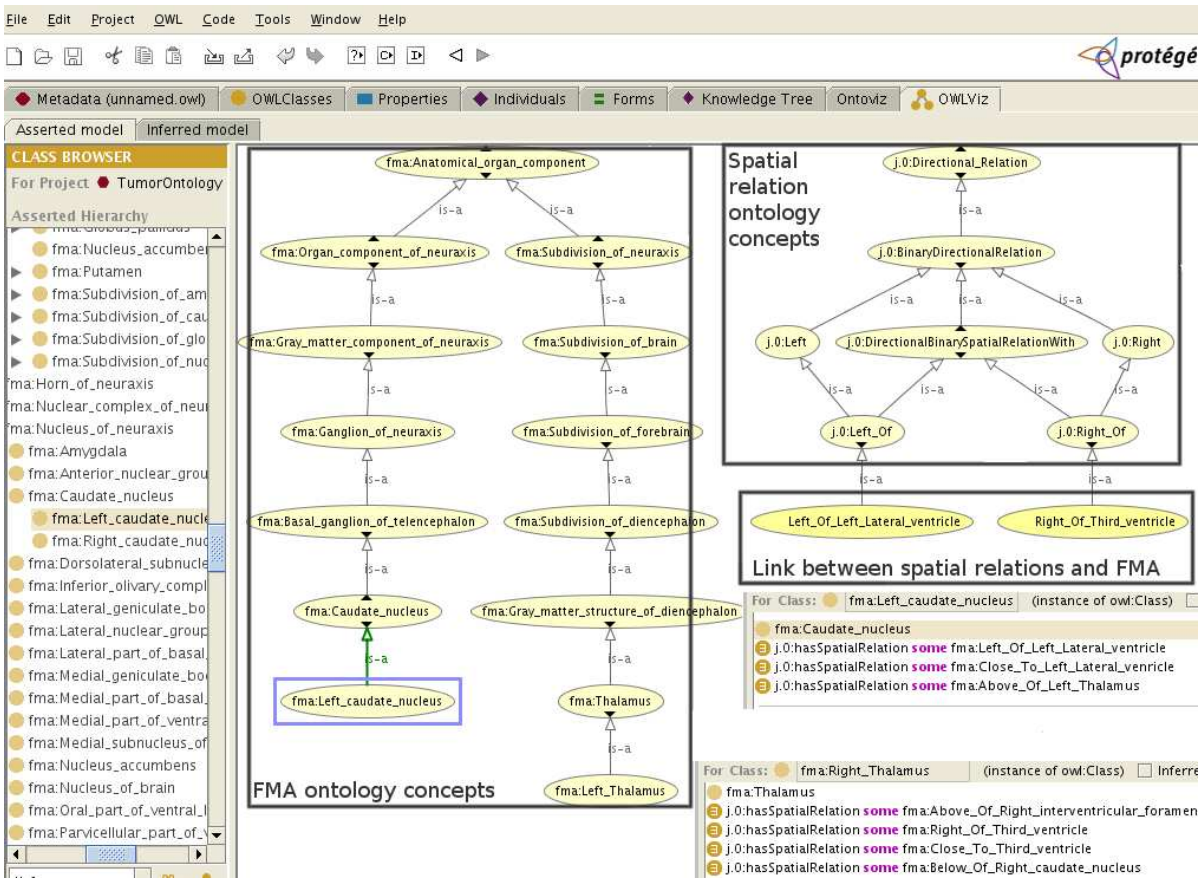

Figure 5.5: A part of the FMA ontology, the spatial relation ontology and the link between them (the concepts of the FMA and spatial relation ontology are prefixed by *fma* and *J.0*).

the degree to which P belongs to the fuzzy object. Objects defined as classical crisp sets are particular cases, where μ takes only values 0 and 1.

Topological relations Binary topological relations between two objects are based on notions of intersection, interior, exterior. Relations such as "intersects" (connection relation of the mereotopology), "in the interior of" (inclusion), "exterior to" (exclusion) can be simply defined from fuzzy set theoretical concepts (complementation c, t-norms t, t-conorms T [Dubois and Prade, 1980]). For example, it is possible to define the degree to which a fuzzy object ν is included in another one μ by [Bloch, 2005]:

$$\inf_{x \in \mathcal{S}} T(c(\nu(x)), \mu(x)).$$

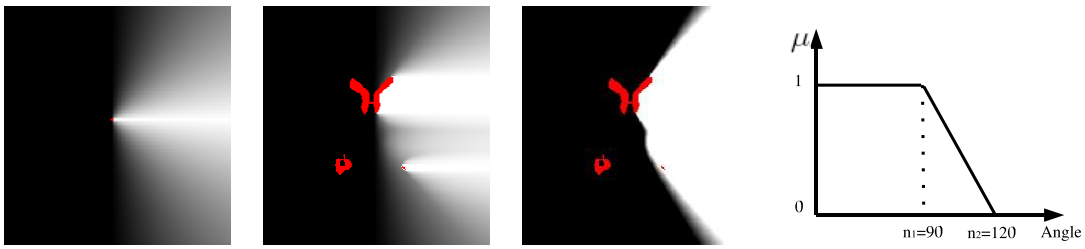

(a) (b) (c) (d)

Figure 5.6: Fuzzy set representing a directional relation. (a) Fuzzy structuring element representing "to the right of". (b) Fuzzy dilation of the lateral ventricle by the corresponding structuring element. (c) Fuzzy subset representing "right of the lateral ventricle". (d) Trapezoidal interval of the relation (c). (In all the images the brighter areas correspond to higher satisfaction degrees).

Directional relations The most used relations are related to three axes of references: "To the right of", "To the left of", "Above","Below", "In front of" and "Behind". We consider a reference object R and a directional relation to be evaluated. A fuzzy "landscape" is defined around the reference object R as a fuzzy set such that the membership value of each point corresponds to the degree of satisfaction of the considered spatial relation. This is formally defined by a fuzzy dilation of R by a fuzzy structuring element representing the desired relation with respect to the origin (Figure 5.6).

Let u be a unit vector corresponding to the direction under consideration, P be a point of space, Q a point of reference object R and $\beta(P,Q)$ the angle between vectors QP and u computed in $[0,\pi]$. For every point P the following function is defined [Bloch, 1999a]:

$$\beta_{min}(P) = \min_{Q \in R} \beta(P,Q)$$

and:

$$\mu_\alpha(P) = g(\beta_{min}(P))$$

is a fuzzy subset of the image space representing the relation (g is a decreasing function from $[0,\pi]$ to $[0,1]$). Bloch in [Bloch, 1999a] has shown that $\mu_\alpha(p)$ is equal to a fuzzy dilation of the reference object by a structuring element defined as:

$$\forall P \in \mathcal{S},\ \nu(P) = g(\beta_{min}(O,P)), \tag{5.1}$$

where O is the center of the structuring element. A common choice for g can be a trapezoidal interval (Figure 5.6 (d)). In Figure 5.6 the representation and fuzzification of the relation "right of the lateral ventricle" is illustrated.

Distances Distances are also very commonly used to describe the spatial arrangement of objects such as "At a distance approximately of", "Close to" and "Far from". To represent these relations by fuzzy sets, we use a fuzzy interval f of trapezoidal

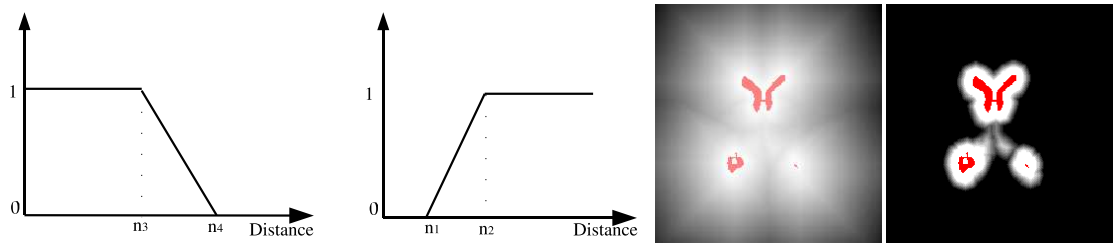

(a) (b) (c) (d)

Figure 5.7: Fuzzy set representing a distance relation. (a),(b) Fuzzy interval on the set of distances corresponding to relations "close to" and "far from". (c) Distance map of the lateral ventricle (this map is obtained by a fuzzy dilation using the distance structuring element). (d) Fuzzy subset representing "close to lateral ventricle" (here $n_3 = 10$ and $n_4 = 20$).

shape on the set of distances $\mathbb{R}^+$ [Bloch, 1999b] (Figure 5.7). The kernel of f is $[n_2, n_3]$ and its support is $[n_1, n_4]$, where $0 \leq n_1 \leq n_2 \leq n_3 \leq n_4$. For example for the "Close to" relation $n_1 = n_2 = 0$ and n_3 and n_4 are defined based on the minimum and maximum distances between target and reference objects where $n_3 > d_{min}(A, R)$ and $n_4 > d_{max}(A, R)$. To obtain a fuzzy subset of the image space, f is combined with a distance map d_R:

$$\mu_d(P) = f(d_R(P)).$$

Parameter learning For a given spatial relation, the parameters should be set so that the corresponding fuzzy set enclose the target object. In the case of the fuzzy intervals of trapezoidal shape, their kernel and their support are defined based on the maximum (or minimum) distance or angle. For the distance relation "Close to", the training consists in the computation of the maximum distance from a point P of the target object A to the reference object R. Similarly, for the relation "far from", the minimum distance is computed. For directions, the maximum value of $\beta_{min}(P)$ for points P in the target object A is calculated. The parameters are learned from an image data base where anatomical structures have been segmented. The mean m and standard deviation σ of maximum (or minimum) distance or $\beta_{min}(P)$ of the training set (computed from segmented image database) are computed. Fuzzy intervals are then chosen with kernel $[0, m]$ and support $[0, m + 2\sigma]$ [Colliot et al., 2006].

5.6 Tumor-specific spatial relations

The adaptation of the framework developed previously for normal images to pathological cases requires addressing the fundamental question: given a pathology, what kinds of spatial relations do remain consistent, with respect to the set of relevant relations

defined for normal cases? The answer depends on the type of tumor. In addition, learning the parameters for spatial relations is depended on the tumor type.

5.6.1 Tumor classification

We consider in this work a classification of brain tumors according to their spatial characteristics and the nature of the potential alterations of the brain structural organization they induce. We distinguish two main types tumors as explained in Section 1.9: small deforming tumors and large deforming tumors. Identifying the type of the tumor is based on the segmentation result.

For this purpose, we developed a simple ontology which allows classifying the tumor based on the information extracted from the segmentation results. The ontology of tumor classification has been developed with the software Protégé OWL and has the following entities (illustrated in Figure 5.8 as a Venn diagram):

- ***Disease*** which refers to the type of disease. Here we have a subclass ***Brain-Tumor***.
- ***Behavior*** refers to the behavior of disease. This class consists of the ***Infiltrating*** and ***Non-infiltrating*** subclasses.
- ***Location*** refers to the anatomical location of disease. We add the anatomical locations as the subclasses to this class.
- ***Appearance*** refers to the visual appearance of tumors on the contrast enhanced MR images. This class consists of 3 subclasses: ***Enhanced***, ***Ring-Enhanced*** and ***Non-Enhanced***.
- ***Component*** refers to the components of disease such as ***edema*** and ***necrosis***.
- ***Size*** refers to the size of tumor. Here we define three subclasses: ***SmallSize***, ***MiddleSize*** and ***BigSize***. The classification of tumor to one of these classes can be done by the user or by a learning method.
- ***SignalIntensity*** refers to the signal intensity of tumor in medical imaging such as ***Hypointense*** and ***Hyperintense***.

To link these concepts to the tumor classification we define another class ***Alteration*** which refers to the type of tumor alteration on internal structures of the brain. This class has two subclasses: ***SmallDeforming*** and ***LargeDeforming***. We use the following properties to link the classes:

- *has_for_location*,

- *has_for_behavior*,
- *has_for_component*,
- *has_for_size*,
- *has_for_signal_intensity*,
- *has_for_enhancement*.

A part of this ontology can be seen in Figure 5.9.

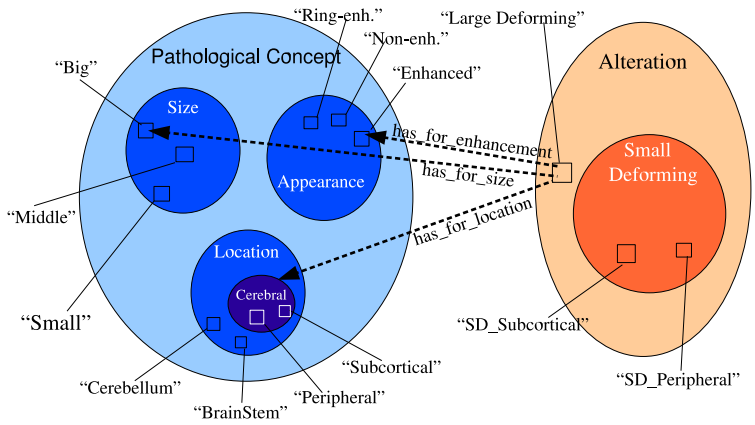

Figure 5.8: Main concepts of the tumor ontology. This diagram represents the main concepts and their relations. For example "Large Deforming" is a ***Alteration***, it has the "Big" ***Size***, it has the "Enhanced" ***Appearance*** and it has the "Cerebral" ***Location***.

5.6.2 Stable spatial relations

Some spatial relations are more stable than others in the presence of a tumor. Intuitively, topological relations imply less instability than metric ones. For example, an adjacency relation can be preserved even if large deformations are considered in a given structural organization; on the contrary metric relations, even if formulated with fuzzy sets, are prone to significant modifications in case of large tumors and should therefore be avoided or manipulated with great care. Reasoning about distances requires to take into account the granularity level of the relation expression. For example the distance predicates "far from" and "close to" are naturally more vague than the predicate "at a distance of about 1cm", which makes them more stable. In the case of tumor-specific spatial relations, if the tumor is large deforming, only relations such as "far from" and "close to" are retained. The choice of cancelling or maintaining a spatial relation in the presence of a tumor is first motivated by clinical considerations, namely the localization, size and type of the tumor.

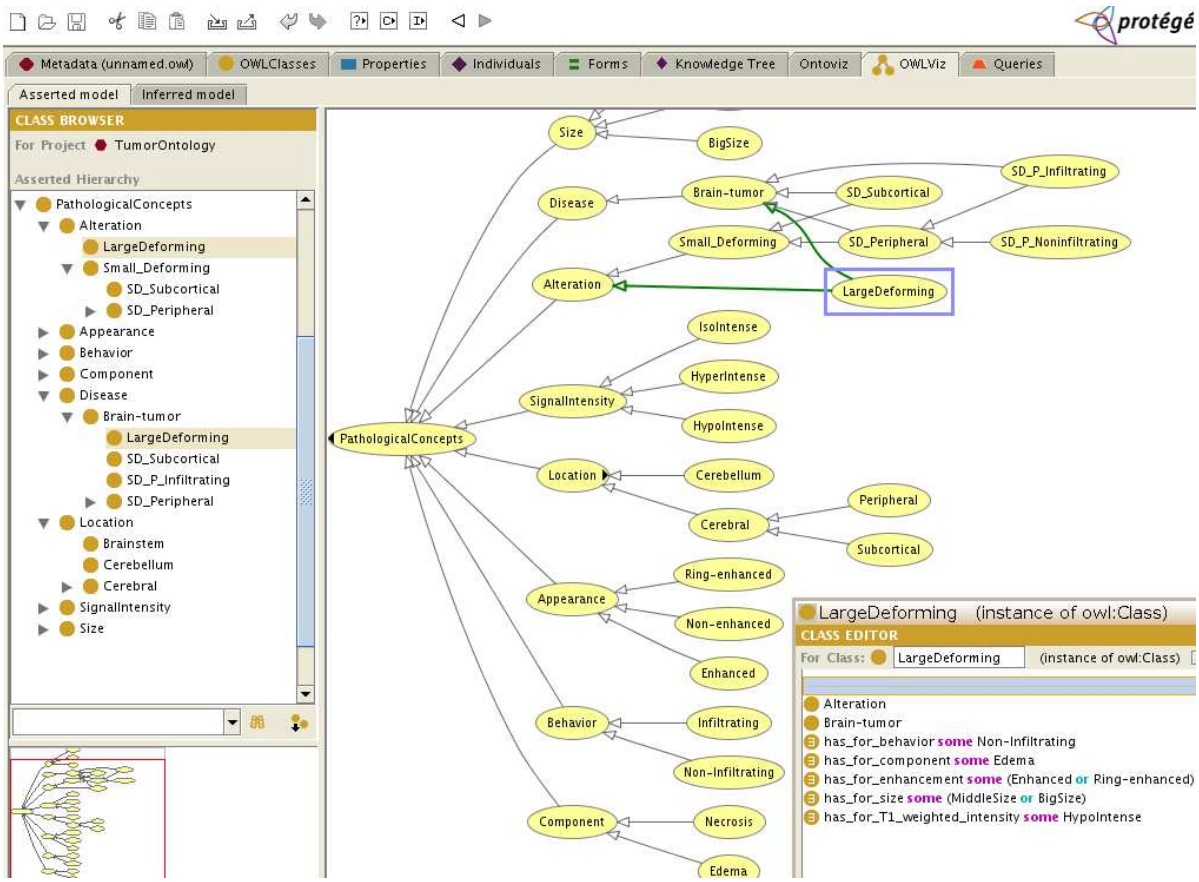

Figure 5.9: A part of the tumor ontology visualized by Protégé.

Table 5.1 summarizes our current list of tumor-based spatial relations [Khotanlou et al., 2007a ; Atif et al., 2006a].

Spatial characteristics of tumors		**Spatial relations preserved**
Large deforming (LD)		Adjacency, Direction, Distance (far, near)
Small deforming (SD)	Peripheral (SD-P)	Adjacency, Direction, Symmetry, Distance
	Subcortical (SD-SC)	Adjacency, Direction, Distance (far, near)

Table 5.1: Spatial relations for internal brain structures depending on the tumor's type.

5.7 Structure segmentation

The proposed method for internal brain structures segmentation, such as for tumors, has two phases: initialization and refinement. In other words, we first segment the brain tissues (consequently the internal structures of the brain) and since this segmentation for internal brain structures is not fine enough, we then refine them one by one using prior information. To perform these two phases, the segmentation procedure consists of the following steps:

1. global segmentation of the brain,
2. retrieving spatial relations,
3. selecting the valid spatial relations,
4. fuzzification and fusion of relations and providing the ROI,
5. searching the initial segmentation of structure,
6. refining the initial segmentation,
7. repeating from step 2 for other structures.

Global segmentation of the brain To segment the brain tissues and its structures we use two methods, the first one is the MPFCM method and the second one is the multiphase level sets.

In the MPFCM method we classify the segmented brain into 5 or 6 classes based on the tumor type (as explained in Section 4.3.1 and if the MPFCM method is applied for tumor segmentation, the same result is used). The internal structures of the brain are partially classified into the gray matter class as seen for one case in Figures 5.11(b) and 5.13(b).

As an alternative method we use the multiphase level sets introduced by [Vese and Chan, 2002]. Our final aim is to integrate the spatial relations to this method to segment the brain structures simultaneously in future works, but here we use it as a classification method. The detail of the method can be found in Appendix C. Here we use a 4-phase level sets and classify the segmented brain (without tumor and edema) into: background, CSF, GM and WM. Such as for the MPFCM method, the internal brain structures are classified partially into the GM class. One example is shown in Figure 5.10.

Retrieving spatial relations In this step we extract information from prior knowledge by querying our ontologies. The goal of the query is to find the spatial relations

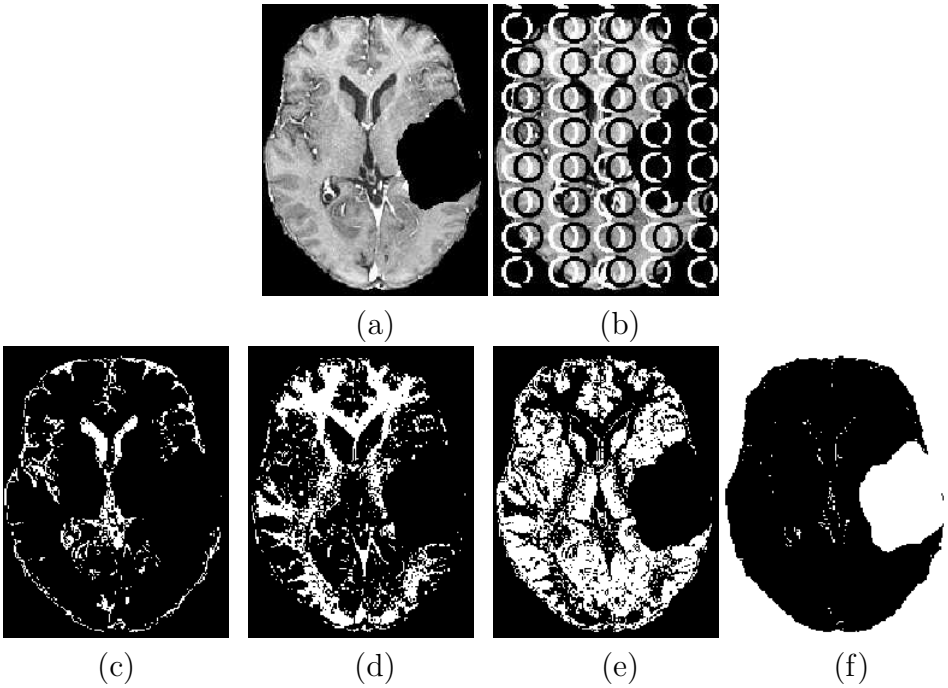

Figure 5.10: Segmentation by multiphase level sets. (a) One axial slice of the original image. (b) Initial level set superimposed on the original image. (c) CSF class. (d) WM class. (e) GM class. (f) Background (the tumor and edema are excluded from the brain). These results are obtained with $\nu = 0.00001$, $h = 1$ and $n = 1000$ (see Appendix C).

involving the corresponding structure. Several query languages have been developed, such as SPARQL by Protégé and nRQL by RACER [Haarslev and Moller, 2001]. Here we use nRQL and a request for the spatial relations of the right thalamus is:

```
(tbox-retrieve (?x)(and
(?y Right_thalamus)
(?y ?x hasSpatialRelation)))
```

The query (tbox-retrieve) means that we request the concepts and not instances of these concepts. In a knowledge base the conceptual knowledge is represented in the T-box and the knowledge about the instances of a domain is represented in the A-box. An answer to this query is: *Right_Of_Third_ventricle*, *Close_To_Third_ventricle* and *Above_Of_Right_Interventricular_foramen*.

The answer consists of all the spatial relations of the right thalamus without considering the reference object. We can also retrieve the spatial relations based on a reference object. For example the following query will give the spatial relations based on the third ventricle:

```
(tbox-retrieve (?x)(and
```

(?y Right_thalamus)
(?y ?x hasSpatialRelation)
(?z Third_ventricle)
(?x ?z hasReferenceObject)))

and the answer is: *Right_Of_Third_ventricle* and *Close_To_Third_ventricle*.

Selecting the valid spatial relations This step selects the spatial relations which remain stable. Based on the information provided by the tumor segmentation, consisting of size, location, appearance, components and behavior, we classify the tumor. We use the developed tumor ontology for this purpose. An example of query by nRQL is:

(tbox-retrieve (?x)(and
(?a Enhanced)
(?b Peripheral)
(?c SmallSize)
(?d Edema)
(?e Infiltrating)
(?x ?a has_for_enhancement)
(?x ?b has_for_location)
(?x ?c has_for_size)
(?x ?d has_for_component)
(?x ?e has_for_behavior)))

the answer to this query is *SD_P_infiltrating*.

We then select the stable spatial relations based on the result of the query (see Table 5.1).

Fuzzification and fusion of the relations and providing the ROI In this step, a region of interest is constructed to restrict the search of the structure and also to be used in the refinement step to constrain a deformable model. This ROI is defined by the fuzzy set corresponding to the relations that should be satisfied by the target structure. So we first fuzzify the selected relations with the extracted parameters using the methods described in Section 5.5. If a single relation is involved in the description of the structure, the ROI is defined by the fuzzy set corresponding to this relation. When several spatial relations are involved, the ROI corresponds to the fusion of the fuzzy sets representing these relations. These relations are combined using a conjunctive fusion operator (a t-norm such as minimum). Eight examples of the relations fusion are illustrated in Figures 5.11-5.14 for the right and left caudate nucleus and the right and left thalamus.

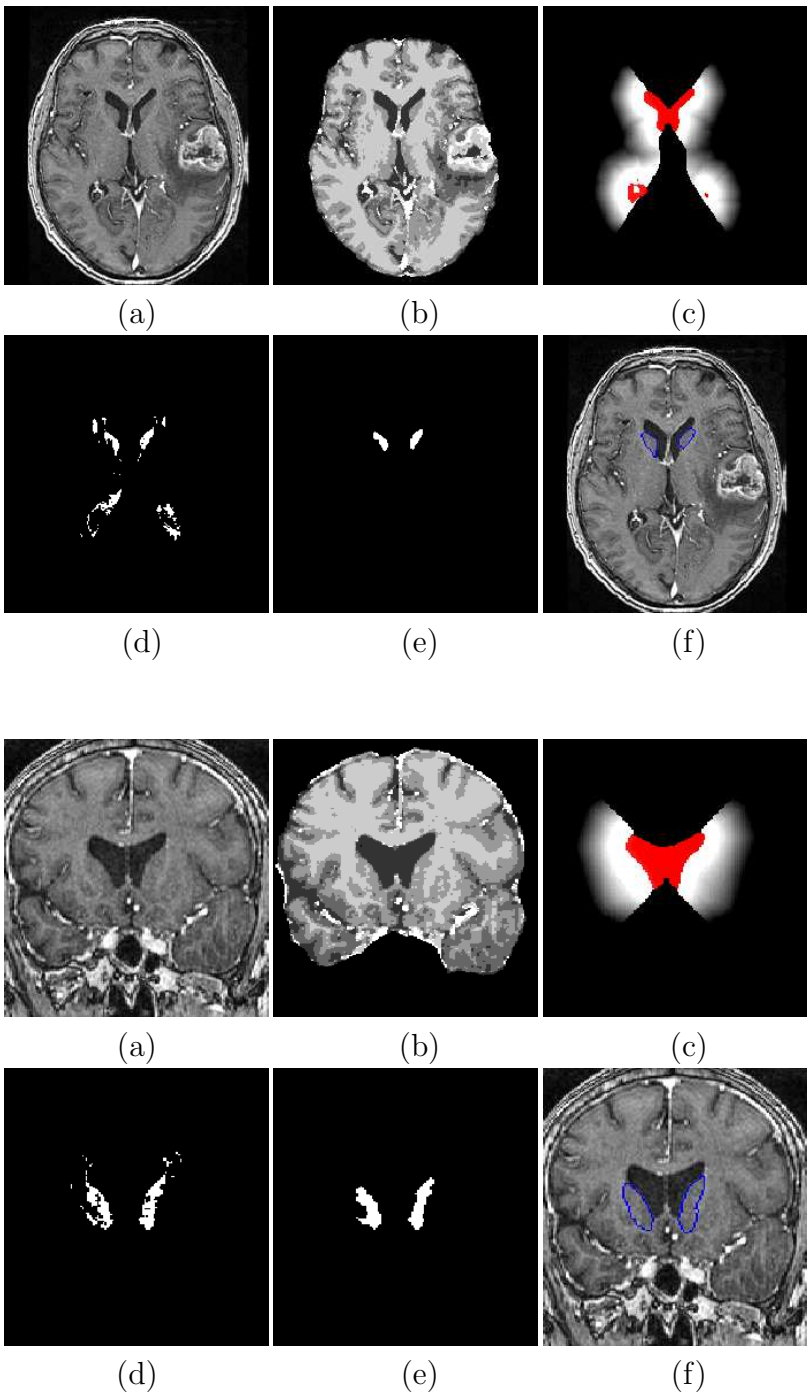

Figure 5.11: Segmentation of the right and the left caudate nucleus (axial and coronal views). (a) Original image. (b) MPFCM classification. (c) Computed ROI. (d) Selected region by the ROI. (e) Initial segmentation. (f) Final result superimposed on the orignal image. Here the reference object is the lateral ventricle and it was segmented before the caudate nuclei.

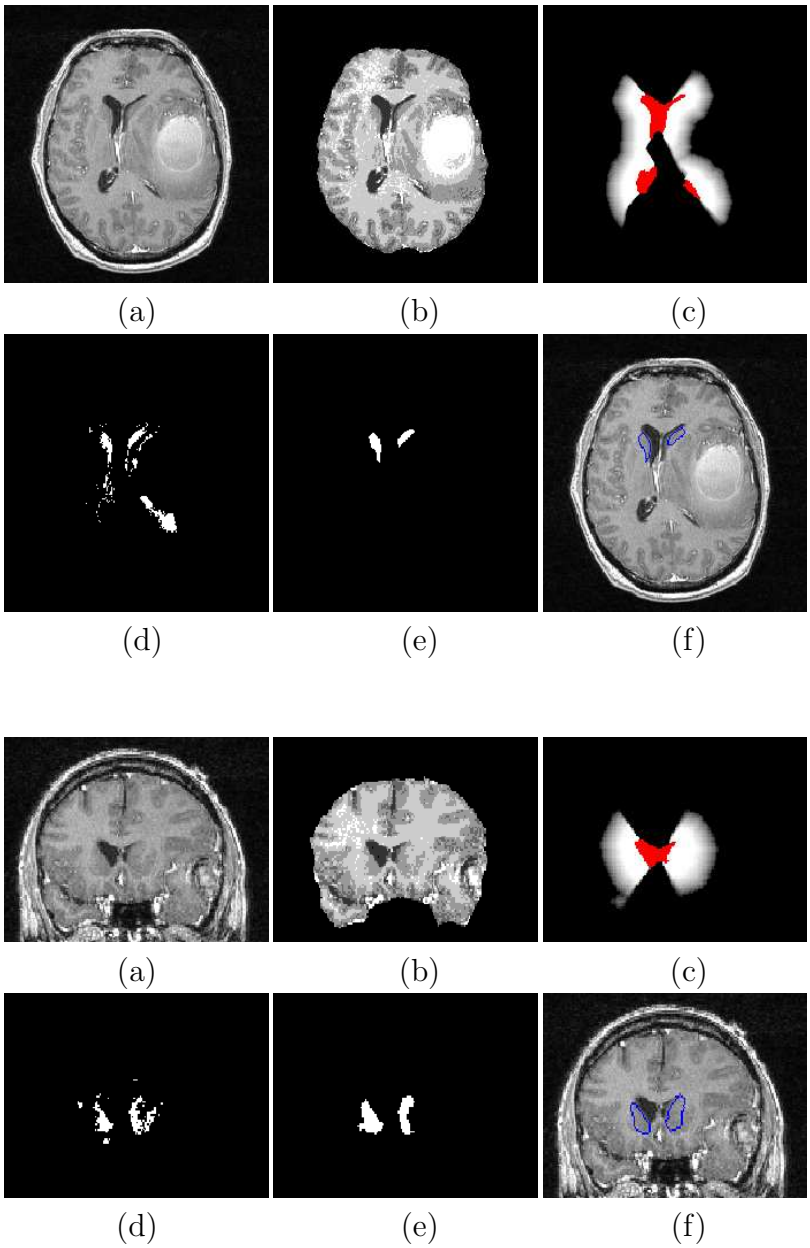

Figure 5.12: Segmentation of the right and the left caudate nucleus (axial and coronal views). (a) Original image. (b) MPFCM classification. (c) Computed ROI. (d) Selected region by the ROI. (e) Initial segmentation. (f) Final result superimposed on the orignal image. Here the reference object is the lateral ventricle and it was segmented before the caudate nuclei.

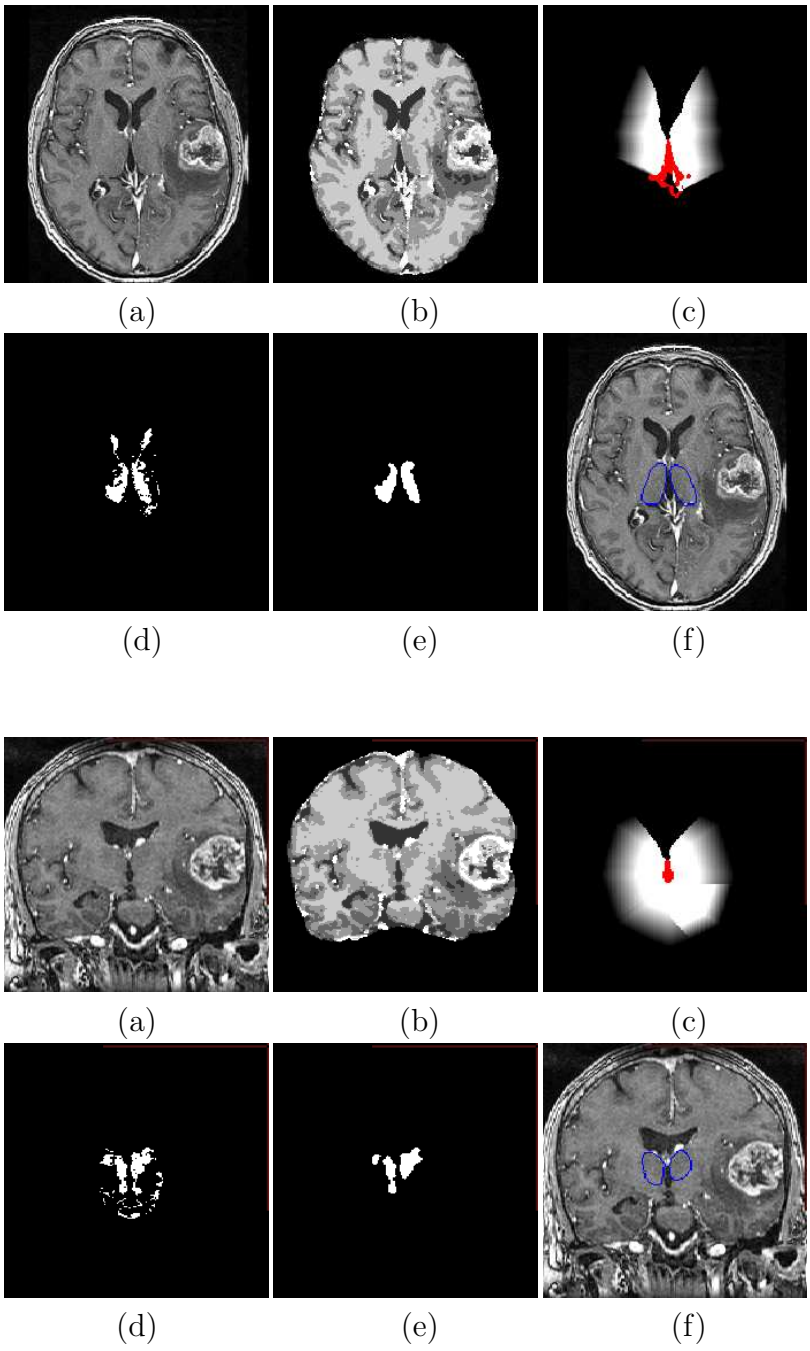

Figure 5.13: Segmentation of the right and the left thalamus (axial and coronal views). (a) Original image. (b) MPFCM classification. (c) Computed ROI. (d) Selected region by the ROI. (e) Initial segmentation. (f) Final result superimposed on the orignal image. Here the reference objects are the third ventricle and the interventricular foramen and they were segmented before the thalamus.

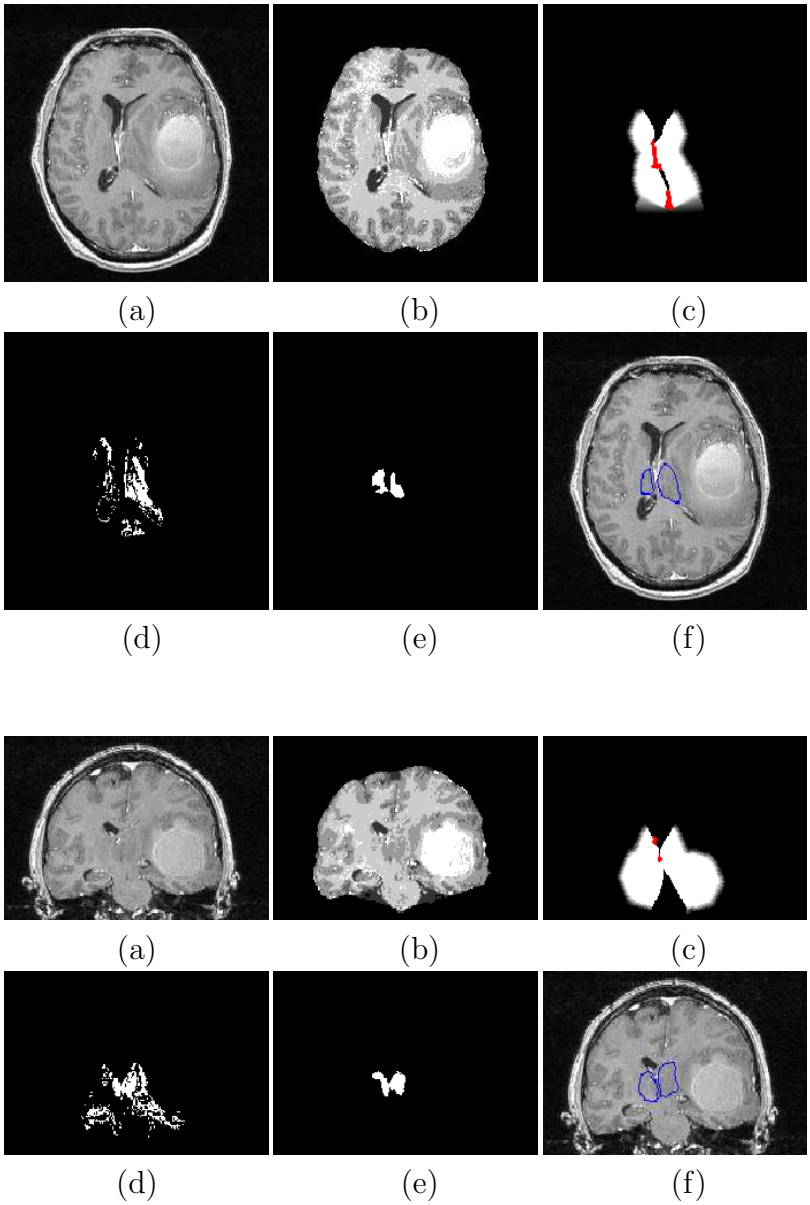

Figure 5.14: Segmentation of the right and the left thalamus (axial and coronal views). (a) Original image. (b) MPFCM classification. (c) Computed ROI. (d) Selected region by the ROI. (e) Initial segmentation. (f) Final result superimposed on the orignal image. Here the reference objects are the third ventricle and the interventricular foramen and they were segmented before the thalamus.

Searching the initial segmentation Now, we can search the initial segmentation of a structure in the globally segmented image. We first select the region of globally segmented image by the corresponding ROI. We then need to separate the different selected objects and to select the one we want to segment. To this purpose, we use a morphological opening, whose optimal size is found iteratively. Openings of increasing size are computed successively until a connected component matching the characteristics of the object is found. At each step, an opening of a given size is performed and the connected components are extracted. If one of the components matches the characteristics of the target object, this component is chosen. If none of the components verifies this condition, the process is iterated with a larger opening. The sizes of the openings are successively defined by using: 6-, 18-, 26-connectivity structuring elements. The characteristics which are used to select the components are composed of the spatial relations associated to the target object as well as its size and position. Finally, possible holes in the previous results are filled and we obtain the initial segmentation. This segmentation is then transformed into a triangulation using an isosurface algorithm based on tetrahedra. It is decimated and converted to a simplex mesh by the dual operation. This simplex mesh is used as the starting point of the deformable model. The initial segmentations for four structures (the right and left caudate nucleus and the right and left thalamus for two patient) are illustrated in Figures 5.11-5.14

Refining the initial segmentation To refine the initial segmentation we use the proposed method in [Colliot et al., 2006] that was described in Section 5.5. To compute F_R (spatial relation force) to constrain the deformable model we use the computed fuzzy ROI in the previous steps. In Figures 5.11 and 5.13 all steps of the segmentation of four structures for one case are shown.

Initialization and repeating This algorithm is repeated for all the internal structures and the order is provided by the user, considering that the lateral ventricle, third ventricle and interventricular foramen should be segmented firstly, because we use them as reference objects for other structures, and in addition their segmentation is easier than the other ones. The spatial relation which is used for segmenting them is "Far from the brain surface". The ventricular initial segmentation has proved sufficient for our purpose and we do not refine it by deformable model. In Figure 5.15 the segmentation of ventricular structures for one case is shown. Recent work by [Fouquier et al., 2007] could also be used to decide automatically the order in which the structures should be segmented.

(a) (b) (c) (d) (e)

Figure 5.15: Ventricular segmentation. (a) MPFCM classification. (b) Relation "Far from the brain surface". (c) Selected class by the ROI. (d) Segmented lateral ventricle. (e) Segmented third ventricle and interventricular foramen.

5.8 Evaluation and results

The proposed method was applied to 10 clinical MRI datasets of various origins and types. We illustrate the results on four cases, for which manual segmentation of several structures was available, and which exhibit tumors with different shapes, locations, sizes, intensities and contrasts. Evaluation of the segmentation results was performed through quantitative comparisons with manual segmentations, using volume and surface measures. Segmentation results are illustrated for ten cases in Figures 5.16-5.19 and quantitative evaluations are provided in Tables 5.2-5.5 showing high accuracy. The voxel size is typically $1 \times 1 \times 1.3\ mm^3$, so that the average error is less than one voxel. The Hausdorff distance represents the error for the worst point, which explains its higher values. Although the segmented structures are relatively small (about 4000 m^3), the volume metrics shows good results. For the similarity index measures, values above 70% are satisfactory [Zijdenbos et al., 1994]. The results show that the segmentation of caudate nuclei is better than thalamus due to their well defined borders. The comparison of the results obtained using the initial segmentation of MPFCM and multiphase level sets illustrates that there is not a large difference between them. But the MPFCM method is faster than the multiphase level sets method.

5.9 Conclusion

Here we proposed a new method for segmentation of pathological brain structures. This method combines prior information of structures and image information (region and edge) for segmentation. To represent the prior information we used ontological engineering tools. We also proposed a simple ontology for a specific classification of tumors and it can be extended for other classification of tumors (such as tumor grading).

The proposed segmentation framework, based on tumor-dependent preserved spatial relations, is able to incorporate some knowledge on tumoral physiology in a new

Dataset	Tumor Type	Structure	M mm^3	S_i %	J_i %	T_p %	F_p %	D_H mm	D_m mm
TNE1	SD-SC	CR	4198.8	86.7	76.9	84.9	11.5	3.55	0.52
TNE1	SD-SC	CL	4661.4	88.8	80.0	85.3	7.4	4.33	0.39
TRE2	LD	CR	3712.9	85.3	74.3	83.1	12.4	6.17	0.66
TRE2	LD	CL	4208.8	82.4	70.1	7.9	12.4	8.4	0.74
TE5	LD	CR	3990.0	85.6	74.8	78.3	5.7	4.29	0.64
TE5	LD	CL	4264.8	83.6	71.8	76.5	7.8	3.80	0.74
TNE3	SD-P	CR	3699.3	88.1	78.8	89.0	12.7	2.96	0.53
TNE3	SD-P	CL	3745.4	88.8	79.8	85.9	8.1	2.81	0.51
TNE8	SD-SC	CR	4910.9	90.5	82.7	86.1	4.5	3.86	0.43
TNE8	SD-SC	CL	4945.2	89.2	80.5	91.6	13.0	3.53	0.49
TNE2	SD-SC	CR	4634.0	89.4	80.8	86.8	7.8	3.86	0.50
TNE2	SD-SC	CL	4340.0	90.8	83.2	89.6	7.9	3.18	0.41
TNE4	SD-P	CR	4547.0	89.1	80.3	88.4	10.1	5.46	0.49
TNE4	SD-P	CL	4506.2	88.3	79.0	87.7	11.1	3.32	0.51
TNE7	SD-SC	CR	4689.8	81.1	68.2	75.1	11.8	6.95	0.85
TNE7	SD-SC	CL	4384.9	89.2	80.5	91.6	13.0	4.45	0.48
TNE9	SD-P	CR	4146.2	82.9	70.8	76.6	9.5	7.26	0.81
TNE9	SD-P	CL	4520.7	80.1	67.7	73.2	10.1	7.87	0.88
TRE5	LD	CR	2843.6	84.2	72.6	78.3	9.0	4.81	0.53
TRE5	LD	CL	3866.8	89.3	80.6	85.5	6.6	3.58	0.45
Ave.			4240.7	86.7	76.7	83.6	9.6	4.72	0.58

Table 5.2: Evaluation of segmentation result of the caudate nuclei (initially segmented by MPFCM) on ten 3D MR datasets (CR and CL denote the right and the left caudate nucleus and for the tumor type see Table 5.1).

Dataset	Tumor Type	Structure	M mm^3	S_i %	J_i %	T_p %	F_p %	D_H mm	D_m mm
TNE1	SD-SC	TR	6832.2	90.2	82.1	92.4	11.9	3.74	0.57
TNE1	SD-SC	TL	8546.8	85.4	74.4	79.7	8.1	5.64	0.93
TRE2	LD	TR	8311.2	84.8	73.6	78.1	7.3	4.86	0.99
TRE2	LD	TL	9002.1	90.5	82.6	85.8	4.2	3.92	0.68
TE5	LD	TR	9885	88.5	79.3	90.0	13.0	4.00	0.86
TE5	LD	TL	9310.8	87.8	78.2	85.5	9.7	4.23	0.83
TNE3	SD-P	TR	8394.3	90.8	83.1	86.2	4.2	4.03	0.64
TNE3	SD-P	TL	8298.1	82.0	69.5	80.9	16.8	5.56	1.16
TNE8	SD-SC	TR	7825.8	88.5	79.4	88.3	11.3	4.92	0.72
TNE8	SD-SC	TL	8135.6	88.0	78.5	87.1	11.1	3.66	0.76
TNE2	SD-SC	TR	8065.7	88.5	79.4	85.5	8.2	4.14	0.78
TNE2	SD-SC	TL	8444.1	88.4	79.2	85.7	8.8	8.79	0.88
TNE4	SD-P	TR	6734.2	89.0	80.2	92.3	14.1	3.66	0.70
TNE4	SD-P	TL	6535.1	86.9	76.8	80.1	5.0	4.19	0.72
TNE7	SD-SC	TR	7825.8	86.7	76.4	87.1	13.8	6.11	0.87
TNE7	SD-SC	TL	7597.7	83.6	71.8	78.2	10.3	4.92	0.95
TNE9	SD-P	TR	7682.1	88.0	78.6	90.3	14.1	5.22	0.79
TNE9	SD-P	TL	6860.7	84.1	72.6	76.0	5.3	4.11	0.91
TRE5	LD	TR	6898.6	86.3	76.0	89.9	16.9	3.66	0.84
TRE5	LD	TL	7248.4	77.5	63.2	71.7	15.8	6.50	1.35
Ave.			7921.8	86.8	76.8	84.5	10.5	4.79	0.85

Table 5.3: Evaluation of segmentation result of the thalamus (initially segmented by MPFCM) on ten 3D MR datasets (CR and CL denote the right and the left caudate nucleus and for the tumor type see Table 5.1).

Dataset	Tumor Type	Structure	M mm^3	S_i %	J_i %	T_p %	F_p %	D_H mm	D_m mm
TNE1	SD-SC	CR	4198.8	85.5	74.6	79.9	8.1	12.75	0.75
TNE1	SD-SC	CL	4661.4	84.9	73.8	80.6	10.3	6.71	0.60
TRE2	LD	CR	3712.9	87.0	77.0	84.8	10.7	6.74	0.60
TRE2	LD	CL	4208.8	82.8	70.1	75.2	7.8	7.6	0.64
TE5	LD	CR	3990.0	86.1	75.6	84.1	11.8	4.17	0.63
TE5	LD	CL	4264.8	84.9	73.7	80.9.5	10.7	3.80	0.70
TNE3	SD-P	CR	3699.3	86.2	75.7	81.4	16.5	6.49	0.70
TNE3	SD-P	CL	3745.4	88.2	78.8	84.3	7.5	5.64	0.57
TNE8	SD-SC	CR	4910.9	88.1	78.8	82.2	5.0	6.71	0.60
TNE8	SD-SC	CL	4945.2	90.1	83.5	88.7	6.6	3.32	0.48
TNE2	SD-SC	CR	4634.0	89.5	81.1	86.9	7.6	3.18	0.50
TNE2	SD-SC	CL	4340.0	89.4	80.8	84.8	5.5	4.14	0.48
TNE4	SD-P	CR	4547.0	89.4	80.9	87.5	8.6	6.82	0.50
TNE4	SD-P	CL	4506.2	86.0	75.4	83.3	11.1	4.68	0.68
TNE7	SD-SC	CR	4689.8	77.9	63.8	70.5	12.9	6.46	0.87
TNE7	SD-SC	CL	4384.9	89.0	80.2	88.3	10.2	8.14	0.54
TNE9	SD-P	CR	4146.2	84.0	72.3	80.8	12.7	3.97	0.73
TNE9	SD-P	CL	4520.7	84.4	72.9	80.0	10.1	5.01	0.72
TRE5	LD	CR	2843.6	76.8	62.2	66.7	9.6	11.5	1.53
TRE5	LD	CL	3866.8	91.0	83.6	87.0	4.5	6.09	0.41
Ave			4240.7	86.1	75.7	81.9	8.9	6.20	0.66

Table 5.4: Evaluation of segmentation result of the caudate nuclei (initially segmented by multiphase level sets) on ten 3D MR datasets (TR and TL denote the right and the left thalamus and for the tumor type see Table 5.1).

Dataset	Tumor Type	Structure	M mm^3	S_i %	J_i %	T_p %	F_p %	D_H mm	D_m mm
TNE1	SD-SC	TR	6832.2	72.6	57.0	60.4	9.0	6.06	1.49
TNE1	SD-SC	TL	8546.8	82.7	70.6	74.1	6.4	7.15	1.05
TRE2	LD	TR	8311.2	86.2	75.7	80.4	7.2	3.49	0.92
TRE2	LD	TL	9002.1	86.8	76.6	83.0	9.1	4.38	0.93
TE5	LD	TR	9885	84.1	72.6	83.0	14.8	5.83	1.20
TE5	LD	TL	9310.8	88.4	79.2	87.5	10.7	5.95	0.81
TNE3	SD-P	TR	8394.3	91.0	83.5	91.3	9.2	3.14	0.64
TNE3	SD-P	TL	8298.1	87.6	78.0	86.5	11.2	6.64	0.87
TNE8	SD-SC	TR	7825.8	89.4	80.7	87.4	8.6	3.69	0.73
TNE8	SD-SC	TL	8135.6	81.8	69.3	72.3	5.8	7.29	1.18
TNE2	SD-SC	TR	8065.7	87.5	77.8	82.3	6.6	3.53	0.84
TNE2	SD-SC	TL	8444.1	87.9	78.4	81.5	4.5	3.14	0.82
TNE4	SD-P	TR	6734.2	86.6	76.4	86.5	13.3	4.92	0.87
TNE4	SD-P	TL	6535.1	90.1	81.9	86.4	5.9	4.03	0.62
TNE7	SD-SC	TR	7825.8	84.5	73.1	77.3	6.9	6.49	1.04
TNE7	SD-SC	TL	7597.7	82.3	70.0	72.3	4.5	5.62	1.06
TNE9	SD-P	TR	7682.1	83.7	72.0	76.8	7.6	4.68	1.04
TNE9	SD-P	TL	6860.7	85.7	74.9	80.5	8.3	3.18	0.85
TRE5	LD	TR	6898.6	86.5	76.2	87.1	14.0	8.37	0.97
TRE5	LD	TL	7248.4	85.5	74.7	80.6	8.8	4.86	0.94
Ave.			7921.8	85.6	75.0	80.1	8.62	5.12	0.94

Table 5.5: Evaluation of segmentation result of the thalamus (initially segmented by multiphase level sets) on ten 3D MR datasets (TR and TL denote the right and the left thalamus and for the tumor type see Table 5.1).

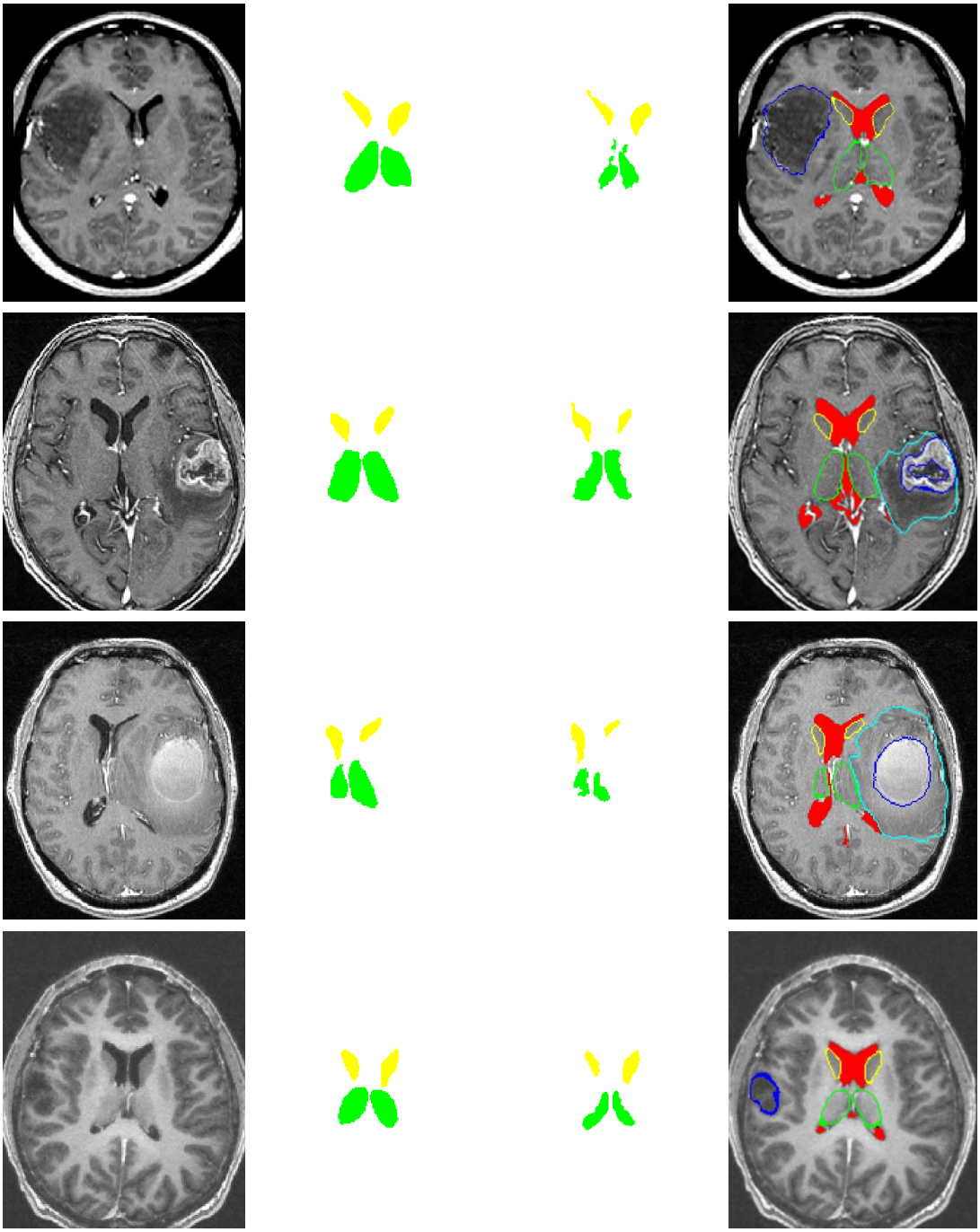

Figure 5.16: Segmentation results. (a) Axial slices from the original MRI data sets. (b) Manual segmentation. (c) Initial segmentation. (d) Superimposition of results on axial slices.

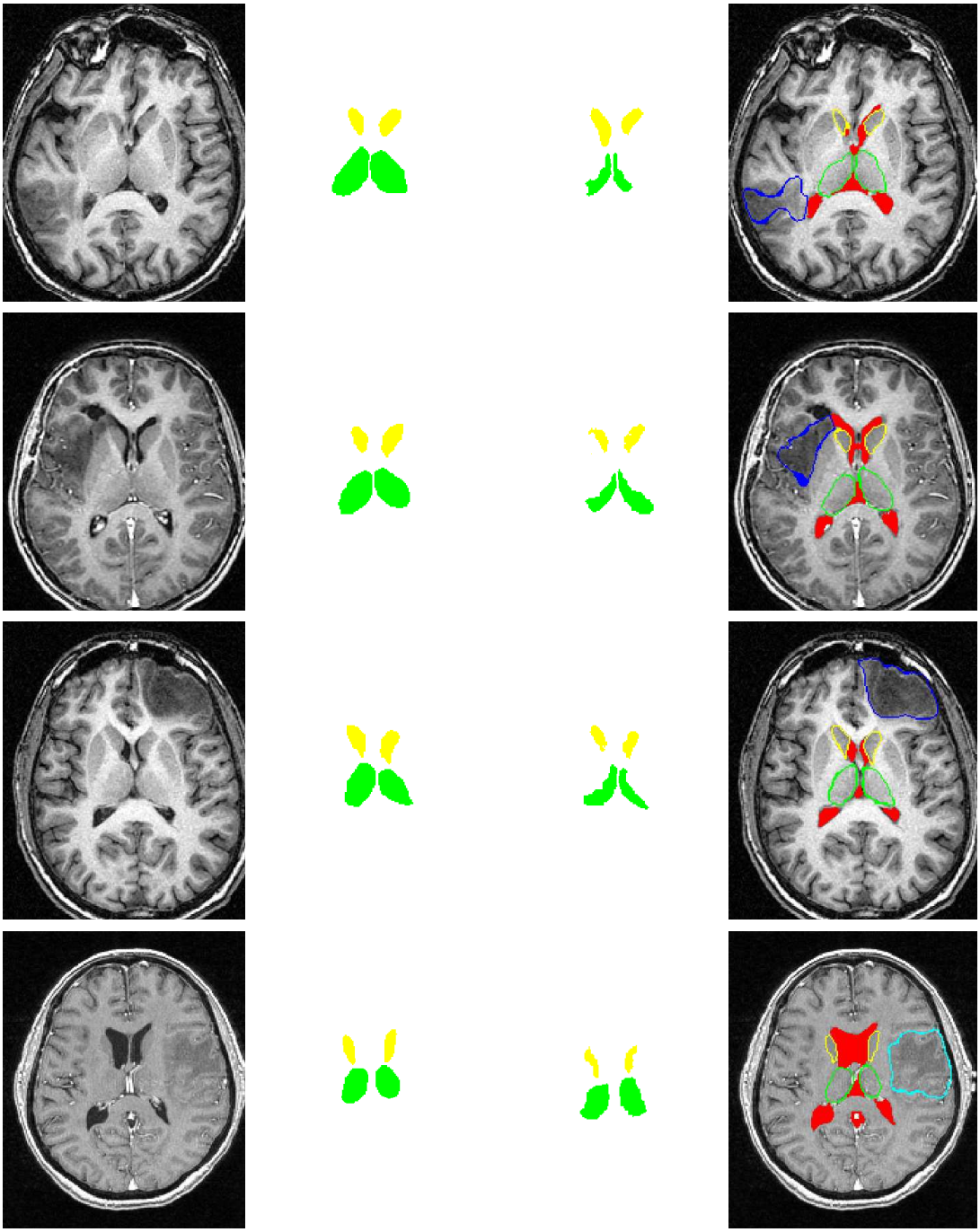

Figure 5.17: Segmentation results. (a) Axial slices from the original MRI data sets. (b) Manual segmentation. (c) Initial segmentation. (d) Superimposition of results on axial slices.

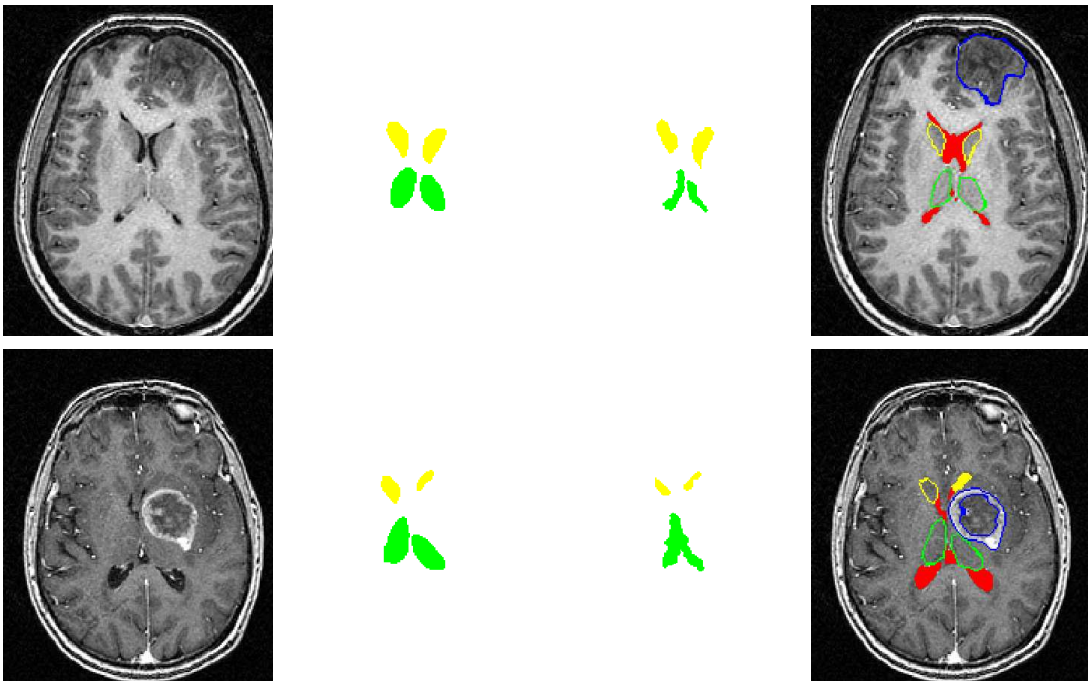

Figure 5.18: Segmentation results. (a) Axial slices from the original MRI data sets. (b) Manual segmentation. (c) Initial segmentation. (d) Superimposition of results on axial slices.

and original way. For example, several teams have recently introduced biomathematical models to quantitatively describe the growth rates of gliomas visualized radiologically [Swanson et al., 2003 ; Clatz et al., 2005]. The model in [Swanson et al., 2003] takes into account the two major biological phenomena underlying the growth of gliomas at the cellular scale: proliferation and migration. Initially, this model was suggested for high-grade gliomas. Most of these anaplastic tumors have an important proliferation index, inducing a mass effect on the normal brain structures, especially in cases of large space-occupying lesions. Thus, internal cerebral structures can be distorted, with a preservation of their spatial relations despite mechanical deformations. In the event of necrosis, very frequent in WHO grade IV gliomas (glioblastomas), it is possible that normal brain tissue is destroyed and not only distorted, eliciting neurological deficit: in these cases, topology may be modified.

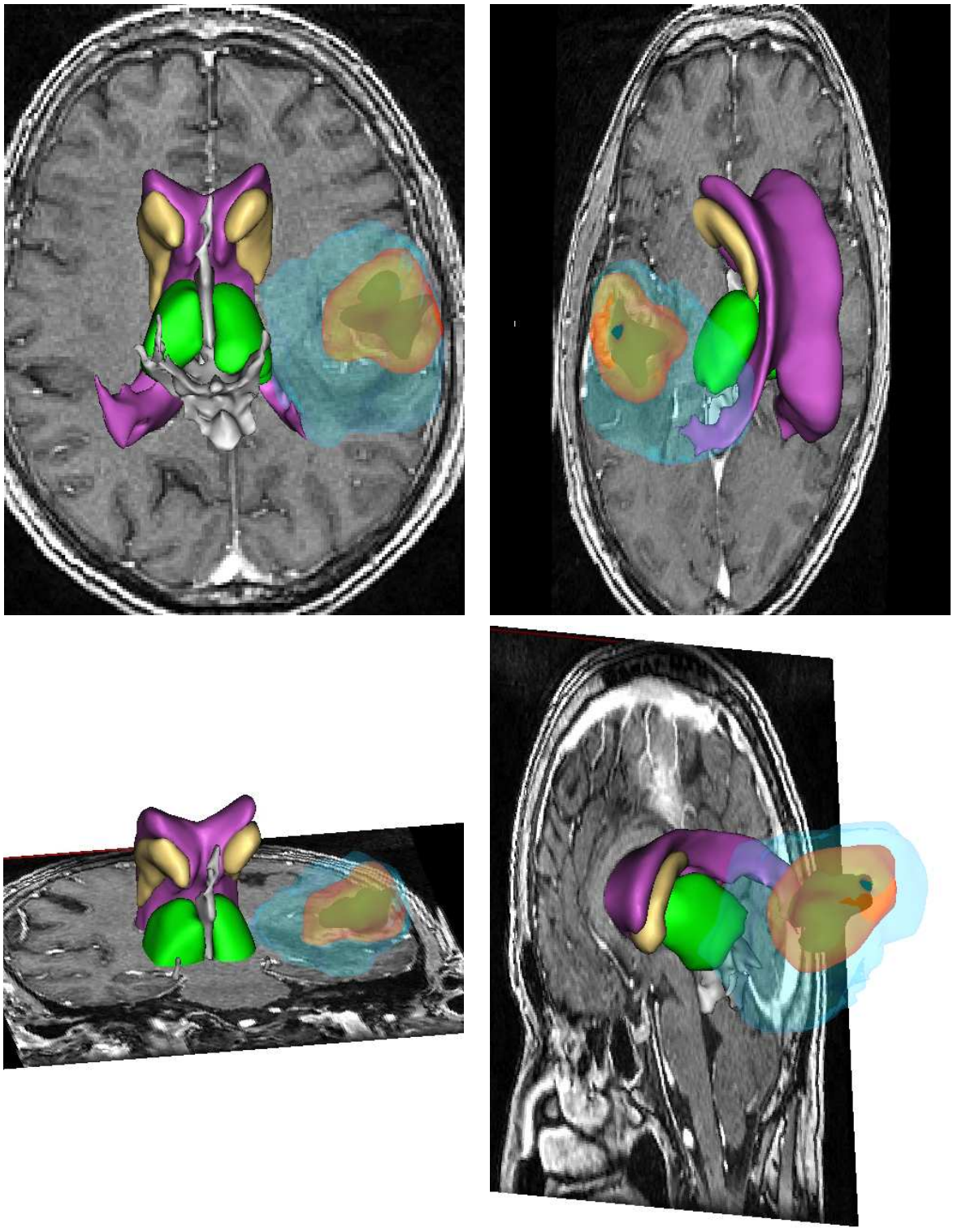

Figure 5.19: 3D view of the segmented structures, tumor, edema and necrosis for one case.

CHAPTER 6

Conclusion

6.1 Review of the contributions

In this thesis we deal with 3D MR images in order to segment brain tumors and internal brain structures for the applications such as treatment and follow-up, surgery, individual modeling, etc. In this chapter we first review the discussed topics and the contributions and following this we discuss possible future directions.

Brain tumor segmentation The proposed method uses contrast enhanced T1-weighted and FLAIR images for segmentation and it consists of two steps: preprocessing and segmentation. In the preprocessing step, in addition to use the classical methods for reducing the noise and inhomogeneity and registration, we proposed a new adapted method for correct and robust brain segmentation. The brain is segmented by a combination of histogram analysis, morphological operations and symmetry analysis. A new symmetry-based histogram analysis was proposed that is able to detect automatically the tumor type and the pathological hemisphere.

For the segmentation, the proposed method combines the information of edge and of region. Region-based methods segment difficult cases of tumors with a high level of automation but they have a main drawback at the boundary of tumors. Due to the partial volume effect the region-based techniques suffer from misclassification of voxels and hence, it is difficult to have a crisp region of tumor. On the other hand boundary-based methods were proposed to solve this problem but they also suffer from initialization problems. To obtain a good result they must be well initialized. The proposed approach tries to combine these two types of methods to remove the problems using the capabilities of each one. For example a region-based method can solve the problem of the initialization of a boundary-based method and a boundary-based method is able to improve the quality of region-based segmentation at the border of objects. So the proposed hybrid method has two main phases: initialization which is

done by a region-based method and refinement that is performed by a boundary-based method.

For initialization we can use any full-automatic approach and here we proposed two new and original methods. The first one is an unsupervised fuzzy classification. This method is a general classification approach and it can be used in order to detect and initially segment brain tumors. This method is a combination of fuzzy c-mean, possibilistic c-mean and spatial regularization constraints. In other words it uses the membership, the typicality and the neighborhood information for data classification.

The second one relies on the asymmetry of pathological brains. We proposed a new method specifically for tumor detection. It is based on the asymmetry detection in the image histogram of the brain hemispheres. It is able to detect a large class of tumors in several brain medical imaging modalities.

The second phase of the segmentation refines the initial segmentation based on edge information. We use a classical 3D snake model which is initialized by the surface of the detected tumor. To address some problems of deformable model such as the leakage at the ill-defined borders and to guide the evolution of surface, we constrain the model by the spatial relationships between the detected tumor and the tumor surrounding tissues.

Internal brain structures segmentation Another contribution of this thesis is the segmentation of internal brain structures. The segmentation of the pathological brain structures is a difficult task due to the different effects of the different tumors. Using prior information such as an atlas or adapting it to guide the segmentation is also difficult because of these different effects.

We proposed a new method, that in addition to region and edge information, uses a type of prior information which is more consistent in pathological cases. The spatial relations between structures is the prior information used in this method. Here we deal with three main problems: explicit representation of spatial relations for each structure, adaptation of spatial relations for pathological cases and segmentation method.

The representation of the spatial relations in general and explicit representations of spatial relations for each structure in particular are implemented using the ontology engineering tools. Knowledge representation using ontologies is a powerful method that is easy to extend, easy to use and reusable by other researchers (as we used the FMA ontology developed by another group). A link between the spatial relations ontology and the FMA ontology provided an explicit representation of spatial relationships between structures.

For adaptation of spatial relations for pathological cases, we used the segmented tumor information. We classify the tumor based on its impact on the other structures. For this we developed a simple ontology. We then decide to retain the spatial relations

which remain stable based on the classification result.

For segmentation we developed a method that integrates a fusion of spatial relations to guide the segmentation in initial and refinement phases. It is a sequential method and is repeated for all the structures in an order defined by the user. This method uses the fused spatial relations (ROI) to search the initial segmentation of a structure and to guide a deformable model to refine this initial segmentation.

6.2 Future work

Brain tumor

The comparison of the quantitative results of tumor segmentation shows that the quality of the segmentation for enhanced tumors is better than for the non-enhanced tumors (especially for the false detection ratio) because of their well-defined boundaries. Improvement of the method for segmenting non-enhanced tumors could still be useful. One of the future directions can be using the probability map, as proposed in [Colliot et al., 2006] for brain structures, to improve the edge detection method. In the symmetry analysis method we can fit a Gaussian model to the tumor peak to find the mean and variance of tumor gray levels. We can then compute the probability map and compute the edge map of this probability map.

For segmentation refinement by a deformable model, the parameters tuning is very important (α and β). Our experience shows that there is a relation between the parameters and the volume of the initial segmentation. As a future work, finding the relation to compute the parameters can be useful.

Interpretation or WHO classification of the tumor is important in clinical applications. At this moment it is done manually using histopathological diagnoses [Julià-Sapé et al., 206]. As reported in [Julià-Sapé et al., 206] using the MR imaging information to classify tumors to WHO classes is correct up to 90%. So by extending the proposed ontology in Section 5.6 and using other information about the patient such as clinical and symptom information as well as the obtained segmentation, it would be possible to provide an automatic method to interpret and classify the detected and segmented tumor.

As noted in Chapter 2, an advantage of geometric deformable models is the ability to automatically handle topology changes (merging or splitting). To segment two or more tumors in a brain (or when a tumor has two sections in the initial segmentation result) it is suitable to use a geometric deformable model to refine the segmentation. So, developing a geometric deformable model constrained by spatial relations, such as in [Atif et al., 2006b], to refine the segmentation is another future direction. Comparison between the results of parametric deformable model and geometric deformable

model can also be done.

Brain structures

In Section 1.9 we proposed a new tumor classification based on the tumor alteration and we select the stable spatial relations using this classification. For a future direction we can extend it to classify the tumors more precisely. For example we can separate the pathological and normal hemisphere and we then use the normal spatial relations in the normal hemispheres and adapted relations in the pathological one. The extension of the proposed ontology is also another future direction. In the proposed method determining the class of tumor size (small, middle and big) and the class of tumor location is still done manually. So by extending the ontology and adding some learning, we can perform the classification automatically.

We used a simple method for learning the spatial relation parameters. This learning is done using all types of tumors. A tumor-specific learning could be another future work. For each class of tumors a learning process can be performed. The results of learning are registered in the spatial relation ontology using a XML Schema datatype. Retrieving the spatial relations of a structure is performed based on the tumor type.

The proposed ontology-based method, associated to the learning procedure, could also be integrated in the method currently developed by O. Nempont et al. [Nempont et al., 2007] to guide the selection of spatial relations to be used for segmenting each structure and to define fuzzy regions of interest, characterizing necessity and possibility of locations of structures.

The proposed method for internal brain structures segmentation is a sequential method and should be repeated for each structure. As a new method we can segment the structures simultaneously. In section 5.7 we used multiphase level sets as an initial segmentation approach which is able to segment several regions at the same time. Future works are expected to integrate the spatial relations in multiphase level sets for segmentation of the internal structures simultaneously.

APPENDIX A

MPFCM objective function solving

A.1 Membership

The problem of minimization of the MPFCM objective function:

$$J_{m,\eta}(U,T,V;X)=\sum_{i=1}^{c}\sum_{k=1}^{n}(au_{ik}^{m}+bt_{ik}^{\eta})D_{ik}+\sum_{i=1}^{c}\gamma_i\sum_{k=1}^{n}(1-t_{ik})^{\eta}+\beta\sum_{i=1}^{c}\sum_{k=1}^{n}(au_{ik}^{m}+bt_{ik}^{\eta})S_{ik} \tag{A.1}$$

subject to the condition $\sum_{j=1}^{c}u_{jk}^{m}=1,\forall k$ will be solved using one Lagrange multiplier:

$$F_m=\sum_{i=1}^{c}\sum_{k=1}^{n}(au_{ik}^{m}+bt_{ik}^{\eta})D_{ik}+\sum_{i=1}^{c}\gamma_i\sum_{k=1}^{n}(1-t_{ik})^{\eta}+\beta\sum_{i=1}^{c}\sum_{k=1}^{n}(au_{ik}^{m}+bt_{ik}^{\eta})S_{ik}+\lambda\left(1-\sum_{i=1}^{c}u_{ik}^{m}\right) \tag{A.2}$$

If we take the derivative of F_m with respect to u_{ik} and set it to zero we have:

$$\frac{\partial F_m}{\partial u_{ik}}=mau_{ik}^{m-1}D_{ik}+\beta mau_{ik}^{m-1}S_{ik}-\lambda=0 \tag{A.3}$$

By solving Equation (A.3) for u_{ik} we get:

$$u_{ik}=\left(\frac{\lambda}{ma(D_{ik}+\beta S_{ik})}\right)^{\frac{1}{m-1}} \tag{A.4}$$

Using the condition $\sum_{j=1}^{c}u_{jk}=1,\forall k$, we have:

$$\sum_{j=1}^{c}\left(\frac{\lambda}{ma(D_{jk}+\beta S_{jk})}\right)^{\frac{1}{m-1}}=1 \tag{A.5}$$

and:

$$\left(\frac{\lambda}{ma}\right)^{\frac{1}{m-1}}\sum_{j=1}^{c}\left(\frac{1}{D_{jk}+\beta S_{jk}}\right)^{\frac{1}{m-1}}=1 \tag{A.6}$$

and:

$$\lambda=\frac{ma}{\left(\sum_{j=1}^{c}\left(\frac{1}{D_{jk}+\beta S_{jk}}\right)^{\frac{1}{m-1}}\right)^{m-1}} \tag{A.7}$$

Combining Equations (A.4) and (A.7) leads to:

$$u_{ik}=\sum_{j=1}^{c}\left(\frac{D_{ik}+\beta S_{ik}}{D_{jk}+\beta S_{jk}}\right)^{\frac{1}{1-m}},1\leq i\leq c,1\leq k\leq n \tag{A.8}$$

A.2 Typicality

The typicality equation can be obtained by taking the derivative of Equation (A.2) with respect to t_{ik} and setting it to zero:

$$\frac{\partial F_m}{\partial t_{ik}}=\eta b t_{ik}^{\eta-1}(D_{ik}+\beta S_{ik})-\gamma_i\eta(1-t_{ik})^{\eta-1}=0 \tag{A.9}$$

By solving this equation we have:

$$bt_{ik}^{\eta-1}(D_{ik}+\beta S_{ik})=\gamma_i(1-t_{ik})^{\eta-1} \tag{A.10}$$

and:

$$\left(\frac{1-t_{ik}}{t_{ik}}\right)^{\eta-1}=\frac{b}{\gamma_i}(D_{ik}+\beta S_{ik}) \tag{A.11}$$

and:

$$t_{ik}=\frac{1}{1+\left(\frac{b}{\gamma_i}D_{ik}+\beta S_{ik}\right)^{1/(\eta-1)}},1\leq i\leq c,1\leq k\leq n \tag{A.12}$$

A.3 Class centers

If we use the standard Euclidean distance and take the derivative of F_m with respect to v_i and setting it to zero we get:

$$\sum_{k=1}^{n}(au_{ik}^{m}+bt_{ik}^{\eta})(x_k-v_i)+\sum_{k=1}^{n}(au_{ik}^{m}+bt_{ik}^{\eta})\beta\sum_{w=1}^{n_w}(x_w-v_i)=0 \tag{A.13}$$

where x_w is a neighbor pixel of x_k in a window around x_k and n_w is the number of neighbors in this window.

By solving Equation (A.13) we get:

$$\sum_{k=1}^{n}(au_{ik}^{m}+bt_{ik}^{\eta})x_k-\sum_{k=1}^{n}(au_{ik}^{m}+bt_{ik}^{\eta})v_i+\sum_{k=1}^{n}(au_{ik}^{m}+bt_{ik}^{\eta})\beta\sum_{w=1}^{n_w}x_w-\sum_{k=1}^{n}(au_{ik}^{m}+bt_{ik}^{\eta})\beta\sum_{w=1}^{n_w}v_i=0 \tag{A.14}$$

and:

$$v_i\left(\sum_{k=1}^{n}(au_{ik}^{m}+bt_{ik}^{\eta})+\sum_{k=1}^{n}(au_{ik}^{m}+bt_{ik}^{\eta})\beta n_w\right)=\sum_{k=1}^{n}(au_{ik}^{m}+bt_{ik}^{\eta})(x_k+\beta\sum_{w=1}^{n_w}x_w) \tag{A.15}$$

and:

$$v_i=\frac{\sum_{k=1}^{n}\left(au_{ik}^{m}+bt_{ik}^{\eta}\right)\left(x_k+\beta R_k\right)}{(1+\alpha)\sum_{k=1}^{n}\left(au_{ik}^{m}+bt_{ik}^{\eta}\right)},1\leq i\leq c \tag{A.16}$$

where $R_k=\sum_{w=1}^{n_w}x_w$ and $\alpha=\beta n_w$.

The convergence theory of the FCM algorithm family was initially studied in [Bezdek., 1981 ; Bezdek et al., 1984] and later improved in [Bezdek et al., 1987 ; Sabin, 1987 ; Hoppner, 2003] and it has been shown that the objective function of FCM family is a descent function. So, to minimize the objective function we can set its derivative to zero.

APPENDIX B

Evaluation of segmentation

Characterizing the performance of image segmentation methods is a challenge in image analysis. An important difficulty we have to face in developing segmentation methods is the lack of a gold standard for their evaluation. Accuracy of a segmentation technique refers to the degree to which the segmentation results agree with the true segmentation. Although physical or digital phantoms can provide a level of known "ground truth", they are still unable to reproduce the full range of imaging characteristics and normal and abnormal anatomical variability observed in clinical data.

Manual segmentation of desired objects by domain experts can be considered as an acceptable approach (it still suffers from inter-expert and intra-expert variability). The result of an automated method is then compared to the manually segmented object by an expert or a group of experts, and if the algorithm generates segmentations sufficiently similar to the ones provided by the experts, it is accepted. A number of metrics have been proposed to measure the similarity between the segmentations, including volume measures and surface measures.

B.1 Volume metrics

A feature most easily accessible is the total volume of a structure. For binary segmentations, we calculate the number of voxels adjusted by the voxel volume. Comparing volumes of segmented structures does not take into account any regional differences and does not give an answer to the question where differences occur. We can define several measures to compare the volumes of two segmented objects. First let A and M denote the filled volume of the automatically and manually ("ground truth") segmented objects and $|x|$ represents the cardinality of the set of voxels x. In the following equations $T_p = M \cap A$, $F_p = A - M$ and $F_n = M - A$ denote to the "true positive", "false positive" and "false negative" respectively [Udupa et al., 2002] (as

seen in Figure B.1)

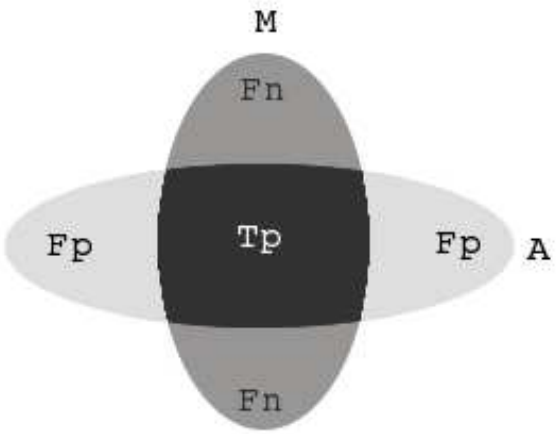

Figure B.1: Representation of M, A, T_p, F_p and F_n as a Venn diagram.

- Similarity index

  The similarity index (also known as Kappa) between two volumes is calculated by the following equation:

$$S_i(A, M) = \frac{2\,|A \cap M|}{|A| + |M|} * 100\% = \frac{2\,|T_p|}{|M| + |A|} * 100\% \tag{B.1}$$

  The similarity index is sensitive to both differences in size and location. For example, the similarity index of two equally sized regions that overlap each other with half of their area results in 50% similarity, and a region completely overlapping a smaller one of half its size yields $S_i = 67\%$. This example shows that, for the similarity index, differences in location are more strongly reflected than differences in size (as illustrated in Figure B.2) and $S_i > 70\%$ indicates a good agreement [Zijdenbos et al., 1994].

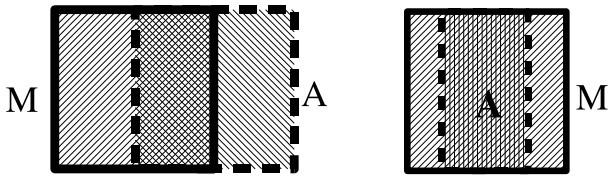

Figure B.2: Illustrative examples for similarity index. In the left image A and M have equal size and the overlap is the half of each one. Here the similarity index is 50%. In the right image A is the half of M and the similarity index is about 67%.

- Jaccard index

The Jaccard index between two volumes is represented as follow:

$$J_i(A, M) = \frac{|A \cap M|}{|A \cup M|} * 100\% = \frac{|T_p|}{|T_p| + |F_n| + |F_p|} * 100\% \tag{B.2}$$

This metric is more sensitive to differences since both denominator and numerator change with increasing or decreasing overlap.

- Correct detection ratio

  The correct detection ratio (sensitivity) is defined by the following equation:

$$T_p = \frac{|A \cap M|}{|M|} * 100\% = \frac{|T_p|}{|M|} * 100\% \tag{B.3}$$

  This metric indicates the correct detection volume normalized by the reference volume and is not sensitive to size. For example, if M is covered by A, T_p is 100% whatever the size of A (as shown in Figure B.3). Therefore T_p solely cannot indicate the similarity and should be used with false detection ratio or other volume metrics.

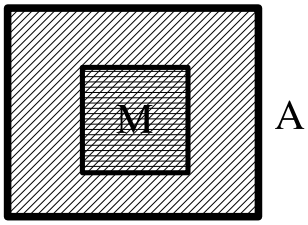

Figure B.3: Illustrative example for correct detection ratio. Here M is covered by A and T_p is 100% whatever the size of A.

- False detection ratio

  The false detection ratio is defined by the following equation:

$$F_p = \frac{|A - M|}{|A|} * 100\% = \frac{|F_p|}{|A|} * 100\% \tag{B.4}$$

  This metric shows the error of the segmentation and indicates the volume that is not located in the true segmentation. Using this metric with the correct detection ratio can give a good evaluation of the segmentation.

However, the overlap measure depends on the size and the shape complexity of the object and is related to the image sampling. Assuming that most of the errors occur at the boundary of objects, small objects are penalized and get a much lower score than large objects [Gerig et al., 2001].

B.2 Surface or distance-based metrics

For some segmentation tasks (such as the tumor segmentation), the delineation of the boundary is critical and is the main objective of the segmentation. In these situations, surface-based metrics are important. They measure the distance between the segmentation boundary and the true boundary.

- Hausdorff distance

  This metric defines the largest difference between two surfaces. Let M and A denote the surfaces of segmented objects. The Hausdorff distance between M and A can be calculated using the following equation:

  $$D_H(M, A) = \max(h(M, A), h(A, M)) \tag{B.5}$$

  where $h(M, A) = \max_{m \in M} \min_{a \in A} d(m, a)$, and $d(m, a)$ denotes the Euclidean distance between m and a (m and a are points of M and A respectively)

  Given two surfaces M and A, we first calculate for each point m on M the minimal distance to all the points on surface A. We calculate this minimal distance for each surface point and take the maximum minimal distance as the worst case distance. The Hausdorff metric calculation is computationally very expensive, as we need to compare each surface point to all the other ones. It can be computed in a more efficient way by computing a distance map using the chamfer algorithm.

- Mean absolute surface distance

  The mean absolute surface distance illustrates how much on average the two surfaces differ. This measure integrates over both over- and under-estimation of a surface. The calculation is not straightforward if point to point correspondence on two surfaces is not available. We use a similar strategy as for the Hausdorff distance computation. We calculate the average distance between A and M and inversely between M and A. We then calculate a common average by combining the two averages. This calculation can be formulated as follow:

  $$D_m(M, a) = \frac{1}{2}\left[d_{mean}(M, A) + d_{mean}(A, M)\right] \tag{B.6}$$

  where:

  $$d_{mean}(M, A) = \frac{1}{N_M} \sum_{m \in M} D(m, A) \tag{B.7}$$

  and $D(m, A) = [min_{a \in A} d(m, a)]$.

The Hausdorff distance and mean absolute distance, as opposed to volume metrics, are independent of the object size and show the quality of the segmentation at the border of the objects.

As a result, the selection of a metric in order to compare two objects depends on the application of the segmentation. The volume metrics solely cannot show the quality of the segmentation and have to be completed with surface metrics.

APPENDIX C

Multiphase level sets segmentation

[Vese and Chan, 2002] introduced a segmentation method which uses a particular case of the Mumford-Shah functional known as "The minimal partition problem" that restricts the problem to piecewise constant functions. This method uses a procedure of energy minimization allowing to detect objects whose boundaries are not necessarily defined by gradient. In addition, this model avoids the typical problems of edge stopping functions that are never exactly zero at the edges, with the negative result that the curve may eventually pass through object boundaries. It is important to note that with this algorithm the contours are automatically detected, and the initial curve can be anywhere in the image. The multiphase model of this method allows to handle complex topologies and multiple individual segments, avoiding the problem of vacuum and overlap. In particular the multiphase segmentation method may be initialized with m level set functions allowing to detect m^2 different regions (phases or segments).

C.1 Multiphase level sets model

Let us consider $m = \log n$ level sets function $\phi_i : \Omega \rightarrow \mathbb{R}$. Let also $\Phi = (\phi_1, ..., \phi_m)$ represent the "vector level sets" and $H(\Phi) = (H(\phi_1), ..., H(\phi_m))$ the "vector Heaviside function" (components of H are only 0 or 1). The segments or phases in the domain Ω are the pixels (or voxels) which have the same value of the Heaviside function, i.e two pixels (x_1, y_1) and (x_2, y_2) belong to the same class if $H(\Phi(x_1, y_1)) = H(\Phi(x_2, y_2))$. There are up to $n = 2^m$ possibilities for the vector values in the image of $H(\Phi)$, i.e we can define up to 2^m phases or classes in the domain Ω. The set of curves C is represented by the union of the zero level sets of the functions ϕ_i.

The simplified Mumford-Shah energy function was defined by [Vese and Chan, 2002] as:

$$F_n(c,\Phi) = \sum_{1\le I\le n=2^m} \int_\Omega (u_0 - c_I)^2 \chi_I dxdy + \sum_{1\le i\le m} \nu \int_\Omega |\nabla H(\phi_i)|$$

where classes are labeled by I and with characteristic function χ_I, $u_0 : \Omega \to \mathbb{R}$ is a given bounded image-function and $c = (c_1, ..., c_n)$ is a constant vector of averages and $c_I = mean(u_0)$. For $n = 4$ phases or classes the energy function is:

$$\begin{aligned} F_4(c,\Phi) &= \int_\Omega (u_0 - c_{11})^2 H(\phi_1)H(\phi_2)dxdy \\ &+ \int_\Omega (u_0 - c_{10})^2 H(\phi_1)(1 - H(\phi_2))dxdy \\ &+ \int_\Omega (u_0 - c_{01})^2 (1 - H(\phi_1))H(\phi_2)dxdy \\ &+ \int_\Omega (u_0 - c_{00})^2 (1 - H(\phi_1))(1 - H(\phi_2))dxdy \\ &+ \nu \int |\nabla H(\phi_1)|dxdy + \nu \int |\nabla H(\phi_2)|dxdy \end{aligned} \tag{C.1}$$

where $c = (c_{11}, c_{10}, c_{01}, c_{00})$ and $\Phi = (\phi_1, \phi_2)$.

With this notation, the image function u can be written as:

$$\begin{aligned} u &= c_{11}H(\phi_1)H(\phi_2) \\ &+ c_{10}H(\phi_1)(1 - H(\phi_2)) \\ &+ c_{01}(1 - H(\phi_1))H(\phi_2) \\ &+ c_{00}(1 - H(\phi_1))(1 - H(\phi_2)) \end{aligned} \tag{C.2}$$

By minimizing the energy function, the following Euler-Lagrange equations with respect to c and Φ are resulted:

$$\begin{aligned} c_{11}(\Phi) &= mean(u_0)\ in\ \{(x,y) : \phi_1(t,x,y) > 0, \phi_2(t,x,y) > 0\}, \\ c_{10}(\Phi) &= mean(u_0)\ in\ \{(x,y) : \phi_1(t,x,y) > 0, \phi_2(t,x,y) < 0\}, \\ c_{01}(\Phi) &= mean(u_0)\ in\ \{(x,y) : \phi_1(t,x,y) < 0, \phi_2(t,x,y) > 0\}, \\ c_{00}(\Phi) &= mean(u_0)\ in\ \{(x,y) : \phi_1(t,x,y) < 0, \phi_2(t,x,y) < 0\}, \end{aligned} \tag{C.3}$$

(if we consider $\phi_1(0,x,y) = \phi_{1,0}(x,y), \phi_2(0,x,y) = \phi_{2,0}(x,y)$).

and:

$$\begin{aligned}\frac{\partial \phi_1}{\partial t} &= \delta_\varepsilon(\phi_1)\{\nu div\left(\frac{\nabla \phi_1}{|\nabla \phi_1|}\right) \\ &\quad -[((u_0 - c_{11})^2 - (u_0 - c_{01})^2)H(\phi_2) \\ &\quad +((u_0 - c_{10})^2 - (u_0 - c_{00})^2)(1 - H(\phi_2))]\}, \end{aligned} \tag{C.4}$$

$$\begin{aligned}\frac{\partial \phi_1}{\partial t} &= \delta_\varepsilon(\phi_2)\{\nu div\left(\frac{\nabla \phi_2}{|\nabla \phi_2|}\right) \\ &\quad -[((u_0 - c_{11})^2 - (u_0 - c_{10})^2)H(\phi_1) + ((u_0 - c_{01})^2 \\ &\quad +(u_0 - c_{00})^2)(1 - H(\phi_1))]\} \end{aligned} \tag{C.5}$$

where $\delta_\varepsilon = H'_\varepsilon$ is a smooth approximation of the Dirac delta function δ_0, $\frac{\nabla \phi}{|\nabla \phi|}$ represents the unit normal to a level curve of ϕ at every point and $div(\frac{\nabla \phi}{|\nabla \phi|})$ represents the curvature of the level curve.

C.2 3D 4-phase level sets numerical algorithm

Here we extend the presented numerical algorithm by [Vese and Chan, 2002] to the 3D case. Let $h = \Delta x = \Delta y = \Delta z$ denote the space steps, Δt the time step, $\varepsilon = h, (x_i, y_i, z_i) = (ih, jh, kh)$ the discrete points, for $1 \leq i, j, k \leq M$ and $u_{0,i,j,k} \approx u_0(x_i, y_i, z_i), \phi^n_{i,j,k} \approx \phi(n\Delta t, x_i, y_i, z_i)$, with $n \geq 0$.

We compute the H_ε and δ_ε using the following equations:

$$\begin{aligned} H_\varepsilon(x) &= \frac{1}{2}\left[1 + \frac{2}{\pi} arctan\left(\frac{x}{\varepsilon}\right)\right], \\ \delta_\varepsilon(x) &= H'_{2,\varepsilon}(x) = \frac{1}{\pi}\frac{\varepsilon}{\varepsilon^2 + x^2} \end{aligned} \tag{C.6}$$

The algorithm consists of the following steps:

1. Initialization: Set $n = 0$ and $\phi^0_{1,i,j,k}, \phi^0_{1,i,j,k}$ with the set of initial contours.
2. Computing the averages c^n_{11}, c^n_{10}, c^n_{01} and c^n_{00} with the following equations:

$$c_{11} = \frac{\int_\Omega u_0 H_\varepsilon(\phi_1) H_\varepsilon(\phi_2) dxdydz}{\int_\Omega H_\varepsilon(\phi_1) H_\varepsilon(\phi_2) dxdydz} \tag{C.7}$$

$$c_{10} = \frac{\int_\Omega u_0 H_\varepsilon(\phi_1)(1 - H_\varepsilon(\phi_2))dxdydz}{\int_\Omega H_\varepsilon(\phi_1)(1 - H_\varepsilon(\phi_2))dxdydz} \tag{C.8}$$

$$c_{01} = \frac{\int_\Omega u_0 (1 - H_\varepsilon(\phi_1)) H_\varepsilon(\phi_2)dxdydz}{\int_\Omega (1 - H_\varepsilon(\phi_1)) H_\varepsilon(\phi_2)dxdydz} \tag{C.9}$$

$$c_{00} = \frac{\int_\Omega u_0 (1 - H_\varepsilon(\phi_1))(1 - H_\varepsilon(\phi_2))dxdydz}{\int_\Omega (1 - H_\varepsilon(\phi_1))(1 - H_\varepsilon(\phi_2))dxdydz} \tag{C.10}$$

3. Computing $\phi^{n+1}_{1,i,j,k}$ by the following equations (the equations are obtained by solving the calculated Euler-Lagrange equations):

$$C_1 = \frac{1}{\sqrt{\left(\frac{\phi^n_{1,i+1,j,k} - \phi^n_{1,i,j,k}}{h}\right)^2 + \left(\frac{\phi^n_{1,i,j+1,k} - \phi^n_{1,i,j-1,k}}{2h}\right)^2 + \left(\frac{\phi^n_{1,i,j,k+1} - \phi^n_{1,i,j,k-1}}{2h}\right)^2}}$$

$$C_2 = \frac{1}{\sqrt{\left(\frac{\phi^n_{1,i,j,k} - \phi^n_{1,i-1,j,k}}{h}\right)^2 + \left(\frac{\phi^n_{1,i-1,j+1,k-1} - \phi^n_{1,i-1,j-1,k-1}}{2h}\right)^2 + \left(\frac{\phi^n_{1,i-1,j-1,k+1} - \phi^n_{1,i-1,j-1,k-1}}{2h}\right)^2}}$$

$$C_3 = \frac{1}{\sqrt{\left(\frac{\phi^n_{1,i+1,j,k} - \phi^n_{1,i-1,j,k}}{2h}\right)^2 + \left(\frac{\phi^n_{1,i,j+1,k} - \phi^n_{1,i,j,k}}{h}\right)^2 + \left(\frac{\phi^n_{1,i,j,k+1} - \phi^n_{1,i,j,k-1}}{2h}\right)^2}}$$

$$C_4 = \frac{1}{\sqrt{\left(\frac{\phi^n_{1,i+1,j-1,k-1} - \phi^n_{1,i-1,j-1,k-1}}{2h}\right)^2 + \left(\frac{\phi^n_{1,i,j,k} - \phi^n_{1,i,j-1,k}}{h}\right)^2 + \left(\frac{\phi^n_{1,i-1,j-1,k+1} - \phi^n_{1,i-1,j-1,k-1}}{2h}\right)^2}}$$

$$C_5 = \frac{1}{\sqrt{\left(\frac{\phi^n_{1,i+1,j,k} - \phi^n_{1,i-1,j,k}}{2h}\right)^2 + \left(\frac{\phi^n_{1,i,j+1,k} - \phi^n_{1,i,j-1,k}}{2h}\right)^2 + \left(\frac{\phi^n_{1,i,j,k+1} - \phi^n_{1,i,j,k}}{h}\right)^2}}$$

$$C_6 = \frac{1}{\sqrt{\left(\frac{\phi^n_{1,i+1,j-1,k-1} - \phi^n_{1,i-1,j-1,k-1}}{2h}\right)^2 + \left(\frac{\phi^n_{1,i-1,j+1,k-1} - \phi^n_{1,i-1,j-1,k-1}}{2h}\right)^2 + \left(\frac{\phi^n_{1,i,j,k} - \phi^n_{1,i,j,k-1}}{h}\right)^2}}$$

Let:

$$P = \frac{\Delta t}{h^2}\delta_\varepsilon(\phi_{1,i,j,k})\nu,\ C = 1 + P(C_1 + C_2 + C_3 + C_4 + C_5 + C_6)$$

then:

$$\begin{aligned}\phi_{1,i,j,k}^{n+1} &= \frac{1}{C}[\phi_{1,i,j,k}^{n} \\ &+P(C_1\phi_{1,i+1,j,k}^{n}+C_2\phi_{1,i-1,j,k}^{n}+C_3\phi_{1,i,j+1,k}^{n} \\ &+C_4\phi_{1,i,j-1,k}^{n}+C_5\phi_{1,i,j,k+1}^{n}+C_6\phi_{1,i,j,k-1}^{n}) \\ &+\Delta t\delta_{\varepsilon}(\phi_{1,i,j,k}) \\ &(-(u_{0,i,j,k}-c_{11}^{n})^2H_{\varepsilon}(\phi_{2,i,j,k}^{n}) \\ &-(u_{0,i,j,k}-c_{10}^{n})^2(1-H_{\varepsilon}(\phi_{2,i,j,k}^{n})) \\ &+(u_{0,i,j,k}-c_{01}^{n})^2H_{\varepsilon}(\phi_{2,i,j,k}^{n}) \\ &+(u_{0,i,j,k}-c_{00}^{n})^2(1-H_{\varepsilon}(\phi_{2,i,j,k}^{n})))] \end{aligned} \tag{C.11}$$

4. Computing $\phi_{2,i,j,k}^{n+1}$ using the following equations:

$$D_1=\frac{1}{\sqrt{\left(\frac{\phi_{2,i+1,j,k}^{n}-\phi_{2,i,j,k}^{n}}{h}\right)^2+\left(\frac{\phi_{2,i,j+1,k}^{n}-\phi_{2,i,j-1,k}^{n}}{2h}\right)^2+\left(\frac{\phi_{2,i,j,k+1}^{n}-\phi_{2,i,j,k-1}^{n}}{2h}\right)^2}}$$

$$D_2=\frac{1}{\sqrt{\left(\frac{\phi_{2,i,j,k}^{n}-\phi_{2,i-1,j,k}^{n}}{h}\right)^2+\left(\frac{\phi_{2,i-1,j+1,k-1}^{n}-\phi_{2,i-1,j-1,k-1}^{n}}{2h}\right)^2+\left(\frac{\phi_{2,i-1,j-1,k+1}^{n}-\phi_{2,i-1,j-1,k-1}^{n}}{2h}\right)^2}}$$

$$D_3=\frac{1}{\sqrt{\left(\frac{\phi_{2,i+1,j,k}^{n}-\phi_{2,i-1,j,k}^{n}}{2h}\right)^2+\left(\frac{\phi_{2,i,j+1,k}^{n}-\phi_{2,i,j,k}^{n}}{h}\right)^2+\left(\frac{\phi_{2,i,j,k+1}^{n}-\phi_{2,i,j,k-1}^{n}}{2h}\right)^2}}$$

$$D_4=\frac{1}{\sqrt{\left(\frac{\phi_{2,i+1,j-1,k-1}^{n}-\phi_{2,i-1,j-1,k-1}^{n}}{2h}\right)^2+\left(\frac{\phi_{2,i,j,k}^{n}-\phi_{2,i,j-1,k}^{n}}{h}\right)^2+\left(\frac{\phi_{2,i-1,j-1,k+1}^{n}-\phi_{2,i-1,j-1,k-1}^{n}}{2h}\right)^2}}$$

$$D_5=\frac{1}{\sqrt{\left(\frac{\phi_{2,i+1,j,k}^{n}-\phi_{2,i-1,j,k}^{n}}{2h}\right)^2+\left(\frac{\phi_{2,i,j+1,k}^{n}-\phi_{2,i,j-1,k}^{n}}{2h}\right)^2+\left(\frac{\phi_{2,i,j,k+1}^{n}-\phi_{2,i,j,k}^{n}}{h}\right)^2}}$$

$$D_6=\frac{1}{\sqrt{\left(\frac{\phi_{2,i+1,j-1,k-1}^{n}-\phi_{2,i-1,j-1,k-1}^{n}}{2h}\right)^2+\left(\frac{\phi_{2,i-1,j+1,k-1}^{n}-\phi_{2,i-1,j-1,k-1}^{n}}{2h}\right)^2+\left(\frac{\phi_{2,i,j,k}^{n}-\phi_{2,i,j,k-1}^{n}}{h}\right)^2}}$$

Let:

$$Q=\frac{\Delta t}{h^2}\delta_{\varepsilon}(\phi_{2,i,j,k})\nu, D=1+Q(D_1+D_2+D_3+D_4+D_5+D_6)$$

then:

$$\begin{aligned}\phi^{n+1}_{2,i,j,k} &= \frac{1}{D}[\phi^{n}_{2,i,j,k} \\ &+Q(D_1\phi^{n}_{2,i+1,j,k} + D_2\phi^{n}_{2,i-1,j,k} + D_3\phi^{n}_{2,i,j+1,k} \\ &+D_4\phi^{n}_{2,i,j-1,k} + D_5\phi^{n}_{2,i,j,k+1} + D_6\phi^{n}_{2,i,j,k-1}) \\ &+\Delta t\delta_{\varepsilon}(\phi_{2,i,j,k}) \\ &(-(u_{0,i,j,k} - c^{n}_{11})^2 H_{\varepsilon}(\phi^{n}_{1,i,j,k}) \\ &-(u_{0,i,j,k} - c^{n}_{10})^2 (1 - H_{\varepsilon}(\phi^{n}_{1,i,j,k})) \\ &+(u_{0,i,j,k} - c^{n}_{01})^2 H_{\varepsilon}(\phi^{n}_{1,i,j,k}) \\ &+(u_{0,i,j,k} - c^{n}_{00})^2 (1 - H_{\varepsilon}(\phi^{n}_{1,i,j,k})))] \end{aligned} \tag{C.12}$$

5. Repeating from step 1 until steady state. The stability is checked in this way: for each i, j, k an error is computed as $|\phi^{n}_{t,i,j,k} - \phi^{n+1}_{t,i,j,k}|$ and the algorithm is stopped when the $max(error) \leq \epsilon$ (ϵ is defined by the user).

Publications

Atif, J., Khotanlou, H., Angelini, E., Duffau, H., and Bloch, I. (2006). Segmentation of Internal Brain Structures in the Presence of a Tumor. In *Medical Image Computing and Computer-Assisted Intervention- Oncology Workshop (MICCAI)*, pages 61–68, Copenhagen.

Khotanlou, H., Atif, J., Angelini, E., Duffau, H., and Bloch, I. (2007a). Adaptive Segmentation of Internal Brain Structures in Pathological MR Images Depending on Tumor Types. In *IEEE International Symposium on Biomedical Imaging (ISBI)*, pages 588–591, Washington DC, USA.

Khotanlou, H., Atif, J., Batrancourt, B., Colliot, O., Angelini, E., and Bloch, I. (2006). Segmentation de tumeurs cérébrales et intégration dans un modèle de l'anatomie. In *Reconnaissance des Formes et Intelligence Artificielle, RFIA'06*, Tours, France. (2nd prize AFRIF).

Khotanlou, H., Atif, J., Colliot, O., and Bloch, I. (2005). 3D Brain Tumor Segmentation Using Fuzzy Classification and Deformable Models. In *WILF2005*, volume 3849 of *Lecture notes in computer science(LNCS)*, pages 312–318.

Khotanlou, H., Colliot, O., Atif, J., and Bloch, I. (2007b). Brain tumor detection and segmentation using fuzzy classification, symmetry analysis and deformable model. *Fuzzy Sets and Systems*. in press.

Khotanlou, H., Colliot, O., and Bloch, I. (2007c). Automatic Brain Tumor Segmentation using Symmetry Analysis and Deformable Models. In *International Conference on Advances in Pattern Recognition (ICAPR)*, pages 198–202, Kolkata, India.

Bibliography

Ahmed, M. N., Yamany, S. M., Mohamed, N., Farag, A. A., and Moriarty, T. (2002). A modified fuzzy C-means algorithm for bias field estimation and segmentation of MRI data. *IEEE Transactions on Medical Imaging*, 21(3):193–199.

Algorri, M. E. and Flores-Mangas, F. (2004). Classification of anatomical structures in MR brain images using fuzzy parameters. *IEEE Transactions on Biomedical Engineering*, 51(9):1599–1608.

Ambroise, C., Dang, M., and Govaert, G. (1995). *Clustering of spatial data by the EM algorithm*, chapter GEOENV I (Geostatistics for Environmental Applications)., pages 493–504. Kluwer Academic Publishers.

Anlauf, J. K. and Biehl, M. (1989). The Adatron: an adaptive perceptron algorithm. *Europhysics Letters*, 10(7):687–692.

Armstrong, T. S., Cohen, M. Z., Weinbrg, J., and Gilbert, M. R. (2004). Imaging techniques in neuro oncology. In *Seminars in Oncology Nursing*, volume 20, pages 231–239.

Atif, J., Khotanlou, H., Angelini, E., Duffau, H., and Bloch, I. (2006a). Segmentation of Internal Brain Structures in the Presence of a Tumor. In *Medical Image Computing and Computer-Assisted Intervention- Oncology Workshop (MICCAI)*, pages 61–68, Copenhagen.

Atif, J., Nempont, O., Colliot, O., Angelini, E., and Bloch, I. (2006b). Level Set Deformable Models Constrained by Fuzzy Spatial Relations. In *Information Processing and Management of Uncertainty in Knowledge-Based Systems, IPMU*, pages 1534–1541, Paris, France.

Aurdal, L. (1997). *Analyse d'images IRM 3D multi-échos pour la détection et la quantification de pathologies cérébrales*. PhD thesis, Telecom Paris.

Bach Cuadra, M., Cuisenaire, O., Meuli, R., and Thiran, J.-P. (2001). Automatic segmentation of internal structures of the brain in MR images using a tandem of affine and non-rigid registration of an anatomical brain atlas. In *ICIP 2001*, pages 1083–1086, Thessaloniki.

Bach Cuadra, M., Pollo, C., Bardera, A., Cuisenaire, O., Villemure, J., and Thiran, J. (2004). Atlas-based segmentation of pathological MR brain images using a model of lesion growth. *IEEE Transactions on Medical Imaging*, 23(10):1301–1313.

Baillard, C., Hellier, P., and Barillot, C. (2001). Segmentation of brain 3D MR images using level sets and dense registration. *Medical Image Analysis*, 5:185–194.

Barra, V. and Boire, J.-Y. (2001). Automatic segmentation of subcortical brain structures in MR images using information fusion. *IEEE Transactions on Medical Imaging*, 20(7):549–558.

Belitz, H., Rohr, K., Müller, H., and Wagenknecht, G. (2006). First results of an automated model-based segmentation system for subcortical structures in human brain MRI data. In *IEEE International Symposium on Biomedical Imaging: From Nano to Macro (ISBI)*, pages 402–405, Arlington, VA, USA.

Bezdek, J., Ehrlich, R., and Full, W. (1984). The fuzzy c-means clustering algorithm. *Computers and Geosciences*, 10:191–203.

Bezdek., J. C. (1981). *Pattern Recognition with Fuzzy Objective Function Algorithms*. Plenum Press, New York.

Bezdek, J. C., Hathaway, R. J., Sabin, M. J., and Tucker, W. T. (1987). Convergence theory for fuzzy c-means: Counterexamples and repairs. *IEEE Transactions on Systems, Man, and Cybernetics*, 17(5):73–877.

Bloch, I. (1999a). Fuzzy relative position between objects in image processing: a morphological approach. *IEEE Transactions on Pattern Analysis and Machine Intelligence*, 21(7):657–664.

Bloch, I. (1999b). On fuzzy distances and their use in image processing under imprecision. *Pattern Recognition*, 32(11):1873–1895.

Bloch, I. (2005). Fuzzy spatial relationships for image processing and interpretation:A review. *Image and Vision Computing*, 23(2):89–110.

Bloch, I., Géraud, T., and Maître, H. (2003). Representation and fusion of heterogeneous fuzzy information in the 3D space for model-based structural recognition - application to 3D brain imaging. *Artificial Intelligence*, 148:141–175.

Bonneville, J.-F., Bonneville, F., and Cattin, F. (2005). Magnetic resonance imaging of pituitary adenomas. *European Radiology*, 15:543–548.

Brown, M. A. and Semelka, R. C. (2003). *MRI: Basic Principles and Applications*. Wiley, third edition.

Burges, C. (1998). A tutorial on support vector machines for pattern recognition. *Data Mining and Knowledge Discovery*, 2(2):121–167.

Burgun, A. (2006). Desiderata for domain reference ontologies in biomedicine. *Journal of Biomedical Informatics*, 39(3):307–313.

Busch, C. (1997). Wavelet based texture segmentation of multi-modal tomographic images. *Computers and Graphics*, 21(3):347–358.

Bushberg, J. T., Seibert, A., Leidholdt, E. M., and Boone, J. M. (2002). *The Essential Physics of Medical Imaging*. Lippincott Williams and Wilkins, 2nd edition.

Cai, H., Verma, R., Ou, Y., Lee, S., Melhem, E. R., and Davatzikos, C. (2007). Probabilistic segmentation of brain tumors based on multi-modality magnetic resonance images. In *IEEE International Symposium on Biomedical Imaging (ISBI)*, pages 600–603.

Capelle, A. S., Colot, O., and Fernandez-Maloigne, C. (2004). Evidential segmentation scheme of multi-echo MR images for the detection of brain tumors using neighborhood information. *Information Fusion*, 5:203–216.

Casati, R., Smith, B., , and Varzi, A. C. (2003). Ontological tools for geographic representation. *Japanese translation in Inter Communication*, 45:80–91.

Caselles, V., Catte, F., Coll, T., and Dibos, F. (1993). A geometric model for active contours. *Numerische Mathematik*, 66:1–31.

Cates, J. E., Lefohn, A. E., and Whitaker, R. T. (2004). GIST: An interactive GPU-based level-set segmentation tool for 3D medical images. *Medical Image Analysis*, 8(3):217–231.

Chaplot, S., Patnaik, L. M., and Jagannathan, N. R. (2006). Classification of magnetic resonance brain images using wavelets as input to support vector machine and neural network. *Biomedical Signal Processing and Control*, 1(1):86–92.

Chen, T. and Metaxas, D. N. (2003). Gibbs prior models, marching cubes, and deformable models: A hybrid framework for 3D medical image segmentation. In *Medical Image Computing and Computer-Assisted Intervention (MICCAI)*, volume 2879 of *LNCS*, pages 703–710, Montreal, Canada.

Ciofolo, C., Barillot, C., and Hellier, P. (2004). Combining fuzzy logic and level set methods for 3D MRI brain segmentation. In *IEEE International Symposium on Biomedical Imaging: Nano to Macro (ISBI2004)*, volume 1, pages 161–164, Arlington, VA, USA.

Clark, M. (1997). *Knowledge-Guided Processing of Magnetic Resonance Images of the Brain.* PhD thesis, University of South Florida.

Clark, M. C., Lawrence, L. O., Golgof, D. B., Velthuizen, R., Murtagh, F. R., and Silbiger, M. S. (1998). Automatic tumor segmentation using knowledge-based techniques. *IEEE Transactions on Medical Imaging*, 17(2):187–201.

Clatz, O., Sermesant, M., Bondiau, P.-Y., Delingette, H., Warfield, S. K., Malandain, G., and Ayache, N. (2005). Realistic simulation of the 3D growth of brain tumors in MR images coupling diffusion with mass effect. *IEEE Transactions on Medical Imaging*, 24(10):1334–1346.

Cocosco, C. A., Kollokian, V., Kwan, R. K. S., and Evans, A. C. (1997). Brainweb: Online interface to a 3D MRI simulated brain database. In *NeuroImage (Proceedings of 3-rd International Conference on Functional Mapping of the Human Brain)*, volume 5, page S425, Copenhagen.

Cointepas, Y., Mangin, J.-F., Garnero, L., Poline, J.-B., and Benali, H. (2001). Brain VISA: Software platform for visualization and analysis of multi-modality brain data. *Neuroimage*, 13(6):S98.

Collins, D. L. (1994). *3D Model-based segmentation of individual brain structures from magnetic resonance imaging data*. PhD thesis, Department of Biomedical Engineering, McGill University, Montreal, Canada.

Colliot, O., Camara, O., and Bloch, I. (2006). Integration of Fuzzy Spatial Relations in Deformable Models - Application to Brain MRI Segmentation. *Pattern Recognition*, 39:1401–1414.

Cootes, T. F., Cooper, D., Taylor, C. J., and Graham, J. (1995). Active shape models - their training and application. *Computer Vision and Image Understanding*, 61(1):38–59.

Corcho, O., Fernandez-Lopez, M., and Gomez-Perez, A. (2003). Methodologies, tools and languages for building ontologies: where is their meeting point? *Data Knowledge Engineering*, 46(1):41–64.

Corso, J. J., Sharon, E., and Yuille, A. (2006). Multilevel segmentation and integrated Bayesian model classification with an application to brain tumor segmentation. In *MICCAI2006*, volume LNCS 4191, pages 790–798, Copenhagen, Denmark.

Cortes, C. and Vapnik, V. N. (1995). Support vector networks. *Machine Learning*, 20:273–297.

Cristani, M. and Cuel, R. (2005). A survey on ontology creation methodologies. *International Journal on Semantic Web and Information System*, 1(2):49–69.

Curran, J. G. and O'connor, E. (2005). Imaging of craniopharyngioma. *Child's Nervous System*, 21:635–639.

Dam, E. and Letteboer, M. L. M. (2004). Integrating automatic and interactive brain tumor segmentation. In *17th International Conference on Pattern Recognition (ICPR 2004)*, volume 3, pages 790– 793, Cambridge, UK.

Dameron, O., Gibaud, B., and Morandi, X. (2004). Numeric and symbolic representation of the cerebral cortex anatomy: Methods and preliminary results. *Surgical and Radiologic Anatomy*, 26(3):191–197.

Dasiopoulou, S., Mezaris, V., Kompatsiaris, I., Papastathis, V. K., and Strintzis, M. G. (2005). Knowledge-assisted semantic video object detection. *IEEE Transactions on Circuits and Systems for Video Technology*, 15(10):1210–1224.

Dauguet, J., Mangin, J. F., Delzescaux, T., and Frouin, V. (2004). Robust inter-slice intensity normalization using histogram scale-space analysis. In Barillot, C., Haynor, D., and Hellier, P., editors, *MICCAI'04*, volume 3216 of *LNCS*, pages 242–249, Saint-Malo, France. Springer Verlag.

Daumas-Duport, C. (1992). Histological grading of gliomas. *Current Opinion in Neurology and neurosurgery*, 5(6):924–931.

Daumas-Duport, C., Beuvon, F., Varlet, P., and Fallet-Bianco, C. (200). Gliomes: Classification de l'OMS et de l'Hoôpital Sainte-Anne. *Ann. Pathology*, 20(5):413–428.

Dawant, B., Hartmann, S., Thirion, J.-P., Maes, F., Vandermeulen, D., and Demaerel, P. (1999a). Automatic segmentation of internal structures of the head using a combination of similarity and free-form transformations: Part I, methodology and validation on normal subjects. *IEEE Transactions on Medical Imaging*, 18(10).

Dawant, B. M., Hartmann, S. L., and Gadamsetty, S. (1999b). Brain atlas deformation in the presence of large space-occupying tumors. In *Medical Image Computing and Computer-Assisted Intervention (MICCAI)*, volume 1679 of *Lecture Notes in Computer Science*, pages 589–596, Cambridge, UK. Springer.

Dawant, M., Hartmann, S. L., Pan, S., and Gadamsetty, S. (2002). Brain atlas deformation in the presence of small and large space-occupying tumors. *Computer Aided Surgery*, 7:1–10.

Delingette, H. (1999). General object reconstruction based on simplex meshes. *International Journal of Computer Vision*, 32(2):111–146.

Dickson, S., Thomas, B. T., and Goddard, P. (1997). Using neural networks to automatically detect brain tumours in MR images. *International Journal of Neural Systems.*, 8(1):91–99.

Dominey, P. F., Boucher, J. D., , and Inui, T. (2004). Building an adaptive spoken language interface for perceptually grounded human-robot interaction. In *In 4th IEEE/RAS International Conference on Humanoid Robots*, pages 168–183.

Donnelly, M., Bittner, T., and Rosse, C. (2006). A formal theory for spatial representation and reasoning in biomedical ontologies. *Artificial Intelligence in Medicine*, 36(1):1–27.

Doolittle, N. D. (2004). State of science in brain tumor classification. In *Seminars in Oncology Nursing*, volume 20, pages 224–230.

Dou, W., Ruan, S., Chen, Y., Bloyet, D., and Constans, J. M. (2007). A framework of fuzzy information fusion for segmentation of brain tumor tissues on MR images. *Image and Vision Computing*, 25:164–171.

Droske, M., Meyer, B., Rumpf, M., and Schaller, C. (2001). An adaptive level set method for medical image segmentation. In *Proceedings of the 17th International Conference on Information Processing in Medical Imaging*, volume 2082 of *LNCS*, pages 416–422. Springer-Verlag.

Dubois, D. and Prade, H. (1980). *Fuzzy Sets and Systems: Theory and Applications*. Academic Press, New-York.

Duta, N. and Sonka, M. (1998). Segmentation and interpretation of MR brain images. An improved active shape model. *IEEE Transactions on Medical Imaging*, 17(6):1049–1062.

Emedicine (2005). http://www.emedicine.com.

Engelhard, H. H. (2001). Progress in the diagnosis and treatment of patients with meningiomas. *Surgical Neurology*, 55:89–101.

Engelhard, H. H., Stelea, A., and Mundt, A. (2003). Oligodendroglioma and anaplastic oligodendroglioma: Clinical features, treatment and prognosis. *Surgical Neurology*, 60:443–456.

Feng, Y. and Chen, W. (2004). Brain MR image segmentation using fuzzy clustering with spatial constraints based on Markov random field theory. In *Second International Workshop on Medical Imaging and Augmented Reality (MIAR)*, volume 3150 of *Lecture Notes in Computer Science*, pages 188–195.

Firenze, F. and Morasso, P. (1993). The capture effect model: a new approach to self-organized clustering. In *The Sixth International Conference on Neural Networks and their Industrial and Cognitive Applications and Exhibition Catalog, NEURO-NIMES 93*, pages 45–54, Nimes, France.

Fischl, B., Salat, D., Busa, E., Albert, M., Dieterich, M., Haselgrove, C., vanderKouwe, A., Killiany, R., Kennedy, D., and Klaveness, S. (2002). Whole brain segmentation. Automated labeling of neuroanatomical structures in the human brain. *Neuron*, 33(3):341–355.

Fletcher-Heath, L. M., Hall, L. O., Goldgof, D. B., and Murtagh, F. (2001). Automatic segmentation of non-enhancing brain tumor in magnetic resonance images. *Artificial Intelligence in Medicine*, 21:43–63.

Fouquier, G., Atif, J., and Bloch, I. (2007). Local reasoning in fuzzy attributes graphs for optimizing sequential segmentation. In *6th IAPR-TC15 Workshop on Graph-based Representations in Pattern Recognition, GbR'07*, volume 4538 of *LNCS*, pages 138–147, Alicante, Spain.

Freeman, J. (1975). The modeling of spatial relations. *Computer Graphics and Image Processing*, 4:156–171.

Garcia, C. and Moreno, J. (2004). Kernel based method for segmentation and modeling of magnetic resonance images. *LNCS*, 3315:636–645.

Geraud, T. (1998). *Segmentation des structures internes du cerveau en imagerie par résonance magnétique tridimensionnelle*. PhD thesis, Telecom Paris, Paris, France.

Gerig, G., Jomier, M., and Chakos, M. (2001). VALMET: a new validation tool for assessing and improving 3D object segmentation. In *MICCAI*, volume 2208, pages 516–523, Utrecht, Netherlands.

Gering, D. T. (2003). *Recognizing Deviations from Normalcy for Brain Tumor Segmentation*. PhD thesis, Massachusetts Institute of Technology.

Gibbs, P., Buckley, D. L., Blackband, S. J., and Horsman, A. (1996). Tumour volume determination from MR images by morphological segmentation. *Physics in Medicine and Biology*, 41(11):2437–2446.

Gomez-Perez, A., Fernandez-Lopez, M., and Corcho, O. (2004). *Ontological Engineering*. Springer-Verlag, first edition.

Grimson, W. E. L. and Golland, P. (2005). Analyzing anatomical structures: Leveraging multiple sources of knowledge. In *CVBIA*, pages 3–12.

Gruber, T. (1993). A Translation Approach to Portable Ontology Specifications. *Knowledge Acquisition*, 5(2):199–220.

Haacke, E. M., Brown, R. W., Thompson, M. R., and Venkatesan, R. (1999). *Magnetic Resonance Imaging: Physical Principles and Sequence Design*. Wiley.

Haarslev, V. and Moller, R. (2001). Racer system description. In *International Joint Conference on Automated Reasoning (IJCAR 2001)*, pages 701–706.

Hajnal, J. V., Saeed, N., Soar, E. J., Oatridge, A., Young, R. I., and Bydder, G. M. (1995). A registration and interpolation procedure for subvoxel matching of serially acquired MR images. *Journal of Computer Assisted Tomography*, 19(2):289–296.

Hall, L. O., Bensaid, A. M., Clarke, L. P., Velthuizen, R. P., Silbiger, M. S., and Bezdek, J. C. (1992). A comparison of neural network and fuzzy clustering techniques in segmenting magnetic resonance images of the brain. *IEEE Transactions on Neural Networks*, 3(5):672 – 682.

Han, D., You, B. J., Kim, Y. S. E., and Suh, I. L. H. (2005). A generic shape matching with anchoring of knowledge primitives of object ontology. In *ICIAR*, volume 3646 of *LNCS*, pages 437–480.

Hata, N., Muragaki, Y., Inomata, T., Maruyama, T., Iseki, H., Hori, T., and Dohi, T. (2005). Interaoperative tumor segmentation and volume measurement in MRI-guided glioma surgery for tumor resection rate control. *Academic Radiology*, 12:116–122.

Held, K., Kops, E., Krause, B., Wells, W., Kikinis, R., and Muller-Gartner, H. (1997). Markov random field segmentation of brain MR images. *IEEE Transactions on Medical Imaging*, 16(6):878–886.

Henson, J. W., Gaviani, P., and Gonzalez, R. G. (2005). MRI in treatment of adult gliomas. *The Lancet Oncology*, 6:167–175.

Herlidou-Meme, S., Constans, J. M., Carsin, B., Olivie, D., Eliat, P. A., Nadal-Desbarats, L., Gondry, C., Rumeur, E. L., Idy-Peretti, I., and de Certaines, J. D. (2003). MRI texture analysis on texture test objects, normal brain and intracranial tumors. *Magnetic Resonance Imaging*, 21:989–993.

Herskovits, H. E., Itoh, R., and Melhem, E. R. (2001). Accuracy for detection of simulated lesions: Comparison of fluid-attenuated inversion-recovery, proton density-weighted, and T2-weighted synthetic brain MR imaging. *American Journal of Roentgenology*, 176:1313–1318.

Ho, S., Bullitt, E., and Gerig, G. (2002). Level set evolution with region competition: Automatic 3D segmentation of brain tumors. In *ICPR*, pages 532–535, Quebec.

Hoppner, F. (2003). A contribution to convergence theory of fuzzy c-means and derivatives. *IEEE Transactions on fuzzy systems*, 11(5):682–694.

Hu, S. and Collins, D. L. (2007). Joint level-set shape modeling and appearance modeling for brain structure segmentation. *NeuroImage*, 36:672–683.

Hudelot, C., Atif, J., and Bloch, I. (2007). Fuzzy Spatial Relation Ontology for Image Interpretation. *Fuzzy Sets and Systems*, To appear.

Iftekharuddin, K. M., Jia, W., and Marsh, R. (2003). Fractal analysis of tumor in brain MR images. *Machine Vision and Applications*, 13:352–362.

Iosifescu, D. V., Shenton, M. E., Warfield, S. K., Kikinis, R., Dengler, J., Jolesz, F. A., and Mc Carley, R. W. (1997). An automated registration algorithm for measuring MRI subcortical brain structures. *NeuroImage*, 6:13–25.

Jain, A. K., Murty, M. N., and Flynn, P. J. (1999). Data clustering: a review. *ACM Computing Surveys*, 31(3):264–323.

Jenkinson, M., Bannister, P. R., Brady, J. M., and Smith., S. M. (2002). Improved optimisation for the robust and accurate linear registration and motion correction of brain images. *NeuroImage*, 17(2):825–841.

Jiang, C., Xinhaua, X., Huang, W., and Mene, C. (2004). Segmentation and quantification of brain tumor. In *IEEE Symposium on Virtual Environments, Human-Computer Interfaces and Measurement Systems (VECIMS)*, pages 61– 66, Boston, MA, USA.

Jiji, G. W. and Ganesan, L. (2005). Unsupervised segmentation using fuzzy logic based texture spectrum for MRI brain images. In *Third World Enformatika Conference (WEC2005)*, pages 155–157, Istanbul, Turkey.

Julià-Sapé, M., Acosta, D., Majós, C., Moreno-Torres, A., Wesseling, P., Acebes, J. J., Griffiths, J. R., and Arús, C. (206). Comparison between neuroimaging classifications and histopathological diagnoses using an international multicenter brain tumor magnetic resonance imaging database. *Journal of neurosurgery*, 105:6–14.

Kantor, G., Loiseau, H., Vital, A., and Mazeron, J. J. (2001). Volume tumoral macroscopique (GTV) et volume cible anatomoclinique (CTV) des tumeurs gliales de l'adulte. *Cancer/Radiother*, 5:581–580.

Kass, M., Witkin, A., and Terzopoulos, D. (1988). Snakes: Active contour models. *International Journal of Computer Vision*, 1(4):321–331.

Kaus, M. R., Warfield, S. K., Nabavi, A., Black, P. M., Jolesz, F. A., and Kikinis, R. (2001). Automated segmentation of MR images of brain tumors. *Radiology*, 218:586–591.

Kaus, M. R., Warfield, S. K., Nabavi, A., Chatzidakis, E., Black, P. M., Jolesz, F. A., and Kikinis, R. (1999). Segmentation of meningiomas and low grade gliomas in MRI. In *MICCAI*, volume LNCS 1679, pages 1–10, Cambridge UK.

Kelemen, A., Szekely, G., and Gerig, G. (1999). Elastic model-based segmentation of 3D neuroradiological data sets. *IEEE Transactions on Medical Imaging*, 18(10):828–839.

Kernohan, J. W., Maybon, R. F., Svien, H. J., and Adson, A. W. (1949). A simplified classification of the gliomas. *Proc Staff Meet Mayo Clin*, 24:71–75.

Khotanlou, H., Atif, J., Angelini, E., Duffau, H., and Bloch, I. (2007a). Adaptive Segmentation of Internal Brain Structures in Pathological MR Images Depending on Tumor Types. In *IEEE International Symposium on Biomedical Imaging (ISBI)*, pages 588–591, Washington DC, USA.

Khotanlou, H., Atif, J., Colliot, O., and Bloch, I. (2005). 3D Brain Tumor Segmentation Using Fuzzy Classification and Deformable Models. In *WILF2005*, volume 3849 of *Lecture notes in computer science(LNCS)*, pages 312–318.

Khotanlou, H., Colliot, O., Atif, J., and Bloch, I. (2007b). Brain tumor detection and segmentation using fuzzy classification, symmetry analysis and deformable model. *Fuzzy Sets and Systems*. in press.

Khotanlou, H., Colliot, O., and Bloch, I. (2007c). Automatic Brain Tumor Segmentation using Symmetry Analysis and Deformable Models. In *International Conference on Advances in Pattern Recognition (ICAPR)*, pages 198–202, Kolkata, India.

Kjaer, L., Ring, P., Thomsen, C., and Henriksen, O. (1995). Texture analysis in quantitative MR imaging. Tissue characterization of normal brain and intracranial tumours at 1.5 T. *Acta Radiologica*, 36(2):127–135.

Klien, E. and Lutz, M. (2005). The role of spatial relations in automating the semantic annotation of geodata. In *Conference on Spatial Information Theory (COSIT 2005)*, volume 3693 of *LNCS*, pages 133–148.

Krishnapuram, R. and Keller, J. M. (1993). A possibilistic approach to clustering. *IEEE Transactions on Fuzzy Systems*, 1(2):98–110.

Krishnapuram, R. and Keller, J. M. (1996). The possibilistic c-means algorithm: insights and recommendations. *IEEE Transactions on Fuzzy Systems*, 4:385–393.

Kruggel, F. and Lohmann, G. (1997). Automatical adaption of the stereotactical coordinate system in brain MRI datasets. In *International Conference on Information Processing in Medical Imaging (IPMI)*, volume 1230 of *LNCS*, pages 471–476, London, UK. Springer-Verlag.

Kufe, D. W., Pollock, R. E., Weichselbaum, R. R., Gansler, T. S., and Bast, R. C., editors (2003). *Holland-Frei Cancer Medicine*. BC Decker Inc., 6th edition.

Kyriacou, S. K., Davatzikos, C., Zinreich, S. J., and Bryan, N. (1999). Nonlinear elastic registration of brain images with tumor pathology using a biomechanical model. *IEEE Transactions on Medical Imaging*, 18(7):580–592.

Law, A. K. W., Lam, F. K., and Chan, F. H. Y. (2002). A fast deformable region model for brain tumor boundary extraction. In *Engineering in Medicine and Biology, EMBS/BMES*, volume 2, pages 1055–1056, Houston, USA.

Law, A. K. W., Zhu, H., Chan, B. C. B., Iu, P. P., Lam, F. K., and Chan, F. H. Y. (2001). Semi-automatic tumor boundary detection in MR image sequences. In *International Symposium on intelligent Multimedia, Video and Speech Processing*, pages 28–31, Hong Kong.

Lee, A. G., Brazis, P. W., Garrity, J. A., and White, M. (2004). Imaging for neuro-ophthalmic and orbital disease. *American Journal of Ophtalmology*, 138(5):852–863.

Lee, C.-H., Schmidt, M., Murtha, A., Bistritz, A., Sander, J., and Greiner, R. (2005). Segmenting brain tumors with conditional random fields and support vector machines. In *LNCS*, volume 3765, pages 469–478.

Leemput, K. V., Maes, F., Vandermeulen, D., Colchester, A., and Suetens, P. (2001). Automated segmentation of multiple sclerosis lesions by model outlier detection. *IEEE Transactions on Medical Imaging*, 20:677–688.

Lefohn, A., Cates, J., and Whitaker, R. (2003). Interactive, GPU-based level sets for 3D brain tumor segmentation. Technical report, University of Utah.

Lerski, R. A., Straughan, K., Schad, L. R., Boyce, D., Bluml, S., and Zuna, I. (1993). MR image texture analysis - An approach to tissue characterization. *Magnetic Resonance Imaging*, 11(6):873–887.

Letteboer, M., Olsen, O., Dam, E., Willems, P., Viergever, M., and Niessen, W. (2004). Segmentation of tumors in magnetic resonance brain images using an interactive multiscale watershed algorithm. *Academic Radiology*, 11(10):1125–1138.

Liew, A. W. C. and H. Yan, H. (2003). An adaptive spatial fuzzy clustering algorithm for 3-D MR image segmentation. *IEEE Transactions on Medical Imaging*, 22(9):1063–1075.

Linguraru, M. G., Gonzalez, M. A., and Ayache, N. (2007). Deformable atlases for the segmentation of internal brain nuclei in magnetic resonance imaging. *International Journal of Computers, Communications and Control*, 2(1):26–36.

Liu, J., Udupa, J. K., Odhner, D., Hackney, D., and Moonis, G. (2005). A system for brain tumor volume estimation via MR imaging and fuzzy connectedness. *Computerized Medical Imaging and Graphics*, 29:21–34.

Liu, Y., Collins, R. T., and Rothfus, W. E. (1996). Automatic extraction of the central symmetry (mid-sagittal) plane from neuroradiology images. Technical report, Carnegie Mellon Univ., Pittsburgh, PA, The Robotics Institute.

Lobato, R. D., Alday, R., Gomez, P. A., Rivas, J. J., Dominguez, J., Cabrera, A., Madero, S., and Ayerbe, J. (1996). Brain oedema in patients with intracranial meningioma. *Acta Neurochirurgica*, 138(5):485–495.

Lopes, M. B. S. and Laws, E. R. (2002). Low-grade central nervous system tumors. *Neurosurg Focus*, 12(2):1–4.

Luo, S., Li, R., and Ourselin, S. (2003). A new deformable model using dynamic gradient vector flow and adaptive balloon forces. In Lovell, B., editor, *APRS Workshop on Digital Image Computing*, Brisbane, Australia.

Ma, L. and Staunton, R. C. (2007). A modified fuzzy c-means image segmentation algorithm for use with uneven illumination patterns. *Pattern Recognition*, 40(11):3005–3011.

Magnotta, V. A., Bockholt, H. J., Johnson, H. J., Christensen, G. E., and Andreasen, N. C. (2003). Subcortical, cerebellar, and magnetic resonance based consistent brain image registration. *NeuroImage*, 19:233–245.

Mahesh, M. R. and Tse, V. (2004). Diagnosis and staging of brain tumors. In *Seminars in Roentgenology*, volume 39, pages 347–360.

Mahmoud-Ghoneima, D., Toussaintb, G., Constansc, J., and de Certainesa, J. D. (2003). Three dimensional texture analysis in MRI: a preliminary evaluation in gliomas. *Magnetic Resonance Imaging*, 21:983–987.

Maillot, N. E. and Thonnat, M. (2007). Ontology based complex object recognition. *Image and Vision Computing*. To appear.

Maintz, J. and Viergever, M. (1998). A survey of medical image registration. *Medical Image Analysis*, 2(1):1–36.

Maksoud, Y. A., Hahn, Y. S., and Engelhard, H. H. (2002). Intracranial ependymoma. *Neurosurg Focus*, 13(3):1–5.

Malladi, R., Sethian, J., and Vemuri, B. C. (1995). Shape modeling with front propagation: A level set approach. *IEEE Transactions on Pattern Analysis and Machine Intelligence*, 17(2):158–175.

Mancas, M. and Gosselin, B. (2004). Toward an automatic tumor segmentation using iterative watersheds. In Fitzpatrick, J. and Sonka, M., editors, *Medical Imaging 2004: Image Processing (SPIE2004)*, volume 5370, pages 1598–1608.

Mandelbrot, B. B. (1982). *The Fractal Geometry of Nature*. W. H. Freeman.

Mangin, J.-F. (2000). Entropy minimization for automatic correction of intensity nonuniformity. In *IEEE Workshop MMBIA*, pages 162–169, South Carolina, USA. IEEE Press.

Mangin, J.-F., Coulon, O., and Frouin, V. (1998). Robust brain segmentation using histogram scale-space analysis and mathematical morphology. In *MICCAI*, pages 1230–1241, Cambridge USA.

Marieb, E. N. (2000). *Human Anatomy and Physiology*. Benjamin-Cummings Publishing Company, 5th edition.

Marquet, G., Dameron, O., Saikali, S., Mosser, J., and Burgun, A. (2007). Grading glioma tumors using OWL-DL and NCI thesaurus. In *Proceedings of the American Medical Informatics Association Conference AMIA'07*.

Masulli, F. and Schenone, A. (1999). A fuzzy clustering based segmentation system as support to diagnosis in medical imaging. *Artificial Intelligence in Medicine*, 16(2):129–147.

Meijering, E. (2002). A chronology of interpolation: From ancient astronomy to modern signal and image processing. *Proceedings of the IEEE*, 90(3):319–342.

Mohamed, A., Shen, D., and Davatzikos, C. (2005). Deformable registration of brain tumor images via a statistical model of tumor-induced deformation. In *MICCAI*, pages 263–270.

Moon, N., Bullitt, E., Leemput, K. V., and Gerig, G. (2002). Model-based brain and tumor segmentation. In *ICPR*, pages 528–531, Quebec.

Moon, T. K. (1996). The expectation-maximization algorithm. *IEEE Signal Processing Magazine*, 13(6):47 – 60.

Moonis, G., Liu, J., Udupa, J. K., and Hackney, D. B. (2002). Estimation of tumor volume with fuzzy-connectedness segmentation of MR images. *American Journal of Neuroradiology*, 23:352–363.

Nain, D., Styner, M., Niethammer, M., Levitt, J. J., Shenton, M., Gerig, G., Bobick, A., and Tannenbaum, A. (2007). Statistical shape analysis of brain structures using spherical wavelets. In *IEEE International Symposium on Biomedical Imaging: From Nano to Macro (ISBI 2007)*, pages 209–212, Washington DC, USA.

Nempont, O., Atif, J., Angelini, E., and Bloch, I. (2007). Combining Radiometric and Spatial Structural Information in a New Metric for Minimal Surface Segmentation. In *Information Processing in Medical Imaging (IPMI 2007)*, volume 4584 of *LNCS*, pages 283–295, Kerkrade, The Netherlands.

Nientiedt, M. (2007). *Remote Sensing Image Mining: Applying Action-Driven Ontologies to the Change of Landuse Patterns*. PhD thesis, Institute for Geoinformatics, Muenster University.

Niu, X. (2006). A semi-automatic framework for highway extraction and vehicle detection based on a geometric deformable model. *ISPRS Journal of Photogrammetry and Remote Sensing*, 61:170–186.

Nowinski, W. and Belov, D. (2005). Toward atlas-assisted automatic interpretation of MRI morphological brain scans in the presence of tumor. *Academic Radiology*, 12(8):1049–1057.

Osher, S. and Sethian, J. (1988). Fronts propagating with curvature dependent speed: Algorithms based on hamilton-jacobi formulations. *Journal of Computational Physics*, 79:12–49.

Pal, N. R., Pal, K., and Bezdek, J. C. (1997). A mixed c-means clustering model. In *IEEE International Conference on Fuzzy Systems*, volume 1, pages 11–21.

Pal, N. R., Pal, K., Keller, J. M., and Bezdek, J. C. (2005). A possibilistic fuzzy c-means clustering algorithm. *IEEE Transactions on Fuzzy Systems*, 13(4):517–530.

Peng, Z., Wee, W., and Lee, J. H. (2005). MR brain imaging segmentation based on spatial Gaussian mixture model and Markov random field. In *IEEE International Conference on Image Processing (ICIP)*, pages 313–316.

Perona, P. and Malik, J. (1990). Scale-space and edge detection using anisotropic diffusion. *IEEE Transactions on Pattern Analysis and Machine Intelligence.*, 12(7):629–639.

Pham, D. L. (2001). Spatial models for fuzzy clustering. *Computer Vision and Image Understanding*, 84(2):285–297.

Pham, D. L., Xu, C., and Prince, J. L. (2000). A survey current methods in segmentation. *Annual Review of Biomedical Engineering*, pages 315–337.

Phillips, W. E., Velthuizen, R. P., Phuphanich, S., Hall, L. O., Clarke, L. P., and Silbeiger, M. L. (1995). Application of fuzzy c-means segmentation technique for tissue differentiation in MR images of a hemorrhagic glioblastoma multiform. *Magnetic Resonance Imaging*, 13(2):277–290.

Piquet, B., Silva, C. T., and Kaufman, A. (1996). Tetra-cubes: an algorithm to generate 3D isosurfaces based upon tetrahedra. In *Brazilian Symposium on Computer Graphics and Image Processing, SIBGRAPI 96*, volume 21, pages 205–210.

Pitiot, A., Toga, A. W., and Thompson, P. M. (2002). Adaptive elastic segmentation of brain MRI via shape-model-guided evolutionary programming. *IEEE Transactions on Medical Imaging*, 21(8):910–923.

Plotkin, S. R. and Batchelor, T. T. (2001). Primary nervous-sytem lymphoma. *The Lancet Oncology*, 2:354–365.

Pohl, K. M., Grimson, W. E. L., Bouix, S., and Kikinis, R. (2004). Anatomical guided segmentation with non-stationary tissue class distributions in an expectation-maximization framework. In *IEEE International Symposium on Biomedical Imaging: Nano to Macro (ISBI)*, pages 81–84, Arlington, VA, USA.

Pollo, C., Bach Cuadra, M., Cuisenaire, O., Villemure, J., and Thiran, J. P. (2005). Segmentation of brain structures in presence of a space-occupying lesion. *Neuroimage*, 24(4):990–996.

Poupon, F., Mangin, J.-F., Hasboun, D., Poupon, C., Magnin, I., and Frouin, V. (1998). Multi-object deformable templates dedicated to the segmentation of brain deep structures. In *MICCAI*, volume 1496 of *LNCS*, pages 1134–1143, MIT. Springer Verlag.

Powell, S., Magnotta, V. A., Johnson, H. J., Jammalamadaka, V. K., and Andreasen, N. C. (2008). Registration and machine learning based automated segmentation of subcortical and cerebellar brain structures. *NeuroImage*. to appear.

Prastawa, M., Bullitt, E., and Gerig, G. (2005). Synthetic ground truth for validation of brain tumor MRI segmentation. In *International Conference on Medical Image Computing and Computer-Assisted Intervention(MICCAI)*, volume 3749 of *Lecture Notes in Computer Science*, pages 26–33. Springer.

Prastawa, M., Bullitt, E., Ho, S., and Gerig, G. (2004). A brain tumor segmentation framework based on outlier detection. *Medical Image Analysis*, 18(3):217–231.

Prastawa, M., Bullitt, E., Moon, N., Leemput, K. V., and Gerig, G. (2003). Automatic brain tumor segmentation by subject specific modification of atlas priors. *Academic Radiology*, 10:1341–1348.

Protégé (2007). http://protege.stanford.edu.

Reddick, W. E., Mulhern, R. K., Elkin, T. D., Glass, J. O., Merchant, T. E., and Langston, J. W. (1998). A hybrid neural network analysis of subtle brain volume differences in children surviving brain tumors. *Magnetic Resonance Imaging*, 16(4):413–421.

Rexilius, J., Hahn, H. K., Klein, J., Lentschig, M. G., and Peitgen, H.-O. (2007). Multispectral brain tumor segmentation based on histogram model adaptation. In *SPIE*, volume 6514, page 65140V, San Diego, USA.

Ricci, P. E. and Dungan, D. H. (2001). Imaging of low- and intermediate-grade gliomas. *Seminars in Radiation Oncoloy, Vol 11, No 2 (April), 2001: pp 103-112*, 11(2):103–112.

Ringertz, J. (1950). Grading of gliomas. *Acta Pathol Microbiol Scand*, pages 27–51.

Roche, A., Malandain, G., Pennec, X., and Ayache, N. (1998). The correlation ratio as a new similarity measure for multimodal image registration. *Lecture Notes in Computer Science*, 1496:1115–1124.

Rohlfing, T., Brandt, R., Menzel, R., and Maurer, C. R. J. (2004). Evaluation of atlas selection strategies for atlas-based image segmentation with application to confocal microscopy images of bee brain. *NeuroImage*, 21:1428–1442.

Rosse, C. and Mejino, J. L. V. (2003). A reference ontology for biomedical informatics: the foundational model of anatomy. *Journal of Biomedical Informatics*, 36(6):478–500.

Ruan, S., Lebonvallet, S., Merabet, A., and Constans, J.-M. (2007). Tumor segmentation from a multispectral MRI images by using support vector machine classification. In *ISBI*, pages 1236–1239, Washington, USA.

Russel, D. S. and Rubinstein, L. J. (1971). Pathology of tumors of the nervous system. *Williams and Wikins*, pages 147–153.

Sabin, M. (1987). Convergence and consistency of fuzzy c-means/isodata algorithms. *IEEE Transactions on Pattern Analysis and Machine Intelligence*, 9(5):661–668.

Saha, P. K. and Udupa, J. K. (2001). Relative fuzzy connectedness among multiple objects: Theory, algorithms, and applications in image segmentation. *Computer Vision and Image Understanding*, 82:42–56.

Saleh, A., Wenserski, F., Cohnen, M., Furst, G., Godehardt, E., and Modder, U. (2004). Exclusion of brain lesions: is MR contrast medium required after a negative fluid-attenuated inversion recovery sequence? *British Journal of Radiology*, 77:183–188.

Schad, L. R., Bluml, S., and Zuna, I. (1993). MR tissue characterization of intracranial tumors by means of texture analysis. *Magnetic Resonance Imaging*, 11(6):889–896.

Schmidt, M., Levner, I., Greiner, R., Murtha, A., and Bistritz, A. (2005). Segmenting brain tumors using alignment-based features. In *IEEE International Conference on Machine learning and Applications (ICMLA2005)*, pages 215–220, Los Angeles,USA.

Schroeter, P., Vesin, J.-M., Langenberger, T., and Meuli, R. (1998). Robust parameter estimation of intensity distribution for brain magnetic resonance imaging. *IEEE Transactions on Medical Imaging*, 17(2):172–186.

Schulz, S., Hahn, U., , and Romacker, M. (2000). Modeling anatomical spatial relations with description logics. In *In Annual Symposium of the American Medical Informatics Association. Converging Information, Technology, and Health Care (AMIA 2000)*, pages 779–783, Los Angeles, CA, USA.

Seer (2007). www.training.seer.cancer.gov.

Serra, J. (1982). *Image analysis and mathematical morphology*. Academic Press Inc., London, UK, 2nd edition.

Sharon, E., Brandt, A., and Basri, R. (2001). Segmentation and boundary detection using multiscale intensity measurements. In *IEEE Conference on Computer Vision and Pattern Recognition*, volume 1, pages 469–476.

Shattuck, D. W. and Leahy, R. M. (2002). BrainSuite: an automated cortical surface identification tool. *Medical Image Analysis*, 6(2):129–142.

Shattuck, D. W., Sandor-Leahy, S. R., Schaper, K. A., Rottenberg, D. A., and Leahy, R. M. (2001). Magnetic resonance image tissue classification using a partial volume model. *NeuroImage*, 13(5):856–876.

Shen, D., Herskovits, E., and Davatzikos, C. (2001). An adaptative-focus statistical shape model for segmentation and shape modeling of 3D brain structures. *IEEE Transactions on Medical Imaging*, 20(4).

Shen, S., Sandham, W., Granat, M., and Sterr, A. (2005). MRI fuzzy segmentation of brain tissue using neighborhood attraction with neural-network optimization. *IEEE Transactions on Information Technology in Biomedicine*, 9(3):459–467.

Shen, S., Sandham, W. A., and Granat, M. H. (2003). Preprocessing and segmentation of brain magnetic resonance images. In *The 4th Annual IEEE Conf. on Information Technology Applications in Biomedicine*, pages 149–152, UK.

Shichun, P., Jian, L., and Guoping, Y. (2005). Neural integration approach for subcortical structure segmentation. In *International Conference on Neural Networks and Brain (ICNN&B2005)*, pages 244–248, Beijing, China.

Sled, J. G. and Pike, G. B. (1998). Understanding intensity non-uniformity in MRI. In *Medical Image Computing and Computer-Assisted Intervention (MICCAI)*, pages 614–622, Cambridge, MA, USA.

Smirniotopoulos, J. G. (1999). The new WHO classification of brain tumors. *Neuroimaging Clin N Am*, 9(4):595–613.

Smith, S. M. (2002). Fast robust automated brain extraction. *Human Brain Mapping*, 17(3):143–155.

Smith, S. M., Bannister, P. R., Beckmann, C. F., Brady, J. M., Clare, S., Flitney, D., nad M. Jenkinson, P. H., Leibovici, D., Ripley, B., Woolrich, M. W., and Zhang, Y. (2001). FSL: new tools for functional and structural brain image analysis. In *International Conference on Functional Mapping of the Human Brain*, volume 13 of *NeuroImage*, page 249, Brighton, UK.

Smith, S. M., Jenkinson, M., Woolrich, M. W., Beckmann, C. F., Behrens, T. E. J., Johansen-Berg, H., Bannister, P. R., Luca, M. D., Drobnjak, I., Flitney, D. E., Niazy, R., Saunders, J., Vickers, J., Zhang, Y., Stefano, N. D., Brady, J. M., and Matthews., P. M. (2004). Advances in functional and structural MR image analysis and implementation as FSL. *NeuroImage*, 23(S1):208–219.

Solomon, J., Butman, J. A., and Sood, A. (2006). Segmentation of brain tumors in 4D MR images using the hidden Markov model. *Computer Methods and Programs in Biomedicine*, 84:76–85.

Soltanian-Zadeh, H., Kharrat, M., and Donald, P. J. (2001). Polynomial transformation for MRI feature extraction. In *SPIE*, volume 4322, pages 1151–1161.

Soltanian-Zadeh, H., Windham, J. P., and Peck, D. J. (1996a). Optimal linear transformation for MRI feature extraction. In *Workshop on Mathematical Methods in Biomedical Image Analysis (MMBIA)*, pages 74–84.

Soltanian-Zadeh, H., Windham, J. P., and Peck, D. J. (1996b). Optimal linear transformation for MRI feature extraction. *IEEE Transactions on medical imaging*, 15(6):749–767.

Sonka, M., Tadikonda, S., and Collins, S. (1996). Knowledge-based interpretation of MR brain images. *IEEE Transactions on Medical Imaging*, 15(4):443–452.

Stark, D. D. and Bradley, W. G. (1999). *Magnetic Resonance Imaging*. Mosby.

Steen, R. G. (1992). Edema and tumor perfusion: Characterization by quantitative HMR imaging. *American Journal of Radiology*, 158:259–264.

Studholme, C., Hawkes, D., and Hill, D. (1998). A normalized entropy measure of 3D medical image alignment. *Medical Imaging*, 3338:132–143.

Swanson, K. R., Bridge, C., Murray, J. D., and Alvord, E. C. (2003). Virtual and real brain tumors: using mathematical modeling to quantify glioma growth and invasion. *Journal of the Neurological Sciences*, 216:1–10.

T. Woolsey, J. H. and Gado, M. (2003). *The Brain Atlas: A Visual Guide to the Human Central Nervous System*. Wiley, 2nd edition.

Taheri, S., Ong, S. H., and Chong, V. (2007). Threshold-based 3D tumor segmentation using level set (TSL). In *IEEE Workshop on Applications of Computer Vision (WACV 07)*, pages 45–51, Texas, USA.

Taron, M., Paragios, N., and Jolly, M.-P. (2005a). Modelling shapes with uncertainties: Higher order polynomials, variable bandwidthkernels and non parametric density estimation. In *IEEE International Conference on Computer Vision (ICCV2005)*, volume 2, pages 1659–1666.

Taron, M., Paragios, N., and Jolly, M.-P. (2005b). Uncertainty-driven non-parametric knowledge-based segmentation: The corpus callosum case. In *International Conference on Computer Vision (ICCV) workshop on Variational Geometric and Level Set Methods (VLSM)*, volume 3752 of *LNCS*, pages 198–209.

Terzopoulos, D. (1987). On matching deformable models to images. *Topical Meeting on Machine Vision*, 12:160–167.

Thirion, J.-P. (1998). Image matching as a diffusion process: an analogy with Maxwells demons. *Medical Image Analysis*, 2(3):243–260.

Tofts, P. (2002). *Quantitative MRI of the brain: Measuring Changes Caused by Disease*. Wiley.

Tolksdorf, R. and Bontas, E. P. (2004). Engineering a domain ontology in a semantic web retrieval system for pathology. In *GI Jahrestagung (2)*, volume 51 of *LNI*, pages 569–573.

Tsuchiya, K., Mizutani, Y., and Hachiya, J. (1996). Preliminary evaluation of fluid-attenuated inversion-recovery MR in the diagnosis of intracranial tumors. *American Journal of Neuroradiology*, 17(6):1081–1086.

Tuzikov, A., Colliot, O., and Bloch, I. (2003). Evaluation of the symmetry plane in 3D MR brain images. *Pattern Recognition Letters*, 24(14):2219–2233.

Udupa, J. K., LeBlanc, V. R., Schmidt, H., Imielinska, C., Saha, P. K., Grevera, G. J., Zhuge, Y., Currie, L. M., Molholt, P., and Jin, Y. (2002). A methodology for evaluating image segmentation algorithms. In *SPIE Medical Imaging 2002*, volume 4684, pages 266–277.

Udupa, J. K. and Samarasekera, S. (1996). Fuzzy connectedness and object definition: theory algorithms, and applications in image segmentation. *Graphical Models and Image Processing*, 58:246–261.

Uemura, K., Toyama, H., Baba, S., Kimura, Y., Senda, M., and Uchiyama, A. (2000). Generation of fractal dimension images and its application to automatic edge detection in brain MRI. *Computerized Medical Imaging and Graphics*, 24:73–85.

Vapnik, V. N. (1999). *Nature of Statistical Learning Theory*. Springer-Verlag (New York), 2nd edition.

Verard, L., Allain, P., Travere, J. M., Baron, J. C., and Bloyer, D. (1997). Fully automatic identification of AC and PC landmarks on brain MRI using scene analysis. *IEEE Transactions on Medical Imaging*, 16(5):610–616.

Vese, L. A. and Chan, T. F. (2002). A multiphase level set framework for image segmentation using the mumford and shah model. *International Journal of Computer Vision*, 50(3):271–293.

Vinitski, S., Iwanaga, T., Gonzalez, C., Andrews, D. G., Knobler, R., and Mack, J. (1997). Fast tissue segmentation based on a 4D feature map: Preliminary results. In *Image Analysis and Processing, 9th International Conference (ICIAP 97)*, volume 2, pages 445–452, Florence, Italy.

Warfield, S. K., Kaus, M., Jolesz, F. A., and Kikinis, R. (2000). Adaptive, template moderated, spatially varying statistical classification. *Medical Image Analysis*, 4(1):43–55.

Wasserman, R., Acharya, R., Sibata, C., and Shin, K. H. (1995). A data fusion approach to tumor delineation. In *International Conference on Image Processing(ICIP1995)*, pages 2476–2479. IEEE.

Waxman, S. G. (1999). *Correlative Neuroanatomy*. McGraw-Hill, 24th edition.

Wen, P. Y., Teoh, S. K., and Black, P. M. (2001). *Brain Tumors*. Churchill Livingstone, 2nd edition.

Woods, R. P., Mazziotta, J. C., and Cherry, S. R. (1993). MRI-PET registration with automated algorithm. *Journal of Computer Assisted Tomography*, 17(4):536–546.

Worth, A., Makris, N., Patti, M., Goodman, J., Hoge, E., Caviness, V., and Kennedy, J. (1998). Precise segmentation of the lateral ventricles and caudate nucleus in MR brain images using anatomically driven histograms. *IEEE Transactions on Medical Imaging*, 17(2):303–310.

W.Toga, A., Thompson, P. M., Mega, M. S., Narr, K. L., and Blanton, R. E. (2001). Probabilistic approaches for atlasing normal and disease-specific brain variability. *Anatomy and Embryology*, 204(4):267–282.

Xie, K., Yang, J., Zhang, Z. G., and Zhu, Y. M. (2005). Semi-automated brain tumor and edema segmentation using MRI. *European Journal of Radiology*, 56:12–19.

Xu, C., Pham, D. L., and Prince, J. L. (2000). *Handbook of Medical Imaging*, volume 2, chapter Medical Image Segmentation Using Deformable Models: Medical Image Processing and Analysis, pages 129–174. SPIE Press.

Xu, C. and Prince, J. L. (1998). Snakes, shapes and gradient vector flow. *IEEE Transactions on Image Processing*, 7(3):359–369.

Xue, J.-H., Ruan, S., Moretti, B., Revenu, M., and Bloyet, D. (2001). Knowledge-based segmentation and labelling of brain structures from MRI images. *Pattern Recognition Letters*, 22:395–405.

Yang, Y., Zheng, C., and Lin, P. (2004). Image thresholding via a modified fuzzy c-means algorithm. In *9th Iberoamerican Congress on Pattern Recognition (CIARP)*, pages 589–596.

Zhang, J. G., Ma, K. K., Er, M. H., and Chong, V. (2004). Tumor segmentation from magnetic resonance imaging by learning via one-class support vector machine. In *International Workshop on Advanced Image Technology (IWAIT 2004)*, pages 207–211, Singapore.

Zhou, J., Chan, K. L., Chong, V. F. H., and Krishnan, S. M. (2005). Extraction of brain tumor from MR images using one-class support vector machine. In *IEEE Conference on Engineering in Medicine and Biology*, pages 6411– 6414.

Zhu, Y. and Yang, H. (1997). Computerized tumor boundary detection using a Hopfield neural network. *IEEE Transactions on Medical Imaging*, 16(1):55–67.

Zijdenbos, A. P., Dawant, B. M., Margolin, R. A., and Palmer, A. C. (1994). Morphometric analysis of white matter lesions in MR images: Method and validation. *IEEE Transactions on Medical Imaging*, 13(4):716–724.

Zizzari, A., Seiffert, U., Michaelis, B., Gademann, G., and Swiderski, S. (2001). Detection of tumor in digital images of the brain. In *Proc. of the IASTED International Conference on Signal Processing, Pattern Recognition and Applications SPPRA 2001*, pages 132–137, Rhodes, Greece.

Zooka, J. M. and Iftekharuddin, K. M. (2005). Statistical analysis of fractal-based brain tumor detection algorithms. *Magnetic Resonance Imaging*, 23(5):671–678.

Index of citations by papers

Ahmed et al. [2002], xxix, 91, 93, 94
Algorri and Flores-Mangas [2004], 148
Ambroise et al. [1995], 42
Anlauf and Biehl [1989], 44
Armstrong et al. [2004], 9–13
Atif et al. [2006a], xlv, 162, 201
Atif et al. [2006b], l, 183
Aurdal [1997], 76, 77
Bach Cuadra et al. [2001], 145
Bach Cuadra et al. [2004], xli, 38, 48, 150
Baillard et al. [2001], 145
Barra and Boire [2001], 147
Belitz et al. [2006], 146
Bezdek et al. [1984], 187
Bezdek et al. [1987], 187
Bezdek. [1981], 187
Bloch et al. [2003], 147
Bloch [1999a], 158
Bloch [1999b], 159
Bloch [2005], xxxii, xlii, xliv, 147, 151, 156, 157
Bonneville et al. [2005], 27
Brown and Semelka [2003], 9
Burges [1998], 44
Burgun [2006], 153
Busch [1997], 38, 50
Bushberg et al. [2002], 9
Cai et al. [2007], 103
Capelle et al. [2004], 38, 53
Casati et al. [2003], 153
Caselles et al. [1993], 58
Cates et al. [2004], 39, 59
Chaplot et al. [2006], 38, 52
Chen and Metaxas [2003], xvii, 39, 61, 62
Ciofolo et al. [2004], 145
Clark et al. [1998], 38, 49
Clark [1997], 49
Clatz et al. [2005], 178
Cocosco et al. [1997], 93
Cointepas et al. [2001], 73, 74
Collins [1994], 144
Colliot et al. [2006], xxxii–xxxiv, xli, xlii, xliv, xlix, 113, 121, 147, 148, 151, 156, 159, 170, 183
Cootes et al. [1995], 145, 147
Corcho et al. [2003], 153
Corso et al. [2006], 38, 41, 102, 127
Cortes and Vapnik [1995], 44
Cristani and Cuel [2005], 153
Curran and O'connor [2005], 26
Dam and Letteboer [2004], 46
Dameron et al. [2004], 153
Dasiopoulou et al. [2005], 153
Dauguet et al. [2004], 68
Daumas-Duport et al. [200], 15, 17
Daumas-Duport [1992], 17
Dawant et al. [1999a], 144, 147, 150
Dawant et al. [1999b], 150
Dawant et al. [2002], 38, 48, 150
Delingette [1999], 113
Dickson et al. [1997], 38, 52
Dominey et al. [2004], 153
Donnelly et al. [2006], 153
Doolittle [2004], 14, 16
Dou et al. [2007], 38, 54, 102, 127
Droske et al. [2001], 39, 58
Dubois and Prade [1980], 157
Duta and Sonka [1998], 146
Emedicine [2005], 17–19, 21, 23, 24, 26, 27
Engelhard et al. [2003], 21, 22
Engelhard [2001], 25
Feng and Chen [2004], 91
Firenze and Morasso [1993], 45
Fischl et al. [2002], 148

Fletcher-Heath et al. [2001], 49
Fouquier et al. [2007], 170
Freeman [1975], 147
Garcia and Moreno [2004], 38, 44
Geraud [1998], 144, 147
Gerig et al. [2001], 191
Gering [2003], 38, 43, 56
Gibbs et al. [1996], 38, 46
Gomez-Perez et al. [2004], 152, 153
Grimson and Golland [2005], 47
Gruber [1993], 152
Haacke et al. [1999], 9
Haarslev and Moller [2001], 164
Hajnal et al. [1995], 69
Hall et al. [1992], 52
Han et al. [2005], 153
Hata et al. [2005], 38, 54
Held et al. [1997], 43
Henson et al. [2005], 17, 22
Herlidou-Meme et al. [2003], 38, 50
Herskovits et al. [2001], 10
Ho et al. [2002], 39, 62
Hoppner [2003], 187
Hu and Collins [2007], 146
Hudelot et al. [2007], xliii, 153–156
Iftekharuddin et al. [2003], 38, 55
Iosifescu et al. [1997], 144
Jain et al. [1999], 45
Jenkinson et al. [2002], 70
Jiang et al. [2004], 39, 57
Jiji and Ganesan [2005], 49
Julià-Sapé et al. [206], l, 183
Kantor et al. [2001], 17, 18
Kass et al. [1988], xxxiii, 57, 113
Kaus et al. [1999], 38, 40, 47
Kaus et al. [2001], 38, 40, 47
Kelemen et al. [1999], 146
Kernohan et al. [1949], 14, 15
Khotanlou et al. [2005], xxix, 96, 201
Khotanlou et al. [2006], 148, 201
Khotanlou et al. [2007a], xlv, 148, 162, 201
Khotanlou et al. [2007b], xxix, xxx, 105, 201
Khotanlou et al. [2007c], xxix, 105, 201
Kjaer et al. [1995], 50
Klien and Lutz [2005], 153
Krishnapuram and Keller [1993], 45, 89, 90
Krishnapuram and Keller [1996], 45
Kruggel and Lohmann [1997], 79
Kufe et al. [2003], 8, 9, 11
Kyriacou et al. [1999], xl, 38, 48, 149
Law et al. [2001], 39, 60
Law et al. [2002], 61
Lee et al. [2004], 9
Lee et al. [2005], 38, 44
Leemput et al. [2001], 42
Lefohn et al. [2003], 39, 59
Lerski et al. [1993], 50
Letteboer et al. [2004], 38, 46
Liew and H. Yan [2003], 91
Linguraru et al. [2007], 145
Liu et al. [1996], 72
Liu et al. [2005], 38, 54
Lobato et al. [1996], 25
Lopes and Laws [2002], 17
Luo et al. [2003], 39, 57
Ma and Staunton [2007], 91
Magnotta et al. [2003], 145
Mahesh and Tse [2004], 18
Mahmoud-Ghoneima et al. [2003], 14, 50
Maillot and Thonnat [2007], 153
Maintz and Viergever [1998], 69
Maksoud et al. [2002], 23
Malladi et al. [1995], 58
Mancas and Gosselin [2004], 38, 46
Mandelbrot [1982], 55
Mangin et al. [1998], 73, 74, 79, 96
Mangin [2000], 68
Marieb [2000], 7
Marquet et al. [2007], 153
Masulli and Schenone [1999], 38, 45
Meijering [2002], 70
Mohamed et al. [2005], 149
Moon et al. [2002], 38, 42, 47
Moonis et al. [2002], 38, 54
Moon [1996], 42
Nain et al. [2007], 146

Nempont et al. [2007], l, 184
Nientiedt [2007], 153
Niu [2006], 58
Nowinski and Belov [2005], xl, 150
Osher and Sethian [1988], 58
Pal et al. [1997], 90
Pal et al. [2005], xxviii, 89, 90
Peng et al. [2005], 79
Perona and Malik [1990], 76
Pham et al. [2000], 47, 52
Pham [2001], 91
Phillips et al. [1995], 38, 45
Piquet et al. [1996], 113
Pitiot et al. [2002], 146
Plotkin and Batchelor [2001], 24
Pohl et al. [2004], 47
Pollo et al. [2005], 150
Poupon et al. [1998], 145
Powell et al. [2008], 148
Prastawa et al. [2003], 42, 47
Prastawa et al. [2004], 38, 42, 47, 102, 127
Prastawa et al. [2005], 13
Protégé [2007], xliii–xlv, 154
Reddick et al. [1998], 52
Rexilius et al. [2007], 38, 46
Ricci and Dungan [2001], 8, 11
Ringertz [1950], 15
Roche et al. [1998], 69
Rohlfing et al. [2004], 47
Rosse and Mejino [2003], xliii, 153, 154
Ruan et al. [2007], 38, 44, 53
Russel and Rubinstein [1971], 14
Sabin [1987], 187
Saha and Udupa [2001], 54
Saleh et al. [2004], 10
Schad et al. [1993], 50
Schmidt et al. [2005], 44
Schroeter et al. [1998], 79
Schulz et al. [2000], 153
Seer [2007], 28
Serra [1982], 46
Sharon et al. [2001], 42
Shattuck and Leahy [2002], 73, 74
Shattuck et al. [2001], 73, 74
Shen et al. [2001], 146
Shen et al. [2003], 38, 45
Shen et al. [2005], 91
Shichun et al. [2005], 148
Sled and Pike [1998], 68
Smirniotopoulos [1999], 15, 17
Smith et al. [2001], 73, 74
Smith et al. [2004], 70
Smith [2002], 73, 74
Solomon et al. [2006], 38, 43
Soltanian-Zadeh et al. [1996a], 38, 51
Soltanian-Zadeh et al. [1996b], 51
Soltanian-Zadeh et al. [2001], 38, 51
Sonka et al. [1996], 148
Stark and Bradley [1999], 9, 10
Steen [1992], 10
Studholme et al. [1998], 70
Swanson et al. [2003], 178
T. Woolsey and Gado [2003], 6
Taheri et al. [2007], 39, 62
Taron et al. [2005a], 146
Taron et al. [2005b], 146
Terzopoulos [1987], 57
Thirion [1998], 48, 144
Tofts [2002], 9
Tolksdorf and Bontas [2004], 153
Tsuchiya et al. [1996], 10
Tuzikov et al. [2003], xxx, 72
Udupa and Samarasekera [1996], 54
Udupa et al. [2002], 189
Uemura et al. [2000], 38, 55
Vapnik [1999], 44
Verard et al. [1997], 79
Vese and Chan [2002], 163, 195, 197
Vinitski et al. [1997], 38, 40, 56
W.Toga et al. [2001], 35
Warfield et al. [2000], 38, 40, 47
Wasserman et al. [1995], 38, 53
Waxman [1999], 5, 6
Wen et al. [2001], 12, 17, 18, 20, 22–26
Woods et al. [1993], 69
Worth et al. [1998], 148
Xie et al. [2005], 39, 59
Xu and Prince [1998], 57, 115

Xu et al. [2000], xxxiii, 57–59, 113
Xue et al. [2001], 145
Yang et al. [2004], 146
Zhang et al. [2004], 38, 44
Zhou et al. [2005], 38, 44
Zhu and Yang [1997], 39, 60
Zijdenbos et al. [1994], 171, 190
Zizzari et al. [2001], 38, 50
Zooka and Iftekharuddin [2005], 55

Glossary

ANN Artificial Neural Network, 36

BBB Blood Brain Barrier, 13

CE-T1w Contrast Enhanced T1-Weighted, 10, 65
CNS Central Nervous System, 5
COM Co-Occurrence Matrix, 50
CSF Cerebrospinal Fluid, 5
CT Computed Tomography, 8

EM Expectation Maximization, 40

FCM Fuzzy C-Mean, 89
FD Fractal Dimension, 55
FEN Full-Enhanced, xxiv
FLAIR Fluid-Attenuated Inversion Recovery, 10
FMA Foundational Model of Anatomy, 153
fMRI Functional Magnetic Resonance Imaging, 12
FPCM Fuzzy Possibilistic C-Mean, 89

GBM Glioblastoma Multiform, 17
GGVF Generalized Gradient Vector Flow, 113
GIS Geographic Information Systems, 153
GM Gray Matter, 5
GMM Gaussian Mixture Model, 79
GVF Gradient Vector Flow, 57

JPA Juvenile Pilocytic Astrocytoma, 8

KNN K-Nearest Neighbors, 40

MAP Maximum A Posteriori, 146
MI Mutual Information, 69
MLG Model of Lesion Growth, 150

MLP Multilayer Perceptron, 52
MPFCM Modified Possibilistic Fuzzy C-Mean, 91
MR Magnetic Resonance, 5
MRA MR Angiography, 12
MRF Markov Random Field, 91
MRS Magnetic Resonance Spectroscopy, 12

NEN Non-Enhanced, xxiv
NMI Normalized Mutual Information, 69

PCA Principal Component Analysis, 50
PCM Possibilistic C-Mean, 89
PDM Point Distribution Model, 145
PET Positron Emission Tomographic, 8
PFCM Possibilistic Fuzzy C-Mean, 90

REN Ring-Enhanced, xxiv
ROI Region Of Interest, 46

SAD Seeded Atlas Deformation, 150
SE Spin-Echo, 10
SOM Self-Organizing Map, 52
SPECT Single Photon Emission Computed Tomographic, 8
SVM Support Vector Machine, 40

T1w T1-Weighted, 8
T2w T2-Weighted, 8

WHO World Health Organization, 14
WM White Matter, 5